Aalborg University

Structural and Civil Engineering

CFD analysis of wave-chamber interaction on the Floating Power Plant hybrid wind-wave platform

Master's thesis

June, 2020

Author:
Miguel Antón Aguilar

Supervisors:
Claes Eskilsson
Morten Bech Kramer

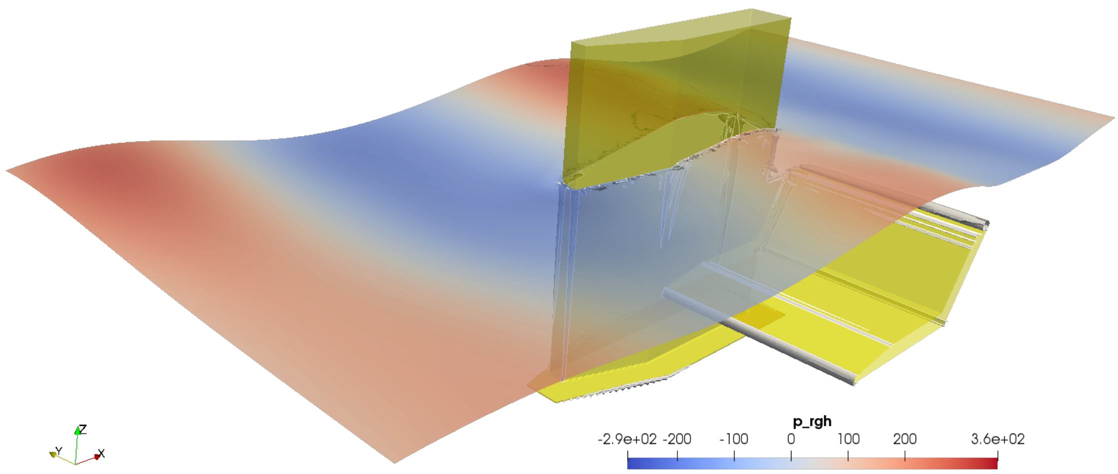

AALBORG UNIVERSITY
STUDENT REPORT

The Faculty of Engineering and Science
Structural & Civil Engineering
Thomas Manns Vej 23
9220 Aalborg SØ
http://www.civil.aau.dk

Title:

CFD analysis of wave-chamber interaction on the Floating Power Plant hybrid wind-wave platform

Project:

MSc 3rd and 4th Semester - Master Thesis

Project period:

September 1st 2019 - June 10th 2020

Author:

Miguel Anton

Supervisors:

Claes Eskilsson
Morten Bech Kramer

Main report: 75 pages
Finished 10-06-2020

Abstract:

The aim of this project is to quantify the wave amplification factor and also to understand the behaviour of the hydrodynamics inside the chamber of the hybrid P80 platform, designed by Floating Power Plant (FPP). It is the first time this topic has been analyzed applying non-linear methods based on CFD, which have been designed taking into account experimental results conducted at Aalborg University by FPP. The methodology applied in this project is based on two major steps, (i) the solution-verification and (ii) the validation of the numerical model.

In the solution-verification step, the temporal and spatial discretization errors are quantified independently by measuring the uncertainties of the numerical model.

The validation step was divided in two stages. The first one takes only into account waves' propagation, whereas the second stage focuses on the validation of the numerical model including the chamber.

Once the model was validated, multiple simulations with different chamber configurations were carried out. At this point, several different parameters were analyzed such as, the wave amplification factor, the free surface elevation, vortical structures, etc. It is worth mentioning, that there was one configuration that was compared with a linear model called WAMIT. In addition to this, a full scale model was simulated to find out whether the results from previous simulations are valid.

This project shows that the wave amplification factor is mainly influenced by three parameters: (i) the wave periods, (ii) the location inside the chamber, and (iii) the shape of the chamber.

Preface

This Master's Thesis in Structural and Civil Engineering at Aalborg University was written from September 2019 till 10th June 2020 by Miguel Antón Aguilar.

The Master's thesis consists of a main report and an appendix.

The Main Report is divided in 4 parts that include a total of 8 chapters. Each part separates the project into different topics, which are: Part one, the Introduction. This part consists of three chapters, where the background of the problem and the aim of this project is introduced, as well as a description of the numerical model is presented and the experimental setup. Part two, Verification and Validation. This part is dived into two chapters that explain the verification and validation procedure of the numerical model. Part three, the Analysis of the Simulations, which explains the results obtained. The part, the Epilogue, where the conclusions and the future work chapters are included.

In the Appendix extra documentation is incorporated to give the reader a deeper understanding of the conclusions obtained on the main report. Moreover, relevant physical theories are included to better explain the complex procedures that has been applied to this master's thesis. The chapters for the appendix are named by the letters of the alphabet, written as A.1, A.2, B.1, B.2... when making the reference to the appendix during the main report.

The author of this report would like to thank the supervisors Claes Eskilsson from AAU and Morten Bech Kramer from AAU/Floating Power Plant and the research assistant at AAU Jacob Andersen for their excellent supervision and input to this project. The author is also very grateful to Floating Power Plant for providing a computer for CFD simulations.

Reading guide

The report uses the harvard-method literature reference, where sources that are used refers to the author's last name and the year of the publication in brackets - Surname [Year]. Tables and figures produced by the author have no sources. In case of a figure or table taken from a source, but which has been modified by the author, a reference to the source is written with a same reference format as mentioned above.

Tables, figures and equations are numbered by chapter, number and location in the chapter.

Miguel Anton

Table of Contents

Part I

Introduction

1 Introduction

This project aims to apply computational fluid dynamics (CFD) modelling to analyze and understand the complex hydrodynamics involved inside the chamber of a hybrid floating wind and wave platform, called P80 multi-used platform. The P80 is a state-of-the-art hybrid platform, designed by the company Floating Power Plant (FPP), that can convert energy from wind and wave resources into electricity on a semi-submersible platform (Illustrated in Figure 1.2). In this chapter the description of the project is introduced, presenting the background of the offshore renewable industry and the FPP's P80 platform. Moreover, an overview of the wind and wave energy resources available in the world is introduced, where this concept can make a significant improvement in the way of harnessing the renewable energy power and lowering the cost of energy.

1.1 Historical context

In the last few decades, the the UNFCCC has been raising awareness to third parties about climate change and global warming. Subsequently, the Kyoto Protocol (1997) and Paris Agreement (2015) brought all nations into a common cause to undertake ambitious efforts to combat climate change, [UNFCCC, 2019]. At the european level, the EU Parliament approved to set an EU renewable energy target of 35% of the total consumption, [MEPs, 17-01-2018]. In addition to this, the power production sector is also changing the course of how to generate energy, from fossil fuels into a more environmentally friendly production of energy. At this point is where renewable energy resources are fundamental to cope with this global issue.

The development and industrialization of countries have had a great impact on energy demand (Figure 1.1a). In the near future a higher demand on energy will be expected, with the corresponding growth of pollution and CO_2 emissions. Therefore, a wide investment on researching new renewable sources has been carried out during the last years. According to IEA [2019]:

> Since 1990, renewable energy sources have grown at an average annual rate of 2.0%, which is slightly higher than the growth rate of world TPES, 1.7%. Growth has been especially high for solar photovoltaic and wind power, which grew at average annual rates of 37.0% and 23.4%, respectively, from very low bases in 1990

In 2017 renewable energy represented only 13.6% of the world total primary energy supply, see Figure 1.1b. Nevertheless, this value is expected to increase in the following years due to i) higher demands on energy supply, and ii) changes on politics and awareness.

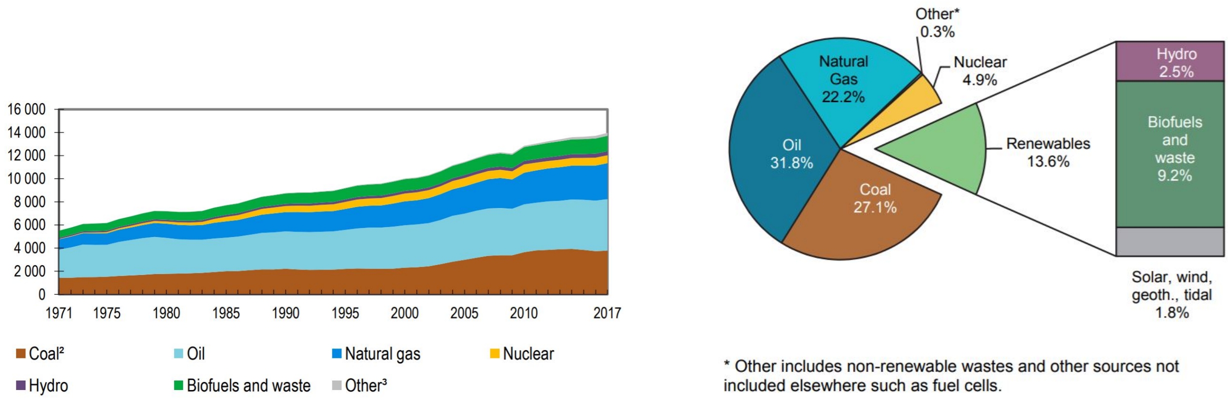

(a) (b)

Figure 1.1: a) World total primary energy supply (TPES) by source (1971 to 2017) - Other. Includes geothermal, solar, wind, tide/wave/ocean, heat and other sources, IEA [2019] b) 2017 fuel shares in world total primary energy supply, IEA [2019]

1.2 Offshore renewable energy

In the last few decades, due to different reasons, a new tendency of off-shore wind farm has been established. Nowadays this industry is rapidly expanding. In 2019 there was a total of 146 offshore wind farms worldwide, with a total of 27.2 GW installed, where 5.2 GW of it went into operation during 2019 [WFO, 2020].

In this early stage of the off-shore renewable industry, shallow water locations have been for many years the preference, as it is technically cheaper and easier to construct. However, due to a higher demand on sustainable energy supply, this sector is moving to deeper waters, which will open a large amount of new markets all around the world. As an example, according to AGI [2020], half of the United States' population lives in coastal areas, concentrated in major coastal cities, where deep waters are predominant. Some other locations such us Western Europe, West coast of South America, Japan, the East coast of China, etc. are important markets that floating offshore wind farms can help to meet the energy needs from nearby sources. Floating off-shore wind farms are entering the commercialization stage with the Kincardine and the Windfloat Atlantic projects under construction in UK and Portugal, respectively, and the 30MW Hywind farm in operation outside Scotland.

Deep waters locations increase the total cost of energy, therefore the integration of Wave Energy Converters (WECs) into offshore wind farms can help to reduce it. The co-location of two different system is most often contemplated when thinking about combining offshore wind and wave energy. However, a hybrid system is a more advanced approach - it combines in the same structure one or more wind turbines and wave energy converters (Pérez-Collazo et al. [2015]). According to Watson et al. [2019], while standard floating wind turbines have reached a technology readiness level (TRL) of 8-9, the hybrid systems are generally at a lower TRLs (4-5).

1.3 Floating Power Plant

Floating Power Plant A/S (FPP) is developing a state-of-the-art floating hybrid wind-wave energy concept, called P80. This technology consists of a semi-submersible platform that combines a wind turbine generator (5-8 MW) and a wave energy converter (2-3.6 MW), see Figure 1.2.

Previous to the P80 platform, FPP designed a hybrid platform called P37, which was field-tested for several years at a 1:25 scale. This first floating structure was the only multi-used platform that successfully delivered power to the grid by two combined resources, wind and waves. P80 device is a second generation hybrid platform, which aims to optimize multiple aspects of the P37 platform thanks to the knowledge gained from several years of tests and investigation.

This combination of two different energy resources, wind and waves, can provide a lower cost of energy in the long run. The platform was preliminary designed to have four absorbers, having each of them their own chamber and Power Take Off system (PTO). Moreover, the P80 is able to freely rotate around the mooring turret, enabling the platform to face incoming waves. Furthermore, the wind turbine always faces the incoming wind as it rotates independently from the platform.

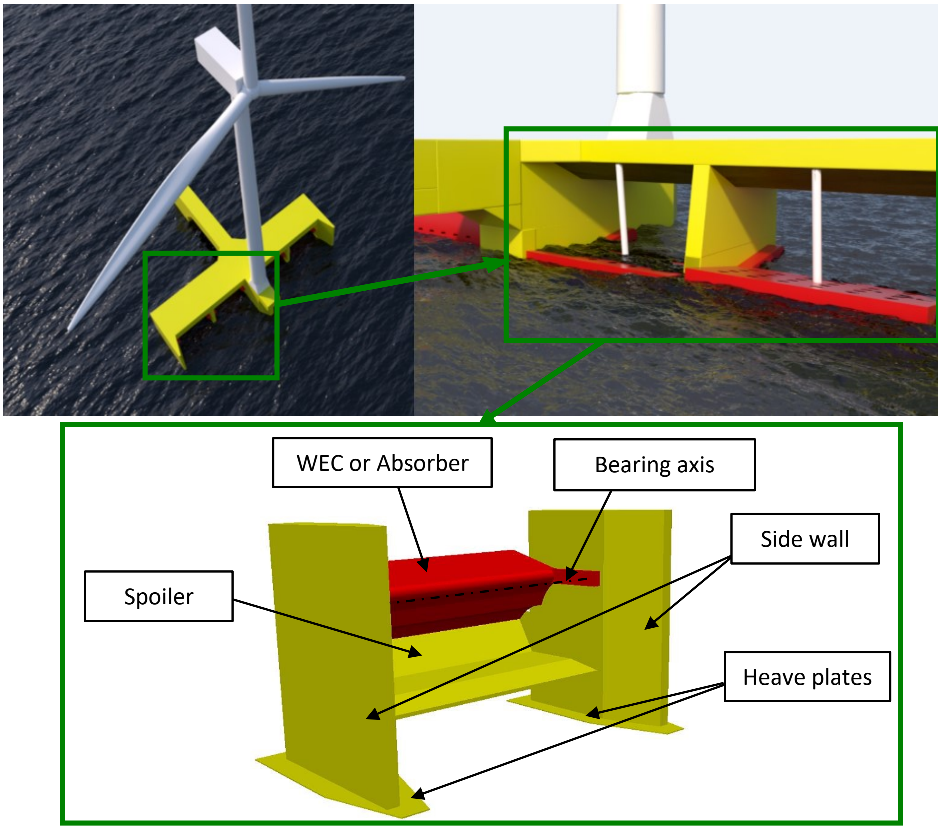

Figure 1.2: Floating Power Plant P80 with A4 chamber configuration with the absorber or WEC included

The mooring and the platform are designed to face the dominant incident waves. Therefore, as waves reach to the platform, the absorber starts to oscillate around the hinge, generating kinematic energy, which is then transformed into electricity by a PTO system. Hence, this wave-structure interaction generates a pitch motion. When the system comes into resonance with the waves, the motion is amplified and the energy production rises. This phenomenon is what aims to be better understood.

In order to obtain a better perspective of the FPP P80 multi-use platform system, Figure 1.2 illustrates a simplification of the A4 chamber model used for CFD and experiments. The model eliminates the central wall that separates two independent absorbers and merges them into a single absorber. From Figure 1.2 seven main parts can be depicted from the chamber configuration. First, the absorber (also referred as WEC in this report) is the moving part. This element aims to absorb incoming waves by oscillating around the bearing axis. Second, the chamber structure it self, which is made of three main elements: (i) side walls, (ii) heave plates and (iii) spoiler. Side walls are vertical structures that separates the area of action for each of the WECs and fix the absorber to the structure so that it can oscillate around the bearing axis. Heave plates are horizontal elements that reduce the heave motion of the structure. Lastly, the spoiler is composed of two plates, one horizontal and one sloped. This element is the main structure that interacts with the waves to increase the wave amplitude. This whole structure is analyzed in different configurations.

1.3.1 Previous work on the FPP device

Off-shore structures have been under investigation for many years, with the main focus on the Oil & Gas industry. Nowadays, the knowledge acquired from this industry is also applied on many other areas, such as fixed and floating structures on the renewable energy sector.

Due to the complexity of the wave-structure interaction and the lack of analytical methods for complex problems, experimental techniques have been widely used to understand them. However, not only empirical methods are not easy to implement, as several factors related to scaling must be taken into account for the analysis, but also physical experiments can be expensive. Consequently, new techniques have been developed over the last few years, including numerical models such as CFD techniques, that can help to understand the complexity of the wave-structure interaction, Westphalen et al. [2014]. Nevertheless, this method always has to be validated with experimental results.

The P80 platform is a complex structure that has been under investigation by different approaches in order to understand the interaction of the body with the waves. Some studies were conducted both, numerically and experimentally, Heras et al. [2019] and Wilhelm [2017] and also a semi-analytic method was developed Georgousis [2019].

From previous analysis, it was found that the response amplitude operator (RAO) depends not only on the absorber configuration, but also on the chamber, as two closed bodies can have a critical impact on the behavior of each one. Therefore, a more detailed analysis was carried out by a numerical wave tank (NWT) to obtain a better understanding of the hydrodynamics involved on the system, Wilhelm [2017] and then compared to experimental results and linear models from a software called WAMIT, Heras et al. [2019]. As it can be seen in Figures 1.3, it was found a second resonance peak when the chamber and the WEC are installed together.

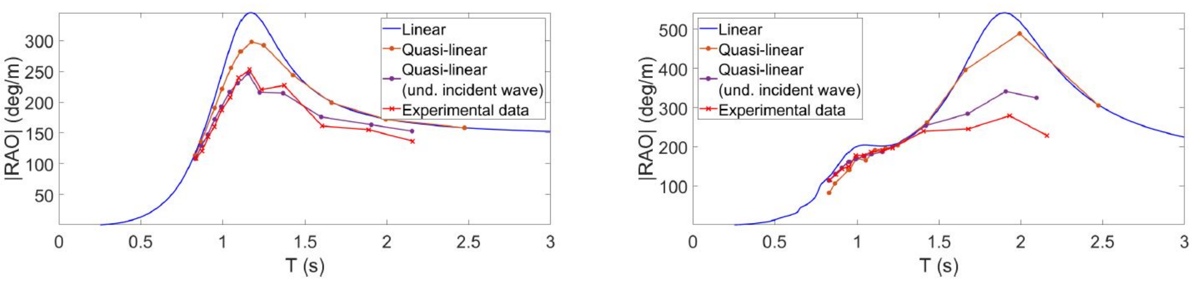

Figure 1.3: Response Amplitude Operator for WEC only (Left) and WEC and Chamber (Right), Heras et al. [2019]

It is believed that while the first peak is caused by the geometry of the absorber and other properties related to this part of the structure, the second peak is caused by the chamber's geometry. For this reason, different chamber configurations were tested in WAMIT, [Lee, 1995], in order to obtain a better understanding of the second resonance peak, Heras et al. [2019]. In this project different approaches were carried out: linear potential flow, quasi-linear, which only takes into account some non-linear effects, and a linear model with some non-linear effect included, Folley [2016]. From this analysis it was found that non-linear effects have to be considered to make better predictions of the RAO. Therefore, neglecting non-linearity effects might lead into an overestimation of the absorber's power production.

In order to consider those non-linear effects, a CFD method, based on Reynolds averaged Navier-Stokes (RANS), is implemented. This method accounts for non-linearities, which gives an advantage compared to potential flow codes. In Wilhelm [2017], a NWT with the WEC is calculated by an open source software called OpenFOAM (Open Source Field Operation and Manipulation). This software has been used for numerous works. Wilhelm [2017] also considers the different absorbers and chambers configurations and a study of the influence on RAO by the interaction between two closed bodies was conducted. A strong dependency between the chamber and absorber's configuration and the resonance peaks was found, see Figure 1.4, which also matches with Heras et al. [2019] conclusions.

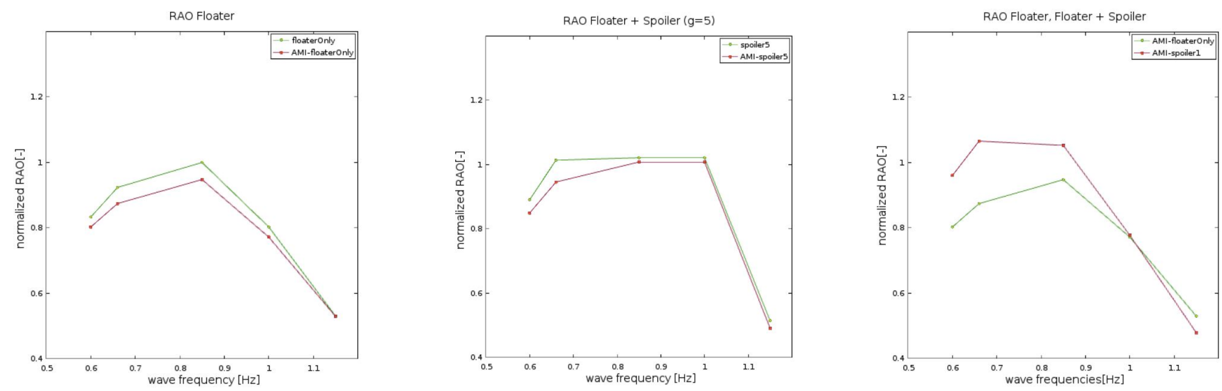

(a) (b) (c)

Figure 1.4: RAO for different configuration Wilhelm [2017] - a) Only spoiler b) Spoiler and chamber configuration 5 c) Spoiler and chamber configuration 1

Last, on Georgousis [2019] a semi-analytical method was developed, and then compared against results from the WAMIT software for its validation. This project aims to give a different approach on the understanding of several potential coefficients, with the main interest on the wave amplification parameter inside the chamber. On Georgousis [2019] the impact of different chamber geometries, such as length, width, inclination, etc. was investigated, giving good results on the resonance frequency, but needing more calibration studies to minimize uncertainties on the amplitudes, see Figures 1.5.

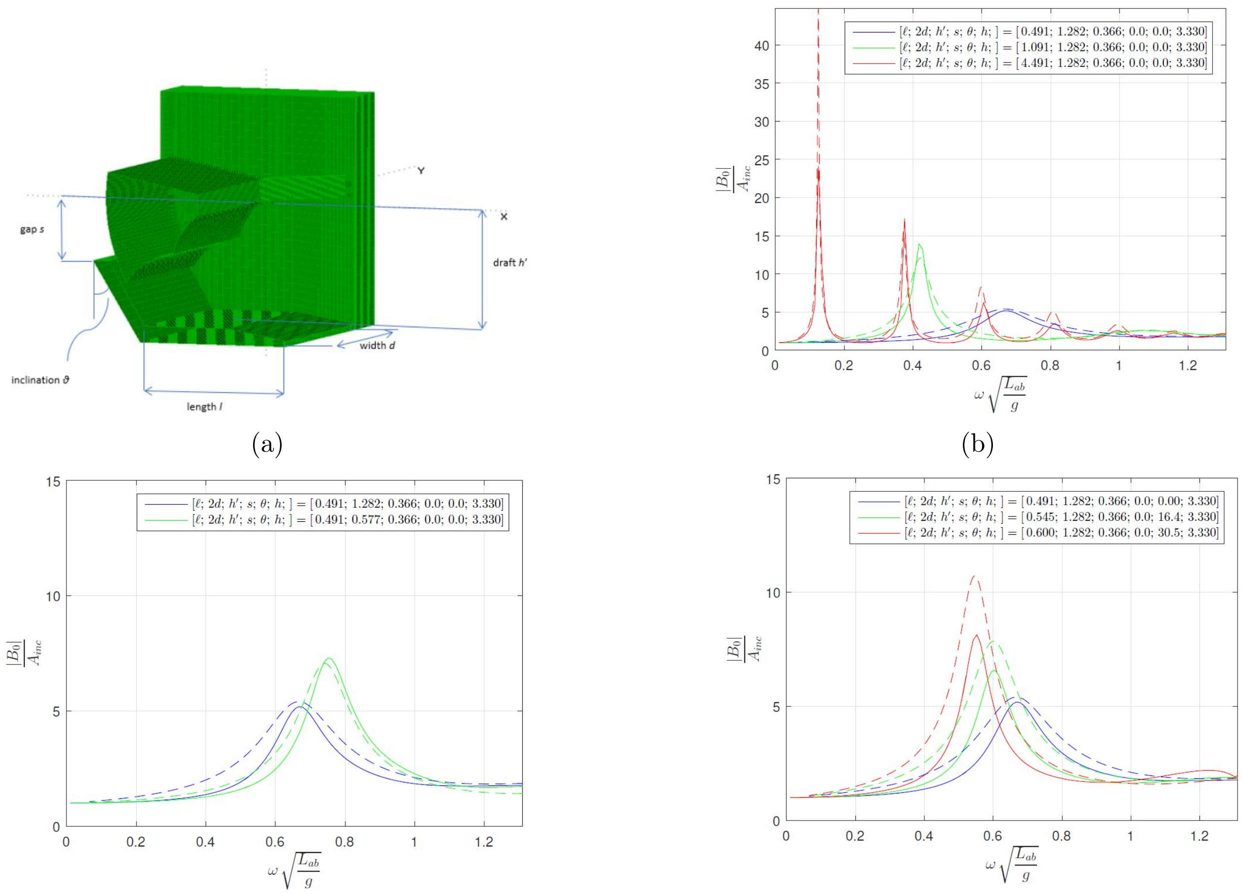

(a) (b) (c) (d)

Figure 1.5: Variation of the wave amplitude inside the chamber with different parameters, solid line: numerical, dash line: semi-analytical Georgousis [2019] - a) Chamber shape b) Length variation c) Width variation 5 d) Angle variation

1.4 Problem statement

As it is described in Section 1.3, P80 is a hybrid platform that combines wind and waves energies. The goal of this master thesis is to better understand the wave-structure interaction by measuring the wave amplification factor inside the chamber, see Figure 1.6. The interaction between the chamber, the absorber, and the waves has been under investigation for some years. In Section 1.3.1, the most recent projects related to wave amplification factor and RAO on P80 platform are explained. In addition to this, the project also pursues to clarify how waves interacts with different chamber configurations using numerical modelling methods.

From Heras et al. [2019] and Wilhelm [2017] it was found that linear models are not reliable enough for understanding this specific and complex wave-structure interaction. In order to cope with this complex field, a more sophisticate method that accounts for non-linearities is implemented by CFD technique. Similarly to Wilhelm [2017], *OpenFOAM* is the software used for modelling. This program includes the possibility of modelling and calculate a wave-structure interaction problem. This technique is used to test different chamber configurations and sea states, see Appendix B and C.1.

(a)

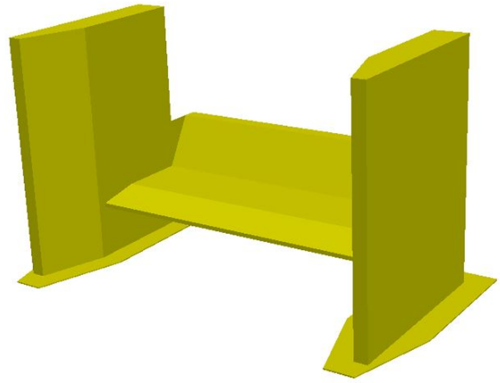

(b)

Figure 1.6: Chamber structure at A4 configuration, see Appendix B - a) Front view b) Perspective view

As explained before, previous projects were more focused on the response amplitude operator (RAO) of the absorber rather than the wave amplitude inside the chamber. However, it is known that both, wave amplitude and RAO, are directly connected. Then, wave-chamber interactions need to be investigated to acquire a better prediction of the absorber RAO for different chamber configurations.

Several investigations on the RAO for both cases (WEC only and WEC with chamber) were carried out, see Figure 1.3. On the one hand, it was found that on the only-WEC configuration, the RAO was small and narrow, having only one resonance peak. On the other hand, in the configuration that combines the WEC and the chamber, a wider and higher RAO was observed. In this case the wider response is characterized by two peaks: the first peak is associated with the absorber, while the second peak is assumed to be caused by the hydrodynamic interaction between both bodies.

Hence, the problem can be formulated as a simplification of the whole P80 structure by analyzing only one chamber separately from the rest of the system. In this manner, the problem that is intended to be solved is the interaction between the waves and a fixed body.

Then, the aim of this report is: **to conduct a study, by CFD modelling, of the wave-chamber interaction to understand the wave amplification factor and the behaviour of the hydrodynamics inside the chamber with different chamber configurations.** Consequently, this analysis is crucial for the understanding of the absorber's RAO. Specifically, it is necessary to quantify the effects of different chamber configuration to better understand the RAO's resonance peaks.

Moreover, a sound knowledge of the wave-structure interaction, can lead to the understanding on how to cover wider sea-states. So, the chamber and the absorber could be designed based on the met-ocean conditions, where the P80 multi-used platform will be located. This could increase the power output achieved by a designed system that would be in resonance with the desired sea state conditions.

Numerical Wave Tank 2

This chapter aims to explain the essential aspects of nonlinear viscous flow models to understand a complex wave-structure interaction problem. In this project an open-source software, OpenFOAM, is used. Furthermore, the steps followed to calculate the geometry, the mesh, hydrodynamic motions, etc are explained.

2.1 Computational Fluid Dynamics (CFD) models

The discipline of CFD has become a viable numerical approach for the simulation of the behaviour of WECs, due to computers are becoming more and more powerful. This method is an excellent tool to study the WEC's design, optimize its performance and many other characteristics. However, still many issues are needed to be resolved to reach the full potential of suitable applications of CFD models.

In CFD modelling, the mathematical expression of the physical laws that describes the fluid flow are based on partial differential equations (PDEs). As it is explained by Folley [2016], the most common equations are the Navier-Stokes equations and the continuity equation, Drazin and Riley [2006]. Also, to complete the mathematical model, not only internal and external boundary conditions are needed, so the geometry of the structure can be defined, but the wave field and the initial conditions too. Then, the system of PDEs has to be solved by approximating solutions via numerical algorithms, which are called solvers, due to the fact that analytical solutions cannot be used for this porpoise. The solution of the relevant variables are calculated at discrete times as the simulation is progressing at discrete points in the computational domain. The accuracy of this variables is dependant on the discretization scheme or the numerical algorithm used.

The most used approach to solve those equations in a CFD model is to discretize the equation stated in the Eulerian frame using the finite volume method (FVM). In the Eulerian approach the computational domain is discretized by a mesh, which contains a finite set of points, where the approximate solutions are calculated. Moreover, the FVM is calculated based on the Gauss divergence theorem, which express spatial partial derivatives as surface integrals, see Causon et al. [2011]. This FVM according to Folley [2016], is widely applied on WEC simulations due to its consistence on physical treatment of the flows across cell boundaries and its geometric flexibility.

Therefore, CFD model is used in this report to generate a numerical wave tank (NWT), which is used for the understanding of wave-chamber interaction. In order to compute this calculations the OpenFOAM framework is used to generate a NWT with different chamber configurations.

2.2 Governing equations

In CFD modelling the discretization of fundamental equations are carried out using control volume scheme, then, the so-called transport equation is used to represent all relevant fluid mechanics equations, such us continuity, momentum and energy equations. The transport of a general property Φ by diffusion and convection in a compressible Newtonian fluid flow is defined in Equation 2.1:

$$\frac{\partial(\rho\phi)}{\partial t} + \nabla \cdot \rho\phi\mathbf{u} = \nabla \cdot \Gamma \operatorname{grad} \phi + S_\phi \tag{2.1}$$

where,

Equation 2.1 is obtained when *Reynolds Transport Theorem* (RTT) is applied to a differential control volume. Therefore, the first term on Equation 2.1 represents the time rate of change of a property called Φ within a control volume. The second and third term describes the convection and diffusion flux of Φ from the control surfaces, where Γ represent the diffusion coefficient. The last term represents any source or sink of the property Φ in the control volume. Once all parts are defined in Equation 2.1 it can be seen that by replacing Φ by any scalar quantity like temperature, pressure, etc, the transport equation for that property is calculated. The continuity equation for an incompressible and steady fluid flow is obtained by replacing $\Phi = 1$, then the equation of conservation of mass is obtained as:

$$\nabla \cdot \mathbf{u} = 0 \tag{2.2}$$

And, when Φ is replaced by the value of the velocity vector $\mathbf{u}$, and also by selecting the correct values for diffusion coefficient and source term, the momentum equations for an incompressible fluid is obtained as:

$$\frac{\partial}{\partial t}(\rho\mathbf{u}) + \nabla \cdot (\rho\mathbf{u}\mathbf{u}) = -\nabla p + \nabla \cdot \mathbf{S} + \rho\mathbf{f_b} \tag{2.3}$$

Equations above are the Navier-Stokes equations with the single fluid assumption. Where $\mathbf{u}$ is the fluid velocity, p is the pressure, ρ is the mixture density, g is the gravity, $\mathbf{S}$ is the viscous stress tensor and f_b is the body force.

2.3 Free surface modeling

Usually, the dynamic and kinematic boundary conditions have to be applied at the interface, but this is still unknown before the problem is solved in the modeling of free surfaces flow. Then, in order to find the solution, the free surface boundary conditions should be applied in a correct way. In OpenFOAM the free surface is modelled by the approach called VoF, Hirt and Nichols [1981]. This is computed by the so-called *interFoam* solver. In this method, an additional equation is introduce to describe the movement of the free surface. From the transport equation point of view, free surface motion of a fluid is a convective type of a property, which is called phase fraction, or α in terms of OpenFOAM, and it indicates the volume fraction of water at every cell. This parameter has values between 1, when the cells are full of water, and 0 for cell full of air, see Figure 2.1.

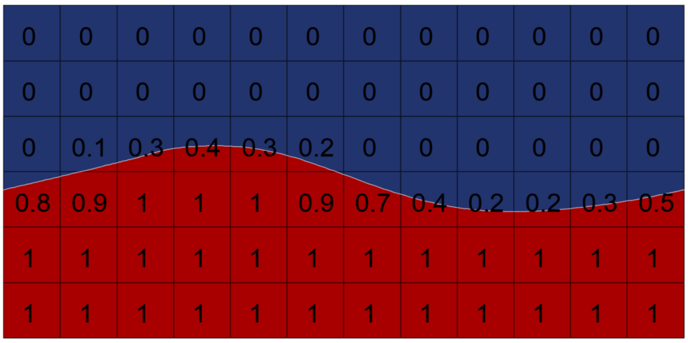

Figure 2.1: VoF approach that represents the free surface and the phase fraction at every cell

In order to obtain the transport equation for the phase fraction, some steps has to be considered before being able to obtain the correct formulation. First, the density of the fluid is described as follows:

$$\rho = \alpha\rho_{\mathrm{w}} + (1-\alpha)\rho_{\mathrm{a}} \tag{2.4}$$

where indexes w denote water and a air.

Then, the transport equation can be written for the phase fraction as:

$$\frac{\partial \alpha}{\partial t} + \nabla \cdot u\alpha = 0 \tag{2.5}$$

From Equation 2.1, the free surface can be estimated. However, this is only a starting point for the VoF approach, as some corrections needs to be added in the schemes in order to get a reliable physical result. Those corrections are conducted to avoid detrimental effects of diffusion in the phase fraction, which can leads into smearing of the sharpness of the interface. Then, the so-called artificial compression is introduced, $\nabla \cdot u_c\alpha(1-\alpha)$. This correction parameter avoids dispersion by introducing a pressure in the interface, so Equation 2.1 can be now written as:

$$\frac{\partial \alpha}{\partial t} + \nabla \cdot u\alpha + \nabla \cdot u_c\alpha(1-\alpha) = 0 \tag{2.6}$$

On Equation 2.6, the new term u_c represents the velocity field normal to the interface, which applies the artificial compression in the interface.

2.4 Turbulence model

Turbulent flows involve randomly fluctuation parameters, which are presented in many natural phenomena applications. This instability is generated by shear, that creates vorticity and fluctuations in the flow field. Also, turbulent flows are three-dimensional, dissipative, diffusive and time dependent. A full description of the turbulent model can be found in Appendix A.2.3.

In order to account for the eddy viscosity, or turbulent viscosity, μ_t, a $k-\omega$ SST model is employed, [Menter, 1994]. This is a combination of two turbulence models, the $k-\epsilon$ and the $k-\omega$ models.

The $k-\omega$ turbulence model is used as a closure for the RANS equations. It is used to predict turbulence by two partial differential equations for the variables called k and ω, being the second one, ω, the specific rate of dissipation. This model is used in the viscous sub-layer, which is located close to the wall, and the log-layer, so it makes low-Re simulations possible with good predictions of the mean flow profiles for simple definitions of the boundary conditions. The $k-\epsilon$ model is used to simulate mean flow characteristics for turbulent flow conditions, where the second transported variable is called ϵ and it represents the turbulent dissipation. So, the $k-\epsilon$ model is used in the free-stream far from the boundaries. Then, when $k-\omega\ SST$ is applied it allows to switch between those two models depending on the conditions of the flow. All formulas that describes the transport equations needed on this model are described in Menter [1994], Versteeg and Malalasekera [2007] and Appendix A.2.3.

A turbulent boundary layer is divided by two regions called the inner and the outer region. Additionally, the inner region, where the viscous forces are equal or greater than the inertia forces, is subdivided into 3 more regions, see Figure 2.2. This subdivision is caused by how the flow behaves. Those layers are characterized by the dimensionless wall distance y^+, [Schlichting and Gersten, 2017]:

$$y^+ = \frac{yu_\tau}{\nu}, \quad u_\tau = \sqrt{\frac{\tau_w}{\rho}}, \quad \tau_w = \frac{C_f \rho U_{ref}^2}{2}, \quad C_f = \frac{0.026}{Re_x^{1/7}}, \quad Re_x = \frac{\rho U_{ref} L}{\mu}, \quad u^+ = \frac{U}{u_\tau} \tag{2.7}$$

Where:

y^+	Dimensionless wall distance	ν	Kinematic viscosity
y	Absolute distance from the wall	C_f	Skin friction coefficient
u_τ	Friction velocity	Re	Reynolds number
τ_w	Wall shear stress		

First, the viscous sub-layer, which is the region closest to the surface $y^+ < 5$. This zone is characterized such as the viscous effects are dominant, so the relation between the velocity and the distance from the wall and is linear $u^+ = y^+$. Second, the buffer layer, where $5 < y^+ < 30$, is the transition region between the region dominated by viscous forces and the the turbulence dominated part of the flow. Last, the logarithmic area, when $y^+ < 30$, turbulence stress are dominant, then the velocity profile varies slowly following a logarithmic function over the y parameter. In this region wall-bounded effects are not important. The dimensionless velocity can be described as:

$$u^+ = \frac{1}{\kappa} \ln\left(y^+\right) + B \tag{2.8}$$

Where the Karman constant $\kappa = 0.41$ and the constant $B = 5.2$.

Then, wall functions are boundary conditions that are able to relate the surface and the center of the cells at the surface. However, despite this is a powerful tool that reduce computational time, it should be avoided to use due to accuracy problems.

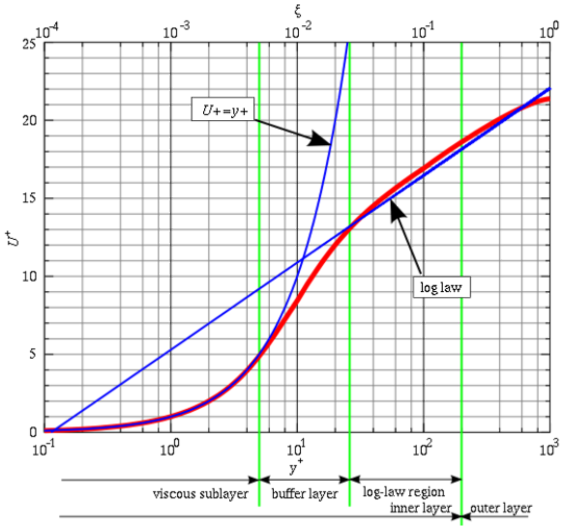

Figure 2.2: Wall regions and layers, [SimScale, 2020]

2.5 Meshing

As it was mentioned before, the aim of this report is to study the interaction between waves and a fixed chamber structure on a numerical model. As any numerical method, the computational domain needs to be discretized in order to deal with the involved partial differential equations. This stage is the most time consuming process of numerical simulations, as it needs to deal with a convergence study based on a verification and validation analysis. This is conducted by an iterative procedure of alternate solution and mesh generation that are combined to obtain reliable results based on prescribed solutions. OpenFOAM deal with it by the so-called utilities *blockMesh* and *snappyHexMesh*. The mesh is generated in both 2D and 3D with polyhedral elements. Also, as it is illustrated in Figure 2.3 objects can be included in the mesh to simulate different scenarios.

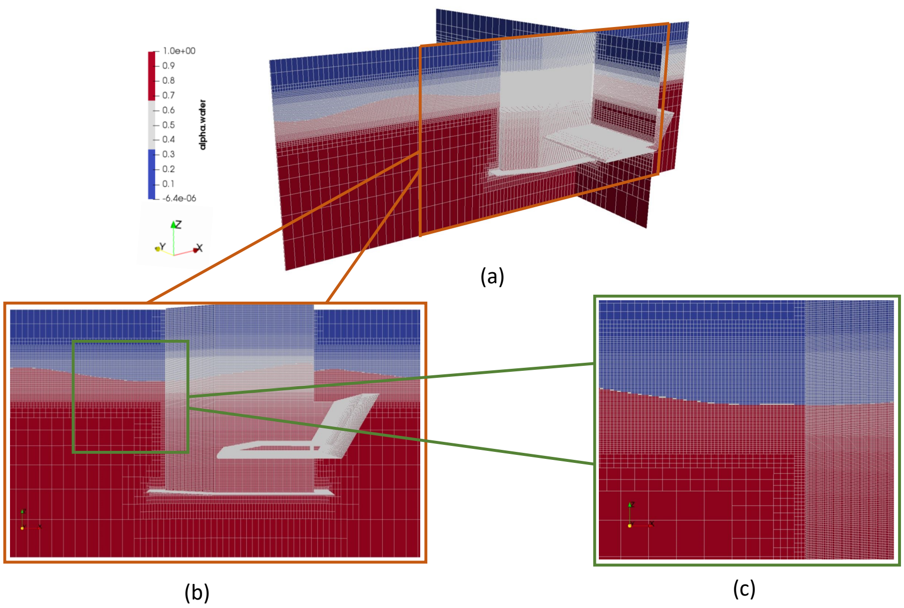

Figure 2.3: Mesh discretization of 3D model and chamber A4 configuration by with *blockMesh* and *snappyHexMesh* - a) 3D model in perspective b) Zoom area around chamber c) Detail of mesh discretization by *snappyHexMesh*

In this report two different refinement procedures are applied. First, when only propagated waves are investigated, the mesh is refined in the region where the surface elevation is expected to occur plus a safety margin, so all important kinematics are captured. The second one is applied when a fixed body is introduced in the numerical model. In this case a similar procedure as before is applied, but then the area around the object needs to be refined, so all kinematics are well captured. This is illustrated in Figure 2.3. In this last case is crucial to achieve a well refinement level at the surface of the object. To do that some parameters that are very sensitive to the refinement level at the surface. The most common is the $y+$ parameter, which is explained in Section 2.4, and in this project the boundary layer is resolved to have a maximum $y+ \leq 300$.

2.6 Modelling of waves in OpenFOAM

OpenFOAM is a power full tool that provides a wide range of customize settings. Several options for generation and absorption of waves are included on it. In this report some are tested to obtain which one gives the most reliable results compared to empirical and analytical data. However, only *waves2Foam* approach is applicable.

The approach called *waves2Foam* includes also both, wave generation and absorption. Those are utilized in the relaxation zones developed by Jacobsen [2017], see Figure 2.4. Relaxation zones are a very powerful tool but with an also high cost, since it increase the domain size.

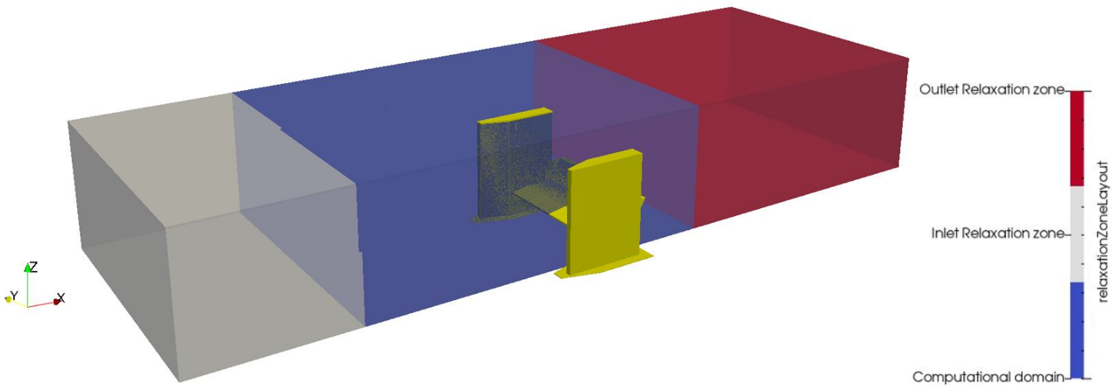

(a)

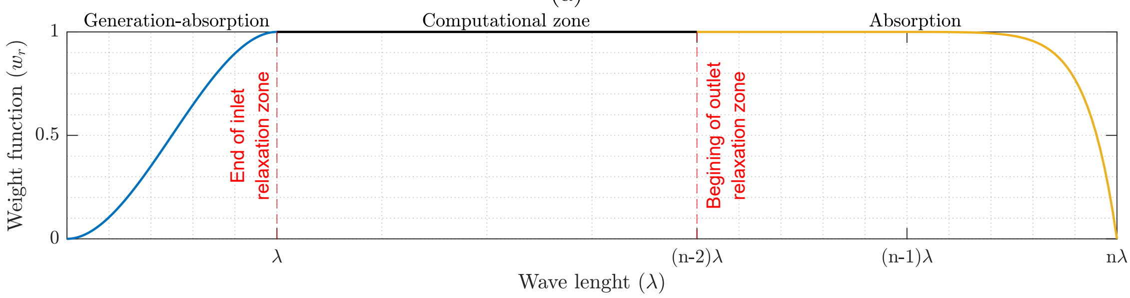

(b)

Figure 2.4: a) Relaxation zone layout for a 3D case with A4 chamber configuration - b) Weighting function sketch for relaxation zones from Equations A.15 and A.16

This method makes uses of a weight function between computational solutions of the velocity field and analytical solutions (see Figure 2.4b), which is highly dependent on the schemes used on the numerical wave tank. In this case the explicit relaxation zone is chosen, as it is the only method applied in *waves2Foam* toolbox. According to Jacobsen [2017], relaxation zones are defined by several parameters, which needs to be defined to get a correct wave generation and absorption zones. This approach is formulated as:

$$\phi = (1 - w_R)\,\phi_{\text{target}} \; + w_R \phi_{\text{computed}} \tag{2.9}$$

Where w_R is the weighting function and it can be defined in different ways. In this project two different weighting functions are employed, which are illustrated in Figure 2.4 and explained in more details in Appendix A.2.4.

The length of both relaxation zones are setup initially based on Miguel et al. [2018] in such a way that both relaxation zones are setup to be dependant on the wave length (λ) for every specific case. While inlet relaxation zones are setup to be 1 λ, outlet relaxation zones are 2 λ. However, for some cases (the steepest waves), the inlet relaxation zone is increased to 2 λ due to a non-physical behaviour found in the simulation, see Section 5.

On this report two different wave theories are applied for generation of waves: *stokesFifth* or *Stokes* 5^{th}*order* and first-order irregular waves called *irregular* or *firts-order irregular wave.*

First, *stokesFifth* is based on Fenton [1990] and Fenton [1985] and covers cases for large non-linearities of the waves. Some parameters are needed for implement *wave2Foam* solver, which are defined on Jacobsen [2017].

Second, *irregular* wave type is a first-order irregular wave theory, which according to Jacobsen [2017] it works as a simple linear superposition of first order Stokes waves. This is computed by an extrapolation of the first order Stokes waves to the free surface as it is indicated in Equation 2.10

$$\eta = \sum_{i}^{N} a_i \cos\left(\omega_i t - \mathbf{k}_i \cdot \mathbf{x} + \varphi_i\right) \tag{2.10}$$

Where:

η	Surface elevation	[m]		$\mathbf{k}_i$	Wave number	$[m^{-1}]$
N	Number of wave components	[-]		x	Distance	[m]
a_i	Wave amplitude	[m]		φ_i	Phase	[rad]
ω_i	Cyclic frequency	$[rad/s]$				

Experimental and Numerical Model Setup 3

This chapter presents the details about the experimental setup and the numerical models used in this report

3.1 Experimental setup

FPP conduct experimental tests in the wave basin at AAU facilities, AAU [2020], called AAU series 7, for a period of time of 4 weeks, from November 5^{th}, 2018 to December 2^{nd}, 2018, see Figure 3.1. During this campaign different configuration were tested under regular and irregular wave conditions. An sketch of the experimental setup is illustrated in Figure 3.2, where the location of all wave gauges are also defined in the illustration. The basin is $13x8.4$ meter with a water depth of 1 meter and the 1:30 model is located in the centre of the basin, see Figure 3.2. This project is focused on the regular wave conditions, where a total of 28 different waves were generated in the basin, those can be found in Table C.1 and and example of only propagated waves is illustrated in Figure 3.3.

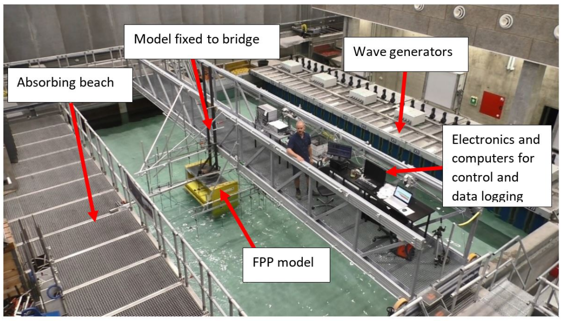

(a)

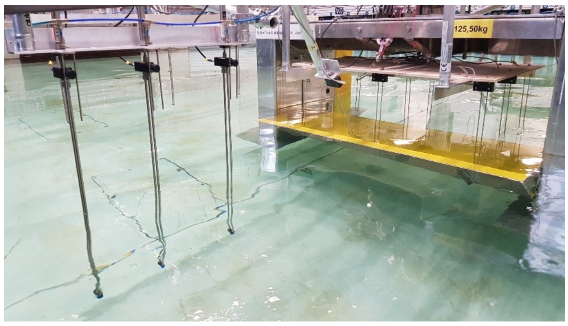

(b)

Figure 3.1: Setup of the FFP experiments at AAU, FPP [2018], M. Krammer [2018] a) Wave Basin setup b) Chamber from the back in its A4 configuration with wave gauges

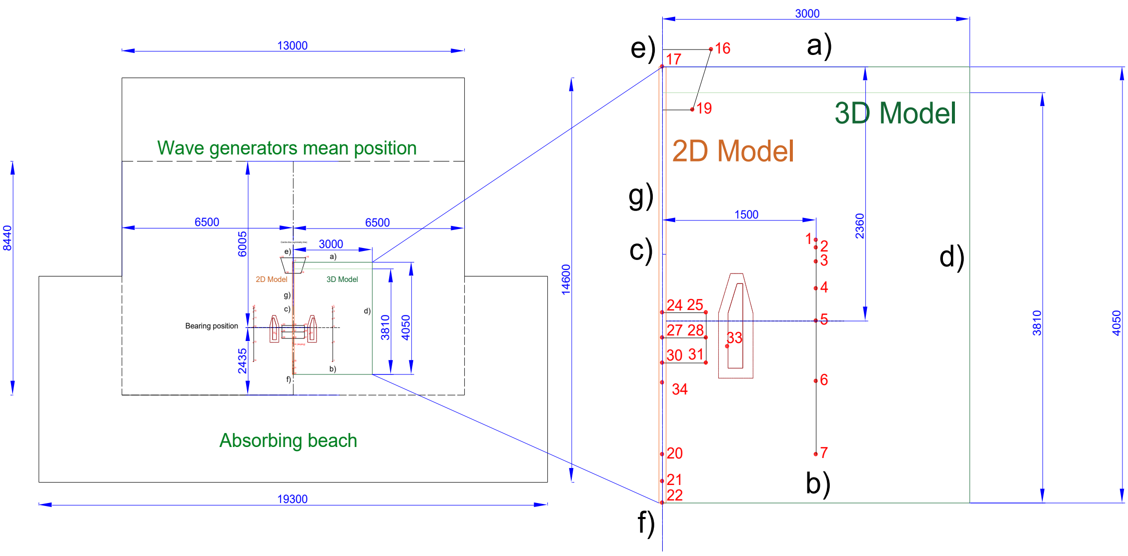

Figure 3.2: Sketch of the wave basin at AAU facilities and 2D and 3D numerical model (3D model has two setup dark and light green) - Numerical boundary conditions: 3D model a) and b) patch, c) symmetry plane, d) wall; 2D model: e) and f) patch, g) empty - For WG location see Figure 3.2

In the validation and verification of the numerical model two regular waves from the experiments are selected, which are wave test number 18, with a steepness of $s = 3.80\%$ and wave test number 20 with a steepness of 6.23%. Those waves are also illustrated in Figure 3.3. Also the properties of those wave are summarized in Table 3.1. Moreover, a Fast Fourier Transformation (FFT) is conducted for wave test number 18 and 20, which is also used for the generation of waves in the numerical model, see Figure 3.4. Also, a Le Mehaute diagram is used in the validation of the wave theory for each wave, which it is further used in the report for the generation of waves in CFD models.

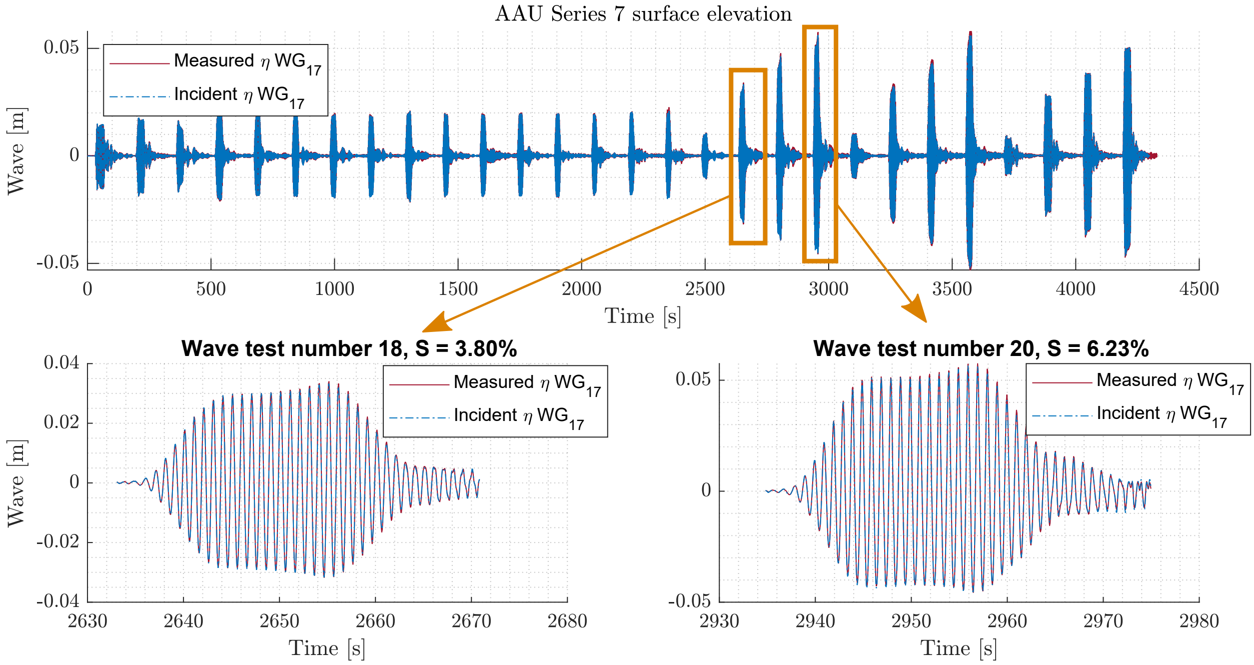

Figure 3.3: Test experiments AAU Series 7, Table C.1

Number	Height	Length	Depth	Period	Steepness	Total height
No	H	λ	h	T	$s = (H/\lambda) * 100$	h_{total}
[−]	[m]	[m]	[m]	[s]	[%]	[m]
18	0.06	1.58	1.00	1.00	3.80	1.40
20	0.10	1.61	1.00	1.00	6.23	1.40

Table 3.1: Wave characteristics and dimensions of the model with cyclic boundaries, Table C.1

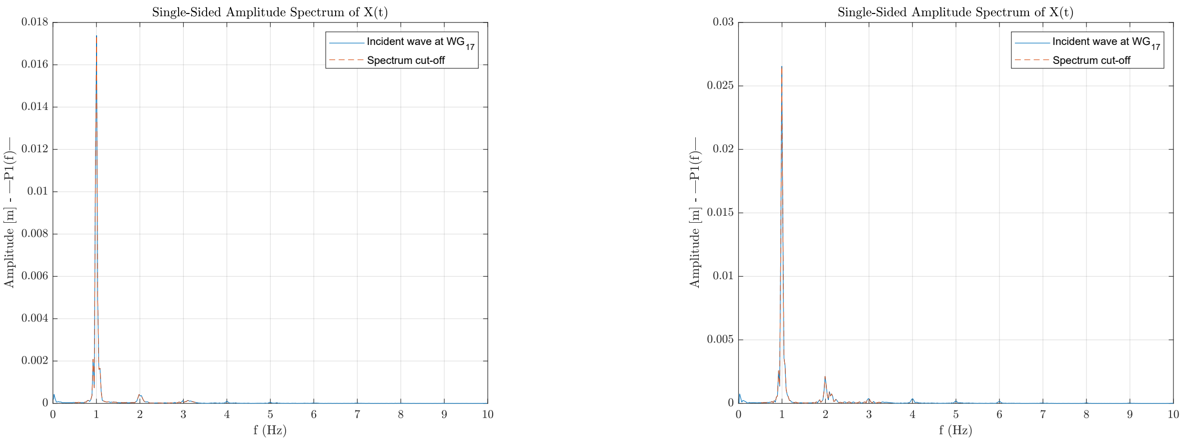

(a) (b)

Figure 3.4: Spectrum from FFT for wave test number: a) 18 b) 20

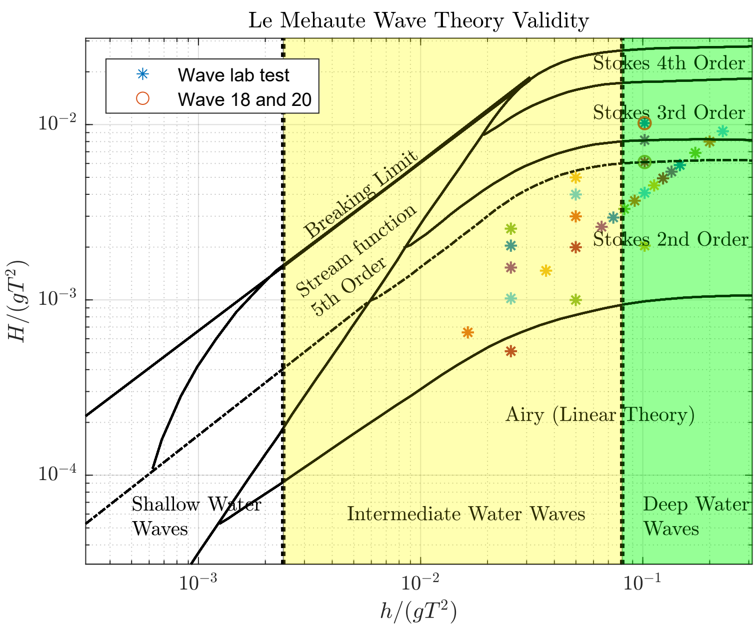

Figure 3.5: Le Mehaute diagram of test performed at AAU facilities, Table C.1

Also, from experimental waves with a wave height of 0.04 meters the wave amplification factor is calculated at 6 different wave gauges, see Figure 3.6, which corresponds to the 3x3 array located inside the chamber, see Figure 3.3. The wave amplification factor is calculated for different structure configurations, so the influence of each part individually can be quantified. This information is very useful in the analysis of the results presented in Section 6.

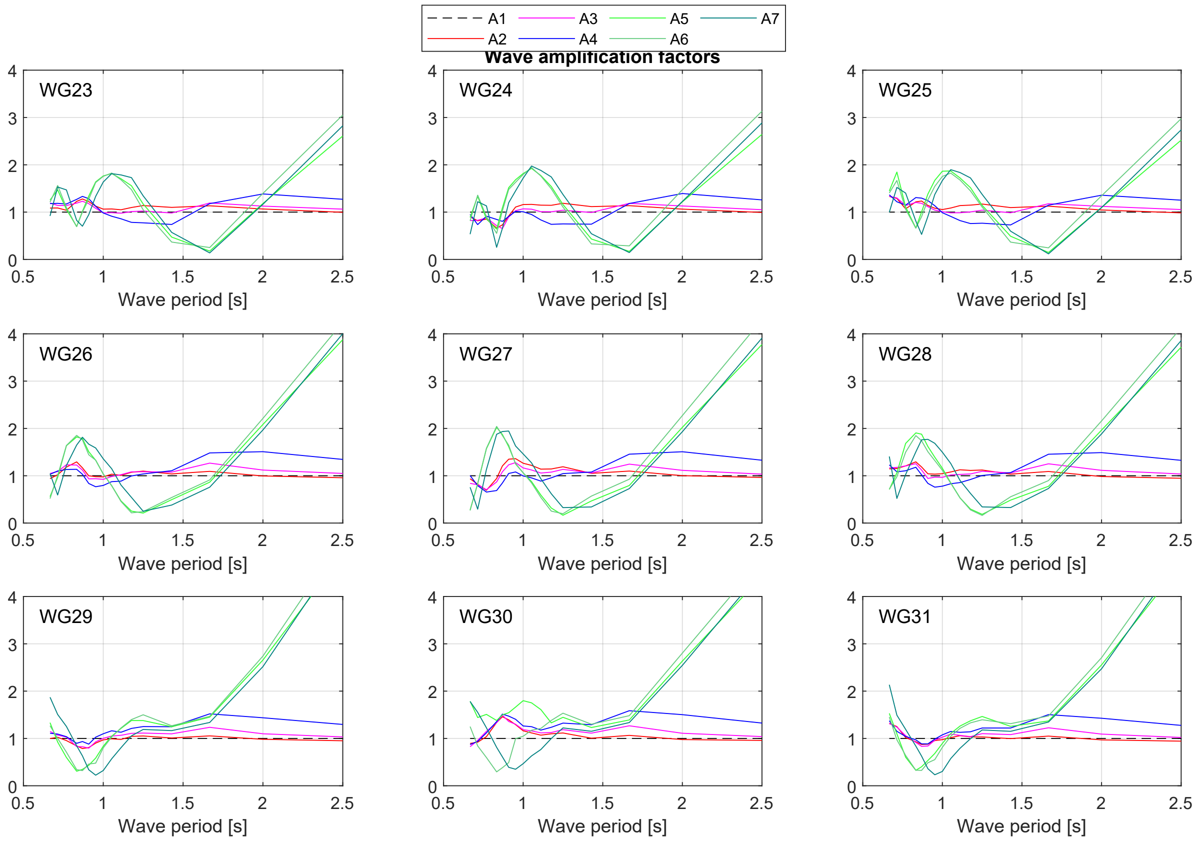

Figure 3.6: Wave amplification factor for different sea states and different chamber configurations. A1 configuration are only propagated waves, A2 only side walls, A3 side walls and bottom spoiler, A4 original configuration, A5 extended spoiler, A6 lowered extended spoiler and moved and A7 lowered spoiler.FPP (2020) and M. Kramer (2020)

3.2 Numerical model details

A description of the three different numerical models used in this report based on OpenFOAM are presented in this section:

- Wave flume with 1 wave length and cyclic boundary conditions.
- AAU wave basin.
  - 2D numerical model for validation of waves.
  - 3D numerical model for validation and analysis of the results.

3.2.1 OpenFOAM

In this report a CFD program called Open Source Field Operation and Manipulation (OpenFOAM) is employed. It is an open source package of C++ libraries and codes. OpenFOAM aims to create applications for numerical modeling of both, solid and fluid mechanics problems.

According to OpenFOAM [2020]:

> OpenFOAM is the free, open source CFD software developed primarily by OpenCFD Ltd since 2004. It has a large user base across most areas of engineering and science,

> from both commercial and academic organisations. OpenFOAM has an extensive range of features to solve anything from complex fluid flows involving chemical reactions, turbulence and heat transfer, to acoustics, solid mechanics and electromagnetic.

The main use of OpenFOAM in this project is to implement a NWT with a chamber inside, which previously has been verified and validated against empirical and analytical data. First, a solver is needed for the implementation of the NWT, it needs to be designed for a specific continuum mechanic problem. The so-called *interFoam* solver deals with this problem, as it is able to solve the RANS equations for 2 incompressible, isothermal immiscible fluids. Also, it makes use of the control volume numerical method for the discretization of the transport equations, as well as it can calculate free surfaces by using a Volume of Fluid (VoF) approach, see section 2.3. Second, utilities are used for data manipulation. As an example of some utilities the so-called *snappyHexMesh* and *blockMesh* are used for the generation of the mesh, see Section 2.5. OpenFOAM uses the Finite Volume Method (FVM). This, and according to Moukalled et al. [2016], is a numerical technique that is used to transform the partial differential equations into discrete algebraic equation over finite volumes or cells.

General settings

In order to solve the flow field an algorithm called PIMPLE is used, which is a combination of the SIMPLE and PISO algorithms, this is done by a solver called *wave2Foam*, which is based on *interFoam* solver. This is employed for 2 incompressible, isothermal immiscible fluids using a VoF approach. Moreover, for the numerical schemes a second-order van Leer scheme is utilized for the convection terms, a second-order central differences for diffusion terms and the turbulence equations are solved by a first-order upwind method. Also, a blended second-order Crank-Nicholson/first order backward Euler scheme is employed in the time-stepping. All schemes and solutions and solvers utilized, with a brief description, can be found in Appendix A.2.5.

The boundary conditions applied in this model are briefly explained (see Figure 3.2). In this report three different model setups are required for the verification, validation and analysis of the data. For the cyclic model *cyclic* boundary condition are defined at the inlet and outlet, Figure 3.7a. For the second case, the 2D model represented in Figure 3.7c, all boundaries are defined as *patch*, *wall* or *empty*. For the last case, the 3D model shown in Figure 3.7b, boundaries are defined in a similar way as in the 2D model. However, boundaries defined as *empty* in the 2D model are changed to be *wall* or *symmetryPlane*. Where the last one is applied to reduce the domain size to one half, as the model is symmetric along the x-axis. The setup can also be foun in Table A.1.

A more detail explanation of this feature can be found in Appendix A.2.2. Also some other important featured needed in OpenFOAM can be found in Appendix A.2

In order to conduct a correct verification and validation analysis, the simulations of all models are carried out based on empirical data, see Section 3.1. Also, a Le Mehaute diagram presented in Figure 3.5 shows that all cases are covered by Stokes Third order theory. Nevertheless, to ensure that all non-linearities are accurately predicted on the CFD model a Stoke Fifth order theory (*Stokes* 5^{th} *order theory*) and *First-order irregular waves* are chosen to generate waves in the numerical model.

3.2.2 Wave flume: 1 wave length and cyclic boundaries

This model is a simplification of the real problem, which is done to verify the quality of the mesh. The model is setup based on the wave length and amplitude, with the implementation of cyclic boundary conditions, as explained in Section A.2.2. Due to this characteristics, the domain can be reduced to only one wave length, see Figure 3.7a. Consequently the computational time in this convergence study is reduced dramatically as the number of elements are reduced compared to a whole numerical wave tank.

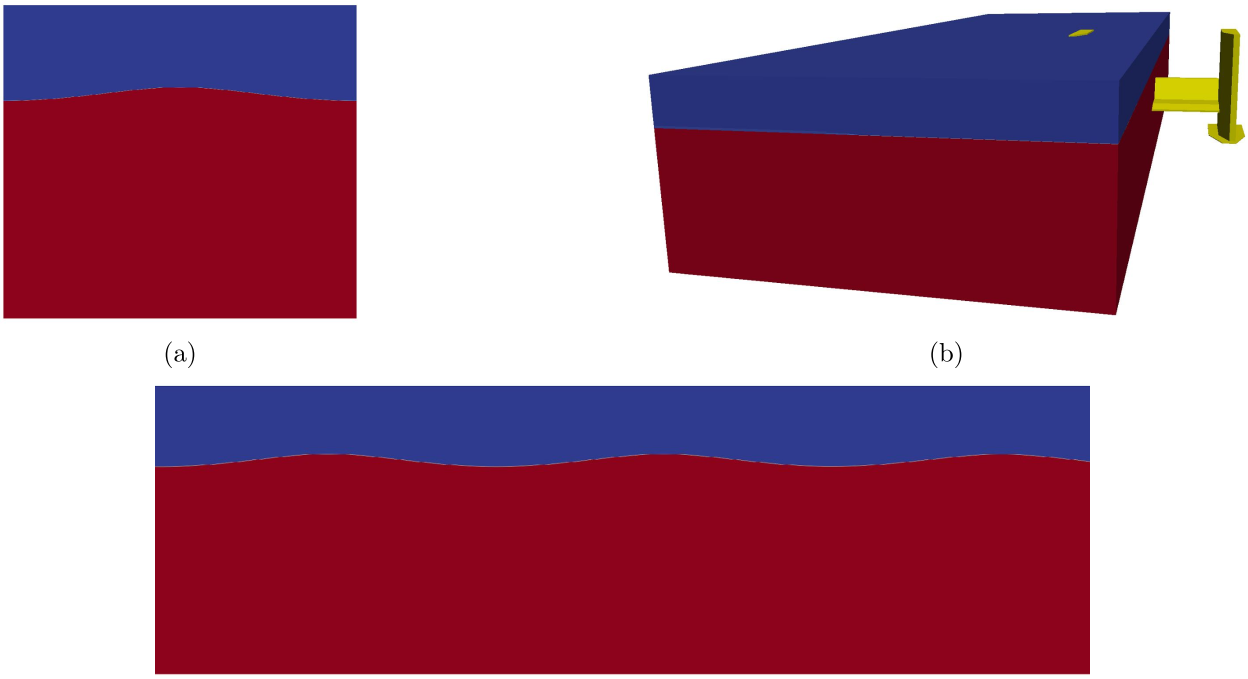

(a) (b) (c)

Figure 3.7: Representation of the phase fraction (alpha water, where red is water and blue is air) for different domain models with each own boundary conditions - a) 2D model with Cyclic BC b) 3D model with symmetry BC c) 2D model

The waves characteristics presented in Table 3.1 are taken into account in different models setup in order to investigate the spatial and temporal discretization. So, a converge study is carried out by changing different parameters related to the grid resolution and the time step to check the sensitivity of each parameter in the final results.

3.2.3 AAU wave basin

The validation of the numerical model is based on the same two experimental waves shown in Figure 3.3. Also, the numerical model is design based on the experimental setup. An sketch of the experimental of both numerical models is illustrated in Figure 3.2. Then, a brief description of the models used for the validation an analysis of the simulations is presented:

- 2D model: Several simulations are performed in this way to validate the wave propagation in the wave basin. This approach is very practical as the model is reduced to 2 dimensions, see Figure 3.7c, which needs less computational time effort. Moreover, the validation is possible to be conducted with a 2D model as the waves generated in the experiments are unidirectional. An sketch of the model is shown in Figure 3.2, and the dimensions are shown in Table 3.2.

In this case four different simulations are conducted for the 2D analysis depending on which wave is chosen, see Table 3.1 and which wave generation theory is utilized, see Section 2.6.

- 3D model: The 3D model is applied in the validation and analysis of the numerical simulation with the implementation of different chamber configurations, see Figure 3.7b. This also represents a simplification of the real wave basin, due to needs on the reduction of computational costs, so only an specific area of the wave basin is numerically computed. The numerical model is illustrated in Figure 3.2 and its dimensions are presented in Table 3.2. This 3D model setup is needed due to the fact that a singular structure is introduce. Therefore, waves are no longer propagating in one direction, which a 2D model is not able to capture, so this 3D model is able to give essential information for the understanding of the wave-chamber interaction.

Model [−]	Total Height h_{total} [m]	Length L [m]	Depth h [m]	Width W [m]	Total nº cells [-]
2D	1.35	4.05	1.00	0.01	90 k
3D	1.35 to 1.60	3.81 to 4.05	1.00	3.00	0.8 M to 11 M
Wave basin	1.50	8.44	1.00	13.00	–

Table 3.2: Dimensions of the numerical models and the wave basin at AAU facilities - The length of the 3D model varies depending on wave characteristics to save computational time - M represent values in millions - k represents values in thousand

Part II

Verification and Validation

4 Solution Verification

In this chapter a solution verification of the wave propagation is performed. This is done by changing the spatial resolution depending on the wave length and wave height and a temporal discretization based on the time step.

4.1 Introduction

Solution verification is a fundamental step that must be taken into consideration before applying any well-established CFD code, see Appendix A.4. This is carried out by comparing analytical values to wave parameters of simulated regular waves.

Non-linear waves are described by non-linear partial differential equations (PDEs). In most cases PDEs do not have exact analytical solutions, then approximation and numerical techniques need to be applied. In this section a well establish numerical model is aim to be obtained to obtain a fast, robust and a stable numerical solution that can give reliable results of the problem. Then, in order to obtain an approximate solution that can give reasonable results a converge study based on errors and uncertainties in the model is conducted. According to Eça and Hoekstra [2010], errors can be divided into numerical errors, modelling errors and simplified geometry errors.

For the 2D cyclic model, which is described in Section 3.2.2, the study is focused on spatial and temporal discretization errors, which are part of the numerical errors. To estimate the uncertainty of the numerical model, the solution verification step, which is part of the Verification and Validation technique is employed. In this section the V&V of Eça and Hoekstra [2014], based on the Richardson extrapolation which measures the convergence of the solution and applies safety factor to calculate uncertainties based on the errors of the model.

In order to obtain the uncertainties, a model with different mesh, or temporal, resolution are generated. Then ratio of the cell size, or temporal ratio, is calculated as:

$$\frac{h_i}{h_1} = \sqrt[1]{\frac{N_1}{N_i}} \tag{4.1}$$

Where h_i indicates the typical cell size of a grid and the i run over the number of grids from highest to lowest density. N_i denotes the total number of cells.

The next step is to calculate the error, called ε, between the numerically obtained result ϕ_i using the ith grid and the exact solution (ϕ_0). This is defined as:

$$\varepsilon = \phi_i - \phi_0 = ah^p \tag{4.2}$$

From Equation 4.2 two new parameters are described. p indicates the order of accuracy and a is a case specific constant. Then, the next step calculate the true error. This is approximated by the error obtained from the Richardson extrapolation (δ_{RE}) indicated as follow:

$$\varepsilon \approx \delta_{RE} = \frac{\phi_i - \phi_1}{(h_i/h_1)^p - 1} \tag{4.3}$$

Then, Roache [1997] propose to use safety factor based on the estimated convergence rate to go from numerical errors (ε) to numerical uncertainties U_ϕ

$$U_\phi = F_S(p)|\varepsilon| \tag{4.4}$$

Those safety factor depends on the order of convergence. The asymptotic range of convergence can be assumed to be $0.95 \leq p \leq 2.05$ if a standard second-order model is assumed. Roache [1997] suggested to use a safety factor of 1.25 in the asymptotic range. And the uncertainty can be calculated as:

$$U_\phi = 1.25\delta_{RE} + U_S \quad \text{if } p \in [0.95, 2.05] \tag{4.5}$$

where U_s is the standard deviation, which are calculated from the least square fits.

This solution verification step is conducted for for 3 different variables, which are two spatial and one temporal parameter, for two different run times and two different steepness, however only the case that corresponds to a steepness of $S = 3.80\%$ and $t/T = 10$ is presented in the main report, the rest of the analysis can be found in Appendix C. Similar conclusions are obtained for the case with $S = 6.23\%$, which can also be found in Appendix C.3 and C.5.

4.2 Spatial discretization

The solution verification step in this section is analyzed for two different independent parameters: number of element per wave height (cells/H) and number of elements per wave length (cells/λ), with 6 different grids refinements, which are described in Tables 4.1 and 4.3 (and also Tables C.4 and C.7 for the steepest cases). In order to make this analysis independent from temporal discretization a $\Delta t = 0.0001$ is chosen. This section is divided into two parts, in the first part the uncertainties from the refinement of cells/H and the second part, which is the analysis of the cells/λ. The numerical uncertainty is evaluated by non-dimensional variables from to the free surface elevation, which are obtained from three different phase fraction ($\alpha = 0.5$, $\alpha = 0.90$ and $\alpha = 0.10$) based on the VOF approach.

4.2.1 Spatial discretization - number of cells/H

This study is based on data shown in Table 4.1 and C.4 for the two different wave steepness. $s = 3.80$ and $s = 6.23$, respectively. To ensure that the analysis is independent from cells/λ this parameter is set up to be 400 for $s = 3.80$, which is large enough to ensure this condition, however for $s = 6.23$ the cells/λ can not keep constant due to some instabilities in the simulation that make it to break, therefore a range of values that goes from 150 to 650 is used depending on the cells/H.

Steepness	Grid	Cells/λ	Cells/H	Cells	Aspect ratio	Reference ratio[1]	Normalized run time[2]
3.80	Grid 1.1.1	400	10	23.515	0.65	6.00	1.00 [3]
	Grid 1.2.1	400	20	47.030	1.30	3.00	1.67
	Grid 1.3.1	400	30	70.545	1.95	2.00	2.72
	Grid 1.4.1	400	40	94.061	2.60	1.50	3.33
	Grid 1.5.1	400	50	117.580	3.25	1.20	2.99
	Grid 1.6.1	400	60	141.090	3.90	1.00	4.75

Table 4.1: Grid characteristics for case of different cells/H - [1]: rate between the maximum cells/H and the one for the grid under investigation. - [2]: ratio between the minimum computational time and the one corresponding to the selected grid - [3] run time of 9.29 hours

In order to have a better view of the data shown in Table 4.1 an illustration of the grids that corresponds to $s = 6.23$ are presented in the following Figures 4.1 and 4.2.

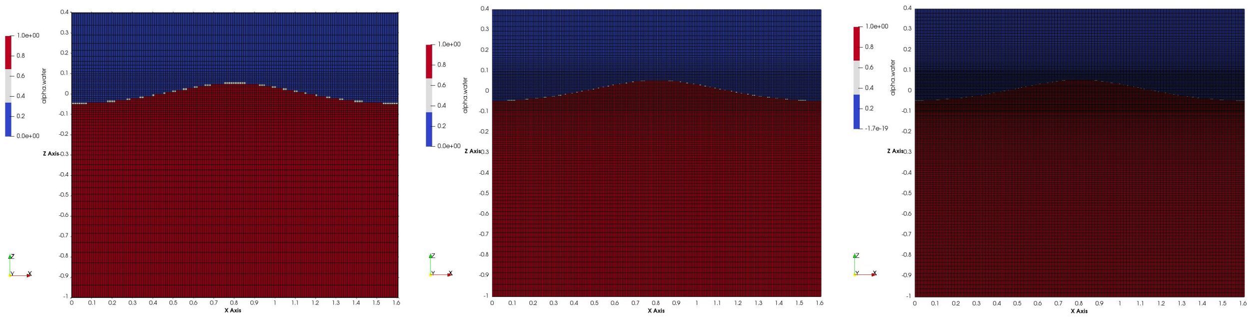

(a) (b) (c)

Figure 4.1: Details of grids that corresponds to $s = 3.80$ - a) Grid 1.1.1 b) Grid 1.2.1 c) Grid 1.3.1

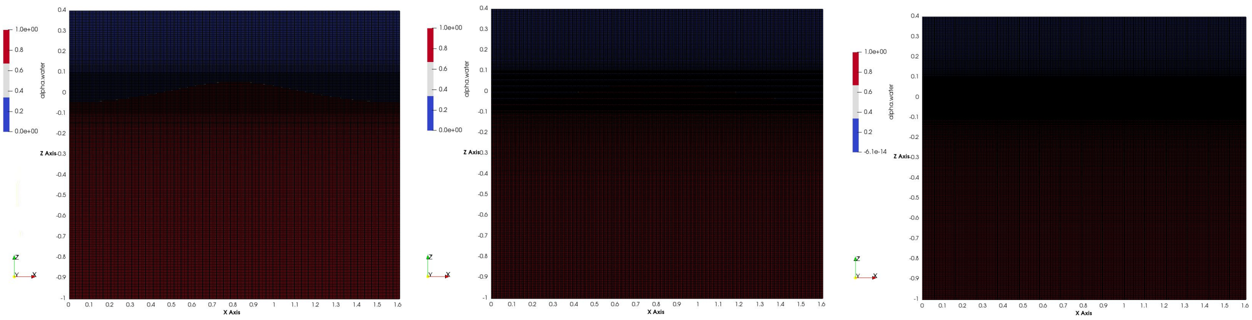

(a) (b) (c)

Figure 4.2: Details of grids that corresponds to $s = 3.80$ - a) Grid 1.4.1 b) Grid 1.5.1 c) Grid 1.6.1

As it can be seen from Figures 4.1 and 4.2 there are different regions according to the level of refinement in the model, see Section 2.5. First, the coarsest region is the one located on the top, which corresponds to the air, as it does not influence the final results due to the low density. Second, the most refined region corresponds to where the kinematics and surface elevation have more influence. This area is bigger than the wave height in z-axis to ensure that all important features are capture. Last, from the surface elevation region to the bottom. As it can be seen from Figures above the cells sizes increases the further is located from the surface elevation. This is possible due to the physics involved on wave interactions and the specific case under investigation that is on intermediate waters. Nevertheless, this refinement region bellow the surface water level is carried out carefully to ensure good results over the depth.

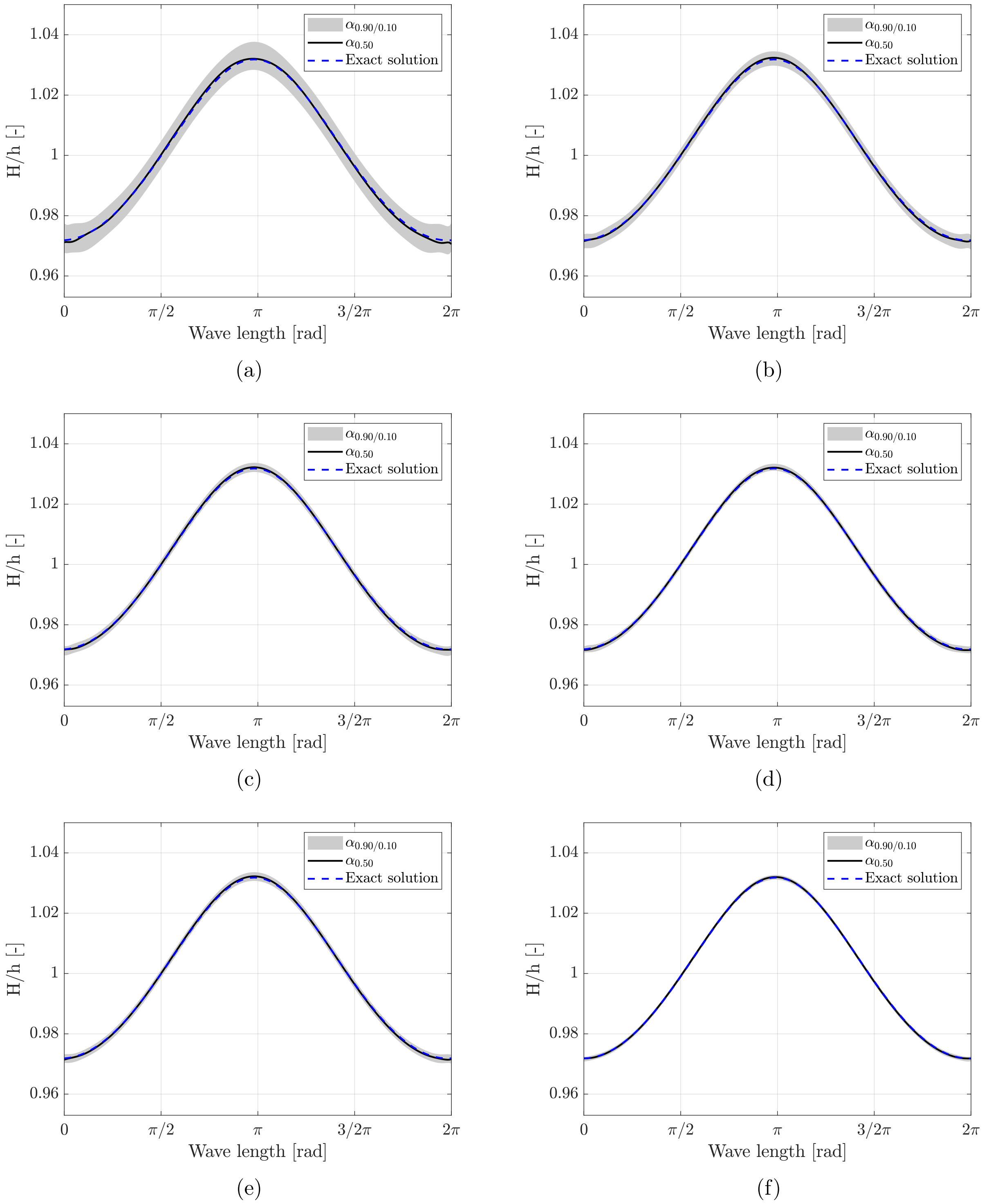

Figure 4.3: Free surface elevation for different grids with analytical solution and $t/T = 10$ - a) Grid 1.1.1 b) Grid 1.2.1 c) Grid 1.3.1 d) Grid 1.4.1 e) Grid 1.5.1 f) Grid 1.6.1

Figures 4.3 illustrates the free surface elevation for data given in Table 4.1 for 10 wave periods (t/T) as terms of interface values, which is presented as α. In those figures the surface elevation is plotted on phase to make easier the evaluation of the results, despite of a phase delay is found in the numerical model, which increases as t/T increase. This behaviour is illustrated in Figure 4.4b. Also, it can be seen the differences in the iso-surfaces for different α values and different mesh refinement. For $\alpha = 0.50$ there is a very little difference between the free surface elevation for different mesh refinement, which might indicate that this using only this parameter is not enough for a correct convergence analysis. For $\alpha = 0.90/0.10$ a gap between both iso-surfaces is apparent, which decreases as the grid is more refined. This iso-surfaces are of major importance due to the fact that a bad weak interface refinement can cause a large negative impact on the results.

Figure 4.4 illustrates the phase delay at $t/T = 10$ mentioned before between the analytical solution and the numerical calculations. This is caused due to the accumulative error in numerical errors, however only a 2.5% error on the phase with respect to the analytical solution is found.

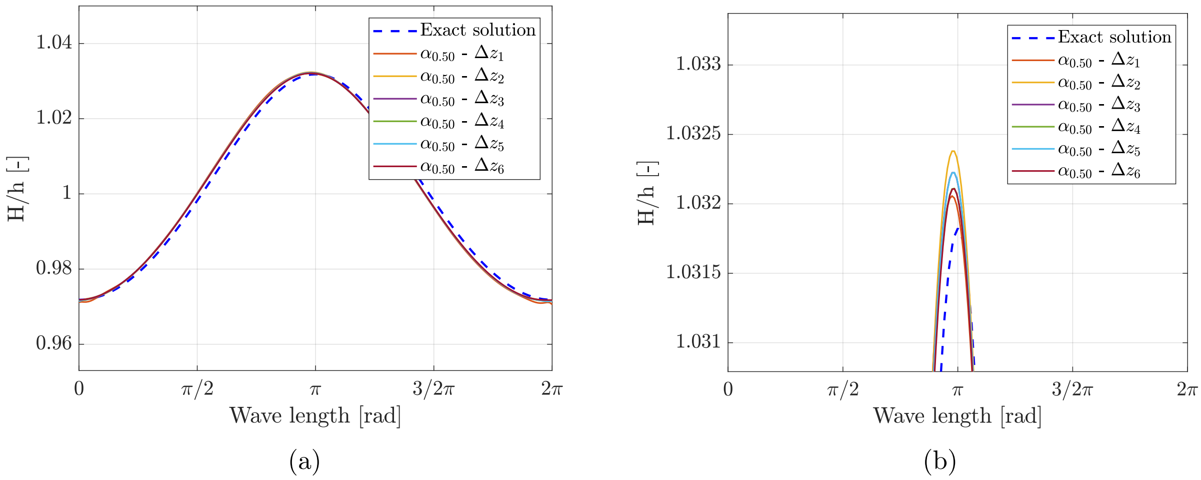

Figure 4.4: Free surface elevation for $\alpha = 0.5$ and 5 different number of cells / H with analytical solution and $t/T = 10$ - a) 1 wave length, b) Detail of the wave crest

An illustration of the Richardson extrapolation and the estimated convergence rate for $\alpha = 0.50$ and $\alpha = 0.90/0.10$ and 10 wave periods is shown in Figure 4.5. For $\alpha = 0.90/0.10$ a behaviour close to an asymptotic convergence is achieved with a converge rate of $p = 1.05$. For $\alpha = 0.50$ the responses shows also a good convergence with a value of $P = 1.52$.

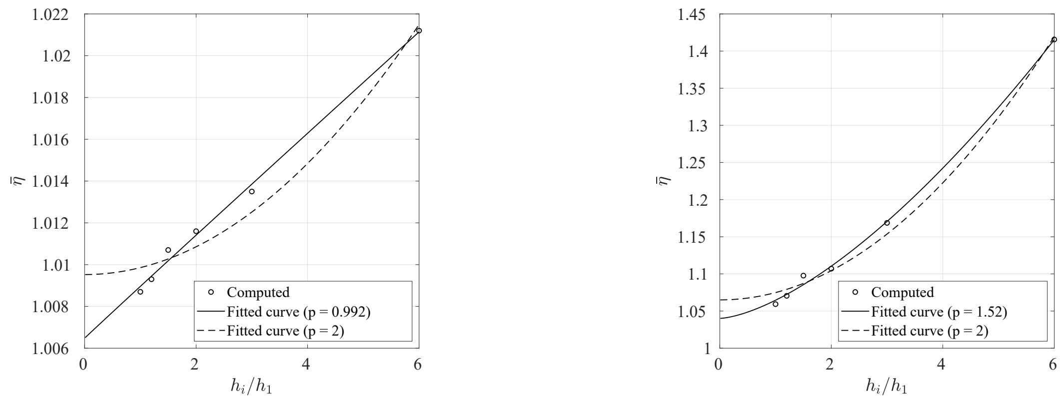

(a) (b)

Figure 4.5: Estimated convergence for the wave propagation of iso-surface for different number of cells/H - a) $t/T = 10$; $\alpha = 0.50$, b) $t/T = 10$; $\alpha = 0.10/0.90$

Next, the resulting spatial and time uncertainty is estimated by Richardson extrapolation and also a simple difference as presented in Equation 4.6. All this data is summarized in Table 4.2

$$\frac{\phi_i - \phi_{G1}}{\phi_{G1}} \tag{4.6}$$

where ϕ_i is the parameter (η_x) investigated and ϕ_{G1} is the parameter (η_x) used as a reference.

t/T	Grid	Grid 1.6.1	Grid 1.5.1	Grid 1.4.1	Grid 1.3.1	Grid 1.2.1	Grid 1.1.1
10	$\bar{\eta}_{0.50}$	1.0087	1.0093	1.0107	1.0116	1.0135	1.0212
	% diff	-	0.06	0.20	0.29	0.48	1.24
	$U_{\bar{\eta}_{0.50}}$	0.35	0.41	0.51	0.66	0.96	1.87
10	$\bar{\eta}_{0.90/0.10}$	1.0593	1.0705	1.0977	1.1071	1.1687	1.4156
	% diff	-	1.05	3.63	4.51	10.33	33.64
	$U_{\bar{\eta}_{0.90/0.10}}$	3.87	4.85	6.48	9.60	17.12	47.70

Table 4.2: Spatial uncertainty for wave propagation over wave height with $s = 3.80$

Several conclusion can be found from Table 4.2. First, the uncertainty values are lower for $\alpha = 0.50$ than $\alpha = 0.90/0.10$, this indicates that a converge analysis of the $\alpha = 0.50$ is not enough to ensure that the numerical model is fully converged. This is clearly seen in Figure 4.3a, where the $\alpha = 0.90/0.10$ iso-surfaces are not closed enough, but the uncertainties in Table 4.2 give a value lower than 5% for grid 1.1.1. Also, the iso-surface 0.90 and 0.10 give a more reliable results due to the variation of diffusion of the interfaces, which explain the importance of the number of cell/H in the spatial discretization, see Figure 4.3b. Moreover, as it is mentioned before, the analysis is also conducted for $t/T = 5$ and $t/T = 10$, comparing the uncertainties from both analysis it is concluded that it increases as as the simulation time increases, which is explained by the fact that numerical errors are accumulated over time.

As a conclusion, only $\alpha = 0.50$ iso-surface is not reliable enough to get a well converge grid, then $\alpha = 0.90/0.10$ is used as a reference for the converge analysis, which indicates that something between 30 to 40 elements per wave height are enough to achieve convergence.

However, the results has to be verified against the wave kinematics, which an analytical solution is known. Then, in order to confirm that 30 to 40 elements per wave height are enough, the velocity profile over depth is compared between analytical and numerical results. Figures 4.6 and 4.7 illustrates 4 different grids with 10 to 40 cells per wave height.

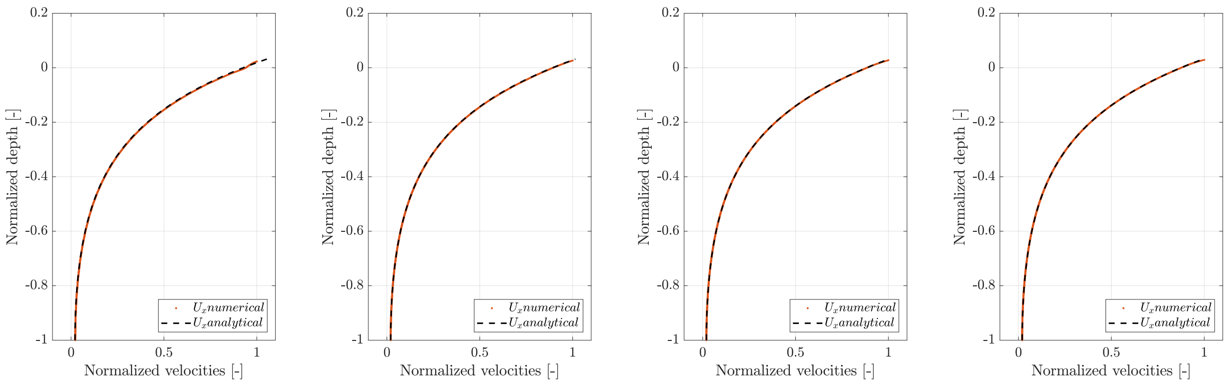

(a) (b) (c) (d)

Figure 4.6: Maximum horizontal velocity profile over depth for 10 wave periods - a) 10 cells/H b) 20 cells/H c) 30 cells/H d) 40 cells/H

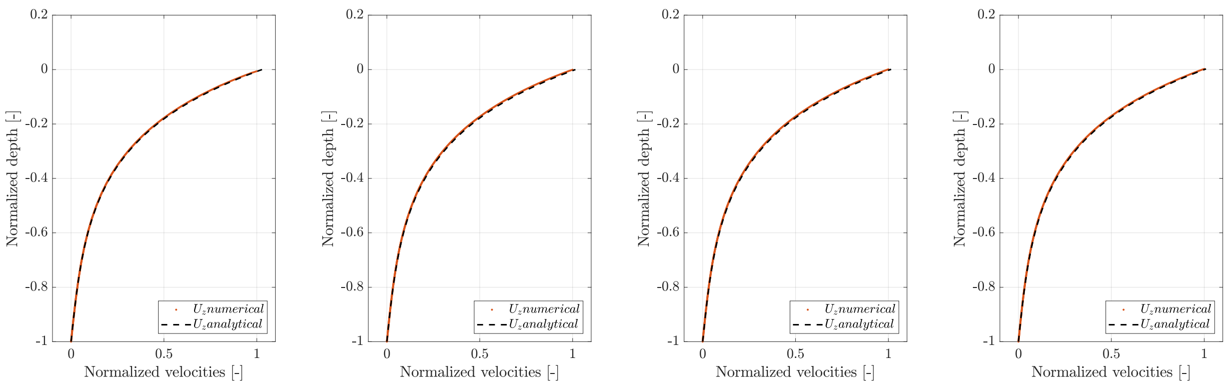

(a) (b) (c) (d)

Figure 4.7: Maximum vertical velocity profile over depth for 10 wave periods - a) 10 cells/H b) 20 cells/H c) 30 cells/H d) 40 cells/H

From Figures 4.6 and 4.7 it si concluded that, 10 cells/H does not shows a good match between both solutions, it can be seen that for the horizontal velocity the numerical data do not reach the maximum peak from the analytical solution. This indicates that some diffusion is affecting the results. The rest of the grids give a good fitting between both solutions, then this comparison shows that wave kinematics are fulfilled for at least 20 cells/H. Then, according to the values presented in Table 4.2 30 to 40 elements per wave height are enough to verify this parameter. The same analysis is conducted for $s = 6.23$ which shows that also 30 to 40 cell per wave height are enough to get uncertainties lower than 5%.

4.2.2 Spatial discretization - number of cells/λ

This section is conducted following the same procedure as cells/H verification analysis, but this analysis is focused on the discretization of cells/λ.

Next, in Table 4.3 the characteristics of 6 grids for s = 3.80 are presented. In this study the number of cells/H is fixed to 40 to ensure that the analysis is independent from this parameter. All necessary information is presented in this section, however a more detailed analysis can be found in Appendix C.2.2 and C.3.2 where also all data related to the steepest wave is included.

Steepness	Grid	Cells/λ	Cells/H	Cells	Aspect ratio	Reference ratio[1]	Normalized run time[2]
3.80	Grid 2.1.1	100	40	23.515	10.40	6.00	1.00[3]
	Grid 2.2.1	200	40	47.030	5.20	3.00	4.96
	Grid 2.3.1	300	40	70.545	3.46	2.00	7.21
	Grid 2.4.1	400	40	94.061	2.60	1.50	9.16
	Grid 2.5.1	500	40	117.580	2.08	1.20	23.71
	Grid 2.6.1	600	40	141.090	1.74	1.00	28.27

Table 4.3: Grid characteristics for case of different cells/λ - [1]: rate between the maximum cells/λ and the one for the grid under investigation. - [2]: ratio between the minimum computational time and the one corresponding to the selected grid - [3] run time of 57 minutes

An illustration of the Richardson extrapolation and the estimated convergence rate for $\alpha = 0.50$ and $\alpha = 0.90/0.10$ and 10 wave periods is presented in Figure 4.8. For $\alpha = 0.90/0.10$ a behaviour close to an asymptotic convergence is achieved with a converge rate of $p = 1.11$. For $\alpha = 0.50$ the responses shows that the behaviour is close to the asymptotic range of converge but higher ($P = 2.22$), which indicates that a different safety factor is applied.

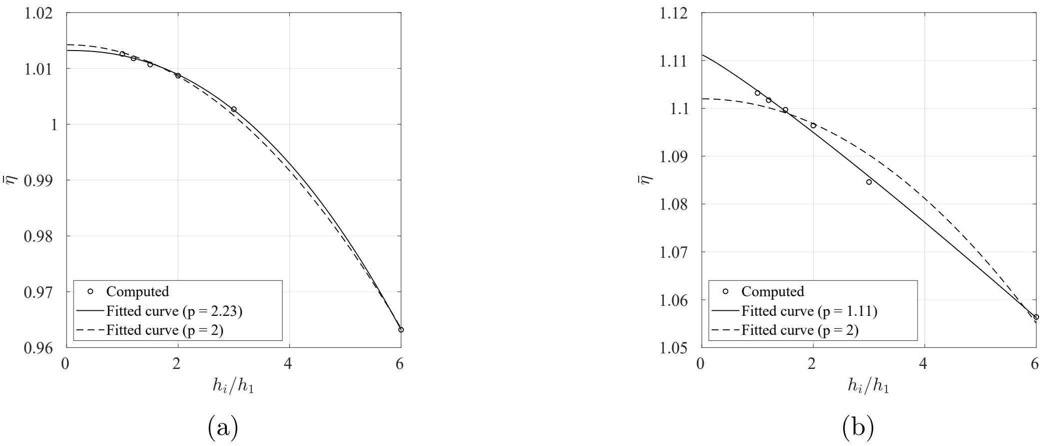

Figure 4.8: Estimated convergence for the wave propagation of iso-surface for different number of cells /λ - a) $t/T = 10$; $\alpha = 0.50$, b) $t/T = 10$; $\alpha = 0.10/0.90$

It is concluded that a better fitting is obtained for $\alpha = 0.50$ than for $\alpha = 0.90/0.10$, however, this convergence ratio does not give enough information for the convergence analysis. So, a deeper analysis need to be conducted for a better understanding of the iso-surface convergence ratio. This is done by Richardson extrapolation method and also a simple difference, which is summarized in Table 4.4.

t/T	Grid	Grid 2.6.1	Grid 2.5.1	Grid 2.4.1	Grid 2.3.1	Grid 2.2.1	Grid 2.1.1
10	$\bar{\eta}_{0.50}$	1.0126	1.0118	1.0107	1.0087	1.0027	0.9632
	% diff	-	0.08	0.19	0.39	0.98	4.88
	$U_{\bar{\eta}_{0.50}}$	0.50	0.69	1.03	1.77	3.89	15.31
10	$\bar{\eta}_{0.90/0.10}$	1.1032	1.1017	1.0997	1.0964	1.0846	1.0564
	% diff	-	0.14	0.32	0.62	1.69	4.24
	$U_{\bar{\eta}_{0.90/0.10}}$	1.05	1.26	1.59	2.14	3.29	6.98

Table 4.4: Spatial uncertainty for wave propagation over wave length with $s = 3.80$

According to Table 4.4 uncertainties values are kept low in all cases except for the coarsest grid (2.1.1). Therefore, the results obtained from the uncertainty analysis shows that the Grid 2.2.1 is enough to verify that the model is already convergence, as the uncertainties are lower than 5%. The next step is to check the wave kinematics over depth.

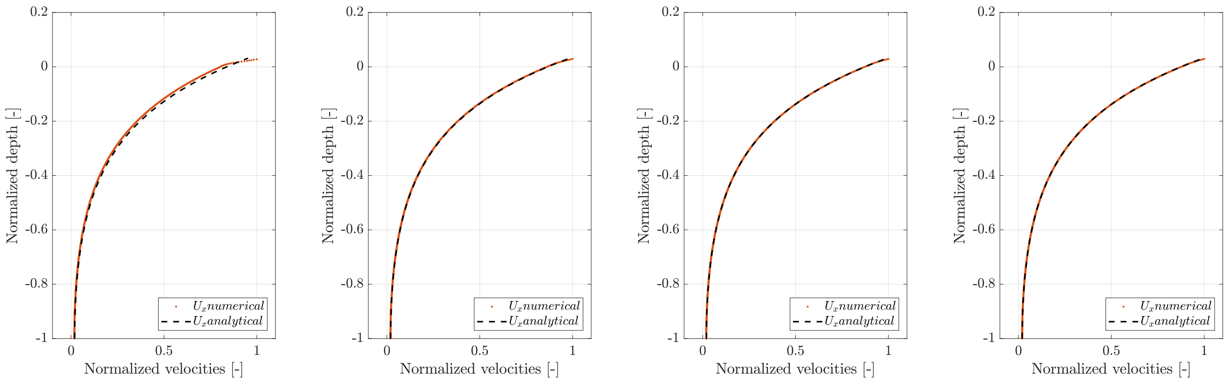

(a) (b) (c) (d)

Figure 4.9: Maximum horizontal velocity profile over depth for 10 wave periods - a) 100 cells/λ b) 200 cells/λ c) 300 cells/λ d) 400 cells/λ

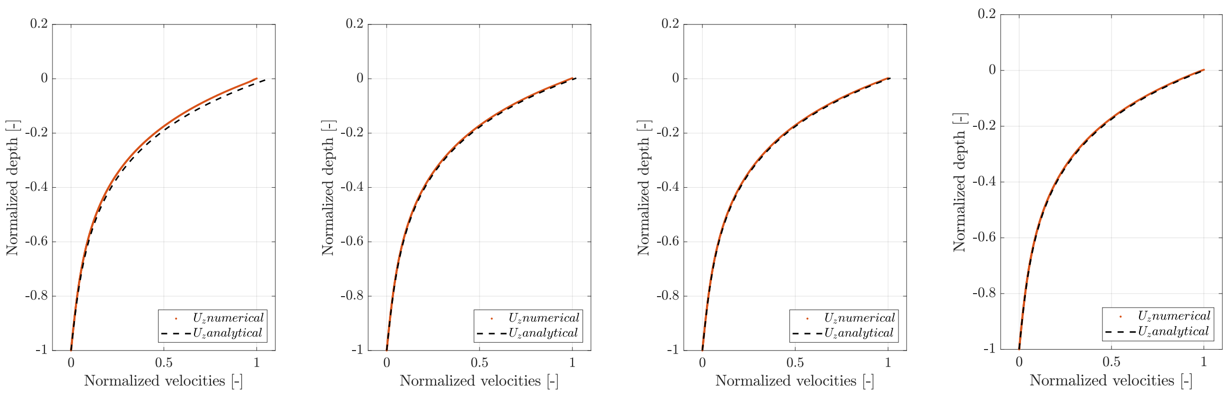

(a) (b) (c) (d)

Figure 4.10: Maximum vertical velocity profile over depth for 10 wave periods - a) 100 cells/λ b) 200 cells/λ c) 300 cells/λ d) 400 cells/λ

The kinematic profiles gives a good understanding of the mesh refinement quality on all regions. From those profiles some interesting conclusions are discussed. First, the horizontal velocity is more influenced by the cells/λ close to the surface than the vertical velocity. Second, the vertical velocity profile is found to have a worst fitting far from the surface elevation, being clear on the comparsion between Figures 4.9a and 4.10a, while Figure 4.9a follows the analytical solution until is closed to the surface Figure 4.10a shows that the vertical velocity profile does not follow the exact solution in the upper half of the velocity profile.

In conclusion, from this analysis and the uncertainties found in Table 4.4, 200 and 300 cells per wave length are enough to achieve a converged solution. The same conclusions are found for the steepest wave.

4.3 Temporal discretization

Despite spatial convergence is assumed to be fulfilled for the cases analyzed above, temporal discretization is not analyzed in detail yet. The following section is focused on the solution verification step of the Δt. The analysis of this section is based on the wave with $s = 3.80$. As similar results are found for $s = 6.23$ the verification analysis of this wave is only included in Appendix C.5.

In order to obtain satisfactory results 5 cases are analyzed with constant values of 40 and 400 elements per wave height and wave length respectively. Those values ensure that the spatial parameters does not influence this analysis. Then, Table 4.5 shows all different Δt values that are analyzed.

Steepness	Model	Δt	Max Courant Number	Mean Courant Number	Ref ratio[1]	Normalized run time[2]
3.80	$\Delta t_{1.1}$	0.00012	0.049	0.003	2.400	1.00[3]
	$\Delta t_{2.1}$	0.00010	0.035	0.003	2.000	1.09
	$\Delta t_{3.1}$	0.00009	0.030	0.002	1.800	1.35
	$\Delta t_{4.1}$	0.00008	0.025	0.002	1.600	1.47
	$\Delta t_{5.1}$	0.00005	0.013	0.001	1.000	2.44

Table 4.5: Different temporal discretization for Grid 2.4.1 (Table 4.1) - [1]: rate between the minimum Δt and the one for the grid under investigation. - [2]: ratio between the minimum computational time and the one corresponding to the selected grid - [3] run time of 23.83 hours

The values Δt (from 0.00012 to 0.00005) are chosen based on all satisfactory simulations that are completed. It is found that for $\Delta t > 0.00012$ numerical models crash without complete the whole simulation, then higher values are not possible to be used. This might compromise the reliability of the results for the temporal discretization. Due to this low values of Δt all Courant (Co) number or Courant–Friedrichs–Lewy (CFL) are found to be extremely low, which indicates that the convergence analysis could be achieved for higher Δt values.

Data from Table 4.5 is analyzed following the same procedure as in Section 4.2. Therefore, first the data for different Δt is presented in Figures 4.11 which represents the comparison between analytical and numerical method for different values of α at the interface and $t/T = 5$ and 10.

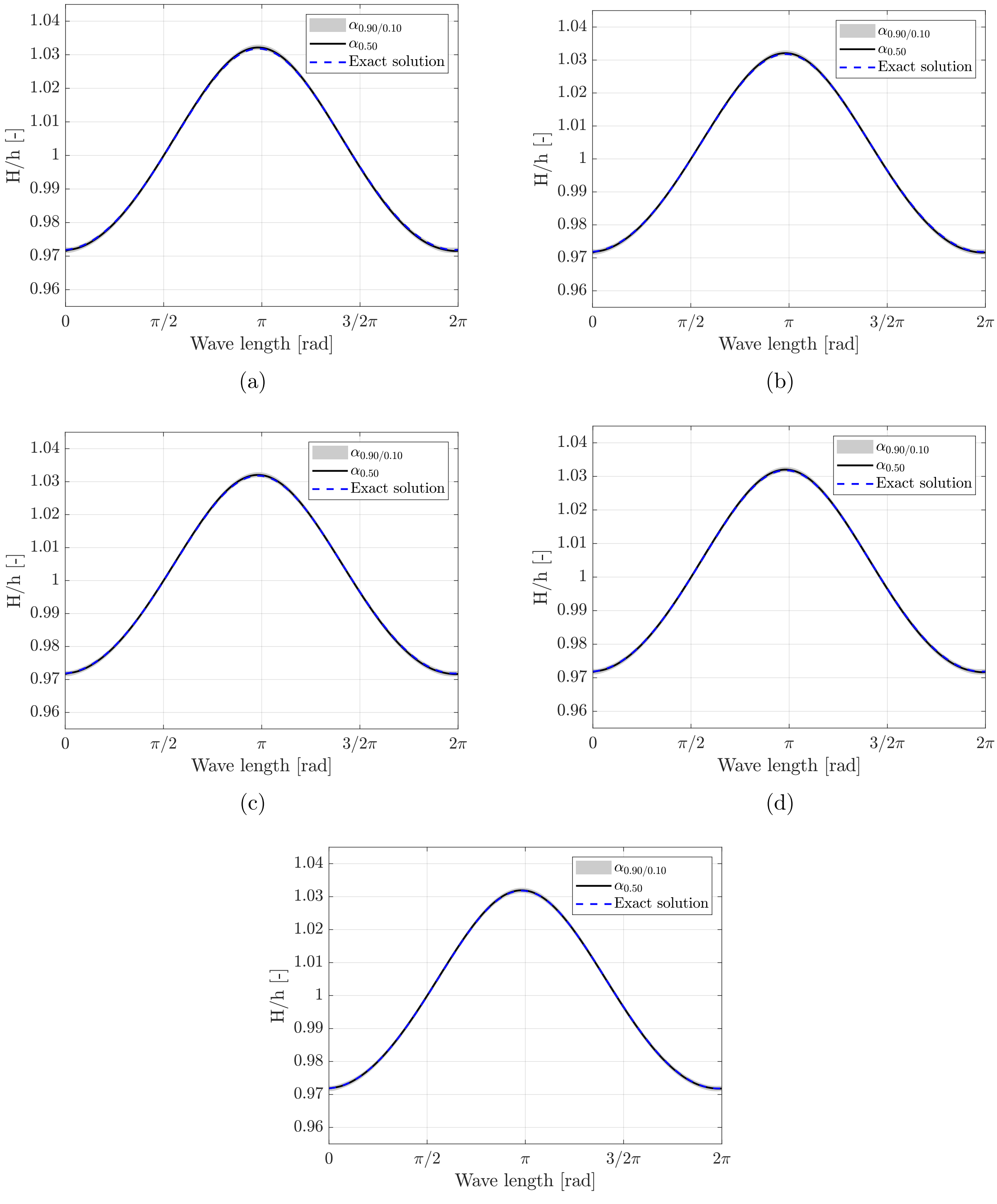

Figure 4.11: Free surface elevation for different Δt with analytical solution and $t/T = 10$ - a) Model $\Delta t_{1.1}$ b) Model $\Delta t_{2.1}$ c) Model $\Delta t_{3.1}$ d) Model $\Delta t_{4.1}$ e) Model $\Delta t_{5.1}$

From Figures 4.11, small differences can be appreciated in the variation of the iso-contours between different Δt changes. This Figures are illustrated to be on phase with the analytical solution although a small phase delay is found, which can be seen in Figures 4.12. This indicates three facts. Firstly, all Δt gives good results in the interface. Secondly, this parameter do not has as much influence as spatial democratization does. Laslty, the phase delay can be caused by spatial discretization errors, as all different Δt are affected by the same phase delay.

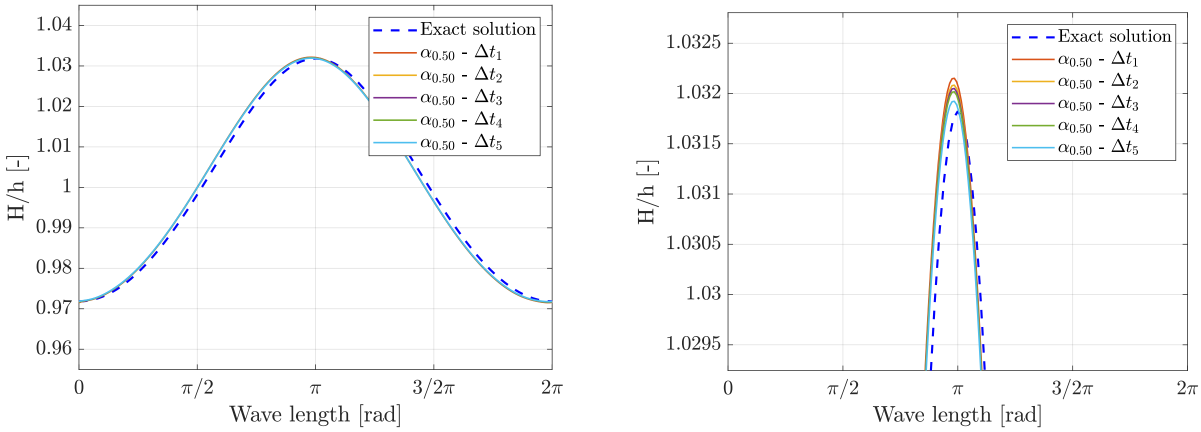

(a) (b)

Figure 4.12: Free surface elevation for $\alpha = 0.5$ and 5 different Δt with analytical solution and $t/T = 10$ - a) 1 wave length, b) Detail of the wave crest

The next step is to calculate the Richardson extrapolation and the estimated convergence rate for $\alpha = 0.50$ and $\alpha = 0.90/0.10$ for 10 wave periods, which is illustrated in Figure 4.13. This results shows that the behaviour in both cases is close to the asymptotic converge with $\alpha = 0.50$ having $p = 0.992$ and $\alpha = 0.90/0.10$ with a converge rate of 1.53.

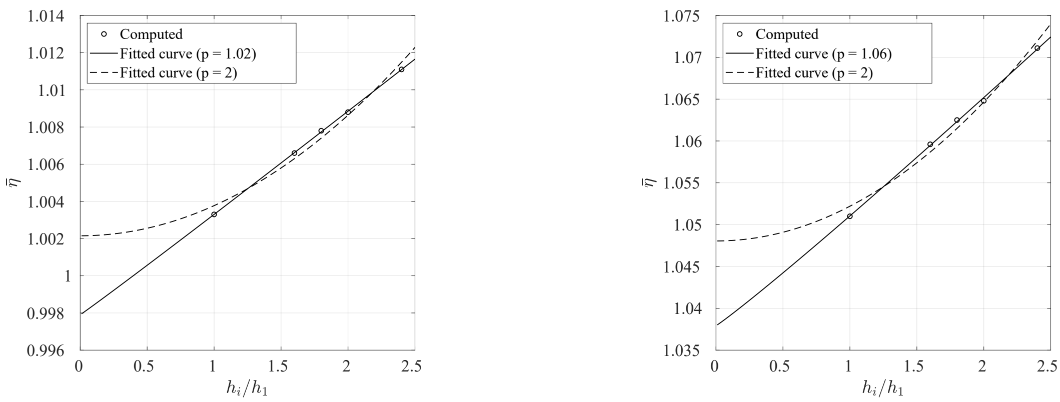

(a) (b)

Figure 4.13: Estimated convergence for the wave propagation of iso-surface for different Δt - a) $t/T = 10$; $\alpha = 0.50$, b) $t/T = 10$; $\alpha = 0.10/0.90$

Once the converge rates are being calculated, the next step is to calculate the uncertainties based on the Richardson extrapolation method with the application of some safety factors. This data is presented in Table 4.6.

t/T	Grid	$\Delta t_{5.1}$	$\Delta t_{4.1}$	$\Delta t_{3.1}$	$\Delta t_{2.1}$	$\Delta t_{1.1}$
10	$\bar{\eta}_{0.50}$	1.0033	1.0066	1.0078	1.0088	1.0111
	% diff	-	0.82	1.09	1.31	1.91
	$U_{\bar{\eta}_{0.50}}$	1.67	2.73	3.08	3.44	4.17
10	$\bar{\eta}_{0.90/0.10}$	1.051	1.0596	1.0625	1.0648	1.0711
	% diff	-	0.81	1.09	1.31	1.91
	$U_{\bar{\eta}_{0.90/0.10}}$	1.67	2.73	3.08	3.44	4.17

Table 4.6: Temporal uncertainty for wave propagation for different Δt with $s = 3.80$

All Δt shows that the uncertainty is lower that 5%. This means that temporal discretization, in this case, does not influence the results as much as the spatial discretization does. So, it is concluded that values around Δt_1 or even higher could be enough to describe a wave. Nevertheless, values higher than Δt_1 can not be analyzed. Also, as it is conducted for the spatial discretization, the velocity profile is verified. This shows all Δt values gives reliable results. Similar conclusions are found for $s = 6.80$. In this case also the lowest Δt investigated gives lower uncertainties than 5%

4.4 Verification's conclusions

To sum up with the solution verification step, which is based on the V&V technique presented in Appendix A.4, the following Table 4.7 collect the main outcome from this analysis. This data is further used in the validation stage. Therefore, Table 4.7 presents the final outcome obtained from the solution verification step analysis from the two different steepens.

Steepness [%]	Cells/H	Cells/λ	Δt [1]	Co [2]	Max Co [3]
3.80	30	200	0.00012	0.049	0.5
6.23	**30**	**200**	**0.00020**	**0.053**	**0.5**

Table 4.7: Verification results - [1] , [2] ΔT and Co might be not reliable enough for the following calculations - [3] Final max Co (Also called CFL) condition used on numerical simulations

As it can be seen, the information obtained from the verification analysis for both cases are similar. The only difference found in the converge analysis between both steepness is the temporal discretization.

Additionally, an extra parameter is included in Table above, called Max Co. As it is indicated in the caption of Table 4.7, the Courant number values obtained from the verification analysis are considerably lower than expected. Then, if this temporal discretization is included in the validation analysis, extremely high time efforts would be required to resolve all simulations. Then, a maximum Courant number is establish as temporal discretization limit. Moreover, as it is found in this analysis, temporal discretizations does not have as much influence in the uncertainties as spatial discretization does. This is in agreement with Eskilsson et al. [2017] and Appendix A.4, where it can be seen that convergence studies are more sensitive to the spatial than to temporal discretization. Then by applying the maximum CFL condition presented in Table 4.7 it is secure that temporal convergence is still achieved.

In addition, 3D models are simulated with a different refinement level, due to time limitation reasons. Then, the final spatial and temporal discretization employed in 3D modelling can be found in Section 5.3 Table 5.2. In that section an explanation of the influence of those new discretization values is described.

Finally an illustration of the grids with the final parameters found in the verification analysis are presented in Figures 4.14a and 4.14b

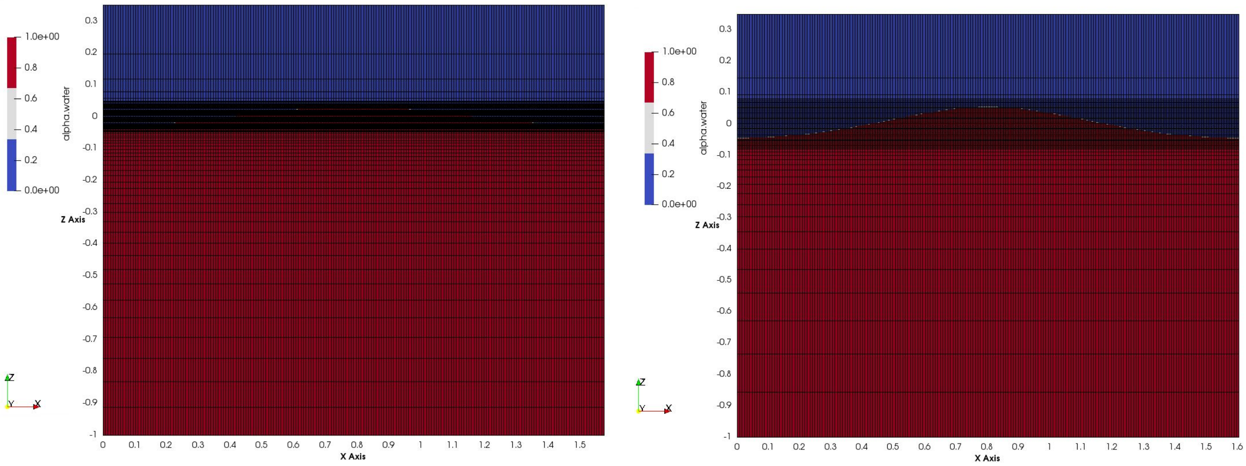

(a) (b)

Figure 4.14: Details of the final grids that corresponds to $s = 3.80$ and $s = 6.23$ from Table 4.7 - a) $s = 3.80$ b) $s = 6.23$

Validation 5

In this chapter the validation analysis of the 2D and 3D model is conducted. The analysis is performed by comparing numerical models with empirical results for both models and checking that the data from the verification analysis give reliable results, see Appendix A.4

5.1 Introduction

Validation consist of ensure that the the numerical model is accurate enough to describe the phenomena under investigation. Accordingly, numerical results are compared to experimental data. As it is mentioned in Section 3.2.3 two different approaches are chosen in order to conduct the validation analysis. A 2D model for only propagation of waves is setup and a 3D model that includes the chamber. The temporal and spatial discretization setup is established based on the verification analysis summarized in Table 4.7.

Both models are validated against the free surface elevation at different wave gauges for the two different regular waves presented Table 3.1. Also, an sketch with the location of the wave gauges is presented in Figure 3.2. The measured surface elevation and incident waves at wave gauge 17 used in this analysis are illustrated in Figure 3.3.

As explained in Section 2.1, two different wave theories are applied for generation of waves *First-order irregular waves* and *StokesFifth*. For the first approach a FFT is conducted, illustrated in Figure 3.4, for incident waves from empirical data. This spectrum contains all the information needed to generate the exact waves at wave gauge 17, which is located at the inlet of the numerical wave tank. Nevertheless, only the most significant region of the spectrum is used, due to some limitations founded in *waves2Foam* solver. For the second approach, a Stokes 5^{th} order method is utilized, which is possible due to the fact that waves are generated as regular waves in the experiments.

The dimensions of the numerical model are variable according to different wave parameters. Despite the wave basin is described as illustrated in Figure 3.2, the size of the model is increased by the so-called relaxation zones, see Section 2.6. This is important to consider as number of element in the numerical model is largely increased.

5.2 2D model

In this section a 2D model is performed to validate the numerical simulation for only propagation of waves. This analysis is able to reproduce laboratory test as waves are uni-directional. This two dimensional model gives an accurate validation while saving computational time due to the reduction of the number of elements in the model. Moreover, the dimensions of the computational wave basin are setup according to Figure 3.2 and Table 3.2, however, relaxation zones are not included in this table. The next stage is to validate the numerical model against incident waves. For the 2D model the wave gauges selected for the validation are the wave gauge number 17, 24, 27, 30, 20, 21 and 22, those are illustrated in Figure 3.2.

Number No [−]	Height H [m]	Length λ [m]	Depth h [m]	Period T [s]	Steepness $s = (H/\lambda) * 100$ [%]	Total height h_{total} [m]
18	0.06	1.58	1.00	1.00	3.80	1.40
20	0.10	1.61	1.00	1.00	6.23	1.40

Table 5.1: Characteristics of wave test number 18 and 20, AAU series 7, Table C.1

This analysis is divided in two different steps. First, the validation of the method chosen for wave generation. Second, the validation of the free surface elevation at different wave gauge locations.

5.2.1 Validation of the wave generation method

The first step is to validate that waves are correctly generated. This is done by comparing incident waves from the experiments and from the numerical models at the inlet (WG 17). In the following Figures 5.1 and 5.2 incident waves and both generation method for wave test number 18 and 20, respectively, are illustrated.

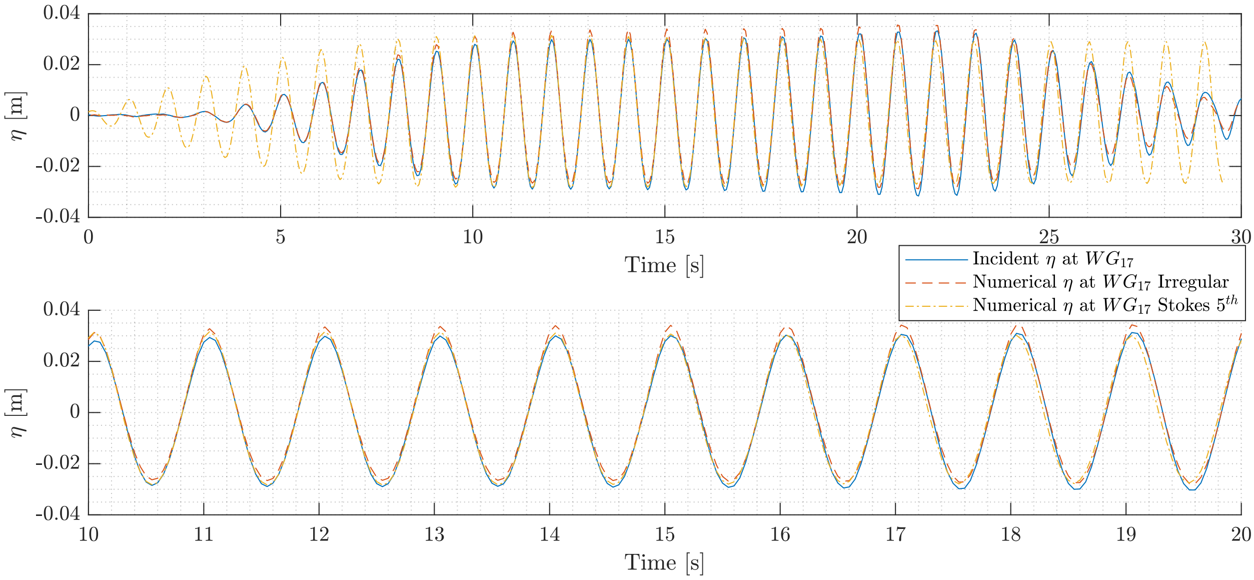

Figure 5.1: Wave test number 18. Comparison between: Incident waves from laboratory measurements *Incident* η *at* WG_{17}, Numerical waves from spectrum from Figure 3.4a *Numerical* η *at* WG_{17} *Irregular* and Numerical waves from Stokes 5^{th} order theory wave generation *Numerical* η *at* WG_{17} *Stokes* 5^{th}.

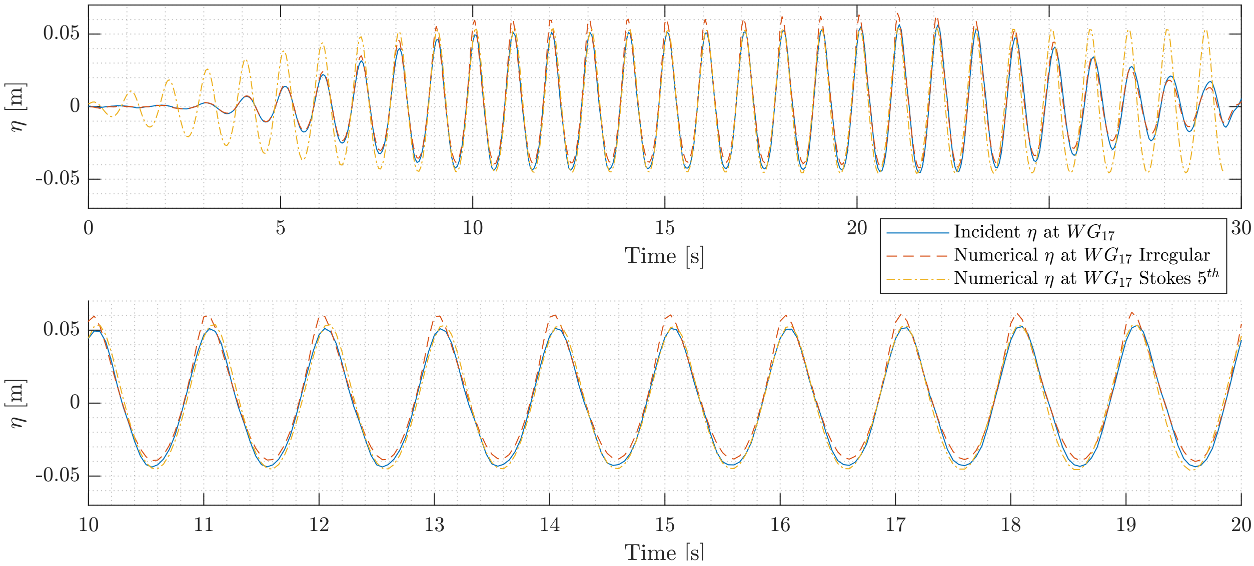

Figure 5.2: Wave test number 20. Comparison between: Incident waves from laboratory measurements *Incident* η *at* WG_{17}, Numerical waves from spectrum from Figure 3.4b *Numerical* η *at* WG_{17} *Irregular* and Numerical waves from Stokes 5^{th} order theory wave generation *Numerical* η *at* WG_{17} *Stokes* 5^{th}.

It can be seen that both waves have better results for Stokes 5^{th} order than *First-order irregular* method, with even worst results for the steepest wave on this last generation method. This indicates that *wave2Foam* can not properly generate this waves, as some second order effects, such as parasitic modes are influencing the results. Also in both wave cases it can be seen that after some fully developed waves a small phase delay and difference in the troughs is founded, with a higher influence on the steepest wave. This can be an indicator that some reflected waves are affecting the results.

Second order effect: The analysis of second order effects is performed based in Madsen et al. [1992]. This measures the wave energy between wave modes by comparing the first two harmonic amplitudes calculated from an FFT, which are the ones that carry most of the energy, over the first two wave length at different locations. The first two harmonics are illustrate in Figure 5.3. This analysis is conducted for the first 5 fully developed waves to get enough data with any alteration from possible reflected waves, this is analyzed further in this section. Then the analysis is performed from $t/T = 11$ to $t/T = 16$. In this section only the analysis corresponding to wave $s = 3.80\%$ is presented.

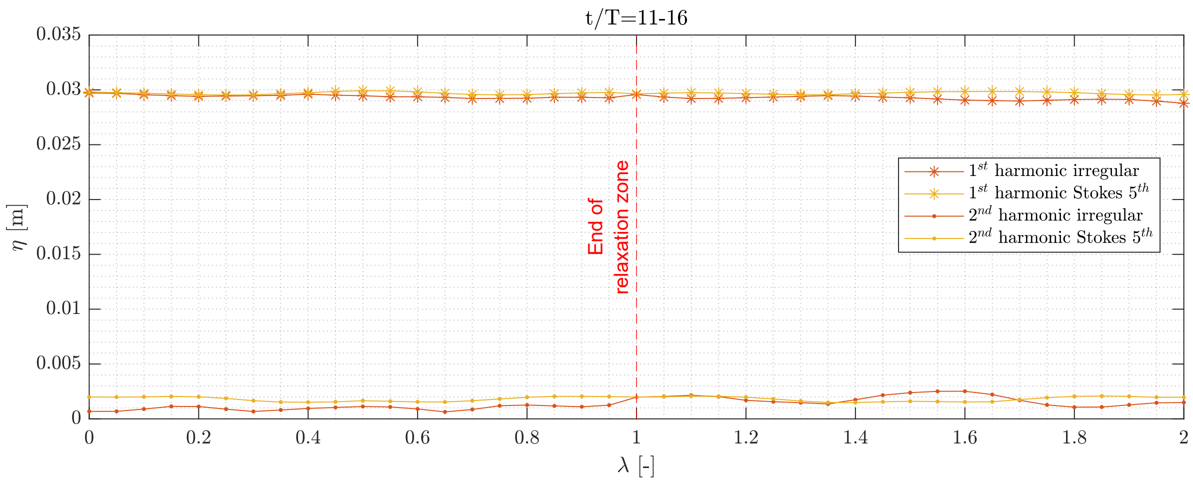

Figure 5.3: Wave amplitude for first and second harmonics for $t/T = 11$ to $t/T = 16$ - wave test number 18

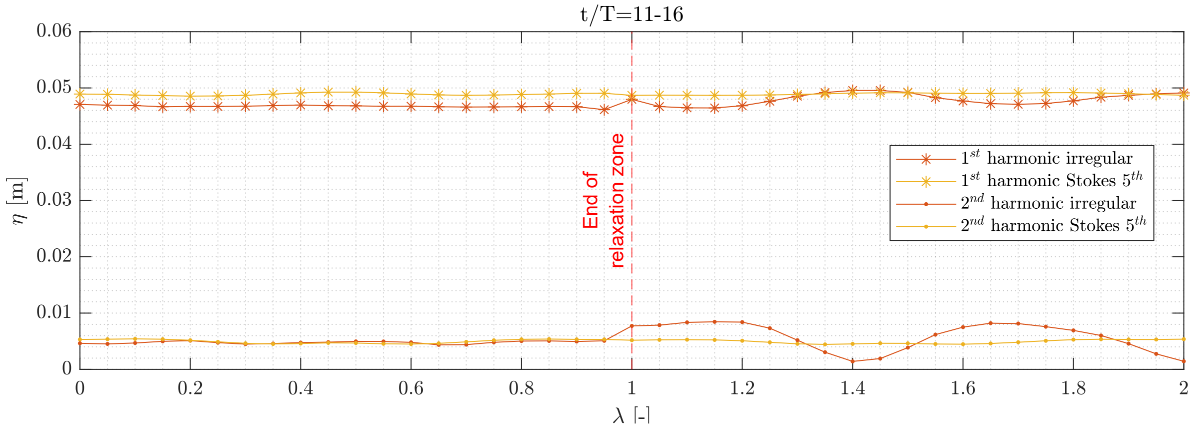

Figure 5.4: Wave amplitude for first and second harmonics for $t/T = 11$ to $t/T = 16$ - wave test number 20

In Figures 5.3 and 5.4 is clear to see a fluctuation in the wave amplitudes, this indicates a transfer of energy between different wave modes. For *First-order irregular waves* suffer some fluctuations along the two wave length, being more significant after the relaxation zone. This indicates that once wave are computed fully numerical the energy transfer is more important. This effect is even more clear on 2^{nd} harmonic. This variation along the space domain explains that *First-order irregular waves* method can not reproduce the waves from laboratory experiments, which are generated as 2^{nd} order irregular waves, due to parasitic waves. Stokes 5^{th} order theory gives better results, however small fluctuations are appreciated. Then it can be concluded that *First-order irregular waves* generation approach is not suitable for the purpose of the validation of waves, so, only Stokes 5^{th} order method is employed and further analyzed.

Similar conclusions are found for the steepest wave as it can be seen in Figure 5.4. For this case the energy transfer between the different wave modes is found to be even more pronounced for the *First-order irregular waves* method, which means that this method is heavily affected by the steepness of the waves.

Reflected waves: The next stage is to study the influence of reflected waves in the NWT, despite relaxation zones are used for absorption purposes. This analysis is only conducted for wave with $s = 3.80\%$, similar results are obtained for $s = 6.23\%$ which can be found in Appendix D.2. A reflection analysis is conducted for according to Eldrup and Andersen [2018], which covers all cases under investigation. This method is applied by a software called *WaveLab*. The main difference of this method is that the bounds and the free waves are separated based on their different celerity. This analysis is carried out at all wave gauges included in the 2D model, however, only WG_{17}, WG_{30} and WG_{22} are included in the main report, which are illustrated in Figure 5.5, the rest of the wave gauges, which gives similar results can be found in Appendix D.1.

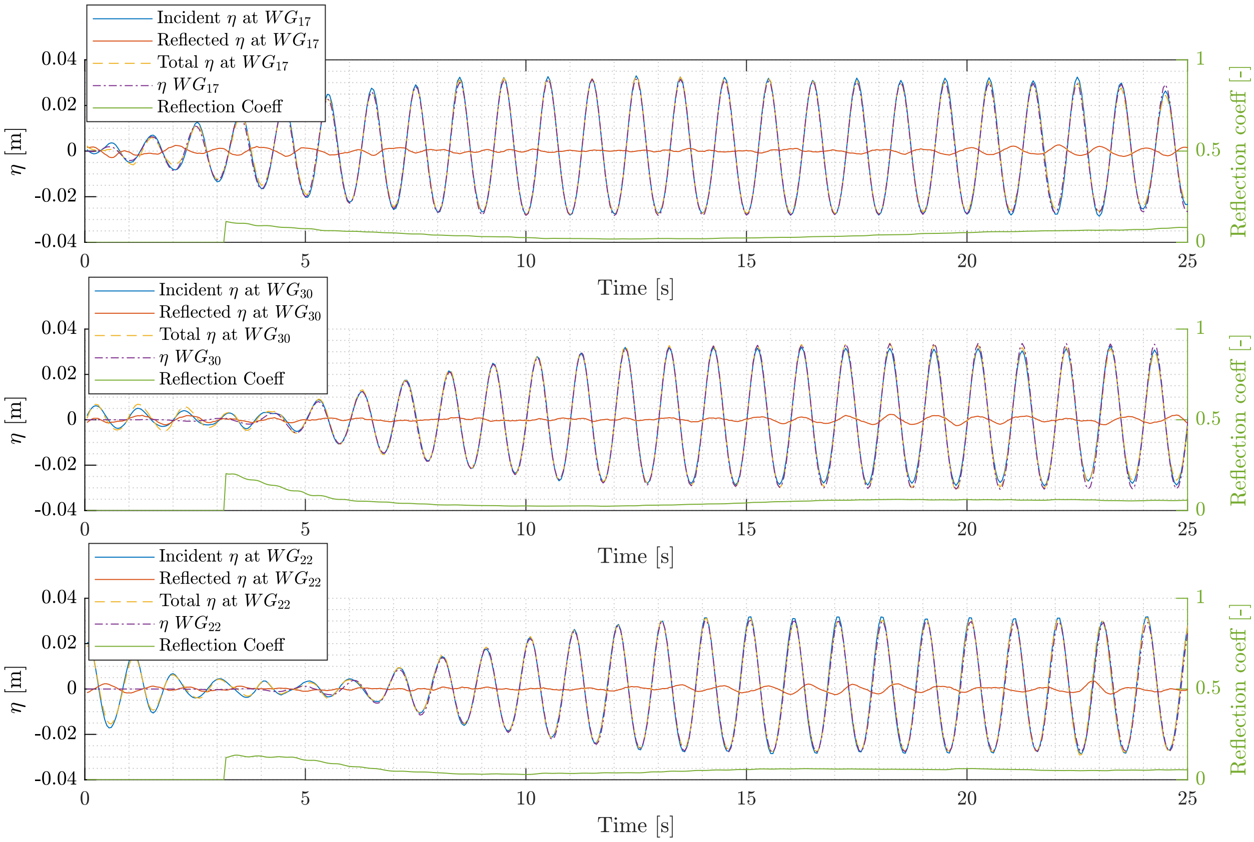

Figure 5.5: Reflection analysis at WG_{17}, WG_{30} and WG_{22} from Stokes 5^{th} order wave generation. *Incident η at WG_{xx}*, *Reflected η at WG_{xx}* and *Total η at WG_{xx}* are obtained from the reflection analysis of η WG_{xx}, which corresponds to the simulated surface elevation at each WG_{xx}.

From Figure above, 5.5, it is clear to see that although an outlet relaxation zone is setup, some reflected waves are influencing the results. Also, a peak on the reflection coefficient can be seen at the beginning of each graph. This peak is caused by small variations in the surface elevation in the numerical wave basin before waves are generated, then this part has to be neglected.

From Figure 5.5 is clear to see that during the first 16 seconds of the simulation at $WG-17$ reflected waves are almost negligible. After this moment the reflection coefficient starts to increase, which means that the outlet relaxation zone does not totally absorbs incoming waves. This means that relaxation zones are not fully absorbing incoming waves. Also, looking at WG_{30} and WG_{22} a similar behaviour, but earlier than at $WG-17$ is found. On this new locations it can be seen that reflected waves are acting before, which is explained by the fact that those WG are located close to the outlet relaxation zone. Moreover, WG_{30} is a crucial location, as the chamber is placed close to this WG.

To conclude, reflected waves influence the results after some periods, but for the first 16 seconds at WG_{17} this phenomenon does not have a large influence on it. Then, only the first few fully developed waves are valid for further analysis, as $WG-30$, where the chamber would be located, shows a increase in the reflection coefficient which could give bad results.

5.2.2 Validation of the free surface elevation

The next stage of the analysis is the validation in the free surface elevation at different wave gauge locations. Those locations are corresponding to wave gauges 24, 27, 30, 20, 21 and 22.

In order to understand the influence of the steepness in the validation of the NWT wave gauges 24, 27 and 30 are analyzed for both steepness, Figures 5.6 and 5.7. However, for 20, 21 and 22 only the $s = 3.80\%$ wave is analyzed in the report, Figure 5.8.

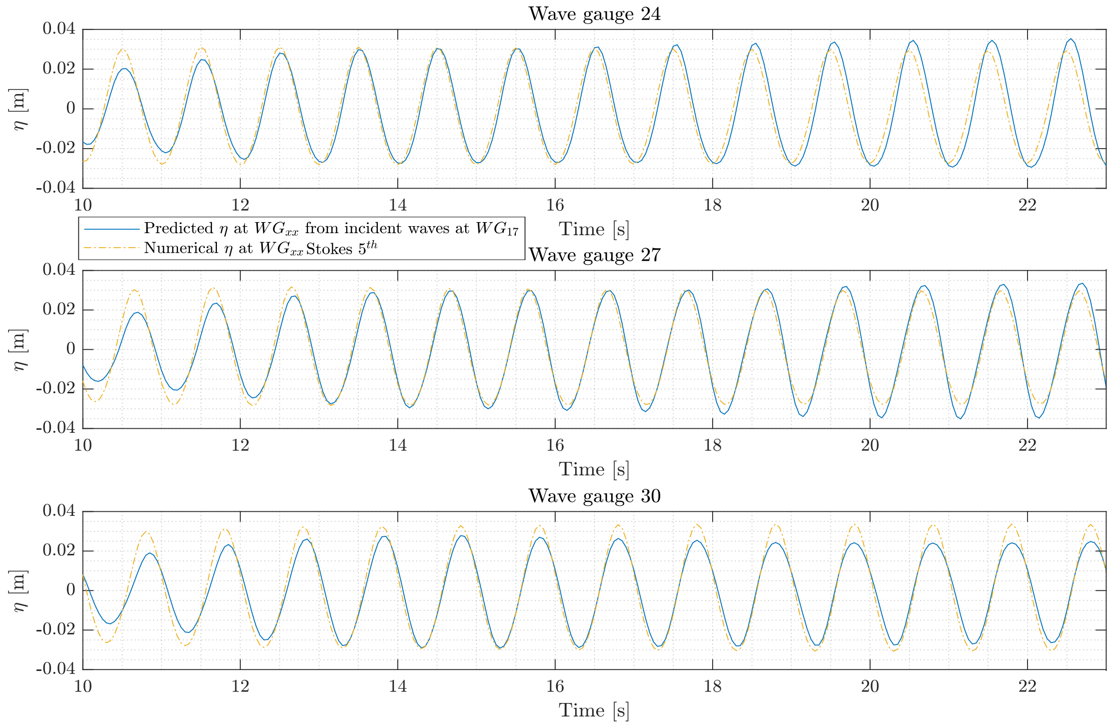

Figure 5.6: $s = 3.80\%$ - Comparison between Incident waves from the laboratory and numerical waves generated by Stokes 5^{th} order at WG_{24}, WG_{27} and WG_{30}

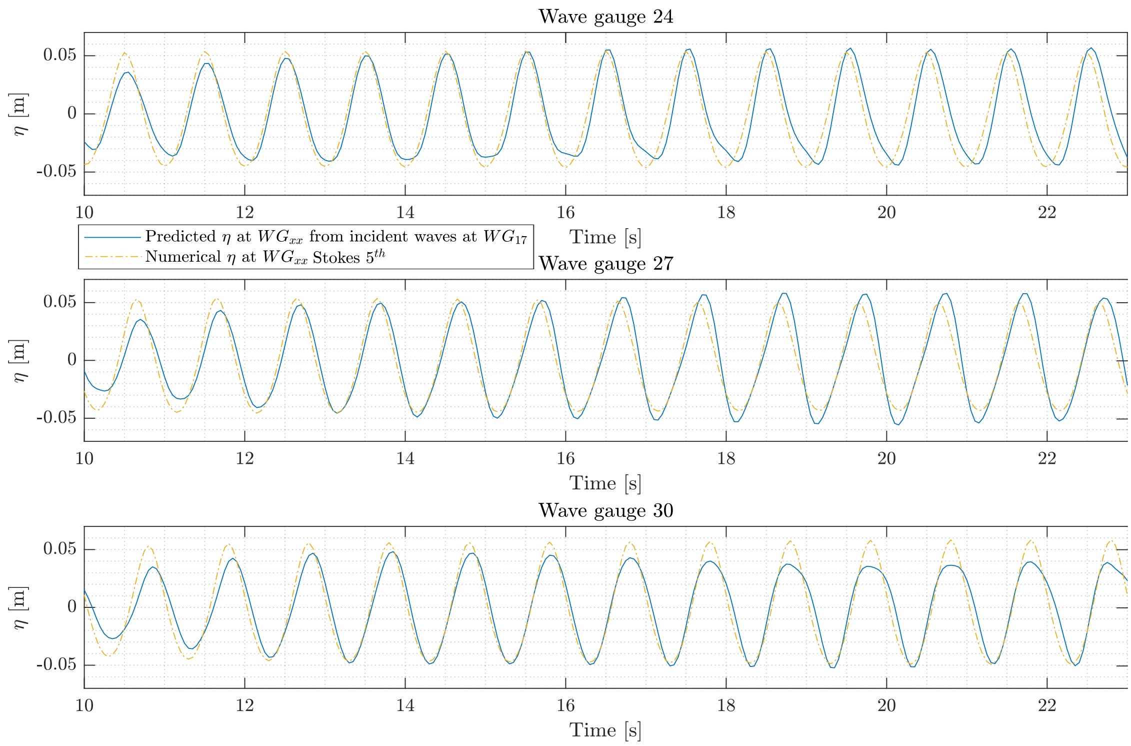

Figure 5.7: $s = 6.23\%$ - Comparison between Incident waves from the laboratory and numerical waves generated by Stokes 5^{th} order at WG_{24}, WG_{27} and WG_{30}

Comparing Figures 5.6 and 5.7 it can be seen that wave with $s = 3.80\%$ is better predicted than $s = 6.23\%$. It is only after 6 fully developed waves when the numerical and experimental model shows a different behaviour. However, it can be seen that the numerical model have a cyclic behaviour, while the experimental data shows large non-linearities, this might indicate that the reflection analysis is not well conducted. Then, for $5-6$ fully developed waves in Figure 5.6 shows good results with some differences in the peaks at $WG-30$. For the steepens wave similar results are found, where the first $5-6$ fully developed waves shows a similar behaviour. However, in this case larger differences are found between both waves after 6 developed waves, when the numerical model does not capture all non-linearities that the experiment shows.

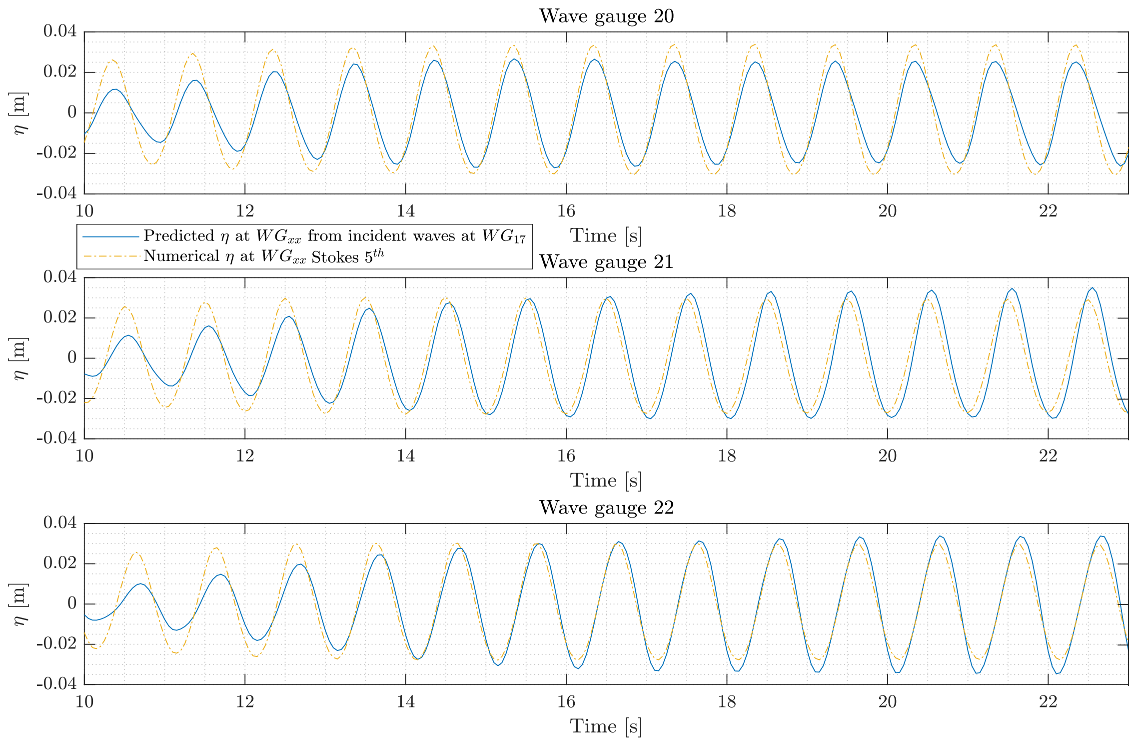

Figure 5.8: $s = 3.80\%$ - Comparison between Incident waves from the laboratory and numerical waves generated by Stokes 5^{th} order at WG_{20}, WG_{21} and WG_{22}

The last step of the validation of the 2D model is focused on the free surface elevation at wave gauges 20, 21 and 22. Figure 5.8 shows that the numerical have a similar behaviour as the experimental data, however some non-linearities in the experiment are not capture by the model. This leads into the same conclusion as $WG-24$, $WG-27$ and $WG-30$. Waves are well predicted for the first few developed waves until large second order effects starts to affect the experiment. From this point the numerical model do not capture this behaviour. Similar conclusions are obtained from the $s = 6.23\%$ where it can be found in Appendix D.2.

To sum up with the validation analysis. First, Stokes 5^{th} order theory is the only wave generation method valid for the simulations. Second, reflected waves are acting in the model, despite of setting up an absorption relaxation, however, the influence is not very important. Last, waves, in general, are well predicted from the numerical model for the first $5-6$ fully developed waves, after this moment large non-linear effects are affecting the experimental data, which the model is not capable of capture them.

5.3 3D model

This stage of the validation is conducted for 2 different chamber configurations, which are A4 and A5 (See Figure 5.9), and the same 2 waves from the 2D validation o analysis. In this section the validation is carried out against measured waves at different wave gauge locations. The size and the boundaries of the 3D models is described in Table 3.2 and Figure 3.2.

(a) (b)

Figure 5.9: a) A4 chamber configuration - b) A5 chamber configuration

As briefly introduced in Section 5.4, all 3D model are not modelled with a full converge mesh. The main reason to use a lower refinement level is due to time limitations and computational efforts. Therefore, a new spatial discretization criteria reduce the refinement of the mesh to the values presented in Table 5.2. Then, this new meshes of the 3D model gives grids between 1 to 11 millions elements. However, temporal refinement is still based on the maximum CFL condition of 0.5. As a consequence of this new spatial refinement the uncertainties in the results of the model are increased, as explained down bellow.

Type	Cells/λ	Cells/H	Max CFL
Verification	200	30	0.5
3D model	**150**	**23**	**0.5**

Table 5.2: Spatial and temporal discretization for 3D models

The increase of the uncertainties can be quantified according to the solution verification step, see Section 4. Then, this reduction is conducted in such a way that the grid can be reduced as much as possible with a low influence in the uncertainties. However, in any case the new uncertainties are over 5% limit. The Cells/λ is reduced from 200 to 150 which increases the uncertainties from $3-5\%$ to $5-7\%$, see Tables 4.4 and C.8. And second, decreasing the number of Cells/H from 30 to 23 increase the uncertainty of the model from $5-8\%$ to $10-12\%$, see Tables 4.2 and C.6. This increase in the uncertainty of the model allows a reduction of the number of cells between $40-50\%$.

The analysis of the validation of the 3D model is divided in two stages. The first one is focused on the A4 chamber configuration, while the second one is focused on A5 configuration. Both validation analysis on the main reports are conducted for the steepest wave. The validation of wave with $s = 3.80\%$ give, on both cases, similar results.

5.3.1 Validation of A4 chamber configuration

The validation analysis of this configuration is conducted for all wave gauges that are included in the 3D numerical model. However, in this section only the main aspects of this analysis are discussed for waves gauges illustrated in Figures 5.10, 5.11 and 5.12.

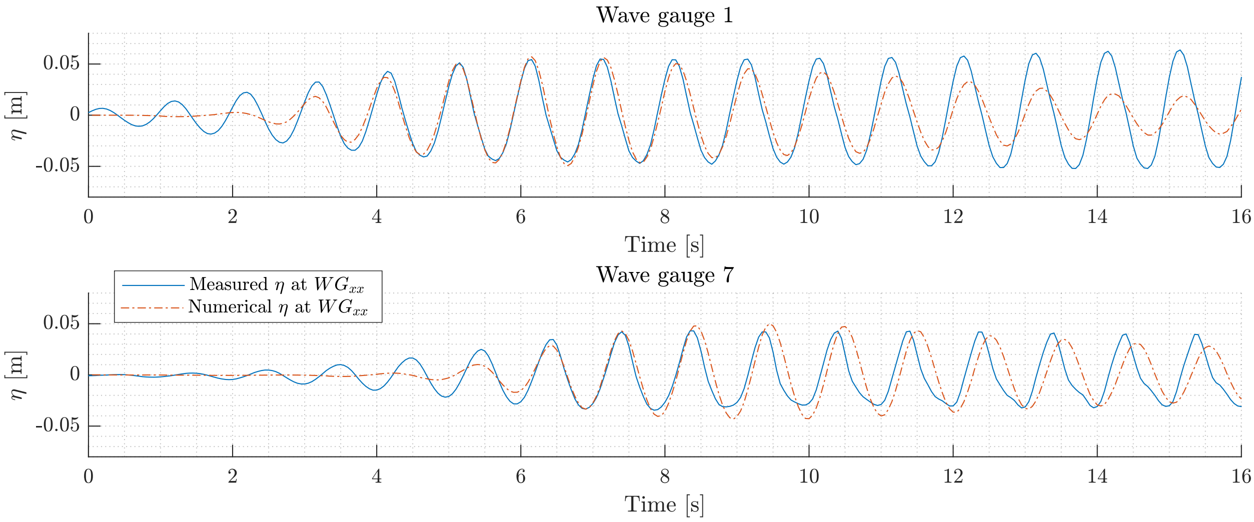

Figure 5.10: Free surface elevation at different wave gauges locations, see Figure B.2, for A4 chamber configuration, see Figure B.3, and wave test number 20

The first part of the analysis is focused on the validation of waves at wave gauges 1 and 7. It can be seen that numerical and experimental data at $WG-1$ behave in a similar manner. However, after 9 seconds a phase delay and a higher difference on peaks and troughs is appreciated. This can indicates that reflected waves are highly influencing the results. Also, the fact that a low grid resolution is applied affects the results too. Moreover, from Figure 5.10 it can be seen that wave propagation is still well captured, however, waves that are not propagating in the direction of the incoming waves, such us diffracted or reflected waves are causing large difference between both numerical and experimental waves. Also, at wave gauge 7 a large difference between numerical and experimental data is found, where second order effects are not well captured in the numerical model.

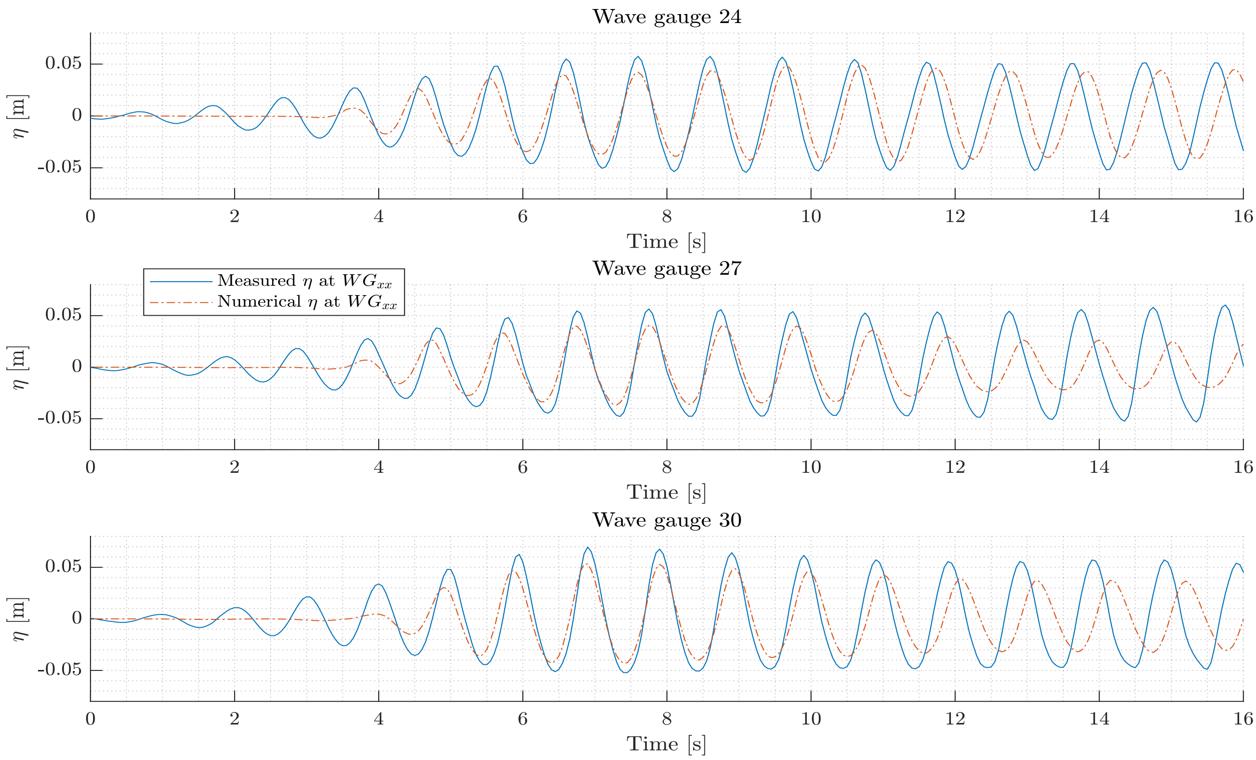

Figure 5.11: Free surface elevation at different wave gauges locations, see Figure B.2, for A4 chamber configuration, see Figure B.3, and wave test number 20

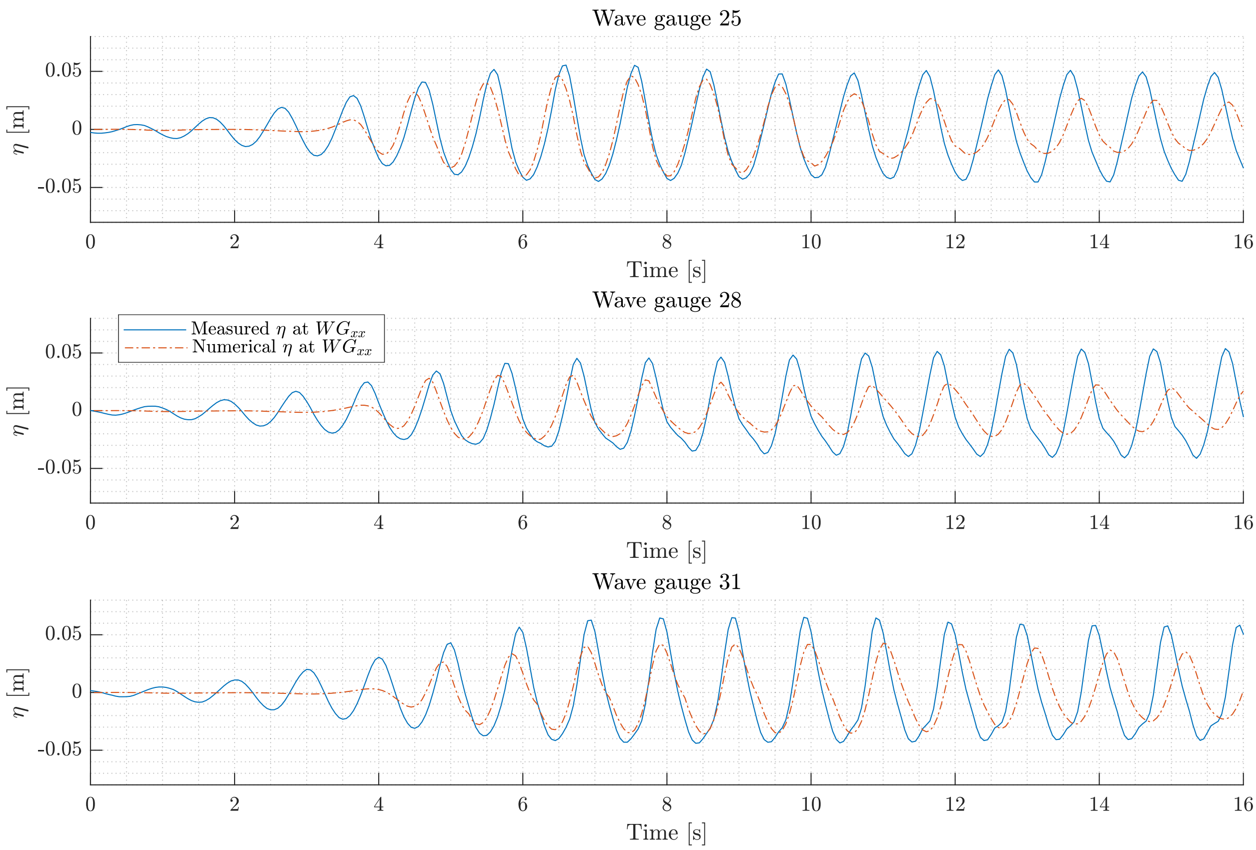

Figure 5.12: Free surface elevation at different wave gauges locations, see Figure B.2, for A4 chamber configuration, see Figure B.3, and wave test number 20

The next part of the analysis is focused on the wave gauges that are located inside the chamber. The centre line array, Figure 5.11, shows a similar behaviour of the free surface elevation for the first 5 fully developed waves. After this moment larger differences are observed with a clear difference between the phases. Moreover, it can be seen that the numerical model is not well capturing the non-linear behaviour inside the chamber. For the other three wave gauges, Figure 5.12, the numerical model gives worst results. It can clearly be seen that at wave gauge 28 and 31 experimental data shows a wave amplification that causes a non-linear behaviour. However, the numerical model can not capture this. This can be caused by large gradients at some regions, specially at wave gauge 28, so a sensitivity analysis is conducted to check this behaviour, but no significant differences are found, see Appendix D.3.2.

It can be concluded that lowering the mesh resolution is causing that the numerical model is not capable of properly capture the non-linear behaviour shown on the experiments. However, for the first few developed a similar behaviour is obtained. Moreover, this large differences on the results are also affected by an even lower cell refinement on the orthogonal direction, which causes larger uncertainties. Therefore, a weak solution is found that makes the numerical model to underestimates the wave-structure interaction in some regions up to 50% and mean value of around 20% of the wave amplitude with respect to measured waves from empirical data. Similar conclusions are obtained for wave with $s = 3.80\%$, which can be found in Appendix D.3.

5.3.2 Validation of A5 chamber configuration

The analysis of A5 chamber configuration is conducted in the same way the validation of A4 chamber presented in Section 5.3.1.

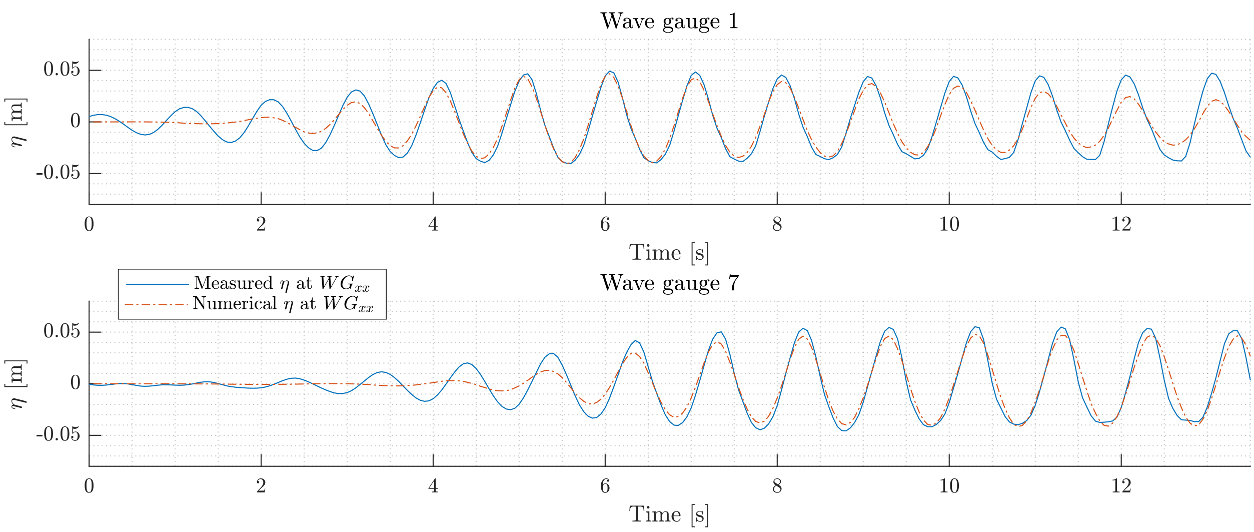

Figure 5.13: Free surface elevation at different wave gauges locations, see Figure B.2, for A5 chamber configuration, see Figure B.4, and wave test number 20

From Figure 5.13 it can be seen that numerical waves have a similar behaviour as experimental waves. At wave gauge 1 it can be seen that only after 5−6 fully developed waves the numerical model shows a different behaviour, which can be caused by a low mesh refinement and it consequently bad prediction of waves. Also, at wave gauge 7 numerical waves behaves similarly to experimental waves. However, the model is not totally able to capture all non-linearities, which is more clear to see after 6 fully developed waves. Then, it can be concluded that at this location, where waves less affected by the structure, the model is able to give good results.

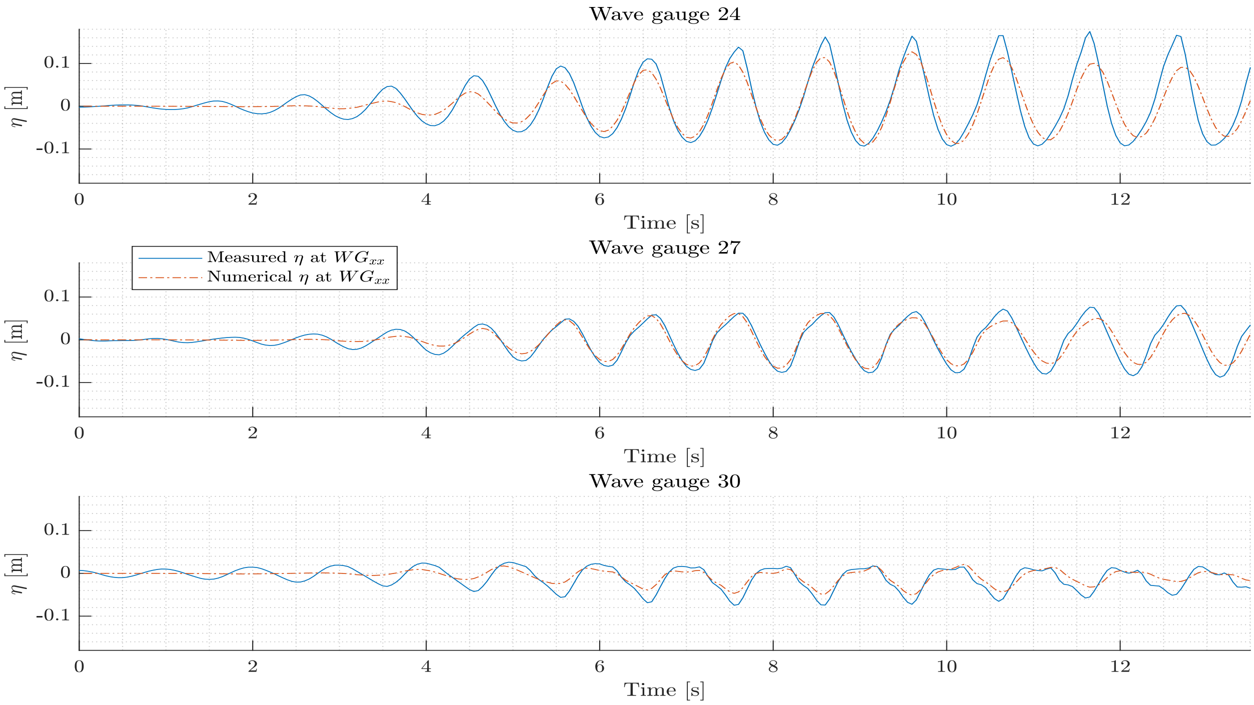

Figure 5.14: Free surface elevation at different wave gauges locations, see Figure B.2, for A5 chamber configuration, see Figure B.4, and wave test number 20

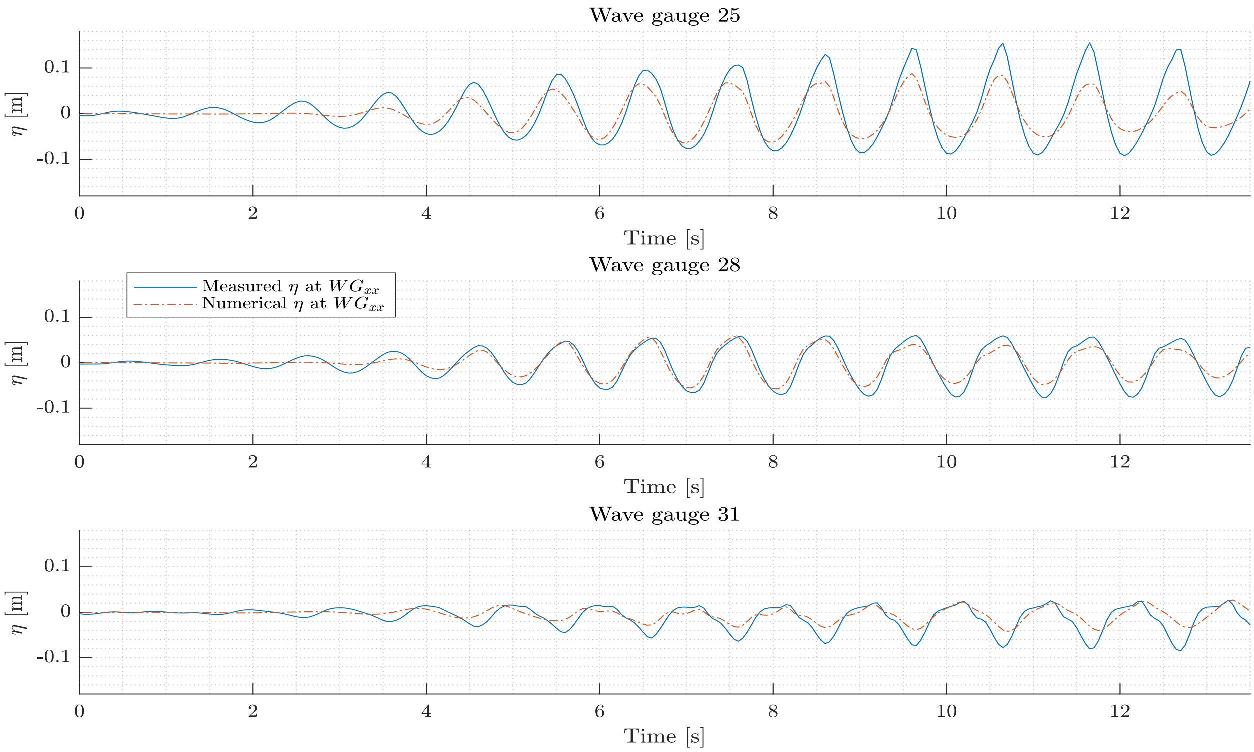

Figure 5.15: Free surface elevation at different wave gauges locations, see Figure B.2, for A5 chamber configuration, see Figure B.4, and wave test number 20

From Figures 5.14 and 5.15 considerable non-linear effects are apparent in experimental waves. Due to a weak mesh resolution, large differences between both data would be expected. However, as it can be seen in figures above the numerical model is, in general, well predicting those non-linear effects, being specially noticeable in the first 6 fully developed waves, after this point also reflected waves are affecting the results. Nonetheless, at wave gauges 24 and 25 experimental waves shows a very steep wave that the numerical model is not totally able to capture, with an under estimation of the peaks and a considerable large phase delay after 11 seconds. At wave gauges 27 and 28 the numerical model is able to capture most of the non-linear effects, however, after also 11 seconds a deviation in the behaviour starts to have a major influence. Last, at wave gauges 30 and 31 it can be seen a similar behaviour, however, troughs are under estimated, probably due to the strong wave-structure interaction at this location.

It can be concluded that the validation of A5 chamber configuration gives good results, not only on wave gauges far from the structure, but also inside the chamber, whit a good estimation of the non-linear effects.

5.4 Validation analysis' conclusion

This section aims to summarize all conclusions obtained in this chapter for the validation of the model.

First, only Stokes 5^{th} order generation method gives reliable results. It is found that parasitic waves are affecting the simulations with first-order irregular wave generation method. Second, waves are not fully absorbed by the outlet relaxation zone, the the model is affected by some reflected waves. Third, the validation analysis conducted for only propagation of waves gives reliable results for the first 6 fully developed waves. Fourth, the 3D model, despite a low grid resolution is employed, gives reliable results at wave gauges 1 to 7 for the first 6 fully developed waves, after this moment reflected waves are also affecting the results. Fifth, reflected and diffracted waves traveling in a different direction than incoming waves are not well captured by the model due to a low grid refinement in the orthogonal direction of the model. Sixth, the numerical model is not able to capture all non linear effects inside the chamber, however it shows a similar behaviour. Seventh, A5 chamber configuration shows that the numerical model is capable of capture most of the non linearities acting inside the chamber. Last, differences between experimental and numerical data are measured to be around 20% of the wave amplitude, with a maximum of 50% difference between both data.

Part III

Analysis of the Simulations

Analysis of the Simulations 6

In this section the analysis of the simulations is described. This is done by evaluating different parameters, such as free surface elevation, vortical structures, wave amplification factor, etc. Moreover, a linear method is included for the comparison of the wave amplification factor. Then, the goal of this section is to clarify different aspect of the wave-chamber interaction.

6.1 Introduction

In this section the analysis of the 3D simulations for 3 different chamber configurations (see Appendix B), A4, A5 and wider A5 configuration, is conducted. Configurations A4 and A5 are analyzed for a total of 13 different sea states, and the A5 configuration with a wider spoiler is analyzed for one sea state. Moreover, a full scale model with A4 configuration is also evaluated. All simulations that are analyzed in this section are presented in Table 6.1, and the characteristics of the waves can be found in Table E.1. Therefore, in this analysis 26 different simulations are carried out. Furthermore, the choice of the periods is based on previous work such as Heras et al. [2019], where the interaction between WEC, the chamber and waves shows two resonances peaks located at $T = 1$ and $T = 2$ seconds with and inflection point around $T = 1.5$ and a drop between $T = 2$ and $T = 2.5$ seconds, see Figure 6.21.

Chamber configuration	Wave period	Wave height					
		0.06	0.10	0.20	0.32	0.44	1.80
A4	1.0	**X**	**X**				
	1.5	**X**	**X**	**X**			
	1.7	**X**	**X**				
	2.0	**X**	**X**		**X**		
	2.5	**X**	**X**			**X**	
Full Scale A4	13.7						**X**
A5	1.0	**X**	**X**				
	1.5	**X**	**X**	**X**			
	2.0	**X**	**X**		**X**		
	2.5	**X**	**X**			**X**	
A5[1] wider	1.5		**X**				

Table 6.1: All numerical models' setup simulated in CFD with its different wave characteristic applied. **X** = test run - Wave periods are indicated in seconds and wave height in meters - [1]: the spoiler is widened 1.5 times the original A5 configuration, see Appendix B Figure B.6

The Le Mehaute diagram, see Figure E.1, is also used to validate the wave theory for each sea state presented in Table 6.1. This shows that all cases except one are covered by Stokes 3^{rd} order, only wave test 13 from Table E.1 is only covered by the Stream Function theory. However, all simulations are setup with Stokes 5^{th} order for the generation of waves. Despite the errors found in the validation of the 3D model, the same refinement level is applied in this section, those parameter are presented in Table 5.2. Moreover, all simulations are refined at the boundary layer of the body to have a maximum $y+ \leq 300$, some examples can be found in Appendix D.3 and D.4.

The analysis of the simulations are divided in different stages. Firstly, the evaluation is focused on the general flow characteristics. Secondly, the wave amplification factor at specific points is analyzed, which is obtained from 5 fully developed waves. Thirdly, the wave amplification factor is now analyzed in a region that includes the chamber and its surroundings, which is conducted with 2 different chamber configurations. In another analysis, the wave amplification factor in the area that would be covered by the absorber is computed, which is also compared to linear models. Lastly, a full scale model is analyzed to measure the influences of non-linear effects in the scaling procedure.

6.2 General flow characteristics

6.2.1 Introduction

In this section the free surface elevation, and vortical structures are investigated with 2 different chamber configurations. Vortexes around the chamber are illustrated with the so-called Q criteria, which represents the second invariant of the velocity gradient tensor, see Appendix A.5 for a detailed explanation of the invariants of the velocity-gradient.

6.2.2 A4 configuration for H=0.1 meters and T=1 seconds

Figures 6.1, 6.2, 6.3 and 6.4 shows the free surface elevation and vortical structures with A4 chamber configuration, more illustrations can be found in Appendix E.3.1 and E.4.1.

This configuration shows that diffracted and reflected waves are affecting the behaviour of the waves, as well as shoaling is acting at the sloped wall of the spoiler. Moreover, vortical structures are formed at some locations of the structure. The most clear is located at the end of the spoiler, which is strongly influenced by the motion of waves. Also, some other vortical structures are located at the front of the side walls, at the beginning of the spoiler and at the side walls, where wall angle changes.

From Figures 6.1 to 6.4 a vortical structure located behind the end corner of the top of the spoiler is apparent. This effect is caused by the turbulence generated in that region, which is governed by the velocity field from the wave-chamber interaction. Then, this vortex is transported upwards, as the vertical velocity is increasing, then when the peak of the wave reaches the end of the spoiler the vortical structure is pushed downstream, and a second vortex is arising from behind the sloped wall (see Figure 6.1). Then, from Figures 6.1 and 6.2, it can be seen how those two vortex are pushed upstream and downwards, due to the direction of the velocity field, so the two vortical structures are diffused and a new one is generated at the corner of the spoiler. This process is cyclically repeated for every period.

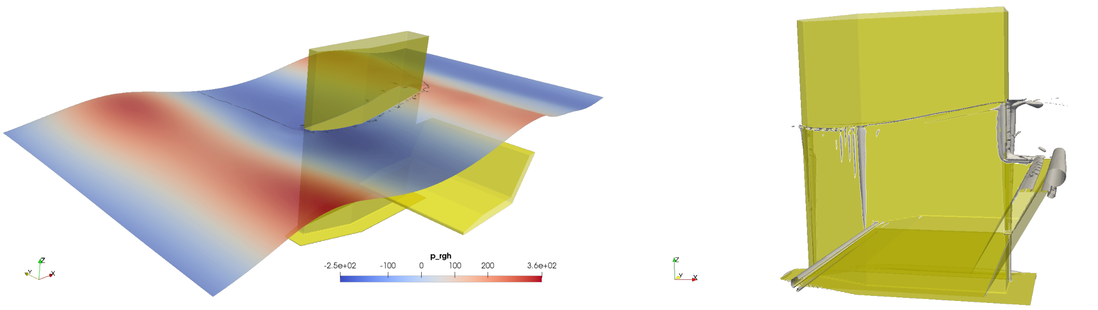

(a) (b)

Figure 6.1: Free surface elevation and Q-factor with $Q = 15$ iso surface for t/T = 0.1 - a) Free surface elevation, b) Q-factor

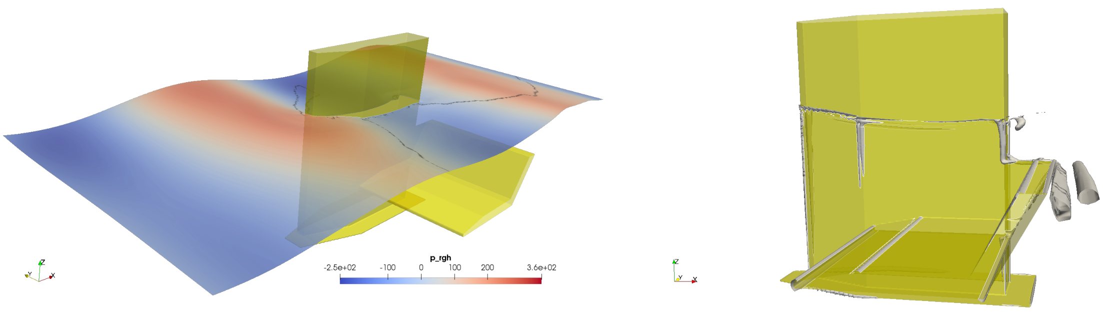

(a) (b)

Figure 6.2: Free surface elevation and Q-factor with $Q = 15$ iso surface for t/T = 0.4 - a) Free surface elevation, b) Q-factor

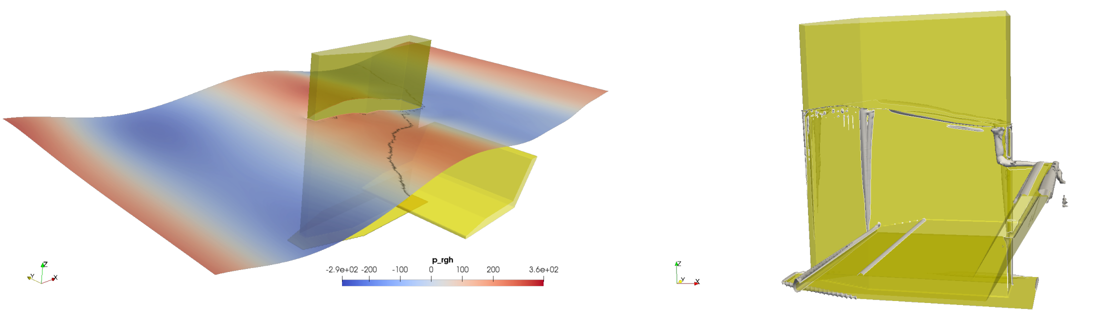

(a) (b)

Figure 6.3: Free surface elevation and Q-factor with $Q = 15$ iso surface for t/T = 0.7 - a) Free surface elevation, b) Q-factor

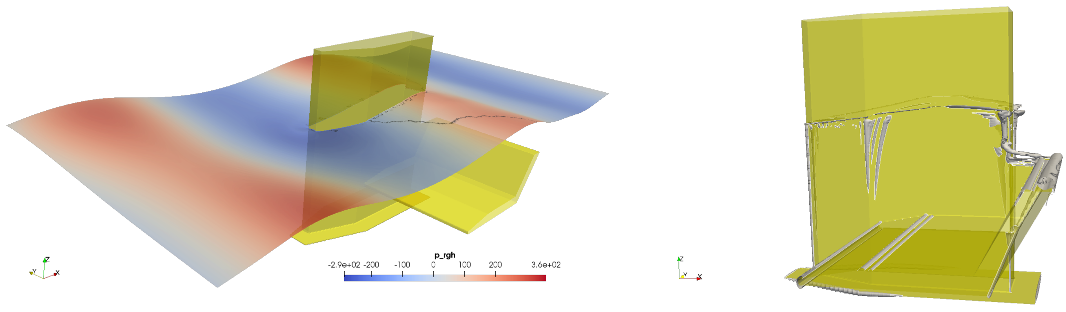

(a) (b)

Figure 6.4: Free surface elevation and Q-factor with $Q = 15$ iso surface for t/T = 1.0 - a) Free surface elevation, b) Q-factor

Therefore, two main conclusions are obtained. Firstly, waves inside and upstream the structure are affected by both diffracted and reflected waves from the wall and the spoiler. Secondly, from this vortical structures it can clearly be seen how the flow and velocity field are distorted by the structure, where vortical structures are mainly generated at the end of the spoiler.

6.2.3 A5 configuration for H=0.1 and T=1

Figures 6.5b, 6.6b, 6.7b and 6.8b illustrates the free surface elevation and vortical structures generated by the A5 chamber configuration.

First, from the free surface elevation it can clearly be seen that A5 configuration has a high influence on the reflection of waves. This effect is the most significant flow feature, not only inside the chamber, but upstream of it. Moreover, a high run-up is found, however, overtopping is not observed in any of the simulations. In addition to this, a combination of both diffraction and reflected waves from the walls gives a tilted waver surface inside the chamber, with the highest peak at the center of the structure. See Appendix E.3.2 for more illustrations this behaviour.

Second, vortical structures are expected to occur at the front of the side walls and in front of the bottom plate, but not on the top of the spoiler as waves are not passing over it. Vortical structures at the bottom plate are highly influenced by reflected waves from the spoiler. It is evident that one vortex is moving from underneath the bottom plate, when a trough is at this location, to above the plate when a crest of the wave goes through it. See Appendix E.4.2 for more illustrations of vortical structures. Also, at the angled spoiler tiny vortical structures are perceptible. This is a numerical artifact caused by a low refinement level, which combined with a large aspect ratio, generates a rough surface at the sloped wall.

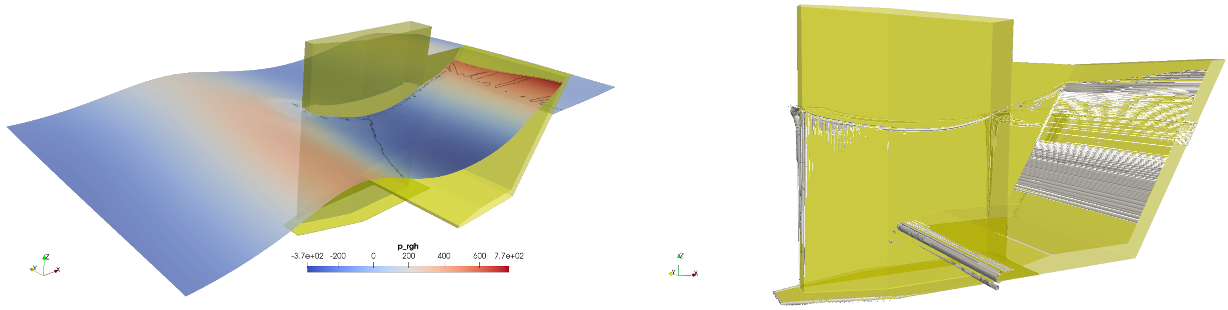

(a) (b)

Figure 6.5: Free surface elevation and Q-factor with Q = 15 iso surface for t/T = 0.2 - a) Free surface elevation, b) Q-factor

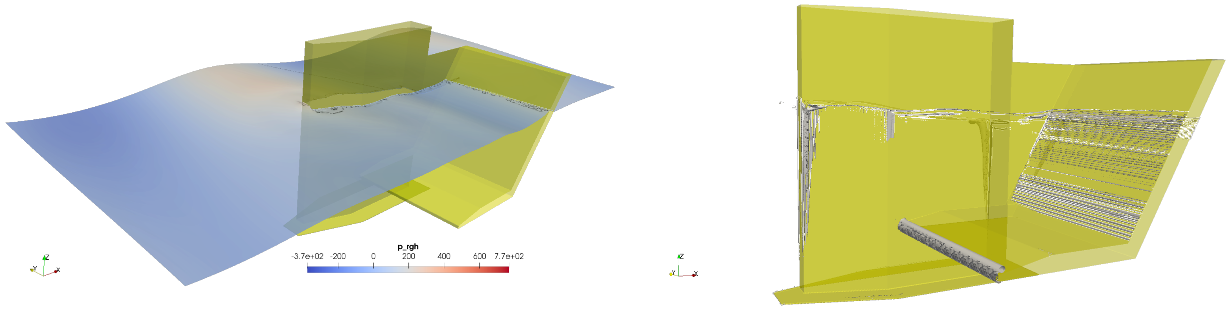

(a) (b)

Figure 6.6: Free surface elevation and Q-factor with Q = 15 iso surface for t/T = 0.4 - a) Free surface elevation, b) Q-factor

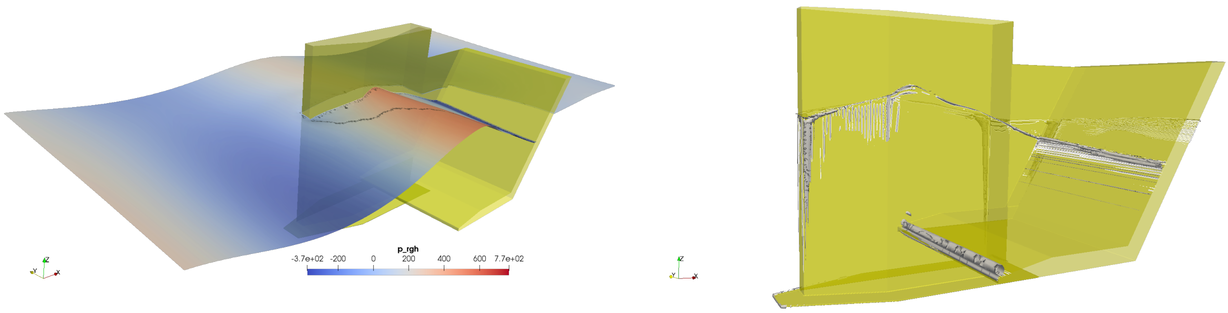

(a) (b)

Figure 6.7: Free surface elevation and Q-factor with Q = 15 iso surface for t/T = 0.6 - a) Free surface elevation, b) Q-factor

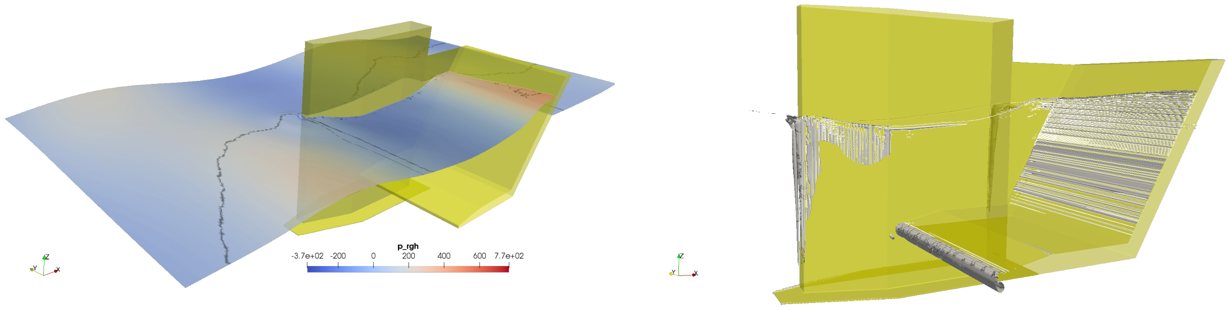

(a) (b)

Figure 6.8: Free surface elevation and Q-factor with $Q = 15$ iso surface for t/T = 1.0 - a) Free surface elevation, b) Q-factor

As a conclusion, this configuration highly interact with waves. The most noticeable flow feature is reflection coming from the spoiler, however, diffracted waves and reflected waves from the side wall are also influencing the wave kinematics at the area under investigation. This generates an uneven free surface elevation in the orthogonal direction of the incoming waves. Furthermore, vortical structures are expected to occur in front of the spoiler, which are highly influenced by wave-structure interaction.

6.3 Wave amplification factor comparison

To understand the impact of each individual part of the structure in this parameter, the analysis of the wave amplification factor is focused on measuring the influence of the wave height and wave periods at different locations inside the chamber. Then, the wave amplification factor from numerical models and experiments are compared in Figure 6.9.

First, A4 chamber configuration presents a similar trend on the result as the empirical data. However, in general wave amplification factors are slightly higher in the numerical model. This overestimation in the results is found to be higher at the center line array for a period of 2 seconds than in any other combination. Moreover, this difference between numerical and experimental data is larger for lower wave heights, as it is perceptible for wave height of 0.06 meters and a period of 2 seconds compared to the same period and $H = 0.1$ meters. The overestimation in this case can be quantified to be up to 70% at wave gauge 24. Nonetheless, in general there is a reasonable agreement as most values are within 10% difference. Moreover, it appears that for the highest wave the same conclusions are applicable.

Second, A5 chamber configuration gives similar results between numerical and experimental waves, except for waves with a period of 1 second, where the difference on all wave gauges are large - up to 50% difference. Moreover, large differences are observed at wave gauges close to the sloped wall. From Figure 6.9 it is evident that the A5 configuration have a maximum value in the order of 3.

Comparing different wave heights it is visible that this parameter does not have a large influence in the amplification of waves. The highest influence in the wave amplification factor is the combination of wave period and chamber configuration. A4 configuration shows a peak at $T = 1.7$ seconds. A5 chamber gives a maximum value of 4 at $T = 2.5$, which is the maximum period investigated. Also, the location inside the chamber strongly influence the amplification of waves, which is analyzed in the following sections.

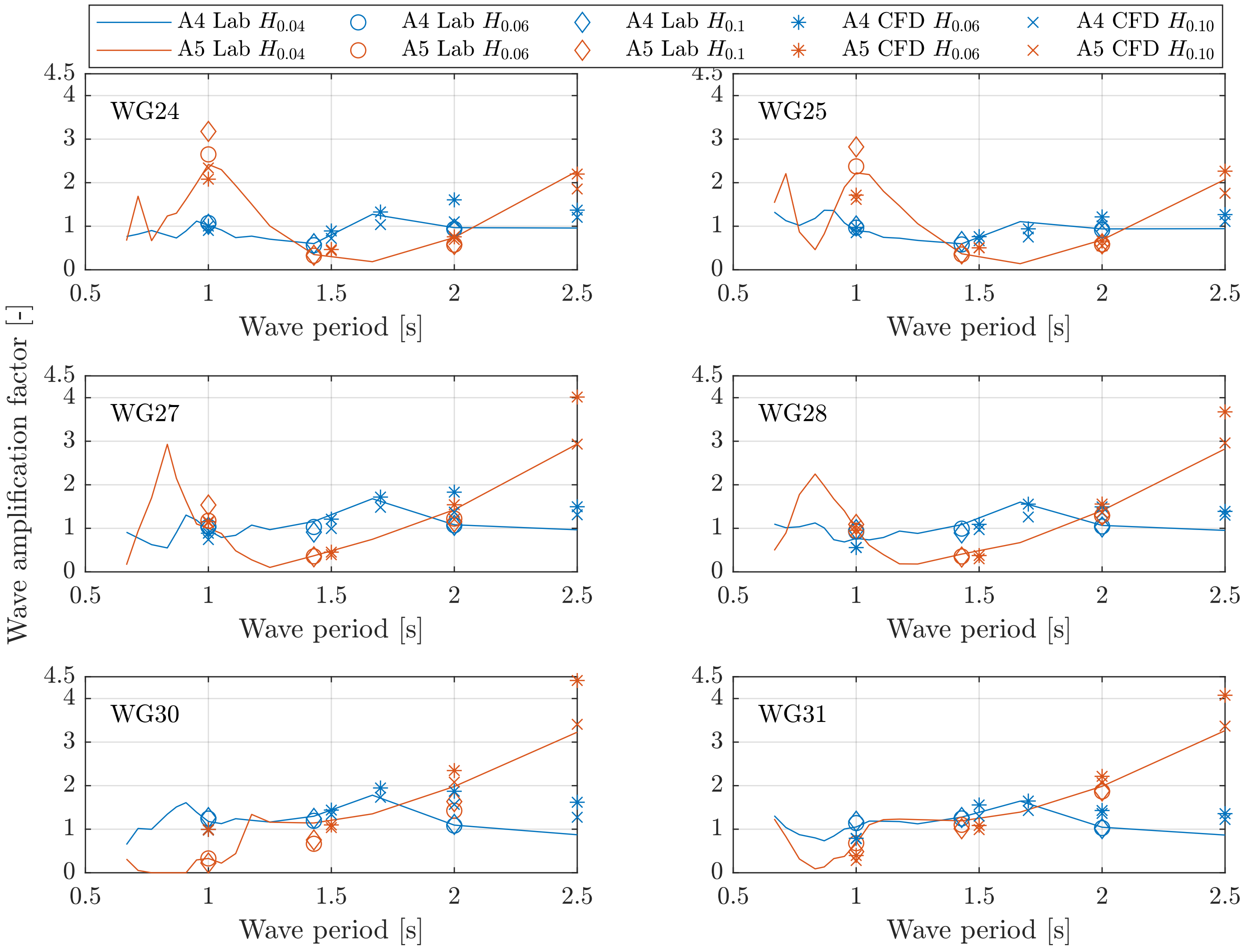

Figure 6.9: Comparison between experimental and numerical wave amplification factors over the periods

6.4 Wave amplification factor with A4 configuration

The wave amplification factor in an specific area around the chamber is calculated and analyzed, see Figures 6.10, 6.11, 6.12, 6.13 and 6.14. This analysis is conducted based on two different wave theories, linear theory, calculated with a software called WAMIT (figure on the bottom), see WAMIT [2020], and non-linear theory by CFD method (figures on the top). Moreover, the non-linear model is calculated for two different wave heights ($H = 0.10$ and $H = 0.06$ meters) and 5 different wave periods, see Table E.1 A4 chamber configuration.

Therefore, in Figures 6.10 to 6.14 it can be clearly seen that the wave amplification factor is dependent on both x and y direction, where waves are higher amplified close to the plane of symmetry than close to the walls. This can be explained by the fact that the reflection and the diffraction from the side walls have a high influence on the results. It can be perceived a section of the walls with and angle pointing inside the chamber. This angle of the wall is designed in such a way that incoming waves are reflected directly pointing into the centre of the chamber. Moreover, in Section 6.2 shoaling effects are apparent at the sloped wall. Therefore, the combination of reflected, diffracted waves and shoaling are provoking that the wave amplification factor is dependant on both directions.

This behaviour in the amplification of waves is presence in all five sea states illustrated in Figures 6.10 to 6.14. However, when comparing both non-linear models it is visible that the region with the highest amplification factor is narrowed for the highest wave height, however, the influence of the wave steepness is not significant. This is very clear for $T = 1.7$ seconds, Figure 6.12, where also the highest wave amplification factor is obtained for this A4 chamber configuration. However, as WAMIT is based on linear theory, this phenomena can not be capture. But, a similar behaviour is obtained, where the highest peak is also found around the centre line. Which means that linear theory is also able to capture diffracted and reflected waves. Also, $T = 1.7$ and $T = 2.0$ linear and non-linear models gives similar results, however, for $T = 2.5$, despite it is a linear wave, large differences are found.

It can be seen that the wave amplification is small for $T \leq 1.5$, Figures 6.10 and 6.11, where a depression in the amplification of waves is found upstream. This effect is very clear for $T = 1.5$, where large diffracted waves are apparent, which might indicate that the wave period is close to the natural resonance period of the chamber. Also, for this two periods it can be seen that shoaling is influencing the results, however, this phenomena has less importance than diffracted waves and reflection from the side walls. For $T = 1$ second, linear model present a similar behaviour, but this model over predict the wave amplification. It is clear that for steep waves, WAMIT is capturing higher shoaling effects acting in the angle wall. Also, this model predicts higher influences from reflected waves from the spoiler upstream the chamber. For $T \geq 1.7$ seconds, a higher wave amplification is apparent inside the chamber. This indicates that shoaling effects have a large influence, especially for $T = 1.7$ and $T = 2.0$ seconds, where the highest peaks are found close to the sloped wall. Then, for $T \geq 1.7$ seconds a higher influence from the sloped wall is expected to occur. Similarly to $T \leq 1.5$ the amplification factor is also influenced upstream the structure, caused by diffracted and reflected waves. Linear theory gives a similar behaviour with similar amplification factors for $T = 1.7$ and $T = 2.0$ seconds, however, larger deviations are found for $T = 2.5$ seconds between both models. Interesting to note is that for the A4 case there is wave amplification taking place also downstream of the chamber for all but the shortest waves.

Another interesting area to consider is the zone around the chamber, as wave-structure interaction is not only happening inside the chamber, but around it. This region is of importance as the platform in its original configuration is built up by two of this simplified structures located side by side, see Figure 1.2. It can be seen that both linear and non-linear models present a similar behaviour in that area, which strongly support that the amplification factor would be different when two structures would be located side by side.

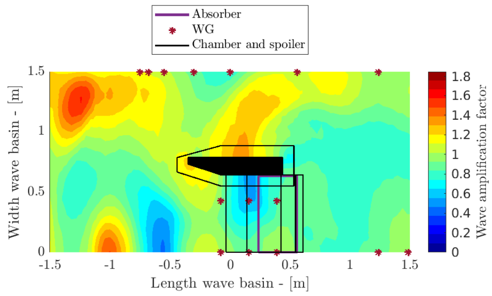

(a) CFD $H = 0.06[m]$

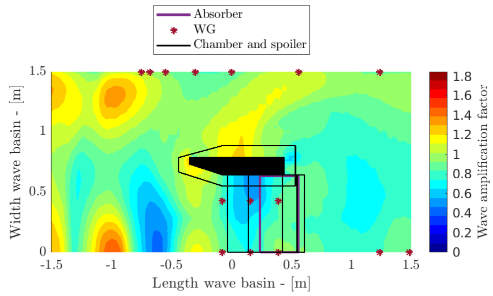

(b) CFD $H = 0.10[m]$

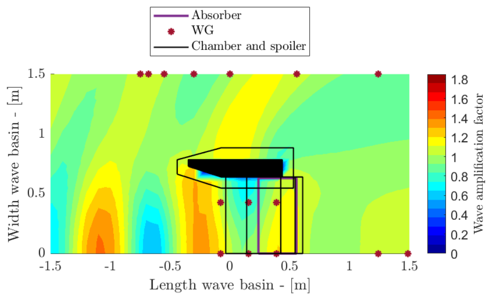

(c) WAMIT

Figure 6.10: Wave amplification factor with A4 chamber configuration from CFD and WAMIT - a) $H = 0.06[m]$ and $T = 1.0[s]$ from CFD, b) $H = 0.10[m]$ and $T = 1.0[s]$ from CFD, c) $T = 0.99$ from WAMIT

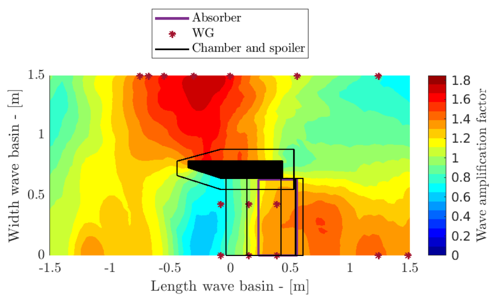

(a) CFD $H = 0.06[m]$

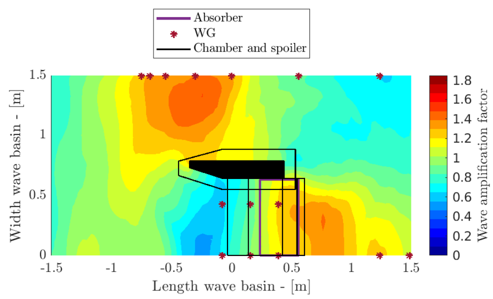

(b) CFD $H = 0.10[m]$

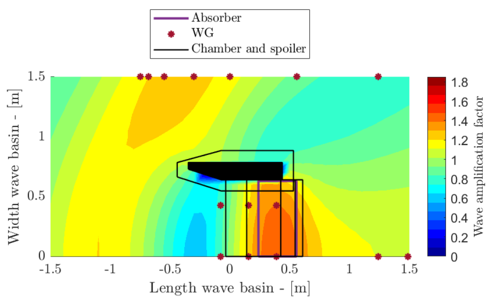

(c) WAMIT

Figure 6.11: Wave amplification factor with A4 chamber configuration from CFD and WAMIT - a) $H = 0.06[m]$ and $T = 1.5[s]$ from CFD, b) $H = 0.10[m]$ and $T = 1.5[s]$ from CFD, c) $T = 1.49$ from WAMIT

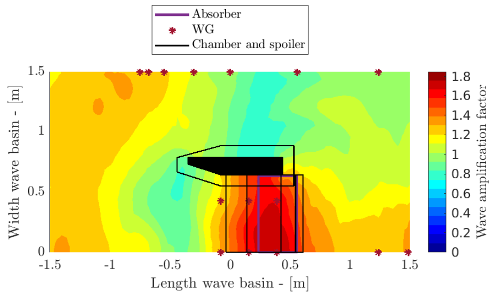

(a) CFD $H = 0.06[m]$

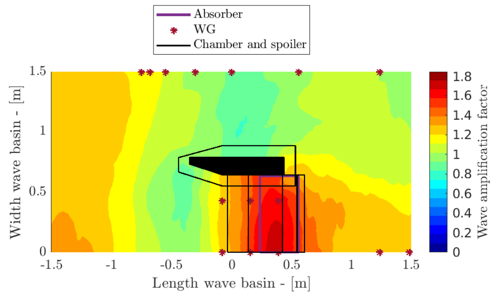

(b) CFD $H = 0.10[m]$

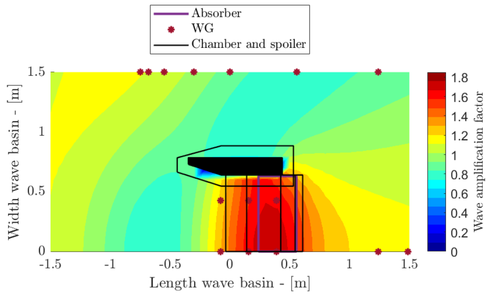

(c) WAMIT

Figure 6.12: Wave amplification factor with A4 chamber configuration from CFD and WAMIT - a) $H = 0.06[m]$ and $T = 1.7[s]$ from CFD, b) $H = 0.10[m]$ and $T = 1.7[s]$ from CFD, c) $T = 1.69$ from WAMIT

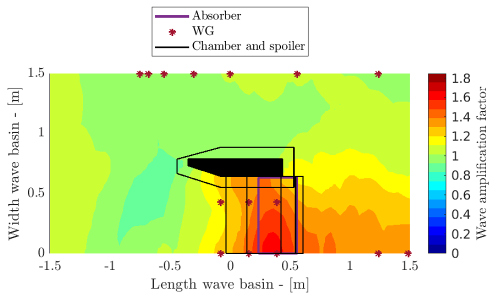

(a) CFD $H = 0.06[m]$

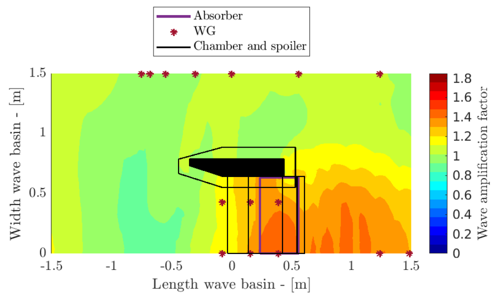

(b) CFD $H = 0.10[m]$

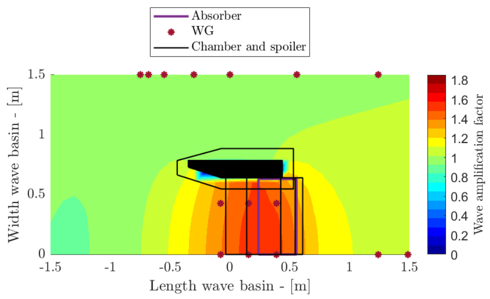

(c) WAMIT

Figure 6.13: Wave amplification factor with A4 chamber configuration from CFD and WAMIT - a) $H = 0.06[m]$ and $T = 2.0[s]$ from CFD, b) $H = 0.10[m]$ and $T = 2.0[s]$ from CFD, c) $T = 2.03$ from WAMIT

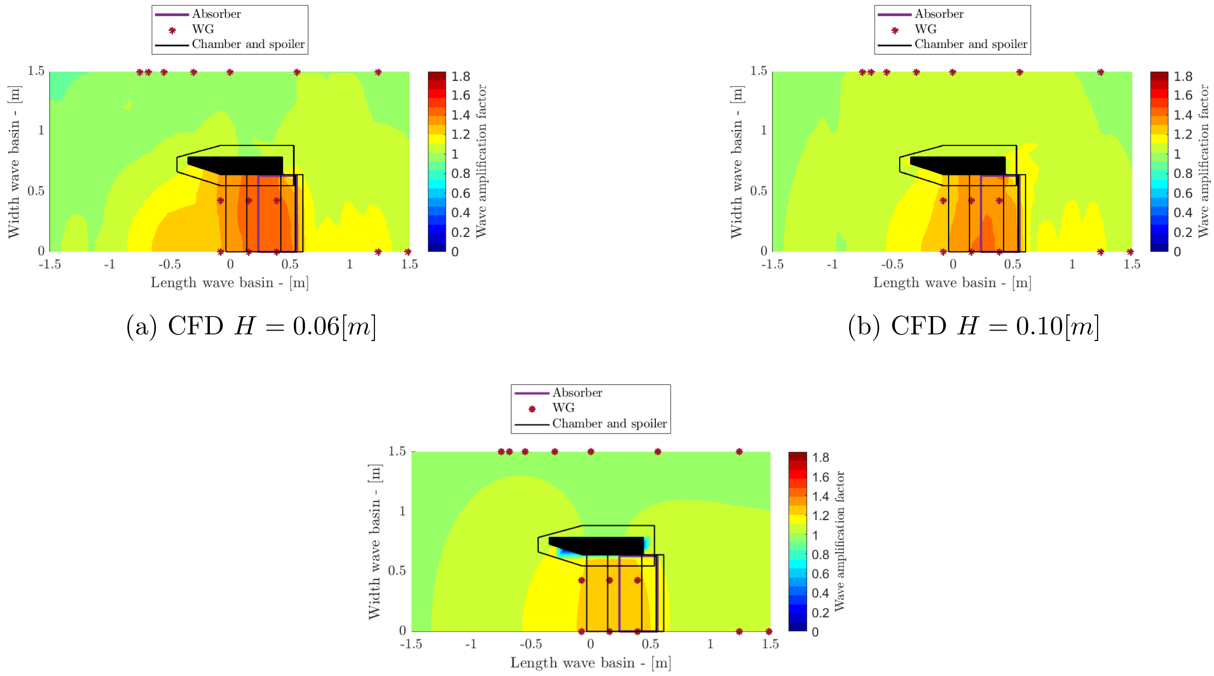

(a) CFD $H = 0.06[m]$

(b) CFD $H = 0.10[m]$

(c) WAMIT

Figure 6.14: Wave amplification factor with A4 chamber configuration from CFD and WAMIT - a) $H = 0.06[m]$ and $T = 2.5[s]$ from CFD, b) $H = 0.10[m]$ and $T = 2.5[s]$ from CFD, c) $T = 2.51$ from WAMIT

As a measure of the effect of different elements of the chamber, Figure 3.6 shows the amplification factor for different chamber configurations. It can be clearly seen that side walls influence the wave amplification at low periods, this indicates that diffracted and reflected waves are of major interest for $T \leq 1.25$, which it obvious to see at wave gauge 27 and 30. A3 configuration shows that the bottom spoiler increases the wave amplification for a large range of periods, this is caused, not only by reflected and diffracted waves, but also by shoaling effects. The introduction of an angle wall (A4) largely increases the amplification of waves inside the chamber for $T \geq 1.25$ due to shoaling.

To conclude, first, A4 chamber amplifies the waves, not only inside, but in the region around the chamber. Moreover, for certain periods, between 1.5 to 2.0 wave are in resonance with the structure, causing a raise in the amplification factor, with a peak at $T = 1.7$ seconds. Second, both linear and non-linear methods gives a similar behaviour, however, as high order effects are affecting the hydrodynamics inside the chamber linear models can not capture them, then it can only be used for a first estimation. Third, some regions inside the chamber are affected by the side walls, by the effects of diffraction and reflection. This means that the wave amplification factor inside the chamber also depends on x and y direction. Fourth, the camber also alter the behaviour of waves in the surrounded areas, which might be of interest as the full scale model has two chambers side by side. Fifth, each part of the chamber (side walls, bottom spoiler, sloped wall of the spoiler...) interacts differently for every sea state. The understanding of these elements separately is crucial for a better optimization of the whole structure. Last, A4 configuration amplifies waves, being the sloped wall the element that have a major impact on it.

6.5 Wave amplification factor with A5 configuration

Wave amplification factors for A5 configuration are illustrated in Figures 6.15 to 6.18. This new configuration shows a totally different behaviour in the amplification of waves. In this case the major influence on this parameter is coming from reflected waves from the spoiler.

For $T \leq 1.5$ seconds small amplification factors inside the chamber are observed, only close to the sloped wall a higher value is found. Also, for $T = 1.0$ seconds it can be observed a peak of the amplification factor at the beginning of the bottom spoiler. This is an indicator of the strong influence of reflected waves for this configuration. For $T > 1.5$ seconds very large amplification factors are found inside the chamber. This means that the peak of resonance is shifted to higher periods. Also, despite a large run up is expected to occur for $T > 1.5$ seconds no overtopping is observed, however, for larger periods overtopping is likely to occur. The run up is highly dependant on the wave length, as described in Stefanakis et al. [2015], in this case one peak is observed at $T = 1.0$ second and then a second peak is expected to occur for $T > 2.5$. This indicates that the run up is dependent on the length of the wave. For any period investigated a large wave amplification factors are observed upstream, which also indicates that reflected waves are of great importance. Despite the highest influence in the amplification of waves is coming from shoaling and reflection from the spoiler, diffracted and reflected waves from the wall are also affecting the results, as the wave amplification factor inside the chamber varies along both x and y axis. Also, it is interesting to analyze the area next to the chamber. This region is also highly affected by the structure. In general the amplification of waves next to the structure is reduced, however for $T = 1.5$ seconds an increase of this parameter is found.

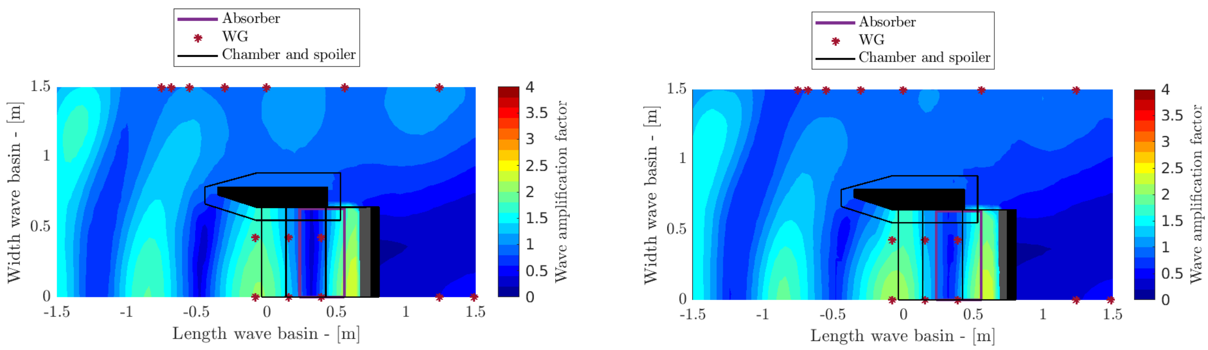

(a) CFD $H = 0.06[m]$

(b) CFD $H = 0.10[m]$

Figure 6.15: Wave amplification factor with A5 chamber configuration from CFD - a) $H = 0.06[m]$ and $T = 1.0[s]$ from CFD, b) $H = 0.10[m]$ and $T = 1.0[s]$ from CFD

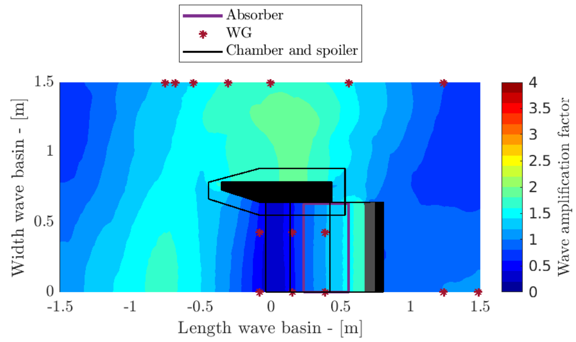

(a) CFD $H = 0.06[m]$

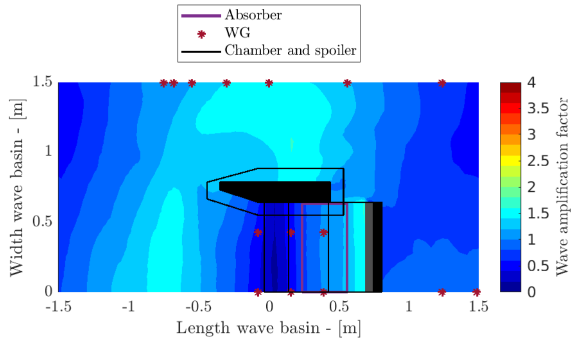

(b) CFD $H = 0.10[m]$

Figure 6.16: Wave amplification factor with A5 chamber configuration from CFD - a) $H = 0.06[m]$ and $T = 1.5[s]$ from CFD, b) $H = 0.10[m]$ and $T = 1.5[s]$ from CFD

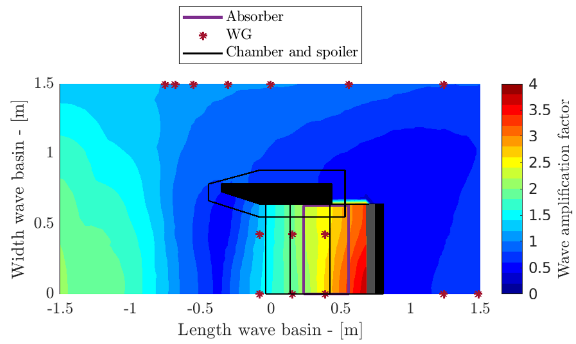

(a) CFD $H = 0.06[m]$

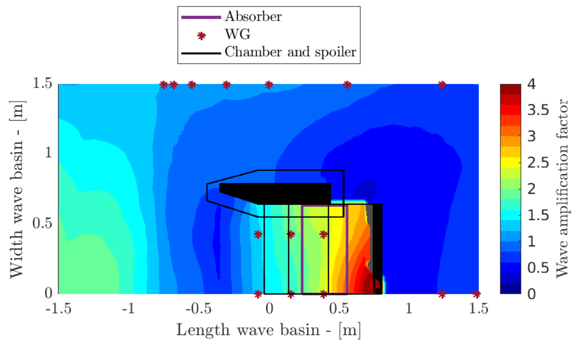

(b) CFD $H = 0.10[m]$

Figure 6.17: Wave amplification factor with A5 chamber configuration from CFD - a) $H = 0.06[m]$ and $T = 2.0[s]$ from CFD, b) $H = 0.10[m]$ and $T = 2.0[s]$ from CFD

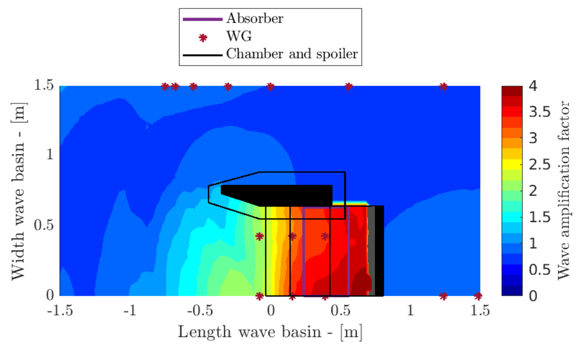

(a) CFD $H = 0.06[m]$

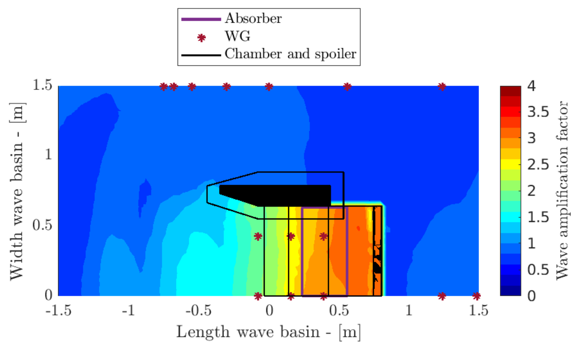

(b) CFD $H = 0.10[m]$

Figure 6.18: Wave amplification factor with A5 chamber configuration from CFD - a) $H = 0.06[m]$ and $T = 2.5[s]$ from CFD, b) $H = 0.10[m]$ and $T = 2.5[s]$ from CFD

Then, the wave amplification factor with A5 configuration is mainly affected by the interaction between waves and the spoiler. In Figure 3.6 it can be seen that increasing length of the sloped wall above the water highly influence the response of the wave amplification factor compared to A4 configuration. This new design minimize the effects from the side walls.

To sum up, first, wave amplification factors for $T > 1.5$ seconds are in the order of 3, however for $T \leq 1.5$ this value is found to be around 1. Second, reflected waves from the spoiler are the main influence on the amplification of waves. Third, diffracted waves are also influencing the amplification of waves, so this parameter is a function of x and y. Last, due to the fact that the major influence on the wave amplification factor is caused by reflected waves from the sloped wall, the introduction of the absorber might minimize this effect.

6.6 Wave amplification factor at the absorber location

In this section a value of the wave amplification factor is computed by extracting the mean at the area that would be covered by the absorber. In addition to the simulations previously analyzed a wider A5 chamber is also included in this comparison. This data is all illustrated in Figure 6.19. this aims to give a better understanding of the resonance peak associated with the chamber geometry found in previous projects, [Heras et al., 2019]. In addition, the wave amplification factor is analyzed as a function of the steepness, see Figure 6.22. This shows the limit of the waves that are able to properly interact with the chamber.

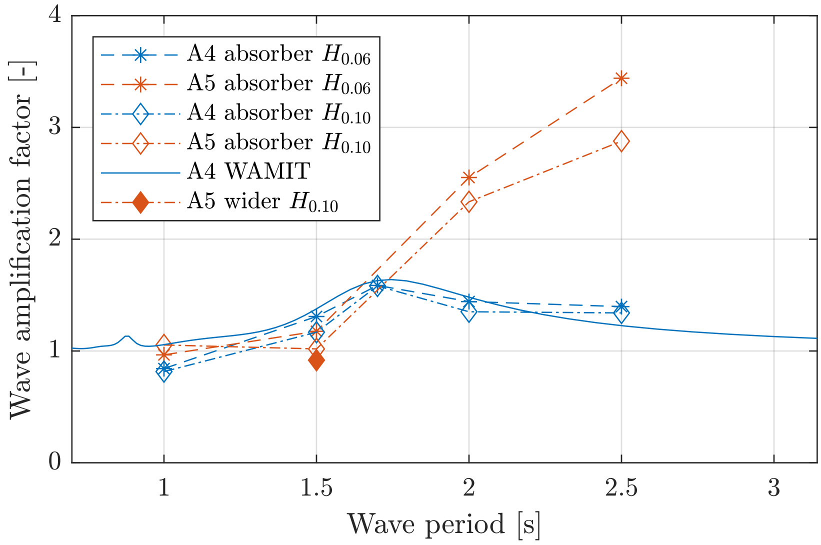

Figure 6.19: Comparison of the mean wave amplification factor over periods at the area where the absorber would be located - CFD and WAMIT results

Looking at Figure 6.19 it is noticeable that wave amplification factor behaves differently in both configurations. A4 configuration shows an amplification peak at $T = 1.7$ seconds. For the A5 configuration the amplification factor increases with increasing the wave period, with a maximum value at $T = 2.5$, which is the maximum investigated.

For the A4 configuration Figure 6.19 shows that both methods are capturing the peak at $T = 1.7$ seconds with similar values, around 1.6. At this point the influence of the steepness is found to be insignificant. For $T > 1.7$ seconds a drop in the amplification factor is observed, which is also capture in both models with similar values at $T = 2$ seconds, but larger differences at $T = 2.5$ seconds. CFD simulations gives a similar amplification factor for $T = 2$ and $T = 2.5$ seconds, around 1.2. However, linear theory shows how this parameter decreases with increasing the wave period. For $T < 1.7$ seconds also a reduction in the wave amplification is found. Both models give a similar values for $T = 1.5$ seconds, but for $T = 1$ seconds a larger difference between both models is found, around 18% to 22%. For the same wave length it is visible that the steepness of the wave do not have a major influence in the amplification of waves.

For A5 case only CFD simulations are conducted. For $T \leq 1.5$ seconds shows that the influence in the wave amplification factor is small, giving values around 1. But for $T > 1.5$ seconds the wave amplification factor increases with increasing wave period. For $T = 2.5$ seconds, which it is the maximum period simulated, a value between 2.9 to 3.4 is obtained. For A5 configuration it is evident that for longer wave the steepness is important. In this case the higher the steepness the lower the amplification factor. For $T = 2$ seconds a difference of $\leq 10\%$ is quantified and for $T = 2.5$ seconds the difference between different steepness is of 19%.

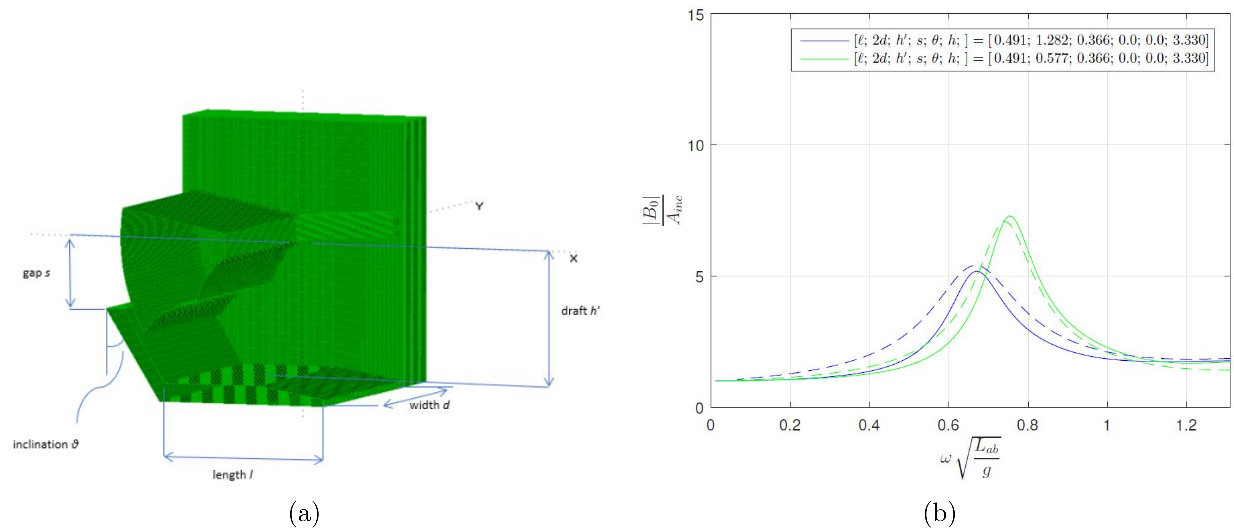

Figure 6.20: Variation of the wave amplitude inside the chamber with different parameters, solid line: numerical, dash line: semi-analytical Georgousis [2019] - a) Chamber shape b) Width variation

An extra simulation for $T = 1.5$ seconds is conducted to measure the influence of the width of the chamber. *A5 wider* $H_{0.10}$ is simulated to be 50% wider than the original A5 configuration (See Figure B.6). This new width reduces the amplification factor in 10%, for the only period simulated, which is not enough data for a conclusion. However, this decrease of the amplification of waves is in accordance with what Georgousis [2019] founds with A4 configuration, where and increment in the width flattens the curve and move it to higher periods, see Figure 6.20b.

To sum up, the spoiler geometry have an important influence on the response of wave chamber interaction. It is found that the wave amplification factor is highly increased by the interaction between the spoiler and waves at the surface level. Then, the A5 configuration increases the wave amplification factor in high wave periods, while lower periods are similarly behaving as A4 configuration.

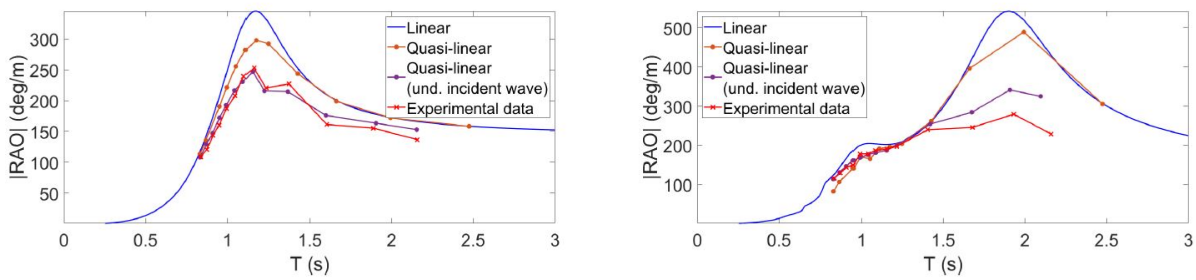

Figure 6.21: Response Amplitude Operator with WEC only (Left) and WEC and Chamber (Right), Heras et al. [2019]

Previous works were focused on the response amplitude operator (RAO) of the WEC, rather than wave-chamber interaction itself. It was found that introducing an structure with the WEC the RAO is highly amplified. This behaviour was found in Heras et al. [2019] which is illustrated in Figure 6.21. It was proposed that the second peak is related with the wave chamber interaction, however any further analysis with only the chamber has been deeply conducted. Thus, in this section a comparison between the RAO, see Figure 6.21 and the wave amplification factor, Figure 6.19, is analyzed.

First of all, it has to be mentioned that chamber geometries from Heras et al. [2019] and the current project are not the same, as both are based on different experiments. Nevertheless, the concept is the same and similarities between both model makes possible a comparison between them.

The smallest peak on the RAO ($T \geq 1.25$) in Figure 6.21 is believed to be caused by the chamber's geometry. This is in totally agreement with the data presented in Figure 6.19, as waves are in resonance with the chamber for a range of period similar to the one described by RAO. Moreover, the wave amplification factor response also describes a similar behaviour as the one found in Heras et al. [2019]. On both, after the peak the same behaviour on the drop is obtained. In this report the maximum peak for the wave amplitude factor if found at $T = 1.7$ while in Heras et al. [2019] this is found at $t = 1.9$. This small difference can be explained by two factors, the first one is the difference between both geometries. The second one is that the WEC is interacting with the chamber geometry with slightly change the response.

Therefore, it can be concluded that the second peak found in previous researches is directly related to the chamber configuration. Nevertheless, the influence of the WEC with A5 chamber configuration needs to be studied to confirm that this new spoiler has a significant advantage with the absorber installed. This is of major importance as the wave amplification factor in A5 configuration is mainly affected by the interaction of hydrodynamics at the surface with the chamber, reflected waves and run-up. Then, the absorber can minimize those effects due to the fact that it is located before the spoiler, so the interaction between the spoiler and wave can be affected.

In Figure 6.22 the amplification of waves as a function of wave steepness presented. In this figure also the sea states corresponding to $H = 0.20$, $H = 0.32$ and $H = 0.44$ in Table 6.1 are included. This analysis shows the limit of the waves that properly interact with the chamber. This illustration shows a clear dependency between amplification factors and wave steepness. Wave a steepness greater than 3% are not amplified by any configuration. For A4 case with steepness values between 0.8% to 2.5% the amplification factor give a similar value with oscillates around 1.3. For A5 case a similar behaviour is found, where the highest amplification factor corresponds to the lowest steep cases. However, for $s = 1.79\%$ and $s = 2.96\%$ the interaction with the chamber gives lower vales. Comparing both chamber configuration it is observed that the wave amplification factor gives similar results for the same steepness, expect for 4 simulations, which corresponds to $T = 2$ and $T = 2.5$ seconds, see Figure E.3.

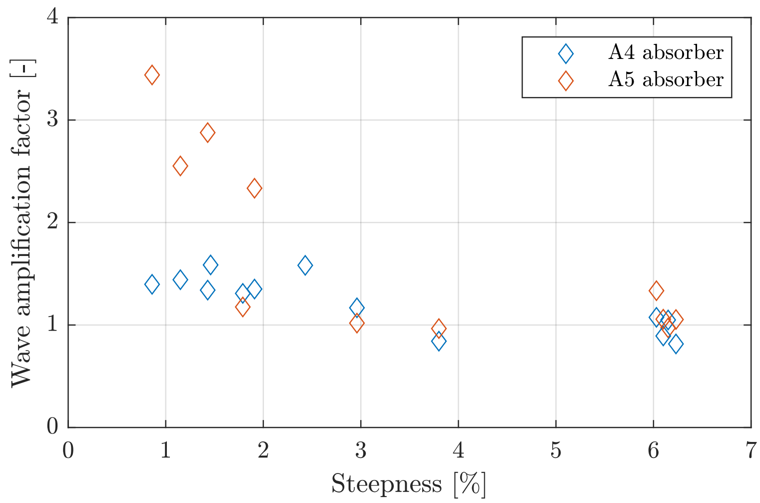

Figure 6.22: Comparison of the mean wave amplification factor over steepness at the area where the absorber would be located for different wave periods, see Figure E.3 for wave amplification factor over periods

6.7 Full scale model: A4 chamber configuration

In this section a comparison between experimental model and a full scale model is conducted.

6.7.1 Froude scaling

The Froude law is chosen as a scaling method of the chamber model for all configurations under investigation. A detailed explanation of the theory of the Froude law scaling method can be found in Appendix A.6. As a small introduction to the scaling factor used in this project the following table summarized the most important:

Parameter	Scaling factor	Value
Length	λ_L	30.00
Time	$\lambda_t = \sqrt{\lambda_L}$	5.48

Table 6.2: Scaling factor parameter based on Froude law, see Appendix A.6

According to Tables 6.2 and E.1 and also Appendix A.6 a full scale prototype can be calculated based on the model used in the experiments and the scaling factor of $\lambda_L = 30$. Therefore, a numerical model based on CFD simulations can be done. The main parameters that needs to be scaled up are presented in Table 6.3

Model	Wave height [m]	Period [s]	Wave number [-]	Water depth [m]	Length chamber[1] [m]	Width chamber[1] [m]	Height chamber[1] [m]	Ref. dim.[2] [m]
Laboratory	0.06	2.50	0.90	1.00	1.05	1.77	1.00	0.285
Full scale	1.8	13.69	0.03	30.00	31.50	53.10	30.00	8.550

Table 6.3: Scaled up parameters from experimental model to full scale model - [1]: Length, width and height measured the maximum distance in each dimension (as a box) - [2]: Ref. dim. is the reference dimension (D) applied in the calculation of the Reynolds number in Section 6.7.2

6.7.2 Reynolds number

The Reynolds number on both full scale model and laboratory scale model is presented. Reynolds number is calculated based on three parameters, see Equation 6.1:

$$Re = \frac{\text{inertial force}}{\text{viscous force}} = \frac{uD}{\nu} = constant \tag{6.1}$$

Where Re is the Reynolds number, u is the velocity of the fluid $[m/s]$, which is chosen to be the maximum horizontal velocity at the surface for non-disturbed waves from the object, D is a reference dimension $[m]$, in this case it is chosen to be the length of the horizontal part of the bottom spoiler and ν is the kinematic viscosity $[m^2/s]$. This last parameter is considered to be the same for both models, then the Reynolds number can be rewritten as:

$$u_{fsm} \cdot D_{fsm} = u_{lsm} \cdot D_{lsm} \tag{6.2}$$

Where u_{fsm} and u_{lsm} are the maximum horizontal particle velocity from the full scale model and the laboratory model, respectively. D_{fsm} and D_{lsm} is the reference dimension from the full scale model and the laboratory model respectively. However, this is difficult to fulfill. In this project, Froude scale model is applied, therefore Reynolds number can be rewritten as follows:

$$Re_{fsc} = \lambda_L^{3/2} Re_{lsm} \tag{6.3}$$

Where Re_{fsc} and Re_{lsm} are the Reynolds number of the full scale model and the laboratory model, respectively.

The Reynolds number is calculated as Equation 6.1 for a reference dimension (see Table 6.3) and for the maximum horizontal particle velocity on undisturbed waves from the chamber. This values are presented in Table 6.4.

Model	Maximum horizontal particle velocity $[m/s]$	Kinematic viscosity $[m^2/s]$	Reynolds Number $[-]$
Laboratory	0.111	10^{-6}	$3.15 * 10^4$
Full scale	0.602	10^{-6}	$5.15 * 10^6$

Table 6.4: Reynolds number from laboratory scale and full scale models

From Table 6.4 it can be seen that a lower Reynolds number is found in the laboratory model, this indicates that viscous forces are more important than in the full scale model, where the Reynolds number is larger.

6.7.3 General flow characteristics

In this analysis vortical structures are compared at the same t/T, where t is the total time and T is the period, at three different times. For a better understanding of the similarities between laboratory scale and full scale model the free surface elevation is illustrated. For the comparison of this parameter laboratory scale model is represented with $Q = 15$ and the full scale model with $Q = 2.74$. From Figures 6.23 to 6.25 it is evident that the vortical structures are smaller in the full scale model compared to the laboratory model. This is clear to see at the end of the sloped wall. Also at the beginning of the spoiler this is difference on the vortex are clear to see. This can be understood by the fact that Reynolds number is not scaled as in Equation 6.2, but as in Equation 6.7.2, then inertia forces are increased with respect to the viscous forces as explained in Section 6.7.2. This is caused by the fact that viscous forces are not scaled proportionally

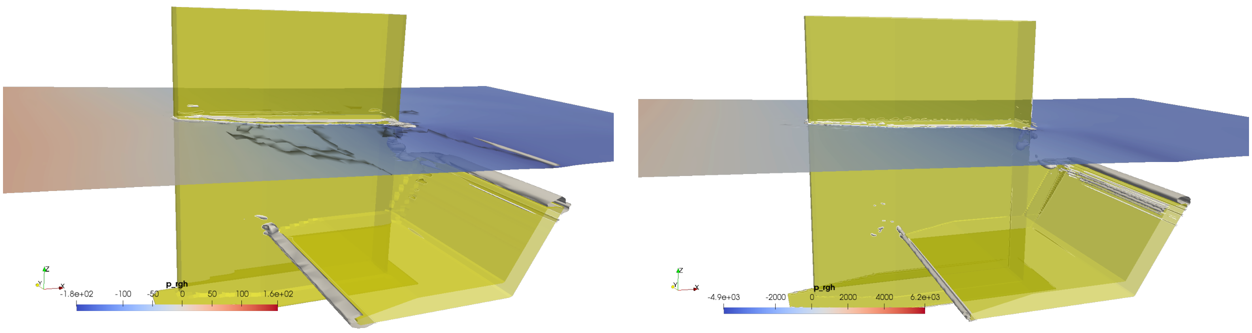

(a) Laboratory scale (b) Full scale

Figure 6.23: Free surface elevation and vortical structures - a) Laboratory model $t = 13.0$ [s] - $Q = 15$, b) Full scale model $t = 71.2$ [s] - $Q = 2.74$

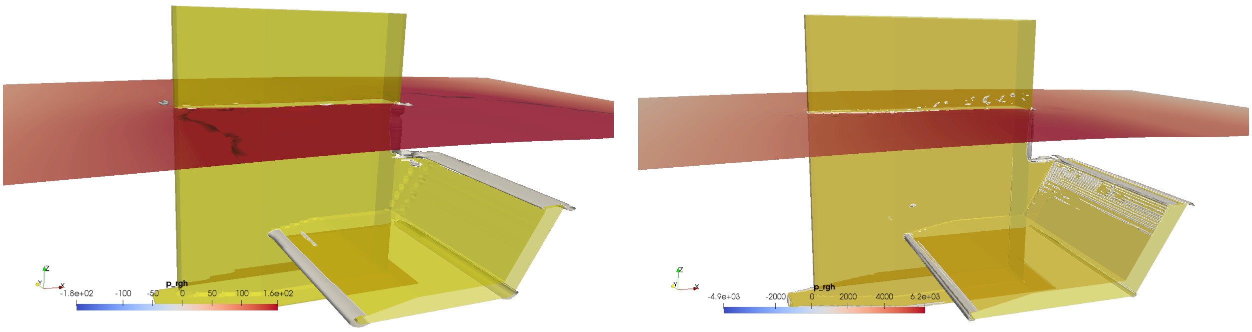

(a) Laboratory scale (b) Full scale

Figure 6.24: Free surface elevation and vortical structures - a) Laboratory model $t = 13.9$ [s] - $Q = 15$, b) Full scale model $t = 75.9$ [s] - $Q = 2.74$

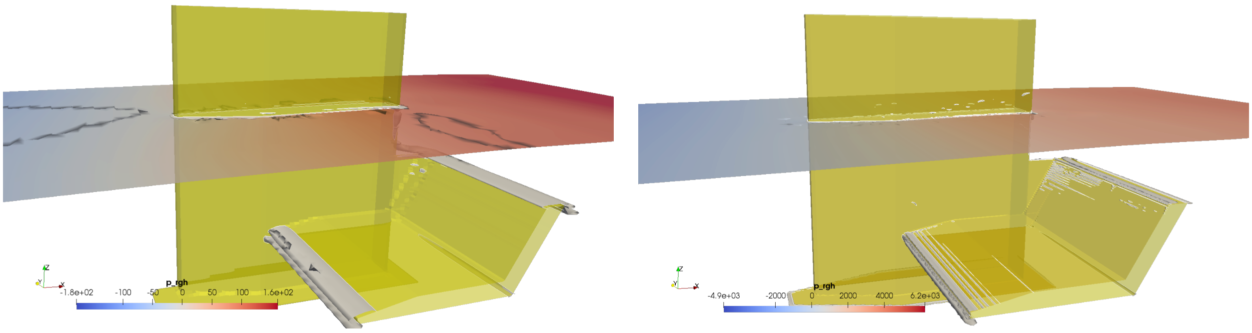

(a) Laboratory scale (b) Full scale

Figure 6.25: Free surface elevation and vortical structures - a) Laboratory model $t = 14.3$ [s] - $Q = 15$, b) Full scale model $t = 78.0$ [s] - $Q = 2.74$

6.7.4 Wave amplification factor

The wave amplification factor shows some differences between laboratory scale and full scale model. Inside the chamber, both models follows a similar behaviour, specially in the area where the absorber would be located. The area next to the chamber is where some differences are apparent, however, the differences in the wave amplification factors are small. The largest difference is found downstream the chamber, where the full scale model does not capture the increase in of the amplification of waves.

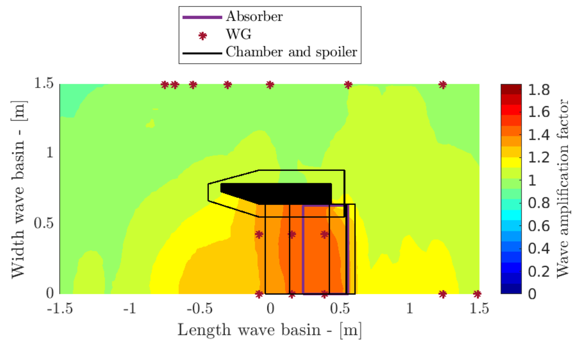

(a) Laboratory scale

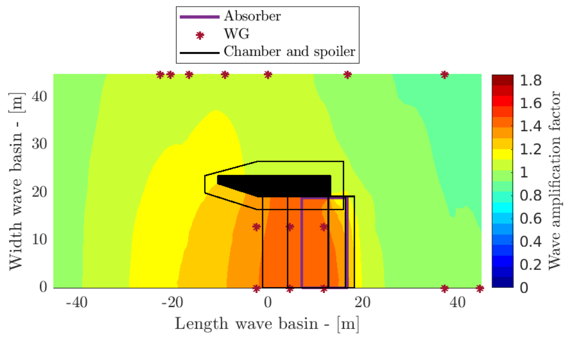

(b) Full scale

Figure 6.26: Wave amplification factor comparison of laboratory and full scale models with A4 chamber configuration - a) Laboratory model for $H = 0.06$ [m] and $T = 2.5$ [s], b) Full scale model for $H = 1.8$ [m] and $T = 13.69$ [s] from CFD

Table 6.5 shows the difference in the wave amplification factors for the maximum, the minimum and the mean value at the area where the absorber would be located. The largest difference is found on the minimum value of the amplification of waves, where the difference is 4.50%. The full scale model gives a value of 3.59% lower than the laboratory model in the mean wave amplification factor. The difference between models presented in Table 6.5 are reasonable low, which means that non-linear effects do not have a large influence in the scaling procedure, and the wave amplification factor gives similar results as the laboratory scale models.

Model	Mean wave amplification factor	Maximum wave amplification factor	Minimum wave amplification factor
Laboratory	1.39	1.47	1.11
Full scale	1.34	1.45	1.06
Difference	3.59%	1.36%	4.50%

Table 6.5: Mean, maximum and minimum wave amplification factor at the absorber location with A4 chamber configuration for laboratory model and full scale model

Part IV

Epilogue

Conclusion 7

This project is focused on the analysis of the wave-chamber interaction of the P80 hybrid platform designed by FPP. The study was conducted employing a two-phase Navier-Stokes simulation in the OpenFOAM software to calculate the wave amplification factor for two different chamber geometries.

The solution-verification phase of the numerical model shows a monotonic convergence for the spatial discretization. Regarding the temporal discretization, a CFL condition is applied.

The validation of the numerical model for wave propagation is considered to have been fulfilled for the first $5-6$ fully developed wave periods. Due to time constraints, a low grid resolution was applied in the validation of the model that included the chamber. This led to an uncompleted validation of the model. Even though a low grid resolution was applied, the CFD model was able to capture some of the non linearities seen on the experiments. The wave amplification factor shows the differences between the experimental data and the numerical data, which is quantified up to 70%. However, in general terms, this difference is not over 10%.

The wave amplification factor is found to depend not only on the wave period but also on the location inside the chamber, being a consequence of reflection and diffraction of the waves from the structure, concretely the side walls and the spoiler. Moreover, the shape of the structure is found to highly influence the amplification of waves. In general, it has been observed that wave's heights do not have a large impact in the amplification factor - only the $T > 1.5$ in an A5 configuration shows a large difference. The A4 configuration amplifies waves with a maximum peak of 1.5 at $T = 1.7$ seconds. In this case, linear and non-linear models give a similar response. This study can confirm what Heras et al. [2019] proposed - the peak of the RAO in the wave energy converter in the P80 FPP device is correlated with the chamber geometry. Furthermore, the A4 case and $T \leq 1.5$ waves are amplifies behind the chamber.

In the A5 chamber configuration, the slopped wall above the water level shifts the peak of the amplification factor to larger periods, with a maximum of 3.4 at $T = 2.5$, which is the largest period analysed in this project. The wave amplification factor in this configuration is mainly influenced by the sloped wall.

All configurations show a limitation in the interaction between the chamber and waves when the steepness of the latter is above 3%. In this case, waves are barely amplified in any of the chamber configurations. It is worth mentioning that both chamber configurations have a large influence on the area next to the device.

Similar conclusions to the ones explained above could be extrapolated to a full scale model.

8 Future Work

Some recommendations for future studies of a similar nature to this report are provided here.

Several problems in the validation of the model with the chamber were found. This was caused by two facts: first, a low grid resolution and second, the validation was only conducted without the structure inside the model. This leads into a not fully validated model. The author recommends, to make a validation analysis with the grid resolution indicated in the solution verification, in case the validation analysis is not fully satisfied, it would be recommended to perform a sensitivity analysis with different grids to measure the uncertainties of the model with the structure.

A good correlation between linear and non-linear methods was obtained for A4 case. A comparison between both methods for A5 configuration is recommended conduct in order to examine if this also occurs in this case.

It was found that A5 configuration gives a higher amplification factor for large periods, which is mainly caused by the interaction between waves and the slopped wall that rises above the water level. The P80 hybrid platform also included absorbers to transform kinetic energy into electricity, which are located in front of the sloped wall. Then, the absorber might influence the interaction between waves and chamber. The author recommends to conduct some simulations with the absorber included to measure if the RAO also shows a similar behaviour as the wave amplification factor.

P80 platform is designed to have two chamber located next to the other. From the analysis of the simulations it is found that the area next to the chamber is highly influence, therefore an analysis with two absorbers side by side would be of interest to conduct.

As it was found on Georgousis [2019], the wave amplification factor is influence by the geometry of the chamber. In this project is was found that side walls influence the wave amplification factor inside the chamber by diffracted and reflected waves. The author suggest to conduct vary different parts of the geometry to measure the difference on the amplification factor.

Bibliography

AAU, 2020. AAU. *Ocean and Coastal Engineering Laboratory*, 2020. URL `https://www.civil.aau.dk/laboratories/ocerg`.

AGI, 2020. AGI. *American Geosciences Institute*, 2020. URL `https://www.americangeosciences.org/critical-issues/faq/what-are-advantages-and-disadvantages-offshore-wind-farms#:~:text=Offshore%20wind%20farms%20have%20many,environmental%20pollutants%20or%20greenhouse%20gases.`

Causon et al., 2011. D. M. Causon, C.G. Mingham and L. Qian. *Introductory Finite Volume Methods for PDEs.* ISBN: 978-87-7681-882-1. Ventus Publishing ApS., first edition edition, 2011.

da Silva and Pereira, 2008. C. B. da Silva and J. C. F. Pereira. *Invariants of the velocity-gradient, rate-of-strain, and rate-of-rotation tensors across the turbulent/nonturbulent interface in jets*, Technical University of Lisbon, 2008.

de Moura and Kubrusly, 2013. Carlos A. de Moura and Carlos S. Kubrusly. *The Courant-Friedrichs-Lewy (CFL) Condition.* ISBN 978-0-8176-8394-8. Springer, e-book edition, 2013.

Drazin and Riley, 2006. P. G. Drazin and N. Riley. *The Navier–Stokes Equations:A Classification of Flows and Exact Solutions.* ISBN-13: 978-0521681629. Cambridge University Press, Cambridge, first edition edition, 2006.

Eldrup and Andersen, 2018. M. Røge Eldrup and T. Lykke Andersen. *Estimation of Incident and Reflected Wave Trains in Highly Nonlinear Two-Dimensional Irregular Waves*, ASCE, 2018.

Eskilsson et al., 2017. C. Eskilsson, J. Palm and L. Bergdahl. *On numerical uncertainty of VOF-RANS simulations of wave energy converters through V&V technique*, Chalmers University of Technology, 2017.

Eça and Hoekstra, 2014. L. Eça and M. Hoekstra. *A procedure for the estimation of the numerical uncertainty of CFD calculations based on grid refinement studies.* vol 262, pp. 104-130. Journal of Computational Physics, 2014.

Eça and Hoekstra, 2010. L. Eça and M. Hoekstra. *A verification and validation exercise for the flow over a backward facing step.* 14-17 June, 2010. Lisbon, Portugal. Fifth European Conference on Computational Fluid Dynamics, 2010.

Fenton, 1985. J. D. Fenton. *A 5th-order Stokes theory for steady waves Journal of Waterway, Port, Coastal and Ocean Engineering 111 (2), 216-234.*, 1985.

Fenton, 1990. J. D. Fenton. *Nonlinear Wave Theories. Wiley, Ch. 1, pp. 3-25, from The Sea. Ideas and Observations on Progress in the Study of the Seas*, 1990. Part A. Editors: B. Le Méhauté and D. M. Hanes.

Folley, 2016. M. Folley. *Numerical Modelling of Wave Energy Converters: State-of-the Art Techniques for Single WEC and Converter Arrays*, Queen's University Belfast, Belfast, 2016.

Georgousis, 2019. D. Georgousis. *Hydrodynamic modelling and optimization of the Floating Power Plant; a combined Wind and Wave Energy Device*, Technical University of Denmark, 2019.

Heras et al., 2019. P. Heras, S. Thomas, M. Kramer and J. P. Kofoed. *Numerical and Experimental Modelling of Wave Energy Converter Pitching in Close Proximity to a Fixed Structure*, Marine Science and Engineering, 2019.

Higuera et al., 2015. Pablo Higuera et al. *Aplicación de la dinámica de fluidos computacional a la acción del oleaje sobre estructuras. Application of computational fluid dynamics to wave action on structures*, UNIVERSIDAD DE CANTABRIA, 2015.

Hirt and Nichols, 1981. C.W. Hirt and B. D. Nichols. *Volume of fluid (VOF) method for the dynamics of free boundaries.* 39, pp. 201-225. Journal of Computational Physics, 1981.

IEA, 2019. IEA. *International Energy Agency, 2019, Global Energy Statistics*, 2019. URL `https://www.iea.org/statistics/electricity/`.

Jacobsen, 2017. Niels G. Jacobsen. *waves2Foam Manual*, 2017.

J.Martín et al., 1998. J.Martín, C.Dopazo and L.Valiño. *Dynamics of velocity gradient invariants in turbulence : Restricted Euler and linear diffusion models*, American Institute of Physics (AIP), 1998.

Lee, 1995. CH Lee. *WAMIT Theory Manual*, Massachusetts Institute of Technology, 1995.

Madsen et al., 1992. P.A Madsen, R. Murray and O. R. Søorensen. *A new form of the Boussinesq equations with improved linear dispersion characteristics pages 371-388*, Coastal Eng, 1992.

Menter, 1994. F. R. Menter. *Two-equation eddy-viscosity turbulence models for engineering applications*, NASA Ames Research Center, Moffett Field, California, 1994.

MEPs, 17-01-2018. MEPs. *MEPs*, 17-01-2018. URL `https://www.europarl.europa.eu/news/en/press-room/20180112IPR91629/meps-set-ambitious-targets-for-cleaner-more-efficient-energy-use`.

Miguel et al., 2018. A. Moreno Miguel, A. Kamath, M. Alagan Chella, R. Archetti and H. Bihs. *Analysis of Different Methods for Wave Generation and Absorption in a CFD-Based Numerical Wave Tank*, Journal of Marine science and Engineering, 2018.

Moukalled et al., 2016. F. Moukalled, L. Mangani and M. Darwish. *The Finite Volume Method in Computational FLuid Dynamics.* ISBN 978-3-319-16874-6. Springer, e-book edition, 2016.

M.S.Chong et al., 1990. M.S.Chong, E.Perry and B.J.Canwell. *A general classification of three-dimensional flow fields*, American Institute of Physics (AIP) 2, 765, 1990.

OpenFOAM, 2020. OpenFOAM. *Official home of The Open Source Computational Fluid Dynamics (CFD) Toolbox*, 2020. URL `https://www.openfoam.com/`.

Pérez-Collazo et al., 2015. C. Pérez-Collazo, D. Greaves and G. Iglesias. *A review of combined wave and offshore wind energy.* Renewable and Sustainable Energy Reviews, 42, 141–153, 2015.

Roache, 1997. P.J. Roache. *Quantification of uncertainty in computational fluid dynamics.* vol 29, pp. 123-160. Annual Review of Fluid Mechanics, 1997.

Schlichting and Gersten, 2017. H. Schlichting and K. Gersten. *Boundary-Layer Theory.* ISBN 978-3-662-52919-5. Springer, e-book edition, 2017.

SimScale, 2020. SimScale. *SimScale*, 2020. URL `https://www.simscale.com/forum/t/what-is-y-yplus/82394`.

Stefanakis et al., 2015. T. Stefanakis, S. Xu, D. Dutykh and F. Dias. *Run-up amplification of transient long waves.*, Quarterly of Applied Mathematics, American Mathematical Society 73, pp.177-199. ff10.1090/S0033-569X-2015-01377-0ff. ffhal-00768597v3f, 2015.

UNFCCC, 2019. UNFCCC. *United Nations Framework Convention on Climate Change*, 2019. URL `https://unfccc.int/`.

Versteeg and Malalasekera, 2007. H. K. Versteeg and W. Malalasekera. *An Introduction to Computational Fluid Dynamics.* ISBN 978-0-13-1427498-3. Pearson Education Limited, second edition edition, 2007.

WAMIT, 2020. WAMIT. *WAMIT INC*, 2020. URL `http://www.wamit.com/`.

Wang et al., 2018. W. Wang, M. Wu, J. Palm and C. Eskilsson. *Estimation of numerical uncertainty in computational fluid dynamics simulations of a passively controlled wave energy converter*, J Engineering for the Maritime Environment, 2018.

Watson et al., 2019. Simon Watson, Alberto Moro, Vera Reis, Charalampos Baniotopoulos, Stephan Barth, Gianni Bartoli, Florian Bauer, Elisa Boelman, Dennis Bosse, Antonello Cherubini, Alessandro Croce, Lorenzo Fagiano, Marco Fontana, Adrian Gambier, Konstantinos Gkoumas, Christopher Golightly, Mikel Iribas Latour, Peter Jamieson, John Kaldellis, Andrew Macdonald, Jimmy Murphy, Michael Muskulus, Francesco Petrini, Luca Pigolotti, Flemming Rasmussen, Philippe Schild, Roland Schmehl, Nafsika Stavridou, John Tande, Nigel Taylor, Thomas Telsnig and Ryan Wiser. *Future emerging technologies in the wind power sector: A European perspective.* Renewable and Sustainable Energy Reviews, 113(109270), 2019.

Westphalen et al., 2014. Jan Westphalen, Deborah M. Greaves, Alison Raby, Zheng Zheng Hu, Derek M. Causon, Clive G. Mingham, Pourya Omidvar, Peter K. Stansby and Benedict D. Rogers. *Investigation of Wave-Structure Interaction Using State of the Art CFD Techniques*, Scientific Research, 2014.

WFO, 2020. WFO. *Global Offshore Wind report 2019*, World Forum Offshore Wind, 2020.

Wilhelm, 2017. M. Wilhelm. *Numerical investigation of a hinged wave energy converter interacting with a close boundary*, TECHNISCHE UNIVERSITAT BERLIN, 2017.

Part V

Appendix

Theory A

A.1 Governing equations

The Navier-Stokes equations with the single fluid (mixture) assumption that reads:

$$\nabla \cdot \mathbf{u} = 0 \tag{A.1}$$

$$\frac{\partial}{\partial t}(\rho \mathbf{u}) + \nabla \cdot (\rho \mathbf{u}\mathbf{u}) = -\nabla p + \nabla \cdot \mathbf{S} + \rho \mathbf{f_b} \tag{A.2}$$

Equations above are the Navier-Stokes equations with the single fluid assumption. Where **u** is the fluid velocity, p is the pressure, ρ is the mixture density, g is the gravity, **S** is the viscous stress tensor and f_b is the body force.

The two-phase problem is solved using the volume of fluid (VoF) technique

$$\frac{\partial \alpha}{\partial t} + \nabla \cdot u\alpha = 0 \tag{A.3}$$

The kinematic viscosity (ν) and the single fluid density are assumed to be linear functions of the volume fraction:

$$\nu = \alpha \nu_w + (1 - \alpha)\nu_a \tag{A.4}$$

$$\rho = \alpha \rho_w + (1 - \alpha)\rho_a \tag{A.5}$$

Indexes w denote water and a air.

Also. if it is assumed that the problem is not affected by heat transfer, the flow field is able to be solved for only considering conservation of mass and momentum equations.

A.1.1 Transport equations

The transport equations are formulated as follow:

$$\frac{\partial(\rho\phi)}{\partial t} + \nabla \cdot (\rho\phi\mathbf{u}) = \nabla \cdot (\Gamma\, \mathrm{grad}(\phi)) + S_\phi \tag{A.6}$$

Also equation above can be written as equation A.7. Which is based on the control volume method. The Gauss divergence theorem is applied for this.

$$\frac{\partial}{\partial t}\left(\int_{\mathrm{CV}}(\rho\phi)\mathrm{d}V\right)+\int_{A}\mathbf{n}\cdot(\rho\phi\mathbf{u})\mathrm{d}A=\int_{A}\mathbf{n}\cdot(\Gamma\,\mathrm{grad}(\phi))\mathrm{d}A+\int_{\mathrm{CV}}S_{\phi}\mathrm{d}V \tag{A.7}$$

Equations above are important for the finite volume method to apply properly the governing equations in a discretized domain of finite control volumes

A.2 OpenFoam setup

OpenFOAM needs an specific directory structure to run the simulations. The structure is divided in three main folders:

- *system/*: It is used for setting parameters associated with the simulation. This folder can contain several files, but at least the following three must be included: *controlDict* (run the control parameters), *fvSchemes* (discretization schemes used in the solution are selected) and *fvSolution* (equation solvers, tolerances and other algorithms that control the simulation are set for)
- *constant/*: This directory contains files with information about physical properties and a full description of the case mesh in a directory called *polyMesh*.
- *0.org/*, *0/* or *"times"* directory: This folder contain data for specific fields in individual files. In this directory boundary conditions and initial values, such us velocity or pressure are defined by the user.

Once the simulation is done additional directories can be generated, which depends on the user selection. This files or folders are thereafter used in the post-processing stage. OpenFOAM can generate a directory called *postProcessing* that is typically generated by function objects data conversion. This folder usually contains the data in the form of time directories with all data parameters that the user demands. The post-processing stage can be analyzed by a large number of tools, however in this report self-made Matlab scripts are used to process the data generated from the numerical models.

A.2.1 Free surface modeling

Also, the artificial compression term, which in *OpenFOAM* is called *CAlpha*, only influence regions with phase fraction that are different from 0 or 1 value. For $CAlpha = 0$ no compression velocity is applied, and $CAlpha > 0$ introduce the corresponding artificial velocities at the interphase.

It is important to keep in mind that α have to be bounded between 0 and 1. This is achieved by a solver called *MULES* (Multidimensional Universal Limiter for Explicit Solutions) that by applying a limiter factor in the fluxes of the discretised divergence term the $\alpha = [01]$ is achieved, see [Higuera et al., 2015].

A.2.2 Boundary conditions

In this report three different model setups are required for the verification, validation and analysis of the data, as it is explained in Sections 3, 4 and 5. Therefore, a model with *cyclic* boundary conditions, a 2D and a 3D model are considered. In this section, only the features applied are described, see Table A.1, as OpenFOAM has a wide range of them.

For the first case mentioned above, *cyclic* boundary condition are defined at the inlet and outlet, Figure 3.7a. This layout makes possible to couple conditions between a pair of patches. For the second case, the 2D model represented in Figure 3.7c, all boundaries are defined as *patch*, *wall* or *empty*. For the last case, the 3D model shown in Figure 3.7b, boundaries are defined in a similar way as in the 2D model. However, boundaries defined as *empty* in the 2D model are changed to be *wall* or *symmetryPlane*. Where the last one is applied to reduce the domain size to one half, as the model is symmetric along the x-axis.

Those boundary conditions explained before for all three models (see Table A.1) are chosen to reproduce as accurate as possible the same conditions as in the experiments). It can be seen in Table A.1 that the model with 3 dimensions have more parameters defined, which are needed to define a turbulence model, see Section 2.4.

Model	Boundary	Type	α	p_{rgh}	U	k	nut	ω	S
Cyclic	Inlet	**cyc**	**cyc**	**cyc**	**cyc**	-	-	-	-
	Outlet	**cyc**	**cyc**	**cyc**	**cyc**	-	-	-	-
	Ground	**wall**	**zGr**	**fFP**	**slip**	-	-	-	-
	Top	**patch**	**inOu**	**tPr**	**pIOV**	-	-	-	-
	Side	**emp**	**emp**	**emp**	**emp**	-	-	-	-
2D	Inlet	**patch**	**wAlp**	**fFP**	**wVel**	-	-	-	-
	Outlet	**patch**	**zGr**	**fFP**	**fVal**	-	-	-	-
	Ground	**wall**	**zGr**	**fFP**	**slip**	-	-	-	-
	Top	**patch**	**inOu**	**tPr**	**pIOV**	-	-	-	-
	Side	**empty**	**emp**	**emp**	**emp**	-	-	-	-
3D	Inlet	**patch**	**wAlp**	**fFP**	**wVel**	**zGr**	**cal**	**fVal**	**fVal**
	Outlet	**patch**	**zGr**	**fFP**	**fVal**	**zGr**	**cal**	**zGr**	**zGr**
	Ground	**wall**	**zGr**	**fFP**	**slip**	**slip**	**slip**	**slip**	**zGr**
	Top	**patch**	**inOu**	**tPr**	**pIOV**	**slip**	**slip**	**slip**	**zGr**
	Side	**wall**	**zGr**	**fFP**	**fVal**	**slip**	**slip**	**slip**	**zGr**
	Symmetric	**syPl**	**syPl**	**syPl**	**syPl**	**syPl**	**syPl**	**syPl**	**syPl**
	Chamber	**wall**	**zGr**	**fFP**	**fVal**	**kLRWF**	**nUBWF**	**oWF**	**zGr**

Table A.1: Boundary conditions layout for 3 different numerical models. Legend: *cyclic* (**cyc**), *zeroGradient* (**zGr**), *fixedFluxPressure* (**fFP**), *slip* (**slip**), *inletOutlet* (**inOu**), *totalPressure* (**tPr**), *pressureInletOutletVelocity* (**pIOV**), *empty* (**emp**), *waveAlpha* (**wAlp**), *waveVelocity* (**wVel**), *fixedValue* (**fVal**), *symmetryPlane* (**syPl**), *calculated* (**cal**), *kLowReWallFunction* (**kLRWF**), *nutUBlendedWallFunction* (**nUBWF**) and *omegaWallFunction* (**oWF**)

A.2.3 Turbulence model

On turbulent flows the continuity equation is satisfied as the same amount of mass, in a control volume, is removed and added despite of eddy motion can occur. However, an extra momentum can be carried by the particles that are transported by eddies, therefore, an extra turbulent stress is found, called Reynolds stresses. Those stresses are accounted by the so-called Reynolds-average Navier-Stokes (RANS) equations, as the non-linearity of the Navier-Stokes equations ensures that fluctuations appears in the RANS equations. The Reynolds decomposition separates a fluid property, Φ, in a steady mean value, Φ, and a fluctuating part, $\Phi'(t)$, as follow:

$$\Phi\left(x_i,t\right)=\bar{\Phi}\left(x_i\right)+\Phi'\left(x_i,t\right) \tag{A.8}$$

By applying Equation A.8 to the Navier-Stokes equations for the case of Newtonian incompressible fluid the RANS equations in tensor notation are defined as follow:

$$\frac{\partial\rho\bar{u}_i}{\partial t}+\frac{\partial\left(\rho\bar{u}_i\bar{u}_j\right)}{\partial x_j}=\rho\bar{b}_i-\frac{\partial\bar{p}}{\partial x_i}+\frac{\partial}{\partial x_j}\mu\left[\frac{\partial\bar{u}_i}{\partial x_j}+\frac{\partial\bar{u}_j}{\partial x_i}\right]-\frac{\partial\rho\overline{u_i'u_j'}}{\partial x_j} \tag{A.9}$$

Form previous Equation (A.9) the dynamic viscosity is defined as μ, the body force as b_i and $\rho\overline{u_i'u_j'}$ refers to the Reynolds stresses. This new term implies that there are more unknowns that equations, which meas that the RANS equations are not closed. In order to deal with this, the RANS equations need to be closed by the inclusion of a turbulence model by the *closure problem*. This is done by introducing the increased viscosity concept, so Reynolds stresses expression leads to:

$$-\overline{\rho u_i'u_j'}=\mu_t\left(\frac{\partial\bar{u}_i}{\partial x_j}+\frac{\partial\bar{u}_j}{\partial x_i}\right)-\frac{2}{3}\rho\delta_{ij}k \tag{A.10}$$

Where the turbulent viscosity is defined as μ_t and the turbulent kinetic energy k as:

$$k=\frac{1}{2}\overline{u_iu_i} \tag{A.11}$$

It can be see that, from Equation A.11, the kinetic energy of the turbulent fluctuations per unit mass, k, is obtained as the sum of the three normal Reynolds stresses multiplied by 1/2. Furthermore, these three normal stresses are assumed to be isotropic, as well as the turbulence viscosity when it is applied on the model using the Boussinesq expression. So, two extra transport equations are introduced, which represents the turbulent properties of the flow. The first one is defined as k, while the second equation introduce a scale of turbulence.

In order to account for the eddy viscosity, or turbulent viscosity, μ_t, a model called $k-\omega\ SST$ is implemented, [Menter, 1994]. This is a combination of two turbulence models, the $k-\epsilon$ and the $k-\omega$ models.

The $k-\omega$ turbulence model is used as a closure for the RANS equations. It is used to predict turbulence by two partial differential equations for the variables called k and ω, being the second one, ω, the specific rate of dissipation. This model is used in the viscous sub-layer, which is located close to the wall, and the log-layer, so it makes low-Re simulations possible with good predictions of the mean flow profiles for simple definitions of the boundary conditions. The $k-\epsilon$ model is used to simulate mean flow characteristics for turbulent flow conditions, where the second transported variable is called ϵ and it represents the turbulent dissipation. So, the $k-\epsilon$ model is used in the free-stream far from the boundaries. Then, when $k-\omega\ SST$ is applied it allows to switch between the models described before depending on the conditions of the flow. All formulas that describes the transport equations needed on this model are described on Menter [1994] and Versteeg and Malalasekera [2007].

A turbulent boundary layer is divided by two regions called the inner and the outer region. Additionally, the inner region, where the viscous forces are equal or greater than the inertia forces, is subdivided into 3 more regions, see Figure A.1. This subdivision is caused by how the flow behaves. Those layers are characterized by the dimensionless wall distance y^+, [Schlichting and Gersten, 2017]:

$$y^+ = \frac{y u_\tau}{\nu}, \quad u_\tau = \sqrt{\frac{\tau_w}{\rho}}, \quad \tau_w = \frac{C_f \rho U_{ref}^2}{2}, \quad C_f = \frac{0.026}{Re_x^{1/7}}, \quad Re_x = \frac{\rho U_{ref} L}{\mu}, \quad u^+ = \frac{U}{u_\tau} \tag{A.12}$$

Where:

y^+	Dimensionless wall distance	ν	Kinematic viscosity
y	Absolute distance from the wall	C_f	Skin friction coefficient
u_τ	Friction velocity	Re	Reynolds number
τ_w	Wall shear stress		

First, the viscous sub-layer, which is the region closest to the surface $y^+ < 5$. This zone is characterized such as the viscous effects are dominant, so the Reynolds shear stress is negligible and the relation between the velocity and the distance from the wall and is linear $u^+ = y^+$. This region must be finely resolved when separation is expected in flows with changing pressure gradients. In this case at least one grid point needs to be defined in the viscous sub-layer for $y^+ = 1$. Second, the buffer layer, where $5 < y^+ < 30$, is the transition region between the region dominated by viscous forces and the the turbulence dominated part of the flow. Here, turbulent and viscous stresses have a similar magnitude, therefore it is a complex region and the velocity profile is not well defined. Last, the logarithmic area, when $y^+ < 30$, turbulence stress are dominant, then the velocity profile varies slowly following a logarithmic function over the y parameter. In this region wall-bounded effects are not important. The dimensionless velocity can be described as:

$$u^+ = \frac{1}{\kappa} \ln\left(y^+\right) + B \tag{A.13}$$

Where the Karman constant $\kappa = 0.41$ and the constant $B = 5.2$.

Then, wall functions are boundary conditions that are able to relate the surface and the center of the cells at the surface. However, despite this is a powerful tool that reduce computational time, it should be avoided to use due to accuracy problems.

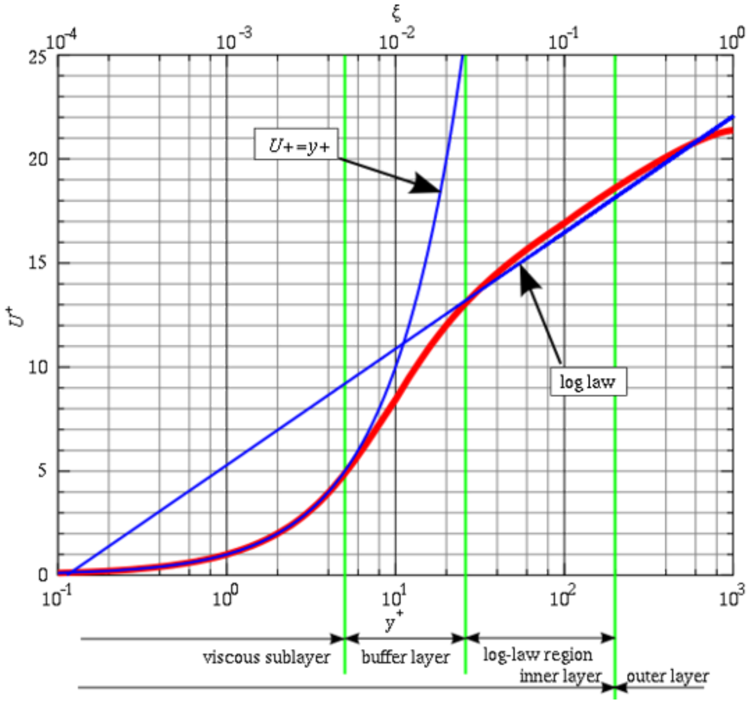

Figure A.1: Wall regions and layers, [SimScale, 2020]

OpenFOAM can distinguish between several models such us laminar, Reynolds-averaged simulation (RAS) and large-eddy simulation (LES). All of those models are defined on the *turbulenceProperties* dictionary. This project makes uses of laminar and RAS modelling as it is explained before. The first one is implemented when only propagation of waves are modelled, while the second one is needed when any of the chamber configurations are included on the NWT. For the RAS model a $k-\omega$ SST turbulence model is implemented in *turbulenceProperties* dictionary. In order to verify in which region the model is places a utility called *yPlus* is used on OpenFOAM.

A.2.4 Modelling of waves in OpenFOAM

The approach called *waves2Foam* includes also both, wave generation and absorption. Those are implemented on the so-called relaxation zones developed by Jacobsen [2017].

This method makes uses of a weight function between computational solutions of the velocity field and analytical solutions. This approach is formulated as:

$$\phi = (1 - w_R)\,\phi_{\text{target}} + w_R \phi_{\text{computed}} \tag{A.14}$$

Where w_R is the weighting function and it can be defined in different ways. In this project two different weighting functions are implemented. The decision of choosing the weighing functions presented further bellow is made after performing several test by an iterative procedure until reliable results are found. Then, at the inlet relaxation zone a third-order polynomial weight function is implemented, which is illustrate as the blue line in Figure 2.4 and it is written as:

$$w_R = -2\tilde{\sigma}^3 + 3\tilde{\sigma}^2 \tag{A.15}$$

Where $\tilde{\sigma} = 1 - \sigma$

At the outlet relaxation zone, where there is not generation of waves, a different weight function is proposed, described as free polynomial weight with an exponent $p = 14$. This is illustrated in Figure 2.4 in yellow color on the absorption zone which formula corresponds to Equation A.16

$$w_R = 1 - \sigma^p \tag{A.16}$$

At the fully absorption zone a different *waveType* is implemented, called *potentialCurrent*. According to Jacobsen [2017] this method introduce a current that is uniform over the depth and it is typically used for outlet relaxation zones, as the velocity vector is set to zero.

A.2.5 Schemes and Solutions

As it is introduced on Section 3.2.1 OpenFOAM requires an specific directory structure, which it is divided into three main folders. In this section a description of *fvSchemes* and *fvSolution* directories, which are located in the *system* directory, are explained.

On one hand, in the *fvSolution* the equation solver, algorithms and tolerances are controlled. This directory contains a set of sub-dictionaries that contains the so-called *solvers*, *relaxationFactors* and *PISO*, *SIMPLE* or *PIMPLE* algorithms.

Then, the sub-dictionary called *solvers* specifies linear-solver for each of the discretized equations. The solvers that are used on this project are: *smoothSolver* (solver that uses a smoother), *PCG* (preconditioned conjugate gradient) and *PBICG* (preconditioned bi-conjugate gradient, for asymmetric matrices). Moreover, some other parameters such as *relTol*, *tolerance*, *preconditioner*, *smoother*, etc are defined in this directory. Those solvers are based on an iterative process which reduce the equation residuals over a succession of solutions. This process is governed by *relTol*, *tolerance,* and *maxIter* when one of this restrictions are reached the solver stops.

Moreover, in OpenFOAM most fluid dynamic solver applications uses the semi-implicit method for pressure linked equations (SIMPLE), the pressure implicit split operator (PISO) or a combination of both (PIMPLE). Those are algorithms that are based on iterative procedures for coupling equations form momentum and mass conservation. Where SIMPLE for steady state and PISO and PIMPLE are used for transient problems. In this case the PIMPLE algorithm is implemented which is composed by one predictor and two correctors. A well detailed explanation of all possible combinations can be found on OpenFOAM [2020].

In the *fvSchemes* dictionary the numerical schemes, as derivatives in equations, are set in applications. In this dictionary a set of sub-dictionaries, which are the terms of desired numerical schemes. In this project those used are: *divSchemes*, *ddtSchemes*, *gradSchemes*, *laplacianSchemes*, *interpolationSchemes* and *snGrandSchemes*.

The time schemes applied (*ddtSchemes*), which is the first time derivative ($\partial/\partial t$), is a second-order Crank-Nicholson/first-order backward Euler scheme.

All gradient terms in the application are implemented in the sub-dictionary called *gradSchemes*. In this case a general interpolation scheme is implemented that is based on the standard volume discretization of Gaussian integration with a linear interpolation scheme.

In the *divSchemes* sub-dictionary all divergence terms are setup, which in this report all are based on the second order Gauss integration, this is a standards finite volume discretization that requires the interpolation of values from cell centres to face centres. For the convection term *div(rhoPhi,U)* of the momentum equation a second-order van Leer scheme is implemented, which an improved version for vector field is implemented, this takes into account the direction of the field. For the transport term *div(phi,alpha)* the a *Gauss vanLeer01*, which is bounded between 0 and 1 is used, that strictly keeps α between those values. Also, the term *div(phirb,alpha)*, that corresponds to the compression term, make uses of *Gauss linear* scheme. The turbulence equations are solved based on the first-order upwind method with a limited gradient scheme *Gauss linearUpWind limitedGrad*.

The Laplacian terms are included in the sub-dictionary called *laplacianSchemes*. In this case the *Gauss* scheme is used for discretization, also an interpolation scheme for the diffusion coefficient is needed, which in this case is selected to be *linear*. Last, a surface normal gradient scheme, which in this case a *corrected* scheme is used. This accounts for explicit non-orthogonal correction.

A.3 Courant number or Courant–Friedrichs–Lewy (CFL) Condition

The convergence of the Courant–Friedrichs–Lewy condition is necessary for solving some partial differential equations or PDEs numerically. According to de Moura and Kubrusly [2013], CFL condition has to be satisfied for stability reasons, which states that the time step has to be proportional to the space step, with also a constant depending on the magnitude of the velocity. This term is an important term for CFD simulations. Also de Moura and Kubrusly [2013] states that CFL condition is necessary to be achieved to guarantee the time stability of explicit time schemes given that high order space discretizations are used. Then, the CFL condition states as:

$$Co = \frac{u\Delta t}{\Delta x} \leq 1 \tag{A.17}$$

A.4 Verification and Validation technique

In this Appendix, the theory involved on the calculation of the numerical uncertainty of VOF-RANS in CFD simulations by the verification and validation technique, also called V&V technique, is presented, which is based on Eskilsson et al. [2017] and Wang et al. [2018]. This aims to give higher confidence in the solutions of numerical models. In general a solution is considered acceptable and reliable when the numerical uncertainties are remained bellow 5%.

The model used for the calculation of the hydrodynamics is based on VOF-RANS, which is capable of handling a large variety of complex problems such us nonlinear waves, overtopping, etc. However, CFD models still presents numerical uncertainties and errors. This estimation of numerical errors, uncertainties and convergence rates has been overlooked in the CFD application on WECs. As it is indicated on Eskilsson et al. [2017], most of the work on convergence studies of CFD simulations on WECs are focused on basic grid convergence studies, which end up with 'grid independent' solutions. However, as it is presented on Eskilsson et al. [2017] and Wang et al. [2018] a solution that is grid independent does not implies that there are no errors in the solution or it is properly converged. In contrast to the ship hydrodynamic field, which has V&V procedures to judge the reliability of a numerical solution, WECs sector is still under development of a procedure to obtain an estimation of the numerical uncertainty based on the solutions.

This V&V technique is based on Richardson extrapolation, which measures the convergence of the solution and applies safety factor to calculate uncertainties based on the errors of the model.

As it is explained on Sections 4 and 5 this technique consist of two major stage, the verification step and the validation step. On one hand, the verification step ensures that the numerical code is working correctly, which is conducted by comparing the code with analytical solutions. On the other hand, the validation step check that the mathematical model implemented is accurate enough to describe the physical phenomenon under investigation. This is carried out by comparing numerical results to empirical data. In Eskilsson et al. [2017] the study is focused on the solution verification step, which 'deals with how to estimate the error/uncertainty of a given calculation, for which in general exact solution is not known' [Eça and Hoekstra, 2014].

Moreover, errors on CFD simulations can be divided in two groups: numerical and modelling errors. Modelling errors are caused by approximations and simplifications of the problem, such us boundary conditions, turbulence models and geometric aspects, among others. Numerical errors are caused by discretization errors, which also can be divided intro 4 blocks: temporal discretization errors, spatial discretization errors, iterative errors and round-off errors. According to Wang et al. [2018] and Eskilsson et al. [2017] round-off errors can be caused by the limit of machine precision, which can be neglected in most of the cases for double precision computations. Iterative errors are 'caused by the nonlinearity of the mathematical problems and the truncation of the iterative process under a proper convergence criterion' [Wang et al., 2018]. And then, spatial and temporal discretization errors, those comes when in the discretization process the high-order terms are neglected.

Then, whit the uncertainties from experimental (U_{exp}), modelling (U_{mod}) and numerical (U_{num}) errors estimated the called model validation uncertainty U_{val} is obtained as, Eça and Hoekstra [2010]:

$$U_{val} = \sqrt{U_{num}^2 + U_{mod}^2 + U_{exp}^2} \tag{A.18}$$

Then, it is possible to resolve whether or not the numerical model is validated by comparing the validation uncertainty (U_{val}) with the difference between numerical models (ϕ_i) and experiment (D) as: $E_i = \phi_i - D$. Therefore, when $|E| \gg U_{val}$ the model can not be said to be validated. However, when $|E| < U_{val}$ in this case the modelling error has a smaller value than the uncertainties, so it can be stated that the model is validated, in addition, as a common rule if E is smaller than 5% it can conclude that it is validated.

In the following the Verification and Validation technique is based on the one proposed on Eça and Hoekstra [2010], which is based on Richardson extrapolation. This procedure needs at least 4 grids with different mesh density to calculate the numerical uncertainties. The grid refinement ratio is defined as Equation A.19. It can be seen that the value of the root is 1, this is explained by the fact that the analysis of this refinement ratio is calculated for one parameter/dimension at a each time, as explained on Sections 4 and 5. Then, the V&V on this project has to ensure that every parameter considered on this procedure is independent from each other to ensure that the V&V technique is valid.

$$\frac{h_i}{h_1} = \sqrt[1]{\frac{N_1}{N_i}} \tag{A.19}$$

Where h_i indicates the typical cell size of a grid and the i run over the number of grids from highest to lowest density. N_i denotes the total number of cells.

The next step is to calculate the error, called ε, between the numerically obtained result ϕ_i using the *ith* grid and the exact solution (ϕ_0). This is defined as:

$$\varepsilon = \phi_i - \phi_0 = ah^p \tag{A.20}$$

From Equation A.20 two new parameters are described. p indicates the order of accuracy and a is a case specific constant. Then, the next step calculate the true error. This is approximated by the error obtained from the Richardson extrapolation (δ_{RE}) indicated as follow:

$$\varepsilon \approx \delta_{RE} = \frac{\phi_i - \phi_1}{(h_i/h_1)^p - 1} \tag{A.21}$$

Another aspect that has to be taken into consideration is that nowadays most CFD models are designed to be second-order accurate in space and time yielding:

$$\delta_{RE}^{02} = \phi_i - \phi_0 = a_{02}h^2 \tag{A.22}$$

And then, if it is assumed that the error is a mix of both first and second order, this can be expanded as a sum of two components.

$$\delta_{RE}^{12} = \phi_i - \phi_0 = a_{11}h + a_{12}h^2 \tag{A.23}$$

Where p and the constants a_{01}, a_{11} and a_{12} are obtained by calculate the errors of the different grids and performing a least square fit. Then, if the estimated order of accuracy is larger than 0 it can be said that the error is monotonically converged.

Then, Roache [1997] propose to use safety factor based on the estimated convergence rate to go from numerical errors (ε) to numerical uncertainties U_ϕ

$$U_\phi = F_S(p)|\varepsilon| \tag{A.24}$$

Those safety factor depends on the order of convergence. The asymptotic range of convergence can be assumed to be $0.95 \leq p \leq 2.25$ if a standard second-order model is assumed. Then, Roache suggested to use a safety factor of 1.25 in the asymptotic range. Otherwise, when the previous condition can not be fulfilled a safety factor of 3.0 is implemented. Then, the uncertainty is calculated as:

$$U_\phi = 1.25\delta_{RE} + U_S \quad \text{if } p \in [0.95, 2.05] \tag{A.25}$$

In case of monotone convergence that is outside the asymptotic range the uncertainty is evaluated as Equations A.26 and A.27.

$$U_\phi = \min\left(1.25\delta_{RE} + U_S, 3\delta_{RE}^{12} + U_S^{12}\right) \text{ if } p < 0.95 \tag{A.26}$$

$$U_\phi = \max\left(1.25\delta_{RE} + U_S, 3\delta_{RE}^{02} + U_S^{02}\right) \text{ if } p > 2.05 \tag{A.27}$$

And U_s, U_S^{02} and U_S^{12} are the standard deviation, which are calculated from the leas square fits.

When the convergence is not monotonic, but oscillatory, the uncertainty can be calculated as:

$$U_\phi = 3\delta_{\Delta M} \tag{A.28}$$

where the error between the maximum and minimum is obtained as

$$\delta_{\Delta M} = \frac{\max|\phi_i - \phi_j|}{\left(h_{N_g}/h_1\right) - 1} \quad 1 \leq i, j \leq N_g \tag{A.29}$$

In case of anomalous behaviour the uncertainty can be estimated as

$$U_\phi = \min\left(3\delta_{\Delta M}, 3\delta_{RE}^{12} + U_S^{12}\right) \tag{A.30}$$

In this project the evaluation of the numerical uncertainty is conducted by using non-dimensional variable, which is the free surface elevation for three different iso-surfaces based on the VOF approach, see Section 2.3. The subscript on $\eta_{0.50}$, $\eta_{0.90}$ and $\eta_{0.10}$ refers to the phase fraction on the VOF approach.

$$\begin{aligned} \bar{\eta}_{0.50} &= \frac{\eta_{0.50}}{H_0} \\ \bar{\eta}_{0.90} &= \frac{\eta_{0.90}}{H_0} \\ \bar{\eta}_{0.10} &= \frac{\eta_{0.10}}{H_0} \end{aligned} \tag{A.31}$$

Where H_0 is the target wave height.

A.5 Invariants of the velocity-gradient tensor

This section aims to explain into more details the invariants of the velocity gradient and it applicability on the characterization of the dynamics, topology and geometry of the flow used on Section 6.2 for the illustration and understanding of vortexes generated by the interaction with the structure. All formulas, theory and concepts explained here are based on M.S.Chong et al. [1990], J.Martín et al. [1998] and da Silva and Pereira [2008].

According to J.Martín et al. [1998], the second invariant, or Q-factor, is used to define regions with strong vorticity for positive values of this parameter, or regions with high values of kinetic energy dissipation are associated with negative values of the Q-factor. Then Q iso-surface are a good indicator of turbulent flow structures.

According to da Silva and Pereira [2008] it is stated that invariants are scalar quantities, which are characterized by its independence of the orientation of the coordinate system. Moreover it contains essential information regarding to the rates of vortex stretching and rotation, and on the geometry and topology of deformation of the infinitesimal fluid components. Then, the study of the invariants of the velocity-gradient (as the turbulence small scales are defined by this velocity gradient) allows to understand the physics involved on this processes with a relatively small number of variables. Then, this invariants are enough to fully determine the dynamical system that it is associated with a local origin. This is a crucial point which allows to determine the small scale motions at each point in the fluid field as it is mentioned on J.Martín et al. [1998], which is based on M.S.Chong et al. [1990].

Then, in order to understand the invariants the definition of this concept is explained in the following, which is based on da Silva and Pereira [2008]:

The first step is to define the velocity gradient tensor:

$$A_{ij} = \partial u_i / \partial x_j \tag{A.32}$$

Which it can be split into a symmetric and a skew-symmetric component as follow:

$$A_{ij} = S_{ij} + \Omega_{ij} \tag{A.33}$$

where S_{ij} is the rate of strain tensor (Equation A.34) and Ω_{ij} is the rate of rotation tensor (Equation A.35).

$$S_{ij} = \frac{1}{2}\left(\partial u_i / \partial x_j + \partial u_j / \partial x_i\right) \tag{A.34}$$

$$\Omega_{ij} = \frac{1}{2}\left(\partial u_i / \partial x_j - \partial u_j / \partial x_i\right) \tag{A.35}$$

Moreover, the velocity gradient tensor (Equation A.33) has a characteristic equation, which is represented on Equation A.36:

$$\lambda_i^3 + P\lambda_i^2 + Q\lambda_i + R = 0 \tag{A.36}$$

where λ_i represents the eigenvalues of the velocity gradient tensor A_{ij}. Then, the three invariants of the velocity gradient tensor are defined as follow:

$$P = -A_{ii} = -S_{ii} \tag{A.37}$$

$$Q = -\frac{1}{2}A_{ij}A_{ji} = \frac{1}{4}\left(\Omega_i\Omega_i - 2S_{ij}S_{ij}\right) \tag{A.38}$$

$$R = -\frac{1}{3}A_{ij}A_{jk}A_{ki} = -\frac{1}{3}\left(S_{ij}S_{jk}S_{ki} + \frac{3}{4}\Omega_i\Omega_j S_{ij}\right) \tag{A.39}$$

where Equation A.37 represents the first invariant, equation A.38 represents the second invariant and Equation A.39 the third invariant of the velocity gradient tensor. And the vorticity field is represented as follow:

$$\Omega_i = \varepsilon_{ijk}\partial u_j/\partial x_k \tag{A.40}$$

Moreover, the invariants of the rate of strain tensor (P_s, Q_s and R_s) and the invariants of the rate of rotation tensor (P_W, Q_W and R_W) can be defined. However, due to incomprehensibility $P_s = 0$ and P_W and R_W are vanish dye to the skew-symmetric character of Ω_{ij}, then those expressions can be defined as:

$$Q_S = -\frac{1}{2}S_{ij}S_{ij} \tag{A.41}$$

$$R_S = -\frac{1}{3}S_{ij}S_{jk}S_{ki} \tag{A.42}$$

$$Q_W = \frac{1}{2}\Omega_{ij}\Omega_{ij} = \frac{1}{4}\Omega_i\Omega_i \tag{A.43}$$

where Equations A.41 and A.42 are the second and third invariants of the rate of strain tensor and Equation A.43 is the second invariant of the rate of rotation tensor.

Moreover, Q_S is always negative and it is related to the kinetic energy dissipation rate, which is defined as $\varepsilon = 2\nu S^2 = -4\nu Q_S$, where $S^2/2 = S_{ij}S_{ij}/2$ is used to define the strain product.

Also, Q_W is always positive, which can be defined as $Q_W = \Omega_i\Omega_i/4$, and it can be seen that this invariant is related to the second invariants of A_{ij} and S_{ij} by $Q_W = Q - Qs$, so it can be concluded that Q_W is proportional to the enstrophy density ($\Omega^2/2 = \Omega_i\Omega_i/2$). Then, we can define the second invariant of the velocity gradient tensor, Q as:

$$Q = \frac{Q_s}{Q_W} \tag{A.44}$$

Then, according to J.Martín et al. [1998] and from Equation A.44 and the definitions above, it can be determined that the sign of the invariant Q is caused by the local balance in the flow between the dissipation and the vorticity strength. Then, regions with vorticity can be defined by positive values of Q and regions with kinetic energy dissipation can be defined by negative values of Q.

A.6 Scaling

A.6.1 Froude scaling criteria

This appendix aims to explain the Froude law scaling method used on the CFD model to simulate a full size model based on experimental and numerical setup.

In order to represent properly the full scale model based on the laboratory model some basic criteria must be applied and fulfilled to achieve a correct scaling procedure. Those criteria are:

- Geometric similarity: It has to be scaled with the same ratio (length, diameter, roughness,etc)
- Kinematic similarity: The motion, i.e. acceleration and velocity of the fluid should be scaled always with the same ratio for all particles for every time step
- Dynamic similarity: The external forces acting on the model have to be scaled whit the same ratio

In this case, the only criteria that is fully fulfilled is the geometric similarity. In case of kinematic similarity only the velocity parameter is scaled proportional to the geometry, however, the acceleration parameter is not scaled in the same manner. Last, the dynamic similarity, in this case only two hydrodynamic scaling laws are fully fulfilled, the Keulegan-Carpenter Number and Froude Number. It is the last one the chosen one on this project due to Froude's scaling criteria is suitable for free surface flows, also this law is commonly applied on offshore and WECs scaling problems. Therefore, Froude scaling model is applied to scale up the model to full scale.

The Froude number needs to keep constant between the laboratory model and the full scale model. Then, Froude number can be defined as follow:

$$Fr = \sqrt{\frac{\text{inertial force}}{\text{gravity force}}} = \frac{U_{lab}}{\sqrt{gL_{lab}}} = \frac{U_{full}}{\sqrt{gL_{full}}} = constant \tag{A.45}$$

Where L represents the length and the U the velocity, also the subscript $_{lab}$ represents the laboratory model and the $_{full}$ the full scale model.

Consequently, the full scale model is scaled up with a rate of 1 : 30 for all length parameters from the laboratory model, as the model tested at AAU facilities has that ratio from the full scale model. Then, $\lambda = 30$ and the rest of the scaling factor can be defined as it is shown on the following Table:

Parameter	Scaling factor	Value
Length	λ_L	30.00
Time	$\lambda_t = \sqrt{\lambda_L}$	5.48

Table A.2: Scaling factor parameter based on Froude law, see Appendix A.6

AAU setup and chamber configurations B

The following Figures illustrates the setup at AAU laboratory, [AAU, 2020], for the so-called AAU series 7 experiments with the chamber inside the wave basin and the chamber configurations set up that are used on this report.

First, Figures B.1 and B.2 illustrates the set up at AAU facilities were the experiments were conducted. The wave generators mean position, absorbing beach, the location of the chamber and the boundaries of the laboratory set up are illustrated on Figure B.1. A more detailed sketch of the experimental setup is presented on Figure B.2. In this Figure the location of all 33 wave gauges used for the measurement of the surface elevation is illustrated.

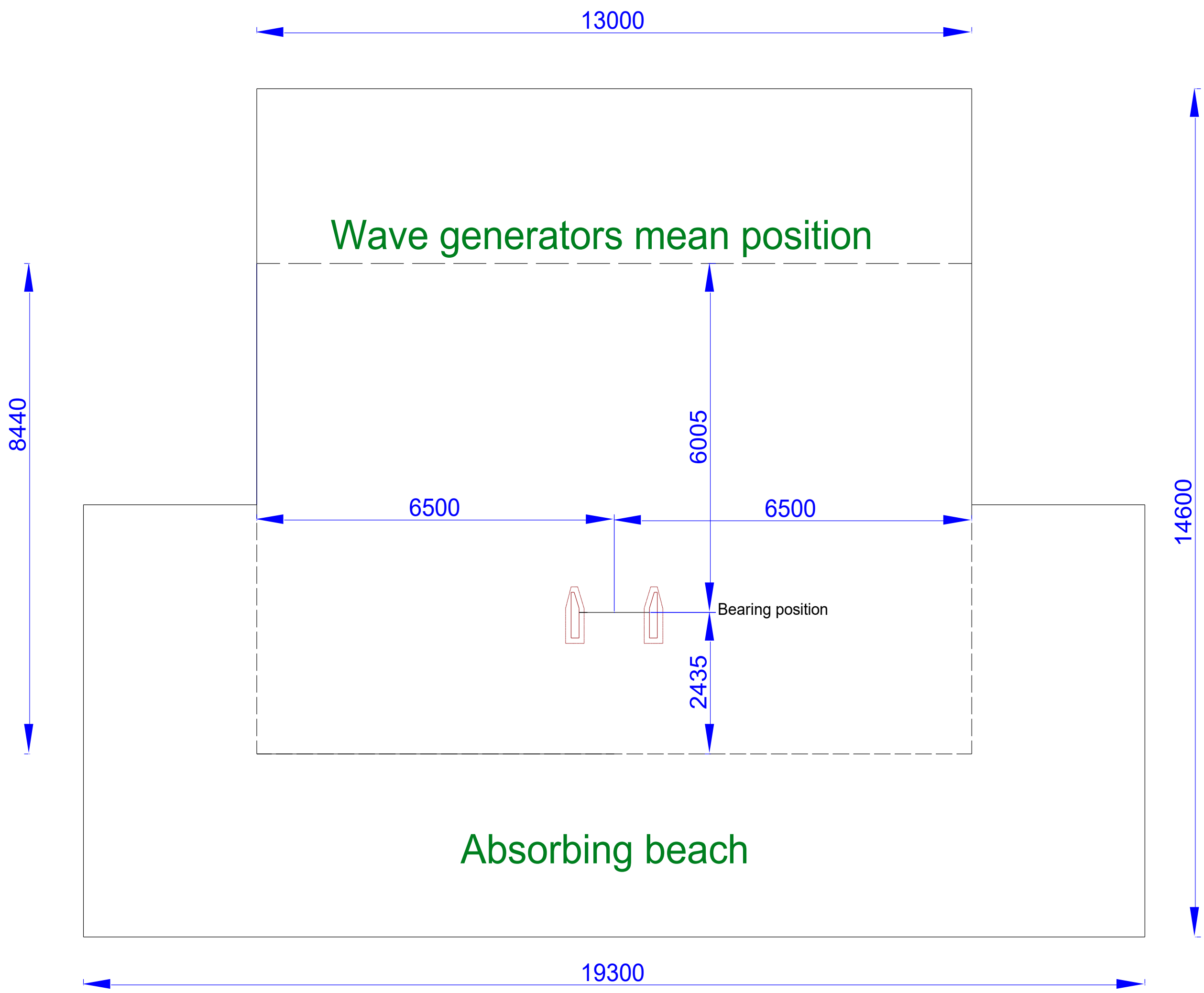

Figure B.1: Wave basin set up at AAU

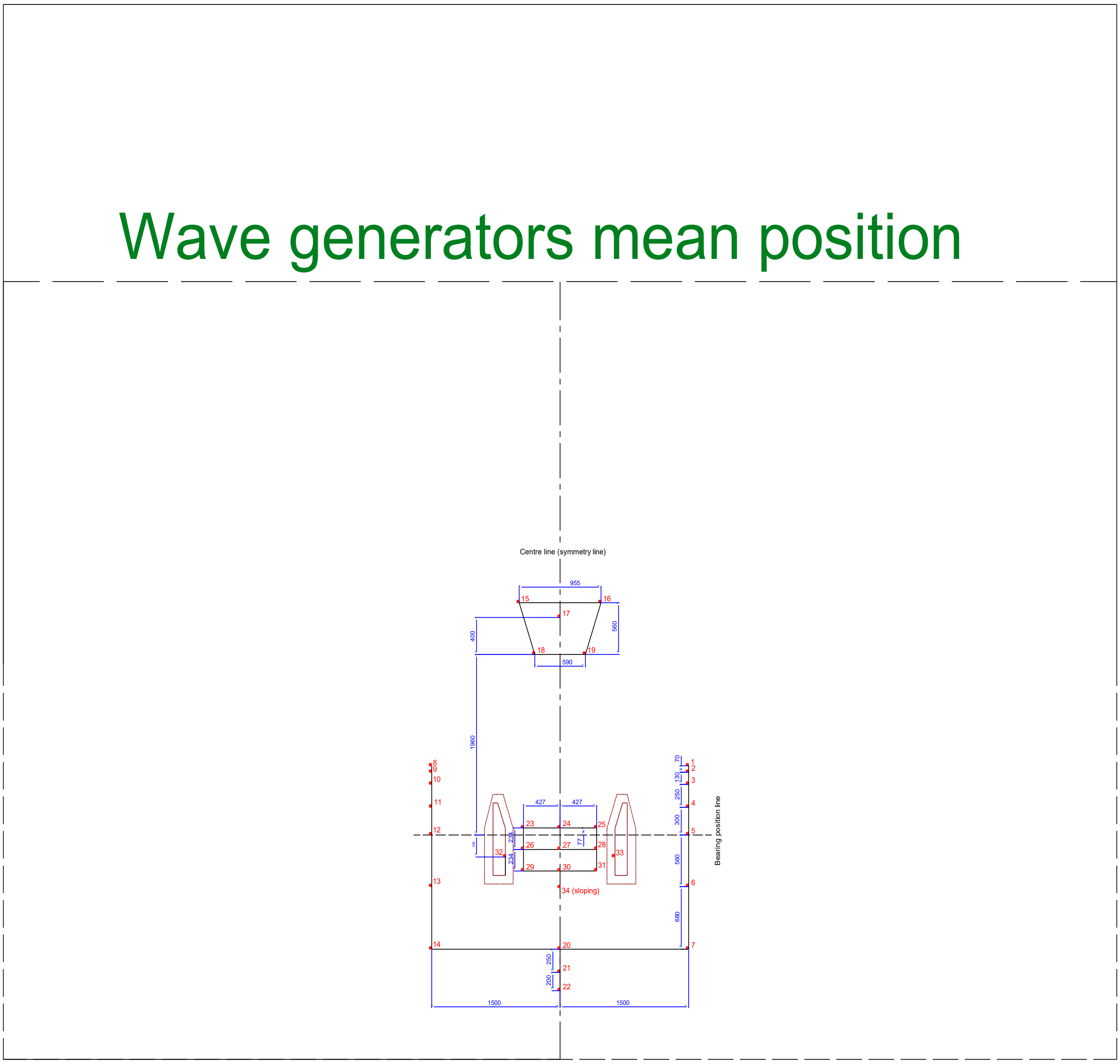

Figure B.2: Wave basin setup with the location of all WG used on the experiments

The following figures are and illustration of the chamber configuration used on this project. As indicated on Section 6 4 different chamber configurations are analyzed, where 3 of them, Figures B.3, B.4 and B.5, are modelled according to the specifications of the model from the experiments and 1, Figure B.6, is a modification of the A5 chamber (Figure B.4), where the spoiler is 1.5 times wider than the original configuration.

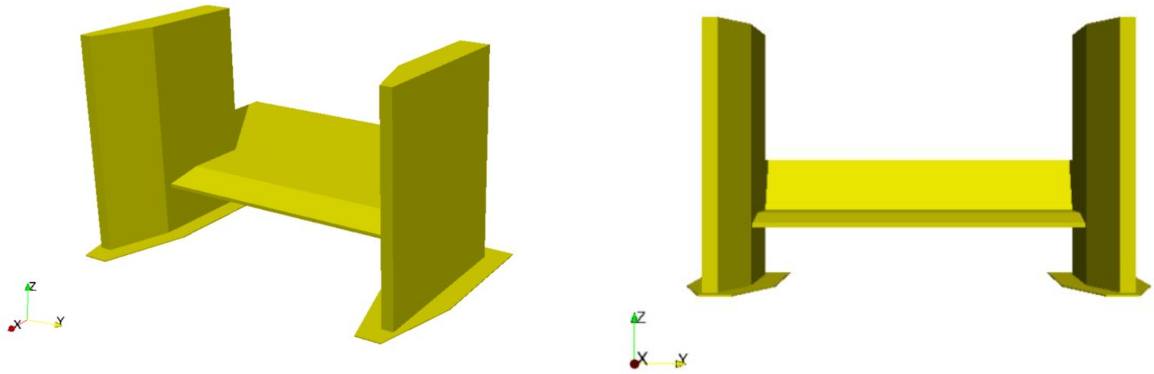

(a) (b)

Figure B.3: Recreation of A4 chamber configuration model on 3D from laboratory experiments at AAU - a) A4 configuration in perspective view; b) A4 configuration in front view

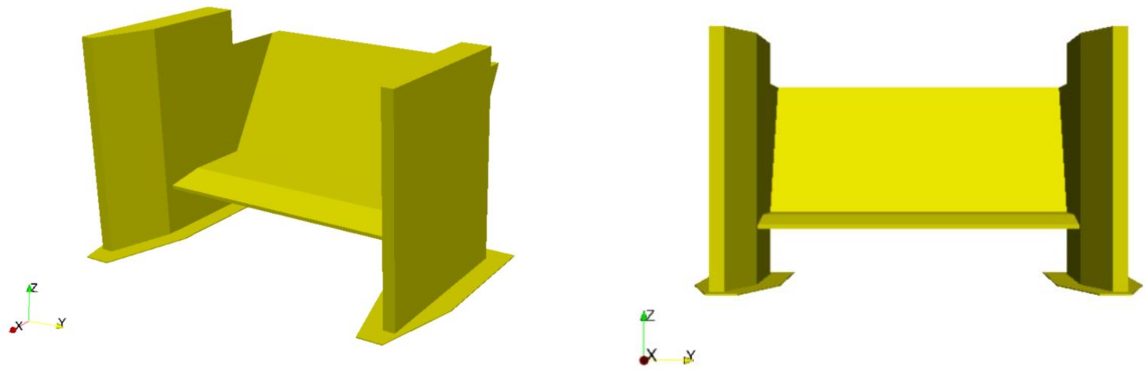

(a) (b)

Figure B.4: Recreation of A5 chamber configuration model on 3D from laboratory experiments at AAU - a) A5 configuration in perspective view; b) A5 configuration in front view

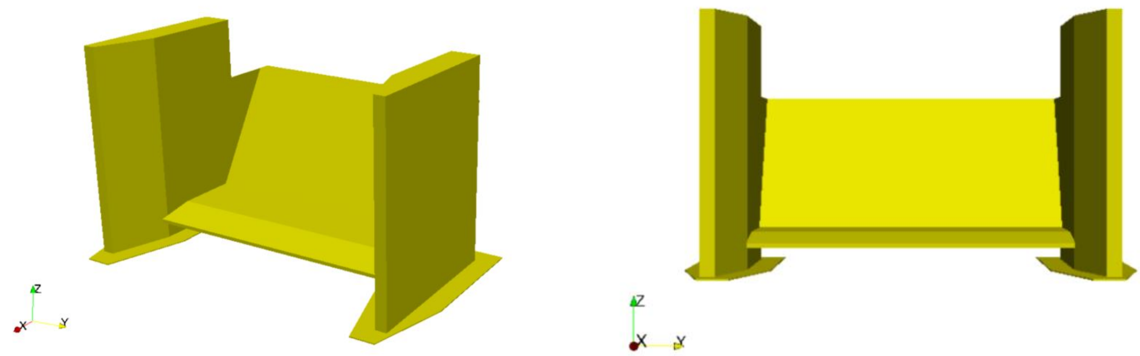

(a) (b)

Figure B.5: Recreation of A6 chamber configuration model on 3D from laboratory experiments at AAU - a) A6 configuration in perspective view; b) A6 configuration in front view

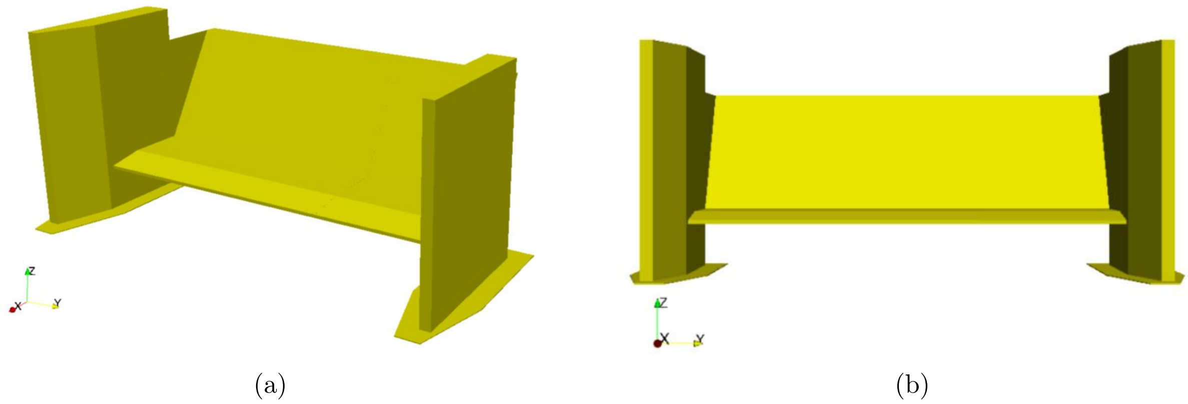

Figure B.6: Recreation of an A5 chamber configuration model with a spoiler 1.5 wider than the original A5 configuration - a) New A5 configuration in perspective view; b) New A5 configuration in front view

C Verification

C.1 Wave characteristics

Number No - [-]	Frequency f - [Hz]	Period T - [s]	Height H_{target} - [m]	Length λ - [m]	Steepness s - [%]	Depth h - [m]
1	0.40	2.50	0.04	7.0028	0.5712	1.00
2	0.50	2.00	0.04	5.2243	0.7656	1.00
3	0.60	1.67	0.04	3.9883	1.0029	1.00
4	0.70	1.43	0.04	3.0866	1.2959	1.00
5	0.80	1.25	0.04	2.4194	1.6533	1.00
6	0.85	1.18	0.04	2.1541	1.8569	1.00
7	0.90	1.11	0.04	1.9297	2.0729	1.00
8	0.95	1.05	0.04	1.7378	2.3018	1.00
9	1.00	1.00	0.04	1.5037	2.5473	1.00
10	1.05	0.95	0.04	1.4256	2.8057	1.00
11	1.10	0.91	0.04	1.3020	3.0772	1.00
12	1.15	0.87	0.04	1.1948	3.3477	1.00
13	1.20	0.83	0.04	1.0977	3.6441	1.00
14	1.30	0.77	0.04	0.9399	4.2557	1.00
15	1.40	0.71	0.04	0.8150	4.9077	1.00
16	1.50	0.67	0.04	0.7162	5.5849	1.00
17	1.00	1.00	0.02	1.5628	1.2797	1.00
18	1.00	1.00	0.06	1.5825	3.8044	1.00
19	1.00	1.00	0.08	1.5991	5.0029	1.00
20	1.00	1.00	0.10	1.6196	6.2282	1.00
21	0.70	1.43	0.02	3.0845	0.6484	1.00
22	0.70	1.43	0.06	3.0926	1.9401	1.00
23	0.70	1.43	0.08	3.1009	2.5799	1.00
24	0.70	1.43	0.10	3.1115	3.2139	1.00
25	0.50	2.00	0.02	5.2039	0.3843	1.00
26	0.50	2.00	0.06	5.2207	1.1493	1.00
27	0.50	2.00	0.08	5.2267	1.5306	1.00
28	0.50	2.00	0.10	5.2382	1.9090	1.00

Table C.1: Wave characteristics generated at AAU facilities

C.2 Spatial discretization for s=3.80

C.2.1 Spatial discretization - number of cells/H

In the following section some illustrations and results related to the spatial discretization over the wave height and $s = 3.80$ is described with a brief explanation.

Number of cells/H and 5 wave periods

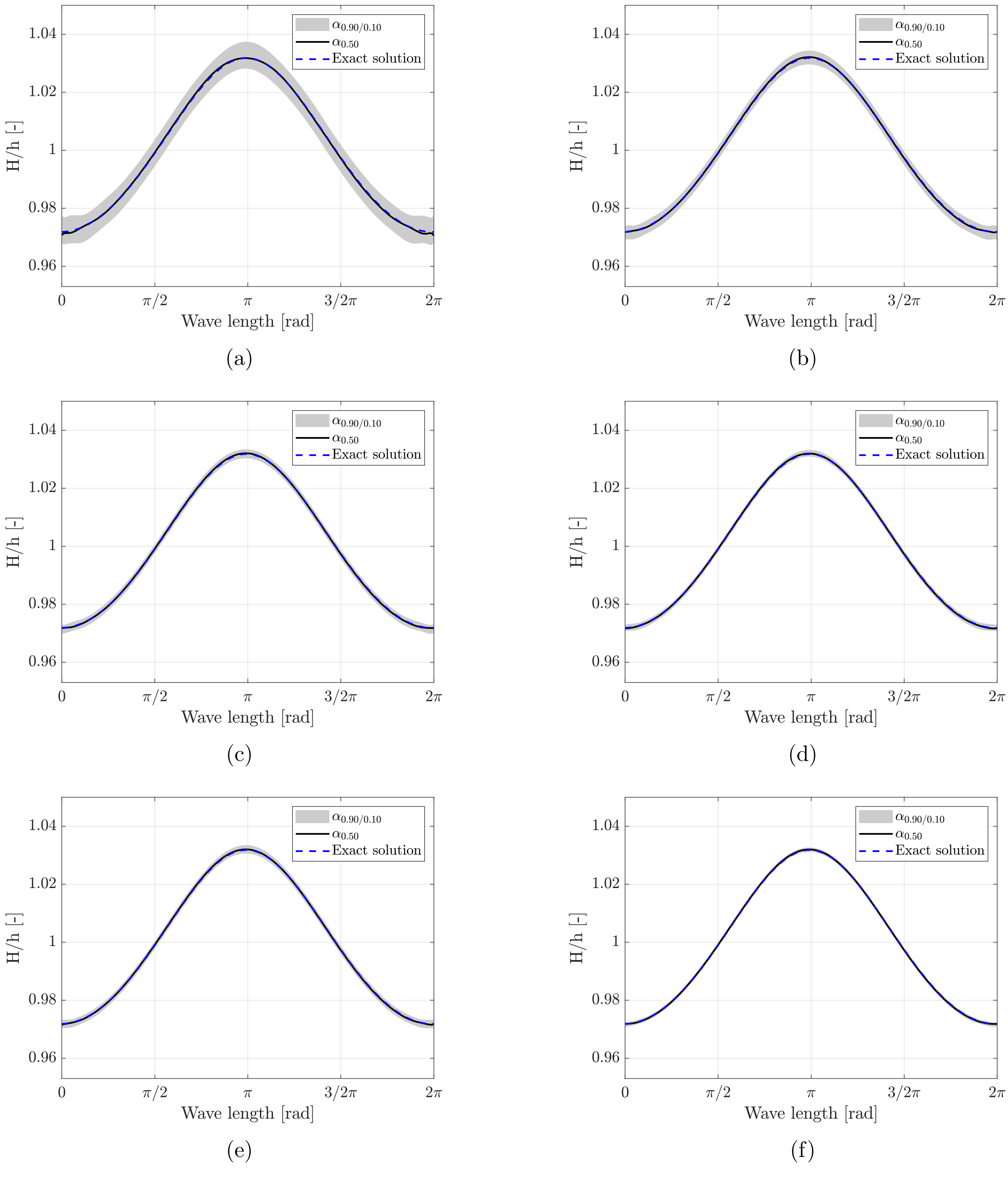

Figure C.1: Free surface elevation for different grids with analytical solution and $t/T = 5$ - a) Grid 1.1.1 b) Grid 1.2.1 c) Grid 1.3.1 d) Grid 1.4.1 e) Grid 1.5.1 f) Grid 1.6.1

Figure C.2 illustrates the phase delay at $t/T = 5$ between the analytical solution and the numerical calculations, which increases as t/T increases as it can be seen if Figure C.2 is compared with 4.4. This is caused due to the accumulative error on numerical errors.

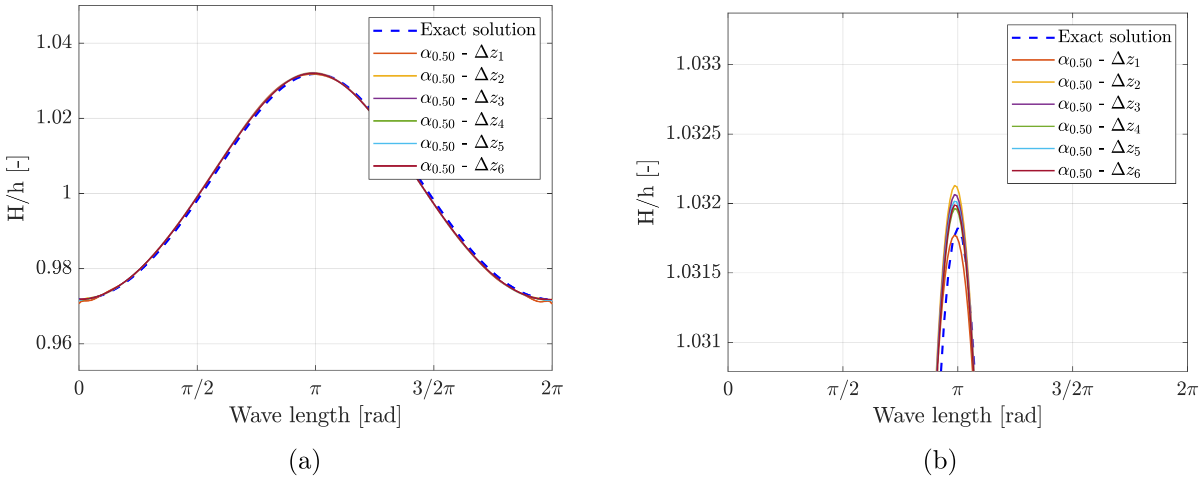

Figure C.2: Free surface elevation for $\alpha = 0.5$ and 5 different number of cells / H with analytical solution and $t/T = 5$ - a) 1 wave length, b) Detail of the wave crest

An illustration of the Richardson extrapolation and the estimated convergence rate for $\alpha = 0.50$ and $\alpha = 0.90/0.10$ and 10 wave periods is found in Figure 4.5. On one hand, for 5 periods with $\alpha = 0.90/0.10$ a behaviour close to an asymptotic convergence is achieved with a converge rate of $p = 1.05$. On the other hand, for $\alpha = 0.50$ the responses shows a converge rate of $P = 0.992$ for $t/T = 5$.

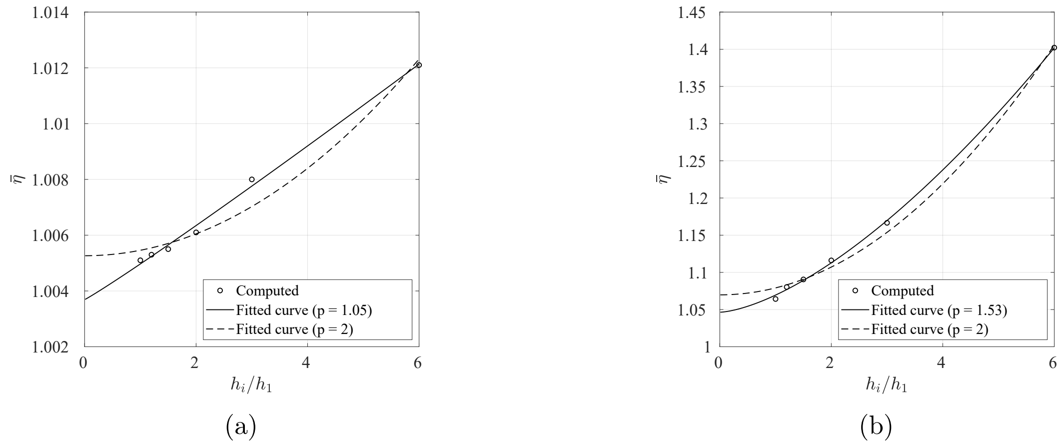

Figure C.3: Estimated convergence for the wave propagation of iso-surface for different number of cells/H - a) $t/T = 5$; $\alpha = 0.50$, b) $t/T = 5$; $\alpha = 0.10/0.90$

t/T	Grid	Grid 1.6.1	Grid 1.5.1	Grid 1.4.1	Grid 1.3.1	Grid 1.2.1	Grid 1.1.1
5	$\bar{\eta}_{0.50}$	1.0051	1.0053	1.0055	1.0061	1.0080	1.0121
	% diff	-	0.02	0.04	0.10	0.29	0.70
	$U_{\bar{\eta}_{0.50}}$	0.18	0.22	0.27	0.36	0.53	1.08
5	$\bar{\eta}_{0.90/0.10}$	1.0642	1.0803	1.0905	1.1161	1.1666	1.4022
	% diff	-	1.51	2.47	4.88	9.62	31.76
	$U_{\bar{\eta}_{0.90/0.10}}$	3.33	4.26	5.80	8.75	15.87	44.88

Table C.2: Spatial uncertainty for wave propagation over wave height with $s = 3.80$

C.2.2 Spatial discretization - number of cells/λ

Number of cells/λ and 5 wave periods

Figures C.4 represents the surface elevation for different iso-surfaces ($\alpha = 0.50$ and $\alpha = 0.90/0.10$) and the analytical solution for Stokes' V order, which is found to be enough to describe all cases under investigation. This Figures are fitted to be in phase with the analytical solution in order to make easier to compare both solutions.

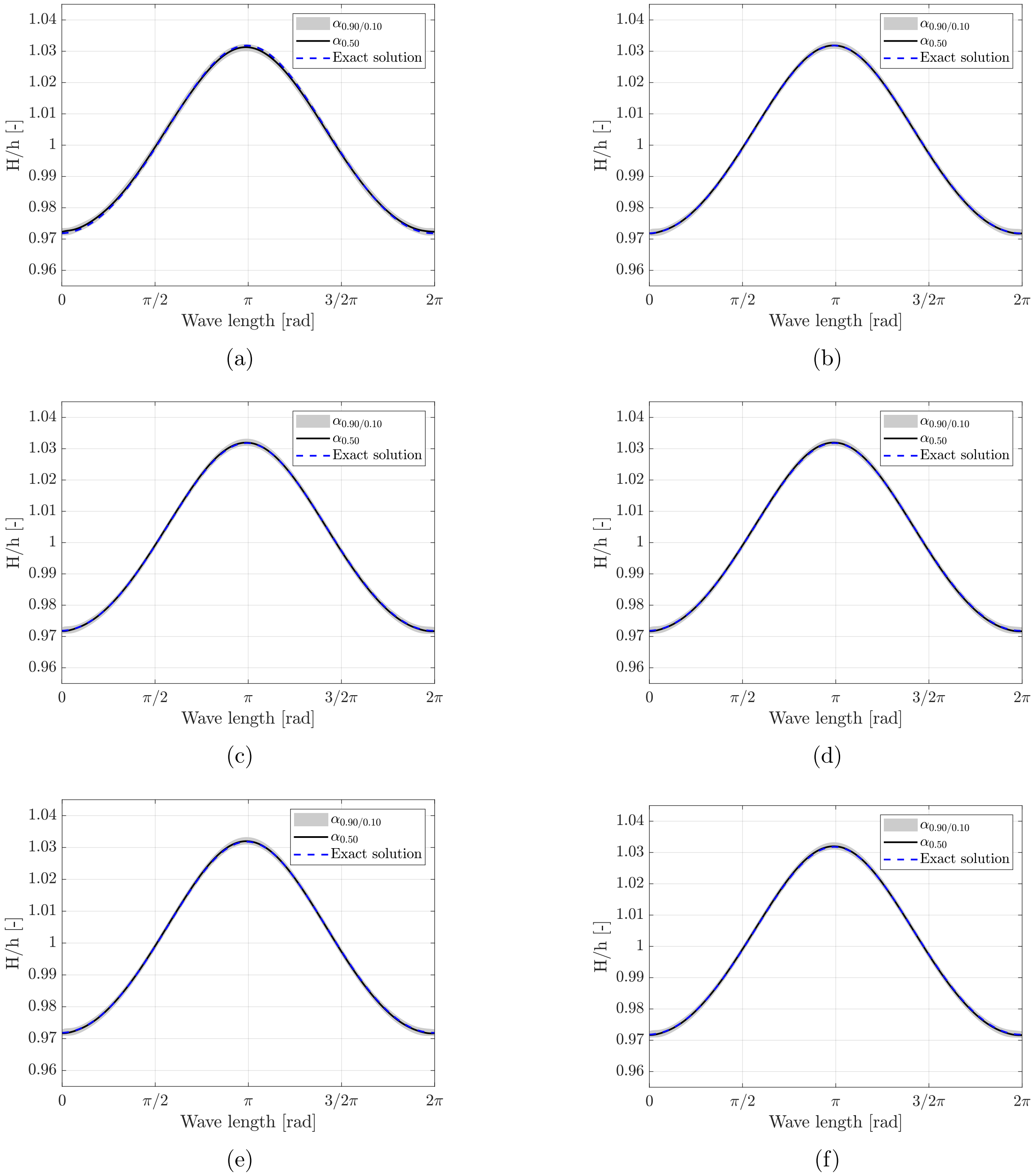

Figure C.4: Free surface elevation for different grids with analytical solution and $t/T = 5$ - a) Grid 2.1.1 b) Grid 2.2.1 c) Grid 2.3.1 d) Grid 2.4.1 e) Grid 2.5.1 f) Grid 2.6.1

Figure C.5 illustrates the phase delay at $t/T = 5$ between the analytical solution and the numerical calculations, which increases as t/T increases. This is caused due to the accumulative error on numerical errors.

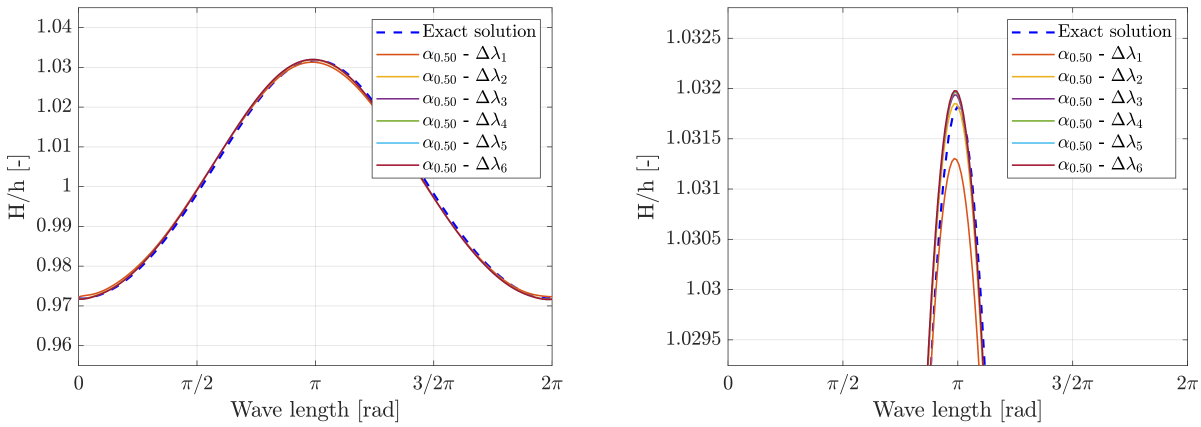

(a) (b)

Figure C.5: Free surface elevation for $\alpha = 0.5$ and 5 different number of cells / λ with analytical solution and $t/T = 10$ - a) 1 wave length, b) Detail of the wave crest

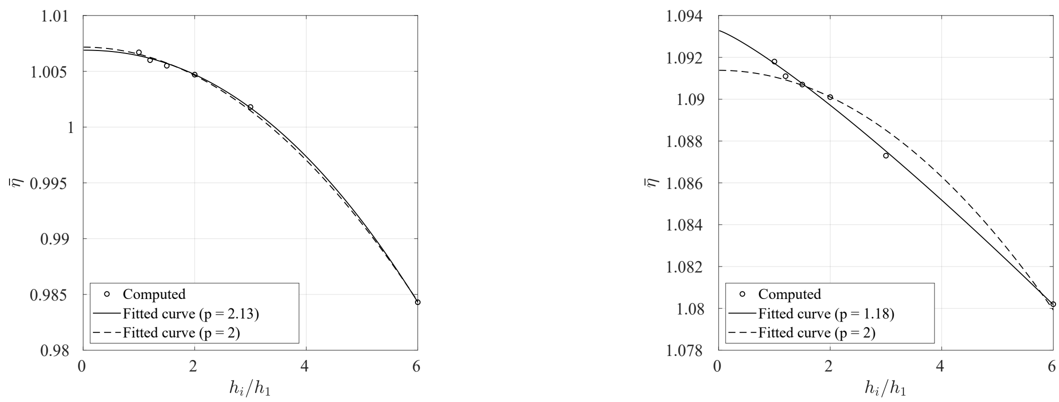

(a) (b)

Figure C.6: Estimated convergence for the wave propagation of iso-surface for different number of cells $/\lambda$ - a) $t/T = 5$; $\alpha = 0.50$, b) $t/T = 5$; $\alpha = 0.10/0.90$

t/T	Grid	Grid 2.6.1	Grid 2.5.1	Grid 2.4.1	Grid 2.3.1	Grid 2.2.1	Grid 2.1.1
5	$\bar{\eta}_{0.50}$	1.0067	1.0060	1.0055	1.0047	1.0018	0.9843
	% diff	-	0.07	0.12	0.20	0.49	2.23
	$U_{\bar{\eta}_{0.50}}$	0.22	0.30	0.46	0.79	1.74	6.87
5	$\bar{\eta}_{0.90/0.10}$	1.0918	1.0911	1.0907	1.0901	1.0873	1.0802
	% diff	-	0.06	0.10	0.16	0.41	1.06
	$U_{\bar{\eta}_{0.90/0.10}}$	0.23	0.27	0.35	0.48	0.75	1.67

Table C.3: Spatial uncertainty for wave propagation over wave length with $s = 3.80$

Number of cells/λ and 10 wave periods

Figures C.7 represents the surface elevation for different iso-surfaces ($\alpha = 0.50$ and $\alpha = 0.90/0.10$) and the analytical solution for Stokes' V order, which is found to be enough to describe all cases under investigation. This Figures are fitted to be in phase with the analytical solution in order to make easier to compare both solutions.

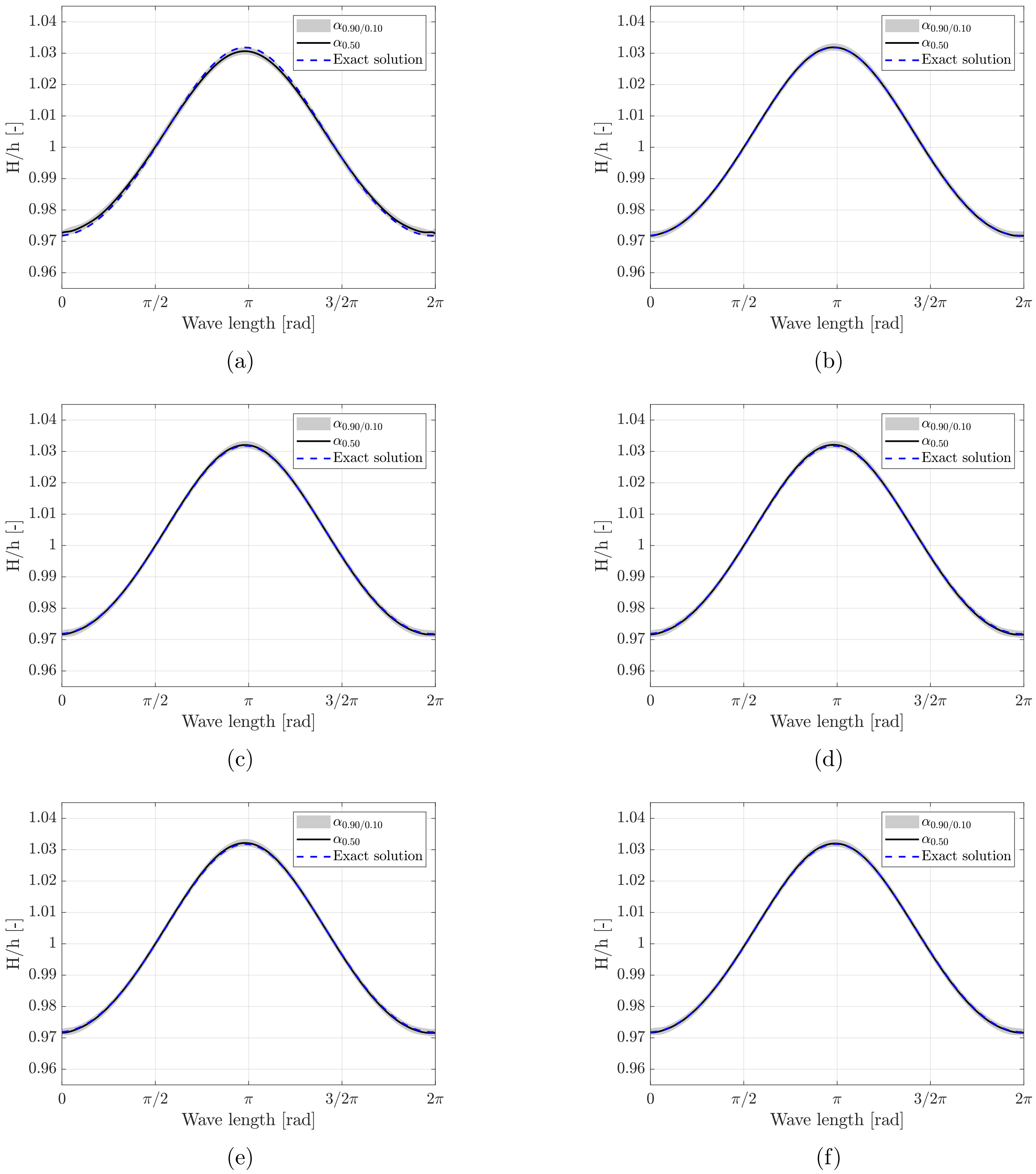

Figure C.7: Free surface elevation for different grids with analytical solution and $t/T = 10$ - a) Grid 2.1.1 b) Grid 2.2.1 c) Grid 2.3.1 d) Grid 2.4.1 e) Grid 2.5.1 f) Grid 2.6.1

Figure C.8 illustrates the phase delay at $t/T = 10$ between the analytical solution and the numerical calculations, which increases as t/T increases. This is caused due to the accumulative error on numerical errors.

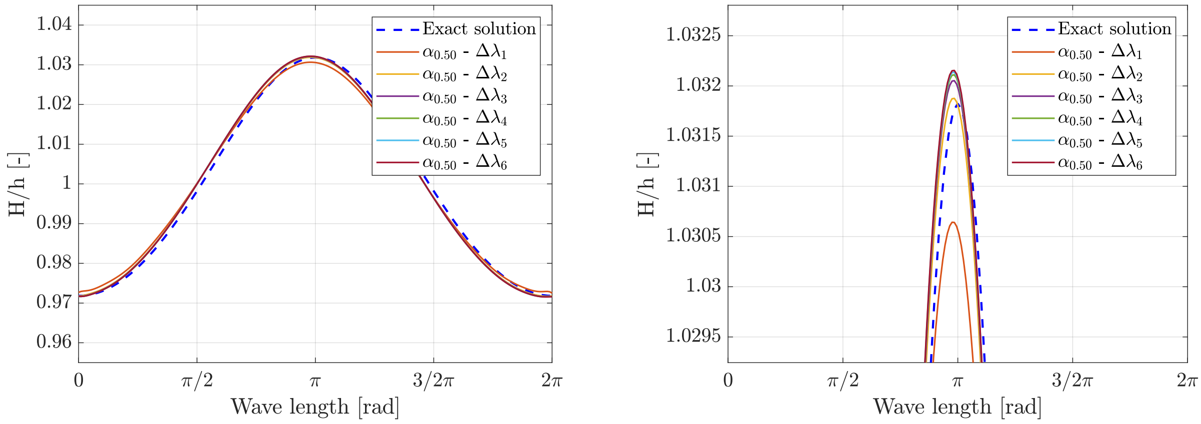

(a) (b)

Figure C.8: Free surface elevation for $\alpha = 0.5$ and 5 different number of cells / λ with analytical solution and $t/T = 10$ - a) 1 wave length, b) Detail of the wave crest

C.3 Spatial discretization for s=6.23

C.3.1 Spatial discretization - number of cells/H

For $s = 6.23$ the cells/λ can not keep constant due to some instabilities on the simulation that make it to break, therefore a range of values that goes from 150 to 650 is used depending on the cells/H.

Steepness	Grid	Cells/λ	Cells/H	Cells	Aspect ratio	Reference ratio[1]	Normalized run time[2]
6.23	Grid 1.1.2	150	10	9.000	1.08	6.00	1.00[4]
	Grid 1.2.2	200	20	24.000	1.62	3.00	2.49
	Grid 1.3.2	320	30	57.600	1.52	2.00	5.36
	Grid 1.4.2	475	40	114.000	1.37	1.50	8.96
	Grid 1.5.2	600	50	180.000	1.35	1.20	12.59
	Grid 1.6.2	650	60	234.000	1.50	1.00	15.03

Table C.4: Grid characteristics for case of different cells/H - [1]: rate between the maximum cells/H and the one for the grid under investigation. - [2]: ratio between the minimum computational time and the one corresponding to the selected grid - [4] run time of 2.45 hours

Number of cells/H and 5 wave periods

Figures C.9 represents the surface elevation for different iso-surfaces ($\alpha = 0.50$ and $\alpha = 0.90/0.10$) and the analytical solution for Stokes' V order, which is found to be enough to describe all cases under investigation. This Figures are fitted to be in phase with the analytical solution in order to make easier to compare both solutions. This Figures are fitted to be in phase with the analytical solution in order to make easier to compare both solutions.

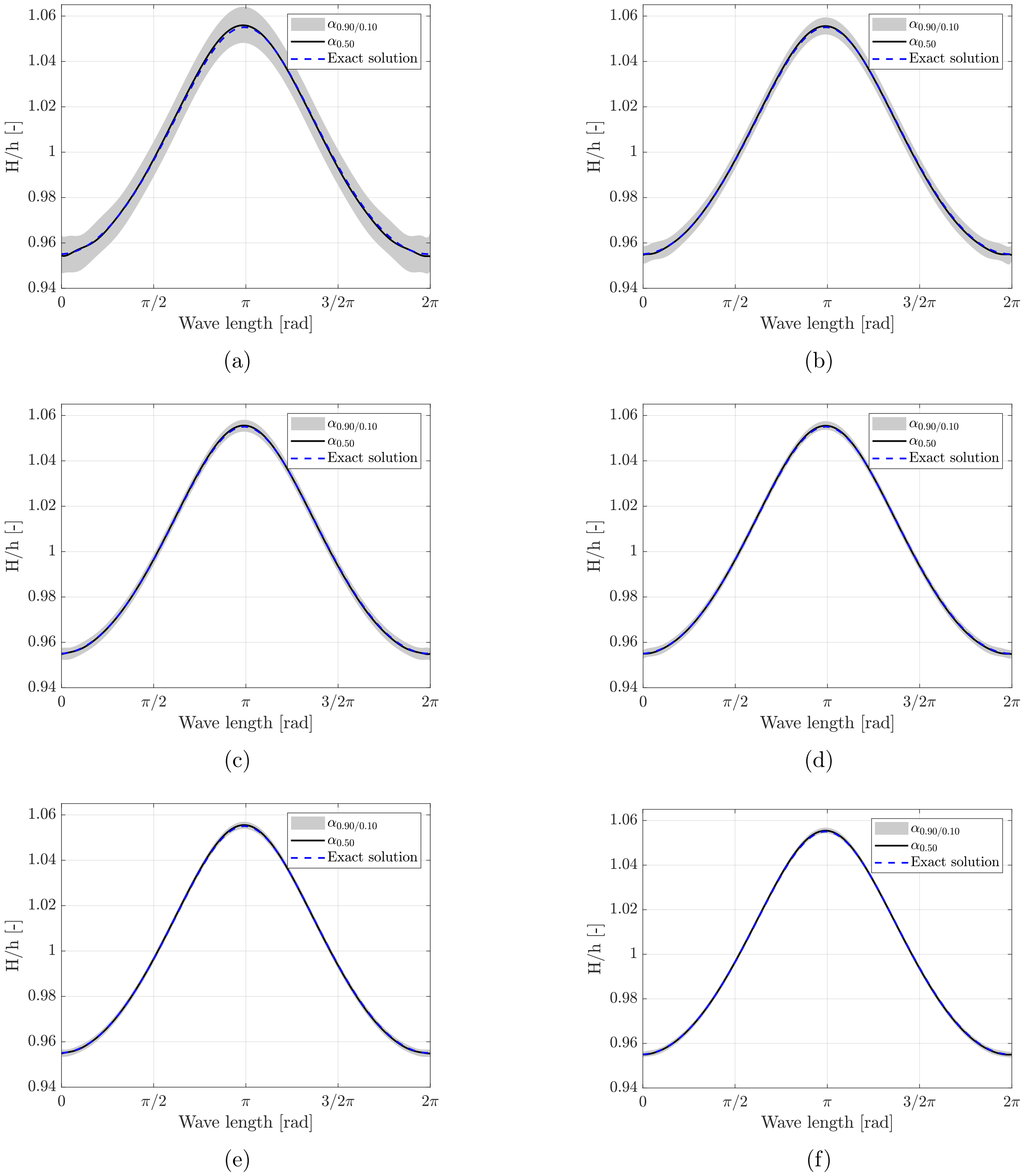

Figure C.9: Free surface elevation for different grids with analytical solution and $t/T = 5$ - a) Grid 1.1.2 b) Grid 1.2.2 c) Grid 1.3.2 d) Grid 1.4.2 e) Grid 1.5.2 f) Grid 1.6.2

Figure C.10 illustrates the phase delay at $t/T = 5$ between the analytical solution and the numerical calculations, which increases as t/T increases. This is caused due to the accumulative error on numerical errors.

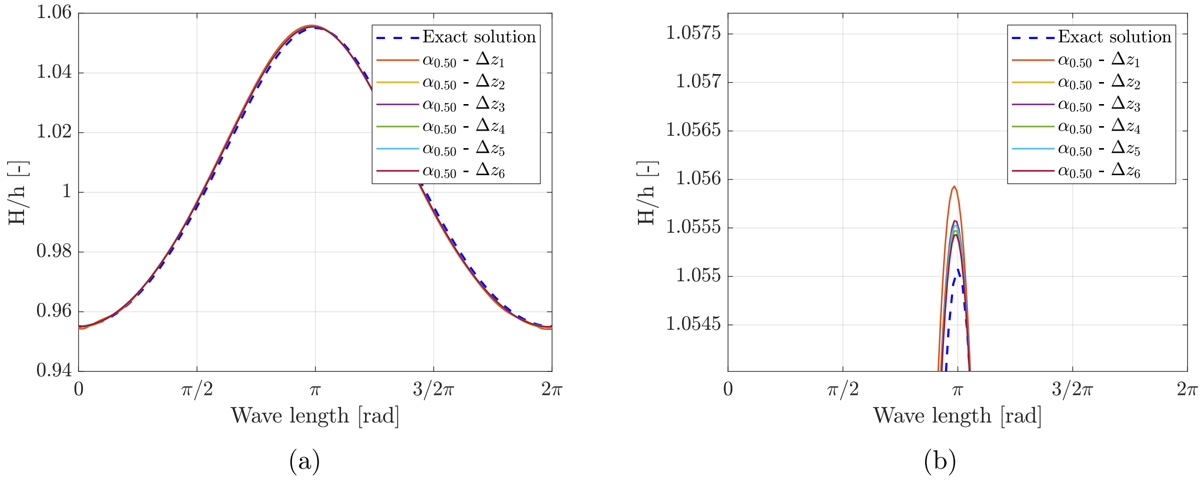

Figure C.10: Free surface elevation for $\alpha = 0.5$ and 5 different number of cells / H with analytical solution and $t/T = 5$ - a) 1 wave length, b) Detail of the wave crest

t/T	Grid	Grid 1.6.2	Grid 1.5.2	Grid 1.4.2	Grid 1.3.2	Grid 1.2.2	Grid 1.1.2
5	$\bar{\eta}_{0.50}$	1.0067	1.0103	1.0082	1.0122	1.0098	1.0230
	% diff	-	0.36	0.15	0.55	0.31	1.62
	$U_{\bar{\eta}_{0.50}}$	0.36	0.41	0.51	0.73	1.34	4.65
5	$\bar{\eta}_{0.90/0.10}$	1.0527	1.0718	1.0762	1.1408	1.4086	1.3690
	% diff	-	2.14	2.36	7.17	8.61	35.13
	$U_{\bar{\eta}_{0.90/0.10}}$	3.84	4.59	5.89	8.55	15.56	48.64

Table C.5: Spatial uncertainty for wave propagation over wave height with $s = 6.23$

Number of cells/H and 10 wave periods

Figures C.11 represents the surface elevation for different iso-surfaces ($\alpha = 0.50$ and $\alpha = 0.90/0.10$) and the analytical solution for Stokes' V order, which is found to be enough to describe all cases under investigation. This Figures are fitted to be in phase with the analytical solution in order to make easier to compare both solutions.

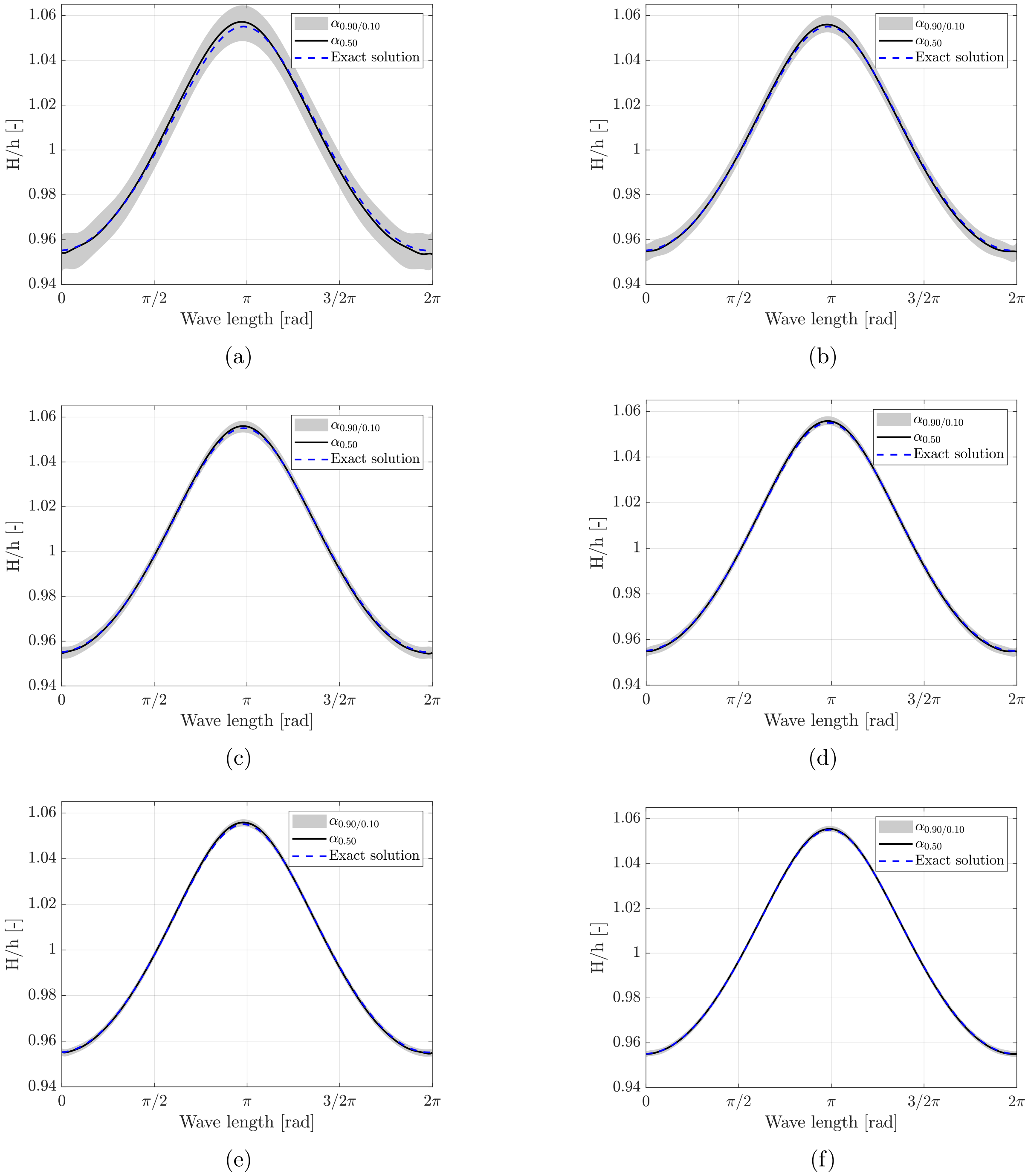

Figure C.11: Free surface elevation for different grids with analytical solution and $t/T = 10$ - a) Grid 1.1.2 b) Grid 1.2.2 c) Grid 1.3.2 d) Grid 1.4.2 e) Grid 1.5.2 f) Grid 1.6.2

Figure C.12 illustrates the phase delay at $t/T = 10$ between the analytical solution and the numerical calculations, which increases as t/T increases. This is caused due to the accumulative error on numerical errors.

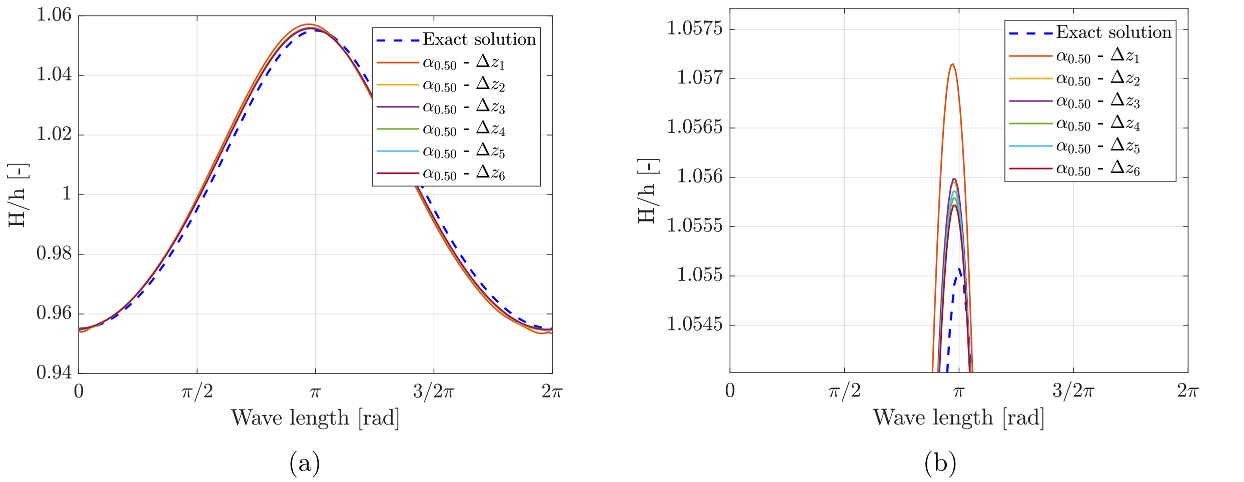

Figure C.12: Free surface elevation for $\alpha = 0.5$ and 5 different number of cells / H with analytical solution and $t/T = 10$ - a) 1 wave length, b) Detail of the wave crest

Figure C.13 shows the Richardson extrapolation of the different grids for the analysis of the convergence conducted for the numbers of cells/H.

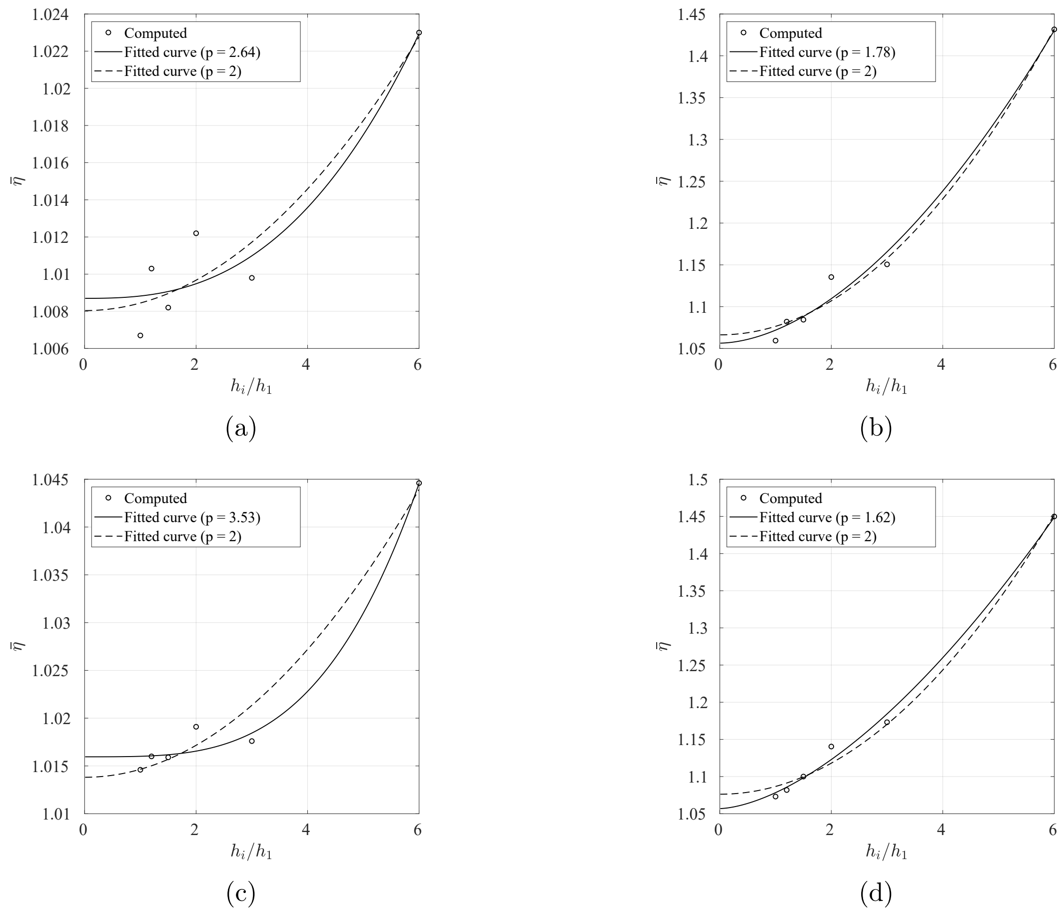

Figure C.13: Estimated convergence for the wave propagation of iso-surface for different number of cells/H - a) $t/T = 5$; $\alpha = 0.50$, b) $t/T = 5$; $\alpha = 0.10/0.90$ c) $t/T = 10$; $\alpha = 0.50$, d) $t/T = 10$; $\alpha = 0.10/0.90$

Figures C.14 and C.15 shows the wave kinematics profile from numerical calculations and from analytical methods for 4 different grids.

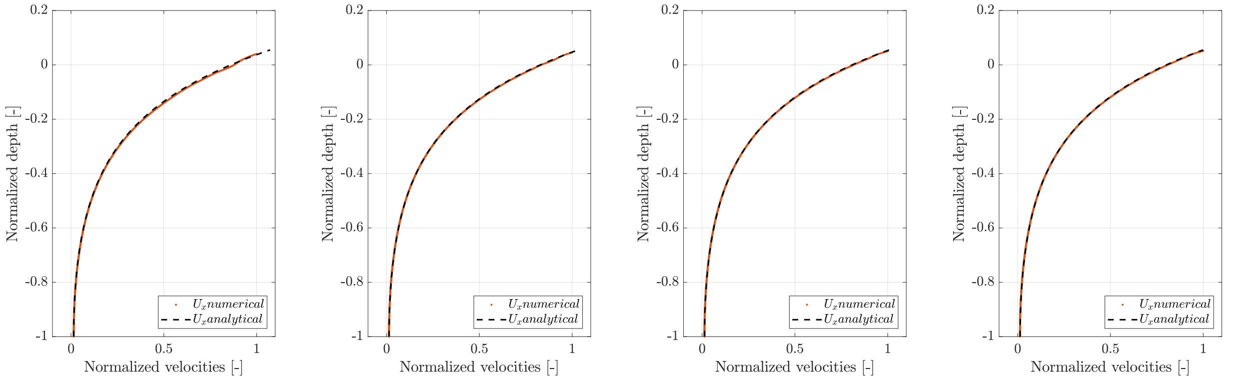

(a) (b) (c) (d)

Figure C.14: Maximum horizontal velocity profile over depth for 10 wave periods - a) 10 cells/H b) 20 cells/H c) 30 cells/H d) 40 cells/H

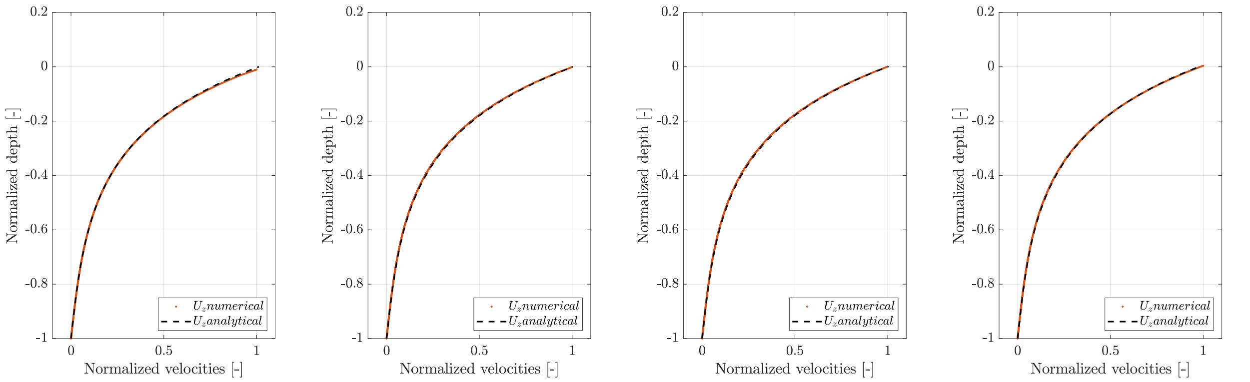

(a) (b) (c) (d)

Figure C.15: Maximum vertical velocity profile over depth for 10 wave periods - a) 10 cells/H b) 20 cells/H c) 30 cells/H d) 40 cells/H

t/T	Grid	Grid 1.6.2	Grid 1.5.2	Grid 1.4.2	Grid 1.3.2	Grid 1.2.2	Grid 1.1.2
10	$\bar{\eta}_{0.50}$	1.0146	1.0160	1.0159	1.0191	1.0176	1.0446
	% diff	-	0.14	0.13	0.44	0.30	2.96
	$U_{\bar{\eta}_{0.50}}$	0.50	0.61	0.82	1.26	2.51	9.29
10	$\bar{\eta}_{0.90/0.10}$	1.0585	1.0659	1.0841	1.1213	1.1555	1.4053
	% diff	-	0.82	2.51	6.27	9.32	35.11
	$U_{\bar{\eta}_{0.90/0.10}}$	3.94	4.86	6.43	9.51	17.18	50.25

Table C.6: Spatial uncertainty for wave propagation over wave height with $s = 6.23$

C.3.2 Spatial discretization - number of cells/λ

Next, on Table C.7 the characteristics of 5 grids for $s = 6.23$ that are setup for the analysis of the spatial discretization over the wave length are presented.

Steepness	Grid	Cells/λ	Cells/H	Cells	Aspect ratio	Reference ratio[1]	Normalized run time[2]
6.23	Grid 2.1.2	100	40	24.000	6.48	6.00	1.00[4]
	Grid 2.2.2	200	40	48.000	3.24	3.00	1.79
	Grid 2.3.2	300	40	72.000	2.16	2.00	2.74
	Grid 2.4.2	400	40	96.000	1.62	1.50	3.48
	Grid 2.5.2	500	40	120.000	1.29	1.20	4.13

Table C.7: Grid characteristics for case of different cells/λ - [1]: rate between the maximum cells/λ and the one for the grid under investigation. - [2]: ratio between the minimum computational time and the one corresponding to the selected grid - [4] run time of 5.12 hours

Number of cells/λ and 5 wave periods

Figures C.16 represents the surface elevation for different iso-surfaces ($\alpha = 0.50$ and $\alpha = 0.90/0.10$) and the analytical solution for Stokes' V order, which is found to be enough to describe all cases under investigation. This Figures are fitted to be in phase with the analytical solution in order to make easier to compare both solutions.

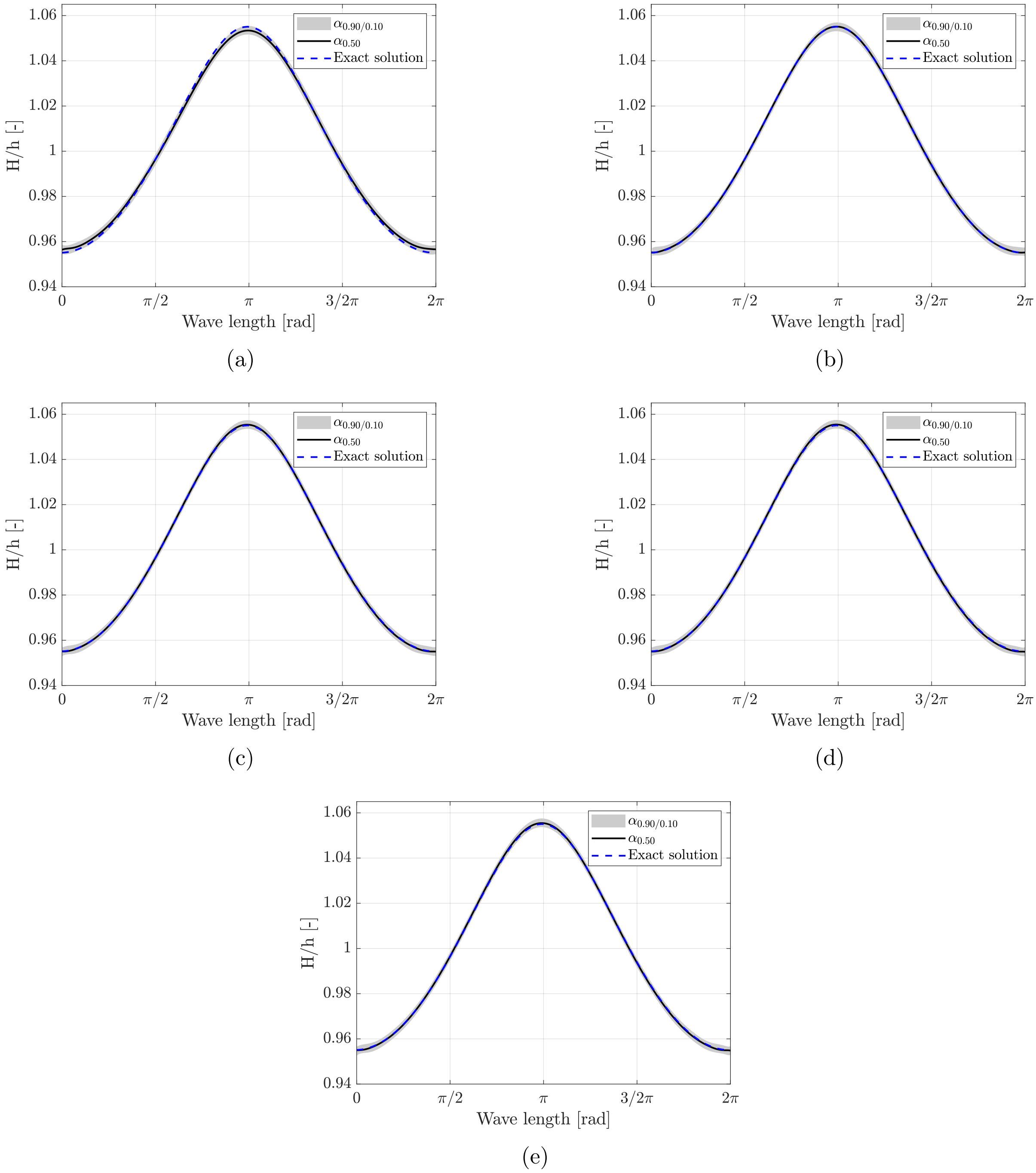

Figure C.16: Free surface elevation for different grids with analytical solution and $t/T = 5$ - a) Grid 2.1 b) Grid 2.2 c) Grid 2.3 d) Grid 2.4 e) Grid 2.5

Figure C.17 illustrates the phase delay at $t/T = 5$ between the analytical solution and the numerical calculations, which increases as t/T increases. This is caused due to the accumulative error on numerical errors.

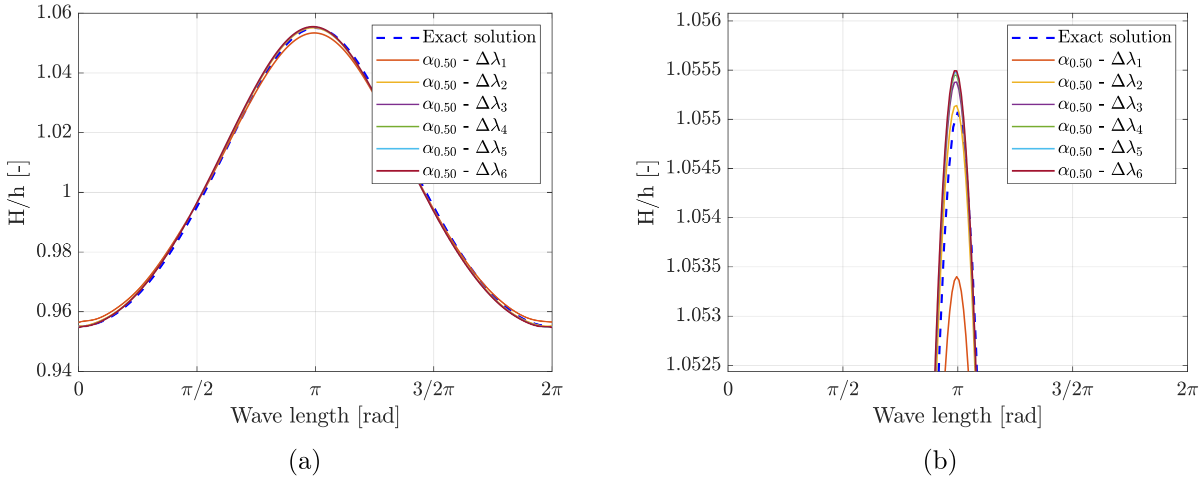

Figure C.17: Free surface elevation for $\alpha = 0.5$ and 5 different number of cells / λ with analytical solution and $t/T = 10$ - a) 1 wave length, b) Detail of the wave crest

Number of cells/λ and 10 wave periods

Figures C.18 represents the surface elevation for different iso-surfaces ($\alpha = 0.50$ and $\alpha = 0.90/0.10$) and the analytical solution for Stokes' V order, which is found to be enough to describe all cases under investigation. This Figures are fitted to be in phase with the analytical solution in order to make easier to compare both solutions.

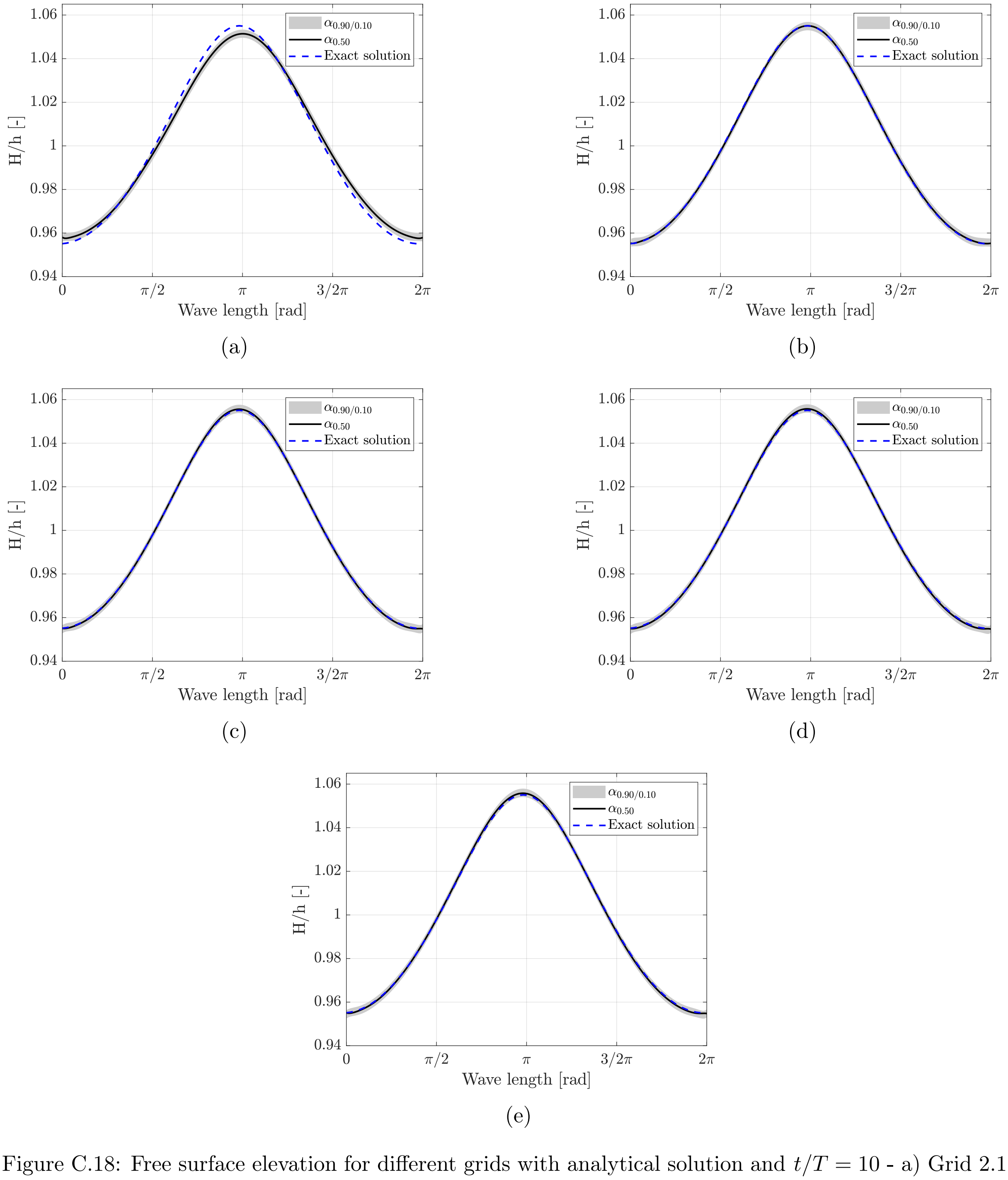

Figure C.18: Free surface elevation for different grids with analytical solution and $t/T = 10$ - a) Grid 2.1 b) Grid 2.2 c) Grid 2.3 d) Grid 2.4 e) Grid 2.5

Figure C.19 illustrates the phase delay at $t/T = 10$ between the analytical solution and the numerical calculations, which increases as t/T increases. This is caused due to the accumulative error on numerical errors.

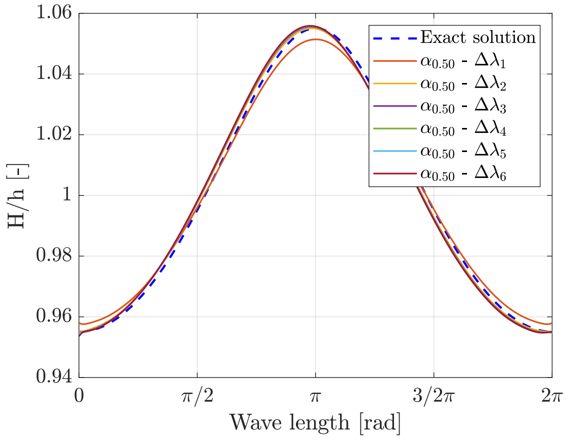

(a)

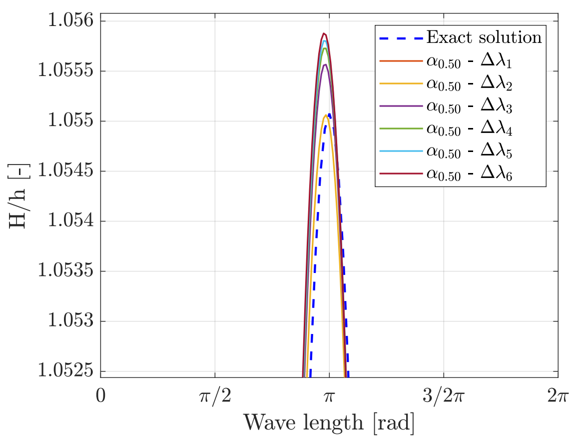

(b)

Figure C.19: Free surface elevation for $\alpha = 0.5$ and 5 different number of cells / λ with analytical solution and $t/T = 10$ - a) 1 wave length, b) Detail of the wave crest

Figure C.20 shows the Richardson extrapolation of the different grids for the analysis of the convergence conducted for the numbers of cells/λ.

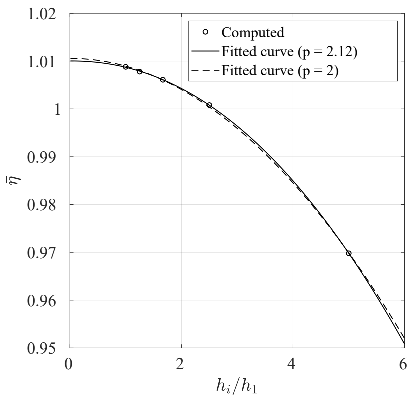

(a)

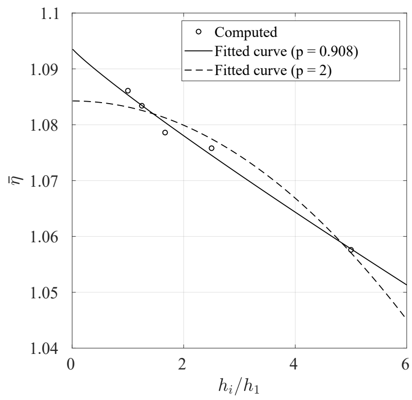

(b)

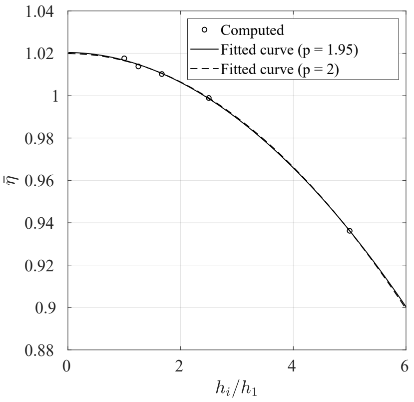

(c)

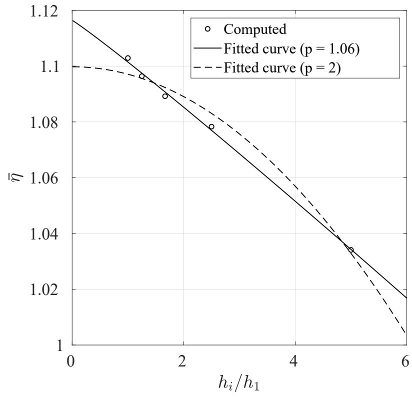

(d)

Figure C.20: Estimated convergence for the wave propagation of iso-surface for different number of cells /λ - a) $t/T = 5$; $\alpha = 0.50$, b) $t/T = 5$; $\alpha = 0.10/0.90$ c) $t/T = 10$; $\alpha = 0.50$, d) $t/T = 10$; $\alpha = 0.10/0.90$

Figures C.21 and C.22 shows the wave kinematics profile from numerical calculations and from analytical methods for 4 different grids.

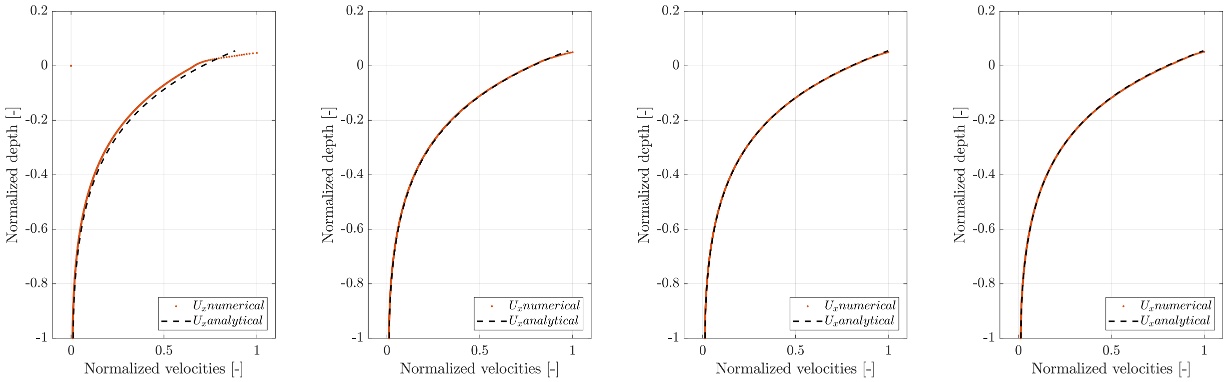

(a) (b) (c) (d)

Figure C.21: Maximum horizontal velocity profile over depth for 10 wave periods - a) 100 cells/λ b) 200 cells/λ c) 300 cells/λ d) 400 cells/λ

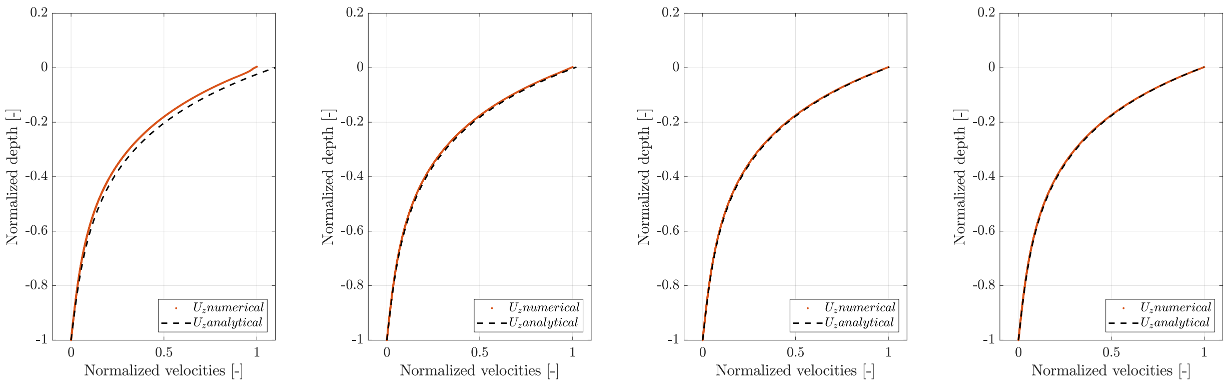

(a) (b) (c) (d)

Figure C.22: Maximum vertical velocity profile over depth for 10 wave periods - a) 100 cells/λ b) 200 cells/λ c) 300 cells/λ d) 400 cells/λ

t/T	Grid	Grid 2.5.2	Grid 2.4.2	Grid 2.3.2	Grid 2.2.2	Grid 2.1.2
5	$\bar{\eta}_{0.50}$	1.0088	1.0078	1.0061	1.0008	0.9698
	% diff	-	0.09	0.27	0.79	3.87
	$U_{\bar{\eta}_{0.50}}$	0.52	0.80	1.39	3.09	12.24
5	$\bar{\eta}_{0.90/0.10}$	1.0773	1.0756	1.0725	1.0750	1.0878
	% diff	-	0.15	0.36	1.14	3.32
	$U_{\bar{\eta}_{0.90/0.10}}$	0.80	1.02	1.43	2.32	5.38
10	$\bar{\eta}_{0.50}$	1.0176	1.0138	1.0102	0.9989	0.9362
	% diff	-	0.37	0.73	1.84	8.00
	$U_{\bar{\eta}_{0.50}}$	0.55	0.80	1.33	2.82	10.61
10	$\bar{\eta}_{0.90/0.10}$	1.0853	1.0826	1.0790	1.0794	1.0979
	% diff	-	0.59	1.24	2.23	6.24
	$U_{\bar{\eta}_{0.90/0.10}}$	2.06	2.56	3.40	5.13	10.46

Table C.8: Spatial uncertainty for wave propagation over wave length with $s = 6.23$

C.4 Temporal discretization for s=3.80

Δt and 5 wave periods

Figures C.23 represents the surface elevation for different iso-surfaces ($\alpha = 0.50$ and $\alpha = 0.90/0.10$) and the analytical solution for Stokes' V order, which is found to be enough to describe all cases under investigation. This Figures are fitted to be in phase with the analytical solution in order to make easier to compare both solutions.

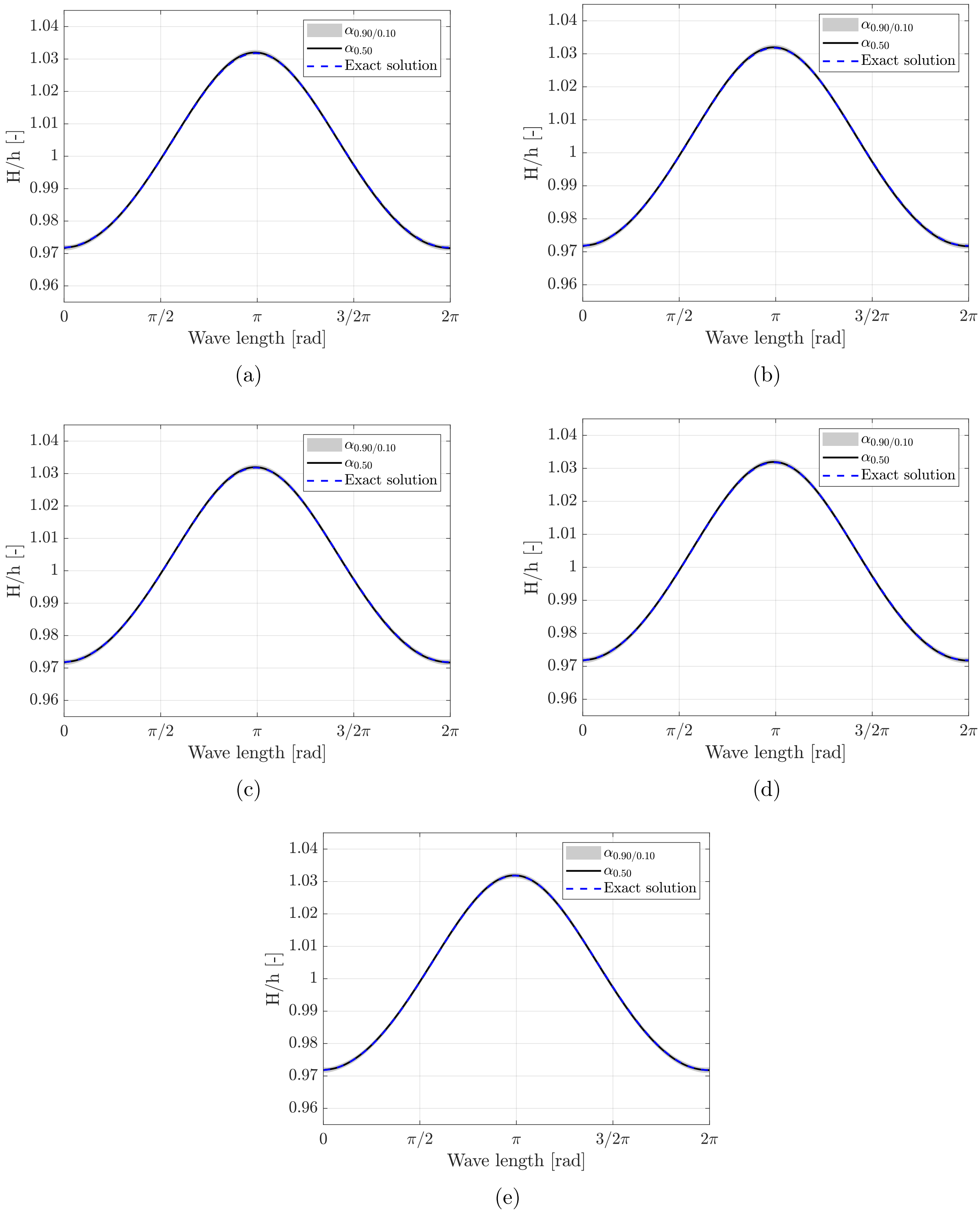

Figure C.23: Free surface elevation for different Δt with analytical solution and $t/T = 5$

Figure C.24 illustrates the phase delay at $t/T = 5$ between the analytical solution and the numerical calculations, which increases as t/T increases. This is caused due to the accumulative error on numerical errors.

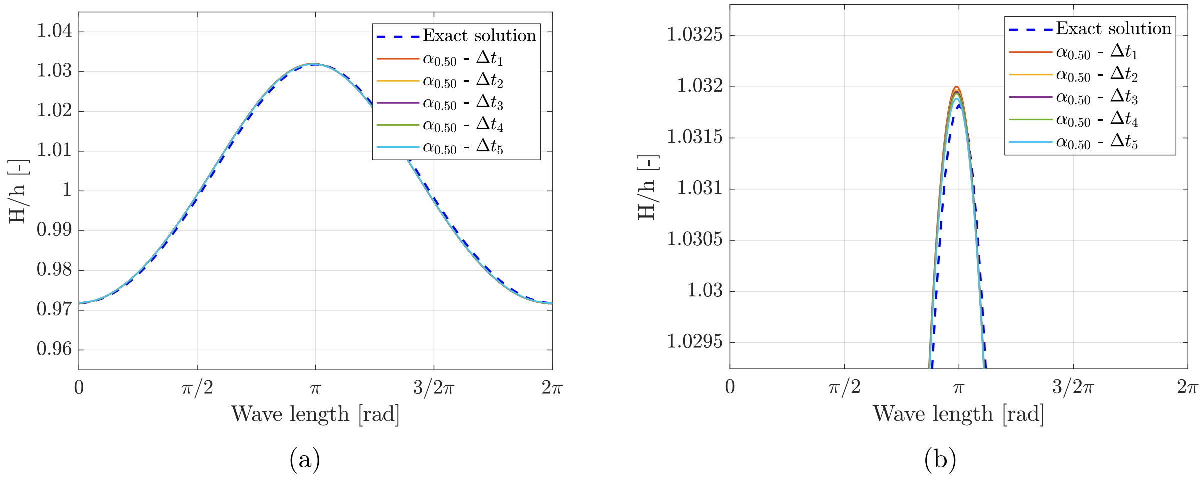

Figure C.24: Estimated convergence for the wave propagation of iso-surface and $t/T = 5$ for different Δt - a) $\alpha = 0.50$, b) $\alpha = 0.10/0.90$

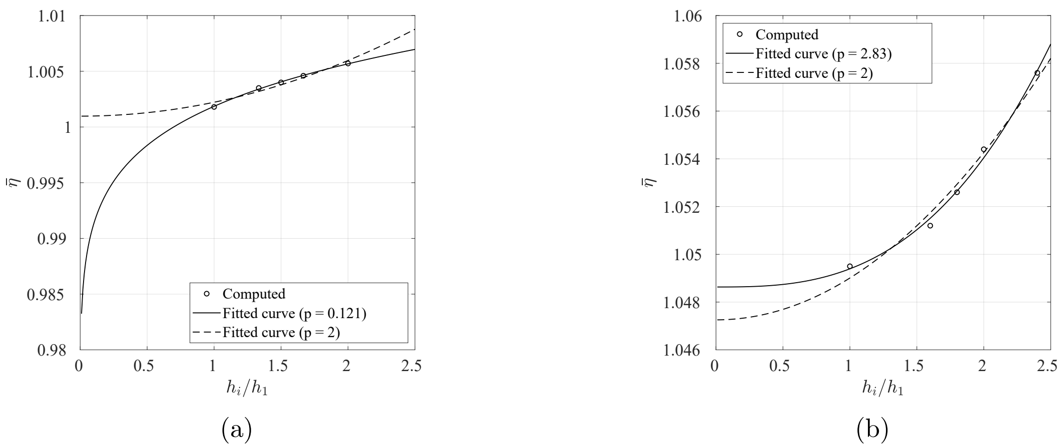

Figure C.25: Estimated convergence for the wave propagation of iso-surface for different Δt - a) $t/T = 5$; $\alpha = 0.50$, b) $t/T = 5$; $\alpha = 0.10/0.90$ c

t/T	Grid	$\Delta t_{5.1}$	$\Delta t_{4.1}$	$\Delta t_{3.1}$	$\Delta t_{2.1}$	$\Delta t_{1.1}$
5	$\bar{\eta}_{0.50}$	1.0018	1.0035	1.0040	1.0046	1.0057
	% diff	-	0.17	0.22	0.28	0.39
	$U_{\bar{\eta}_{0.50}}$	0.36	0.57	0.64	0.70	0.84
5	$\bar{\eta}_{0.90/0.10}$	1.0495	1.0512	1.0526	1.0544	1.0576
	% diff	-	0.16	0.30	0.47	0.77
	$U_{\bar{\eta}_{0.90/0.10}}$	0.59	1.41	1.76	2.16	3.09

Table C.9: Temporal uncertainty for wave propagation for different Δt with $s = 3.80$

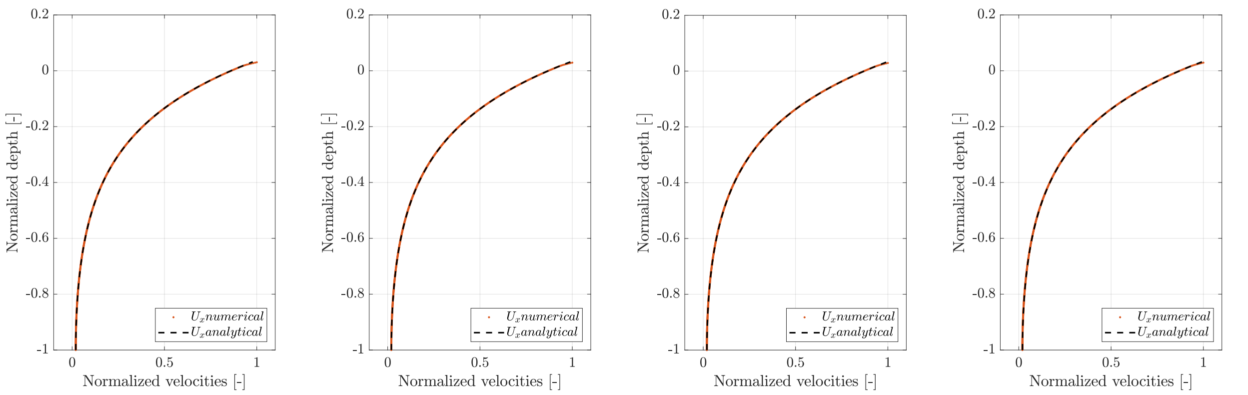

(a) (b) (c) (d)

Figure C.26: Maximum horizontal velocity profile over depth for 10 wave periods - a) $\Delta T_{1.1} = 0.00012$ b) $\Delta T_{2.1} = 0.00010$ c) $\Delta T_{3.1} = 0.00009$ d) $\Delta T_{4.1} = 0.00008$

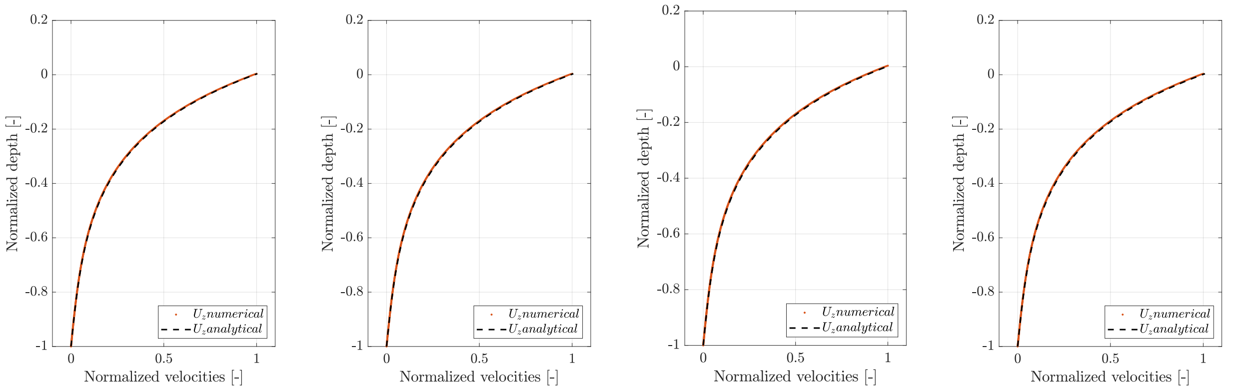

(a) (b) (c) (d)

Figure C.27: Maximum vertical velocity profile over depth for 10 wave periods - a) $\Delta T_{1.1} = 0.00012$ b) $\Delta T_{2.1} = 0.00010$ c) $\Delta T_{3.1} = 0.00009$ d) $\Delta T_{4.1} = 0.00008$

C.5 Temporal discretization for s=6.23

Steepness	Model	Δt	Max Courant Number	Mean Courant Number	Ref ratio[1]	Normalized run time[2]
	$\Delta t_{1.2}$	0.00020	0.053	0.007	2.500	1.00[4]
	$\Delta t_{2.2}$	0.00015	0.034	0.005	1.875	1.22
6.23	$\Delta t_{3.2}$	0.00010	0.020	0.003	1.250	1.60
	$\Delta t_{4.2}$	0.00009	0.018	0.003	1.125	1.70
	$\Delta t_{5.2}$	0.00008	0.016	0.003	1.000	1.78

Table C.10: Different temporal discretization for Grid 2.4.1 (Table 4.1) - [1]: rate between the minimum Δt and the one for the grid under investigation. - [2]: ratio between the minimum computational time and the one corresponding to the selected grid - [4] run time of 15.34 hours

For this steepness the maximum value of Δt is also influence by the fact that the simulations could not be finished when the time steep is setup for $\Delta t > 0.00020$. Hence, this might also influence the temporal discretization giving non reliable results.

Δt and 5 wave periods

Figures C.28 represents the surface elevation for different iso-surfaces ($\alpha = 0.50$ and $\alpha = 0.90/0.10$) and the analytical solution for Stokes' V order, which is found to be enough to describe all cases under investigation. This Figures are fitted to be in phase with the analytical solution in order to make easier to compare both solutions.

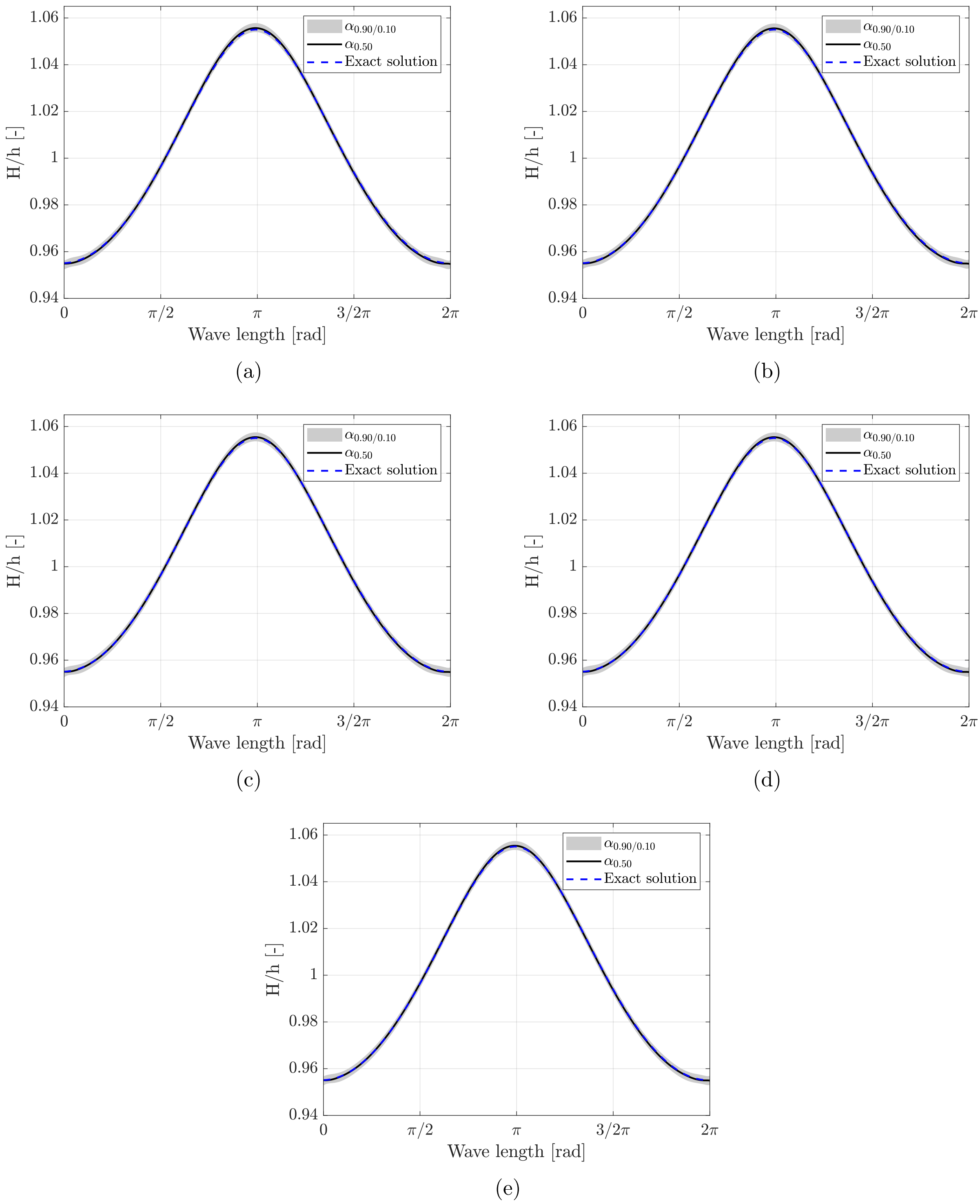

Figure C.28: Free surface elevation for different Δt with analytical solution and $t/T = 10$

Figure C.29 illustrates the phase delay at $t/T = 5$ between the analytical solution and the numerical calculations, which increases as t/T increases. This is caused due to the accumulative error on numerical errors.

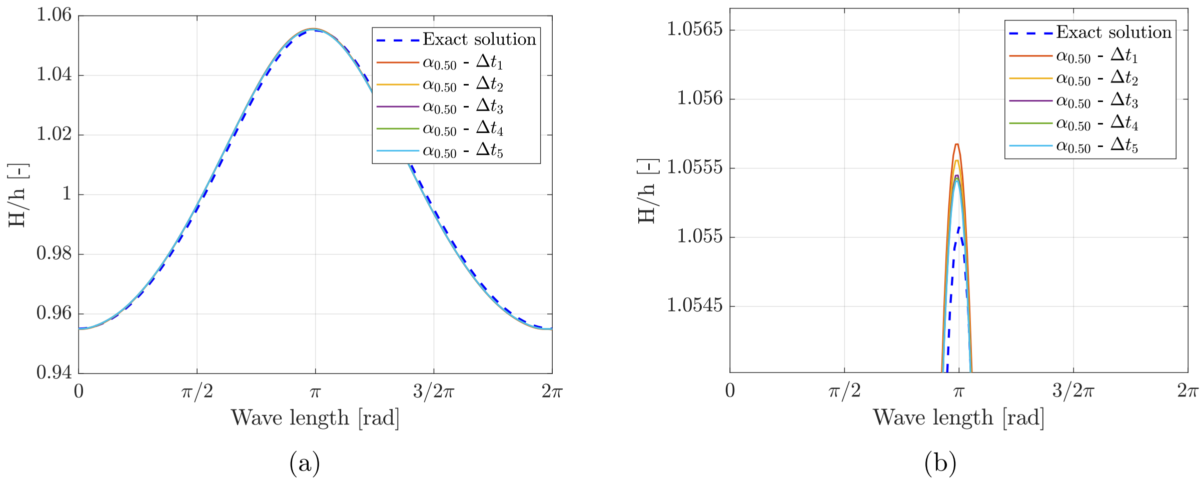

Figure C.29: Estimated convergence for the wave propagation of iso-surface and $t/T = 5$ for different Δt - a) $\alpha = 0.50$, b) $\alpha = 0.10/0.90$

Δt and 10 wave periods

Figures C.30 represents the surface elevation for different iso-surfaces ($\alpha = 0.50$ and $\alpha = 0.90/0.10$) and the analytical solution for Stokes' V order, which is found to be enough to describe all cases under investigation. This Figures are fitted to be in phase with the analytical solution in order to make easier to compare both solutions.

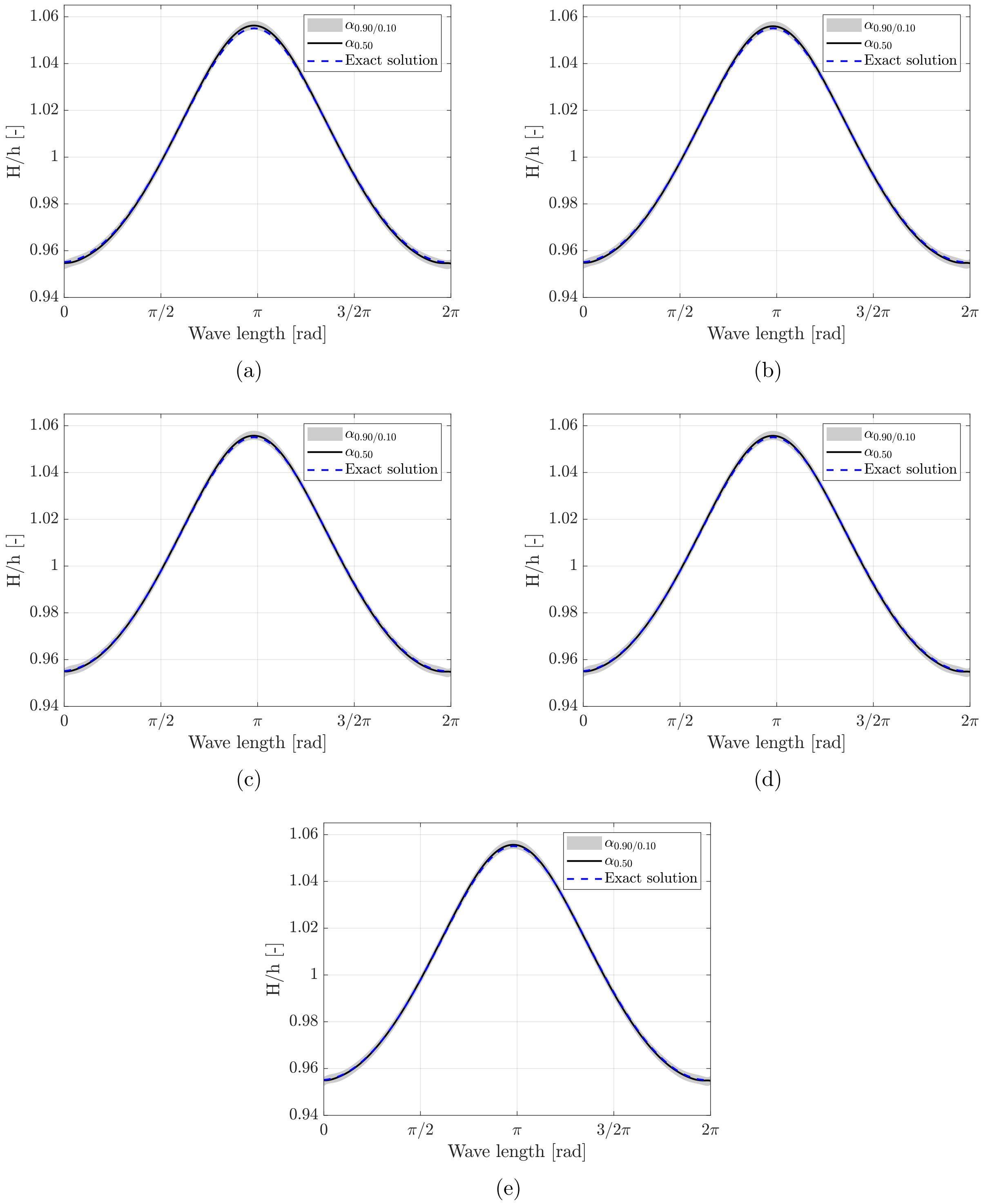

Figure C.30: Free surface elevation for different Δt with analytical solution and $t/T = 10$

Figure C.31 illustrates the phase delay at $t/T = 10$ between the analytical solution and the numerical calculations, which increases as t/T increases. This is caused due to the accumulative error on numerical errors.

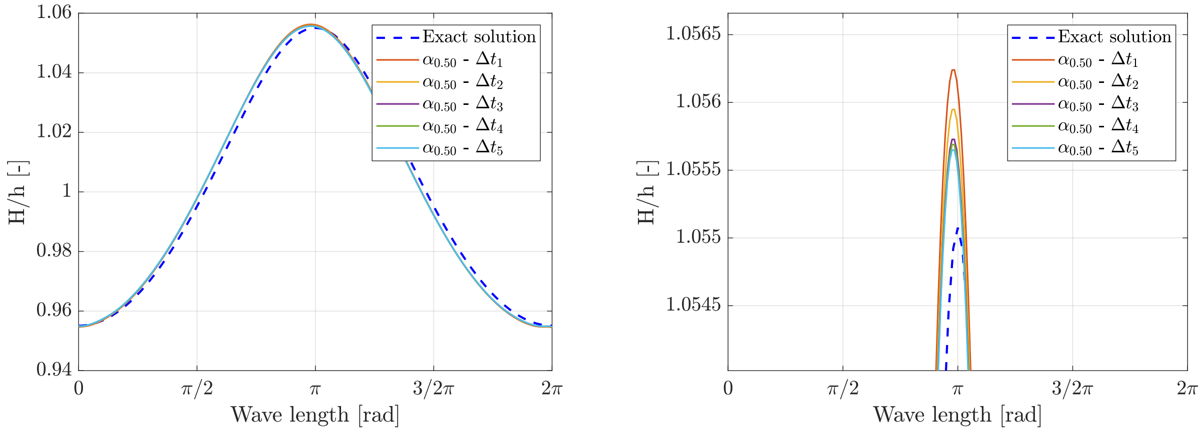

(a) (b)

Figure C.31: Estimated convergence for the wave propagation of iso-surface and $t/T = 10$ for different Δt - a) $\alpha = 0.50$, b) $\alpha = 0.10/0.90$

Figures C.32 and C.33 shows the wave kinematics profile from numerical calculations and from analytical methods for 4 different grids.

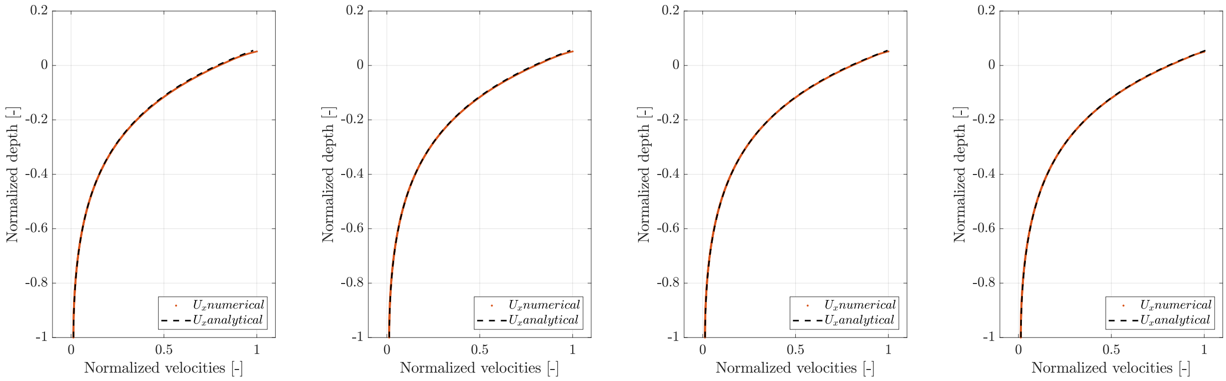

(a) (b) (c) (d)

Figure C.32: Maximum horizontal velocity profile over depth for 10 wave periods - a) $\Delta T_{1.2} = 0.00020$ b) $\Delta T_{2.2} = 0.00015$ c) $\Delta T_{3.2} = 0.00010$ d) $\Delta T_{4.2} = 0.00009$

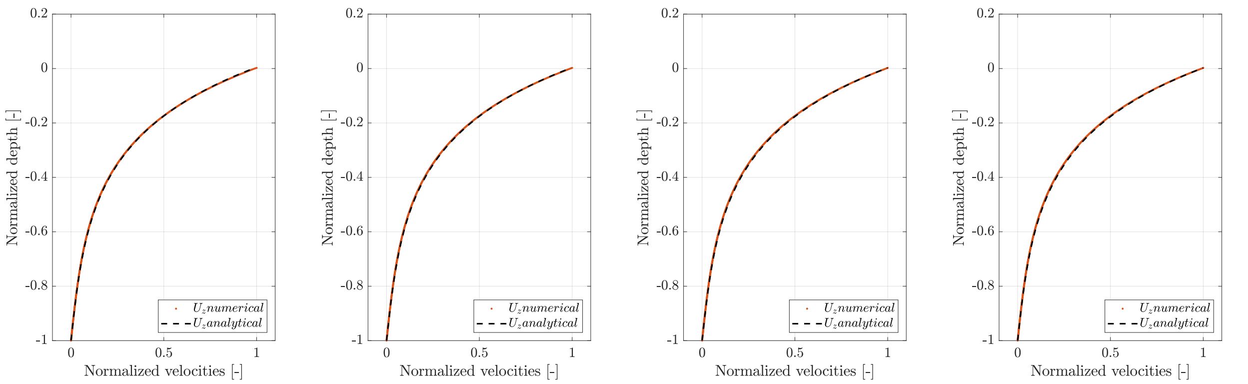

(a) (b) (c) (d)

Figure C.33: Maximum vertical velocity profile over depth for 10 wave periods - a) $\Delta T_{1.2} = 0.00020$ b) $\Delta T_{2.2} = 0.00015$ c) $\Delta T_{3.2} = 0.00010$ d) $\Delta T_{4.2} = 0.00009$

Figures C.34 represent the Richardson extrapolation for all cases under investigation and $s = 6.23$.

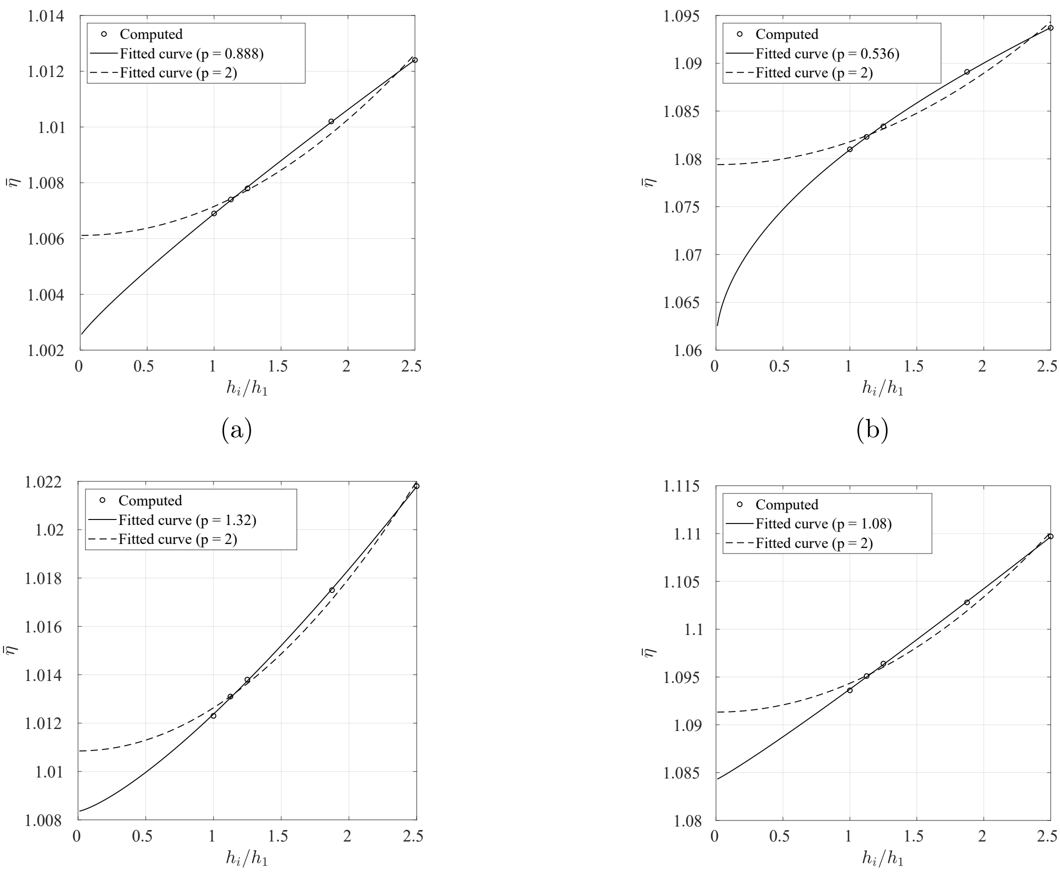

(a) (b) (c) (d)

Figure C.34: Estimated convergence for the wave propagation of iso-surface for different Δt - a) $t/T = 5$; $\alpha = 0.50$, b) $t/T = 5$; $\alpha = 0.10/0.90$ c) $t/T = 10$; $\alpha = 0.50$, d) $t/T = 10$; $\alpha = 0.10/0.90$

The same procedure is conducted for $s = 6.23$ and the results of the temporal uncertainty are presented in Table C.11. A more detailed analysis with all the results is presented on Appendix C.3.2. In addition the values for analysis of Δt and $s = 6.23$ are presented in Table 4.5. In this analysis values of $\Delta t > 0.00020$ are not possible to use owing to the fact that those models could not complete the simulation as the model crash.

t/T	Grid	$\Delta t_{5.2}$	$\Delta t_{4.2}$	$\Delta t_{3.2}$	$\Delta t_{2.2}$	$\Delta t_{1.2}$
5	$\bar{\eta}_{0.50}$	1.0069	1.0074	1.0078	1.0102	1.0124
	% diff	-	0.05	0.09	0.33	0.55
	$U_{\bar{\eta}_{0.50}}$	0.06	0.06	0.07	0.96	1.24
5	$\bar{\eta}_{0.90/0.10}$	1.0741	1.0749	1.0756	1.0789	1.0813
	% diff	-	0.12	0.22	0.75	1.18
	$U_{\bar{\eta}_{0.90/0.10}}$	2.53	2.69	2.85	3.54	4.12
10	$\bar{\eta}_{0.50}$	1.0123	1.0131	1.0138	1.0175	1.0218
	% diff	-	0.08	0.15	0.51	0.94
	$U_{\bar{\eta}_{0.50}}$	0.51	0.60	0.68	1.16	1.69
10	$\bar{\eta}_{0.90/0.10}$	1.0813	1.0820	1.0826	1.0853	1.0879
	% diff	-	0.14	0.26	0.84	1.47
	$U_{\bar{\eta}_{0.90/0.10}}$	1.20	1.36	1.52	2.35	3.19

Table C.11: Temporal uncertainty for wave propagation for different Δt with $s = 6.23$

From Table C.11 it can be seen that that the uncertainty gives small values which are in accordance with the convergence ratios shown in Figures C.34 on Appendix C.5. Also, the convergence ratio gives values similar to the ones found for $s = 3.80$. The reason behind this behaviour is found on the $\%diff$, which have small values for all cases. Therefore it can be conclude that even though the convergence ratios are not good enough, the uncertainties are kept small as it is believed that temporal discretization does not as have much influence on the iso-surface as on the phase delay. In conclusion, something around $\Delta t = 0.00012$) is enough to verify this model for the steeper wave.

Validation D

D.1 2D Validation for s=3.80

In this section the some extra information with regard to the 2D validation analysis of the wave test number 18 with $s = 3.80$ is presented here.

D.1.1 Reflection analysis *First-order irregular waves*

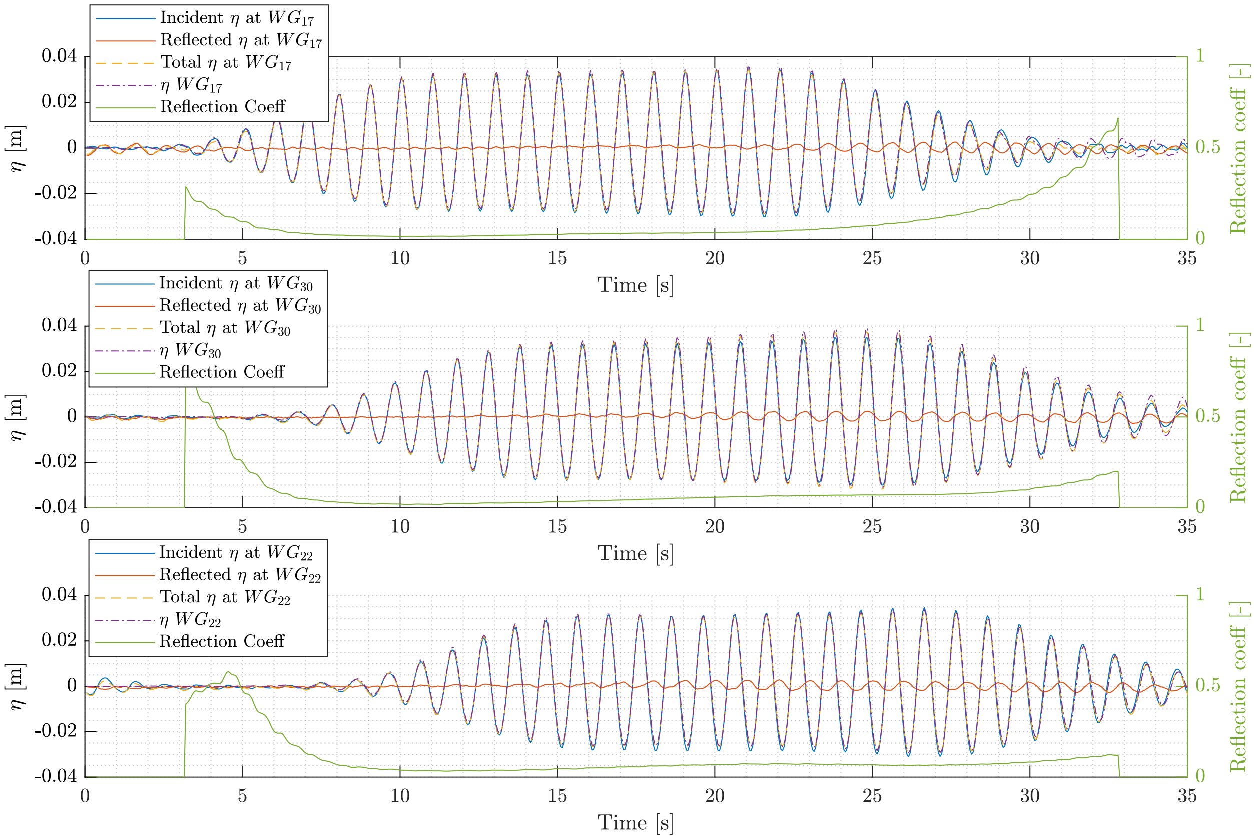

Figure D.1: Reflection analysis at WG_{17}, WG_{30} and WG_{22} for *First-order irregular waves*. *Incident* η *at* WG_{xx}, *Reflected* η *at* WG_{xx} and *Total* η *at* WG_{xx} are obtained from the reflection analysis of η WG_{xx}, which corresponds to the simulated surface elevation at each WG_{xx}.

From Figure above, D.1, it is clear to see that although an outlet relaxation zone is setup, some reflected waves are influencing the results. On one hand, a peak on the reflection coefficient can be seen at the beginning of each graph. This peak is caused by small variations on the surface elevation on the numerical wave basin, before any incoming wave reach the measured point. So this part is neglected on the analysis, as it is not influencing the results. On the other hand, from this analysis it can be concluded that reflected waves are not the main cause to produce the disparity between the numerical waves and the laboratory waves.

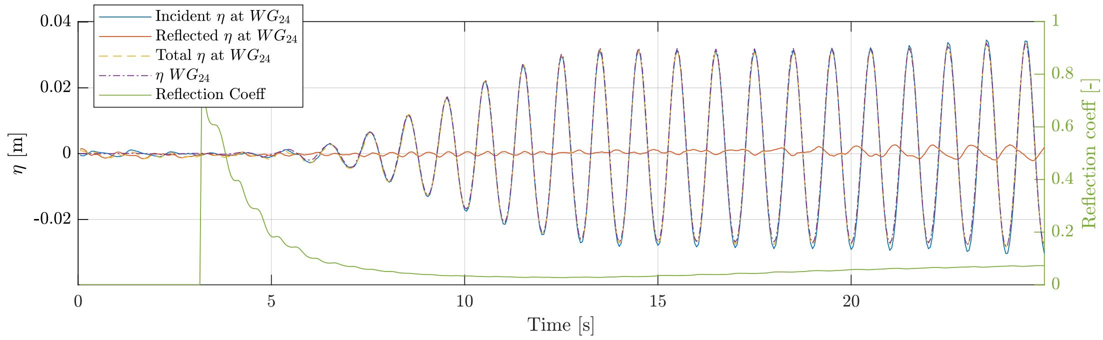

Figure D.2: Reflection analysis at WG_{24} for *First-order irregular waves*. *Incident* η *at* WG_{24}, *Reflected* η *at* WG_{24} and *Total* η *at* WG_{24} are obtained from the reflection analysis of η WG_{24}, which corresponds to the simulated surface elevation at each WG_{24}.

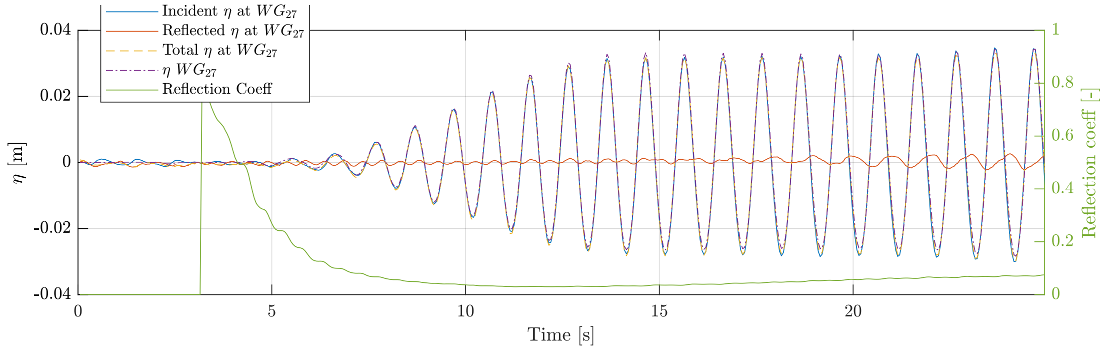

Figure D.3: Reflection analysis at WG_{27} for *First-order irregular waves*. *Incident* η *at* WG_{27}, *Reflected* η *at* WG_{27} and *Total* η *at* WG_{27} are obtained from the reflection analysis of η WG_{27}, which corresponds to the simulated surface elevation at each WG_{27}.

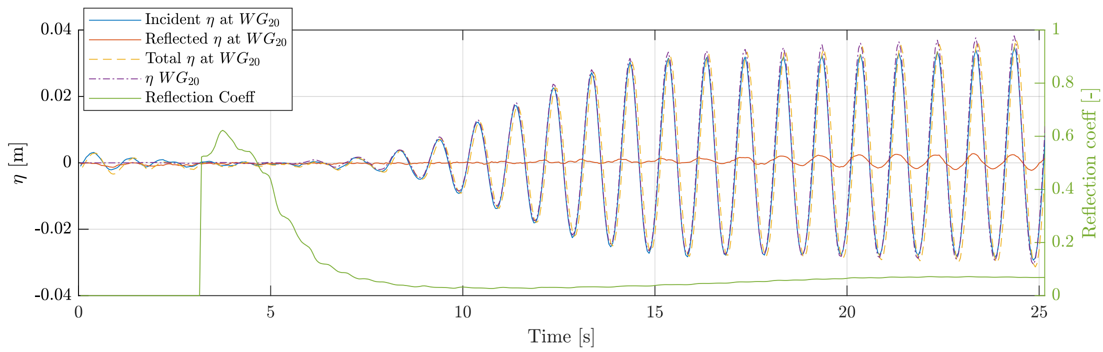

Figure D.4: Reflection analysis at WG_{20} for *First-order irregular waves*. *Incident* η *at* WG_{20}, *Reflected* η *at* WG_{20} and *Total* η *at* WG_{20} are obtained from the reflection analysis of η WG_{20}, which corresponds to the simulated surface elevation at each WG_{20}.

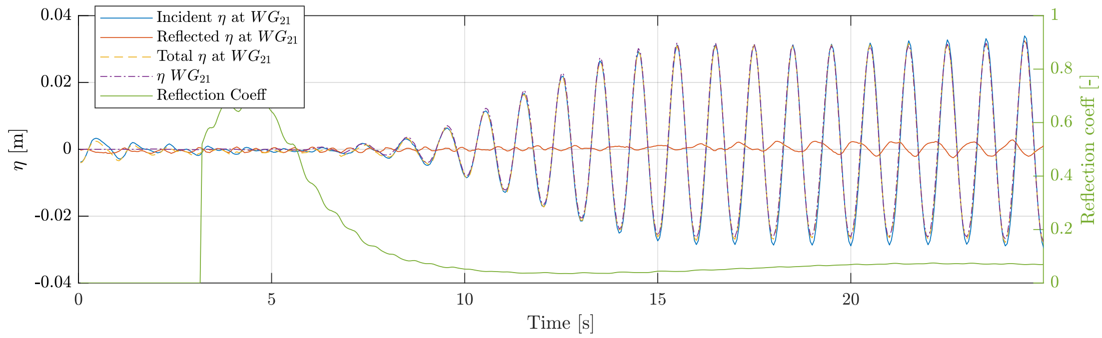

Figure D.5: Reflection analysis at WG_{21} for *First-order irregular waves*. *Incident* η *at* WG_{21}, *Reflected* η *at* WG_{21} and *Total* η *at* WG_{21} are obtained from the reflection analysis of η WG_{21}, which corresponds to the simulated surface elevation at each WG_{21}.

D.1.2 Reflection analysis *Stokes* 5^th *order*

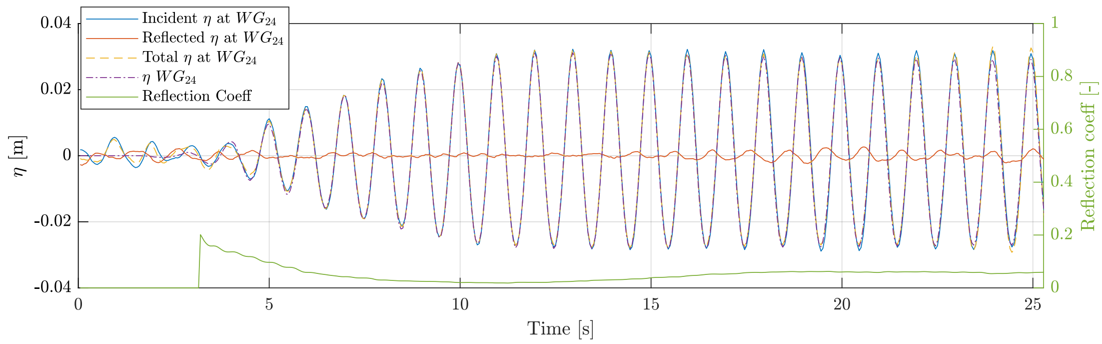

Figure D.6: Reflection analysis at WG_{24} from Stokes 5^{th} order wave generation. *Incident* η *at* WG_{24}, *Reflected* η *at* WG_{24} and *Total* η *at* WG_{24} are obtained from the reflection analysis of η WG_{24}, which corresponds to the simulated surface elevation at each WG_{24}.

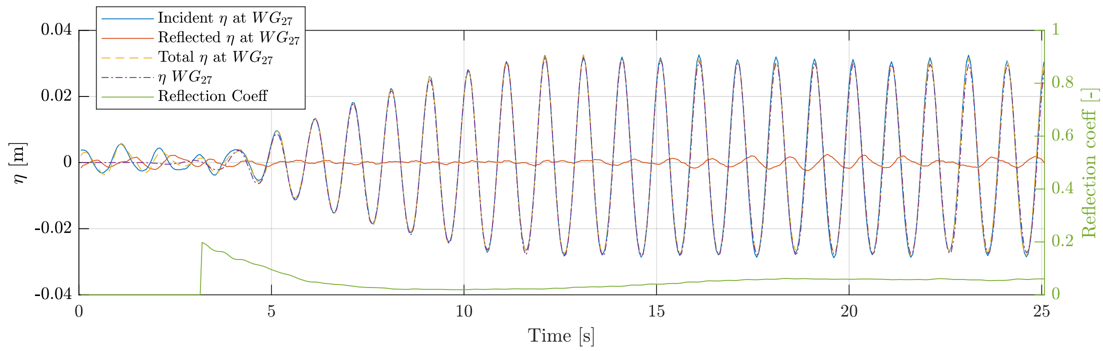

Figure D.7: Reflection analysis at WG_{27} from Stokes 5^{th} order wave generation. *Incident* η *at* WG_{27}, *Reflected* η *at* WG_{27} and *Total* η *at* WG_{27} are obtained from the reflection analysis of η WG_{27}, which corresponds to the simulated surface elevation at each WG_{27}.

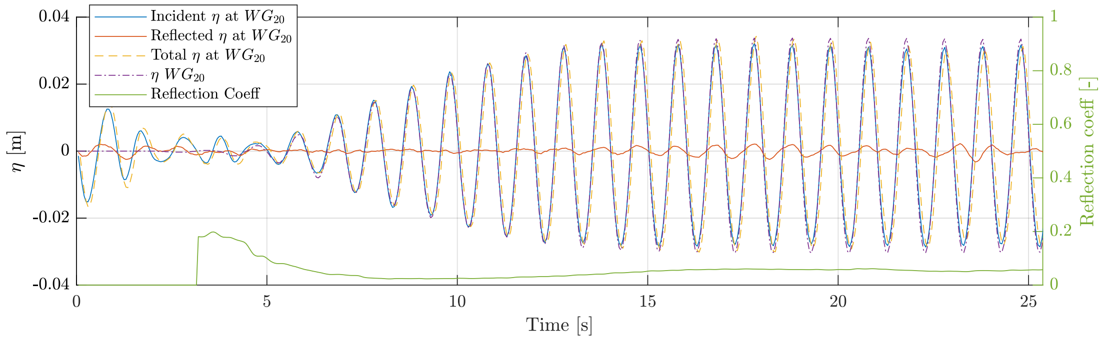

Figure D.8: Reflection analysis at WG_{20} from Stokes 5^{th} order wave generation. *Incident η at WG_{20}*, *Reflected η at WG_{20}* and *Total η at WG_{20}* are obtained from the reflection analysis of η WG_{20}, which corresponds to the simulated surface elevation at each WG_{20}.

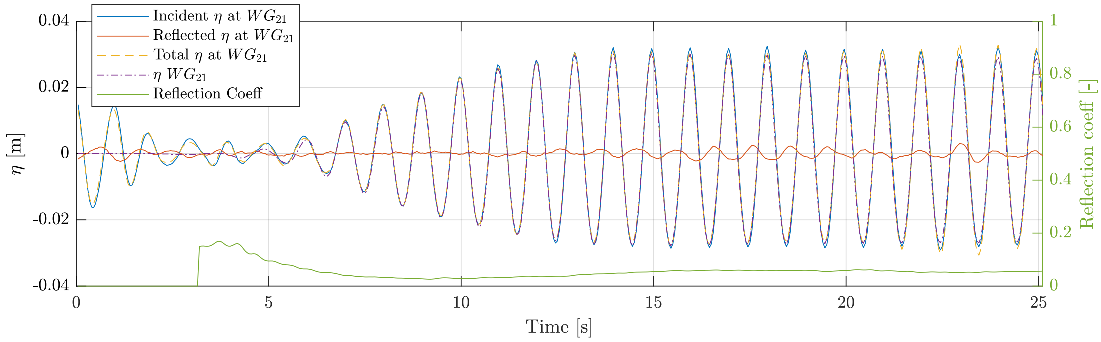

Figure D.9: Reflection analysis at WG_{21} from Stokes 5^{th} order wave generation. *Incident η at WG_{21}*, *Reflected η at WG_{21}* and *Total η at WG_{21}* are obtained from the reflection analysis of η WG_{21}, which corresponds to the simulated surface elevation at each WG_{21}.

D.2 2D Validation for s=6.23

In this section the some extra information with regard to the 2D validation analysis of the wave test number 20 with $s = 6.23$ is presented here.

The free surface elevation for $WG - 20 - 21 - 22$ is illustrated in the following figure:

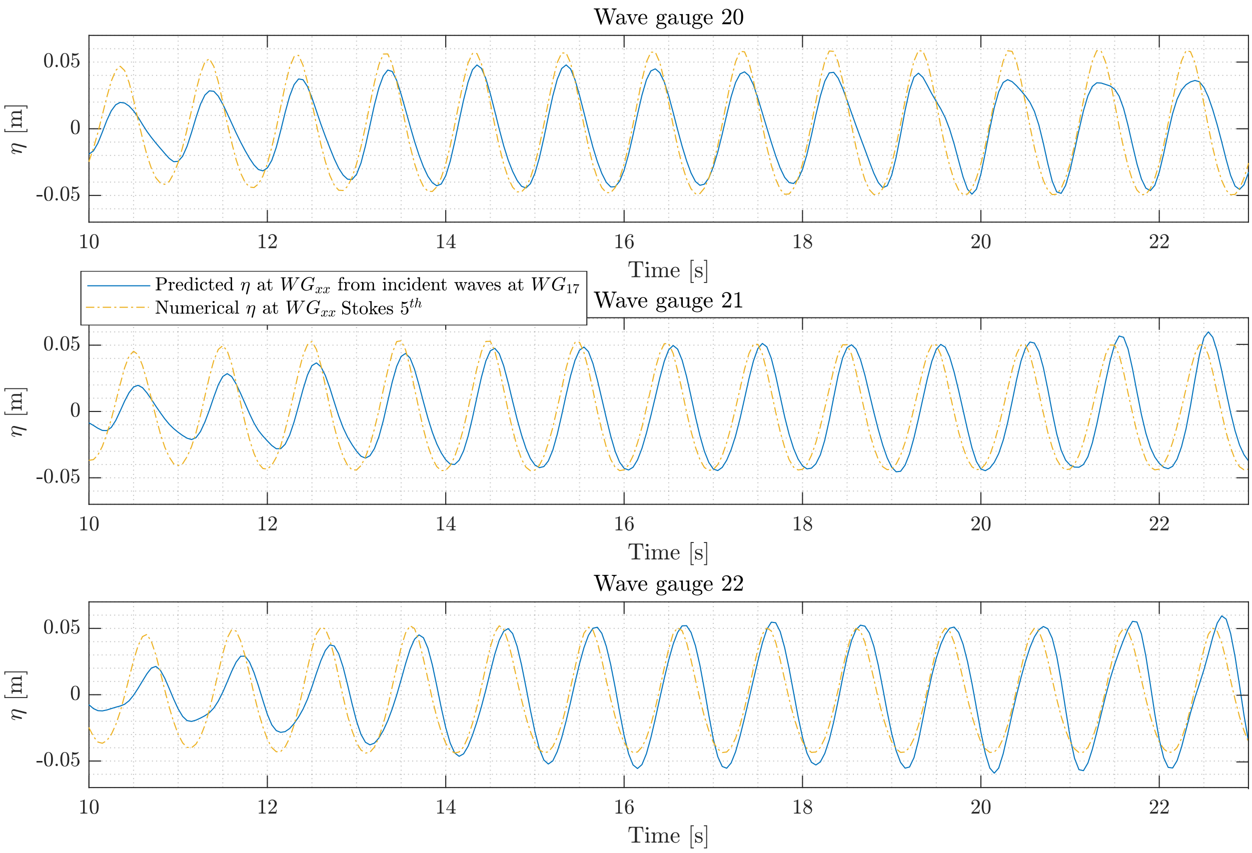

Figure D.10: Comparison of WG_{20}, WG_{21} and WG_{22} between: Predicted waves from laboratory incident waves from WG_{17} *Predicted η at WG_{xx} from incident waves at WG_{17}*, Numerical waves from spectrum from Figure 3.4a *Numerical η at WG_{17} Irregular* and Numerical waves from Stokes 5^{th} order theory wave generation *Numerical η at WG_{17} Stokes 5^{th}*.

D.2.1 Reflection analysis *First-order irregular waves*

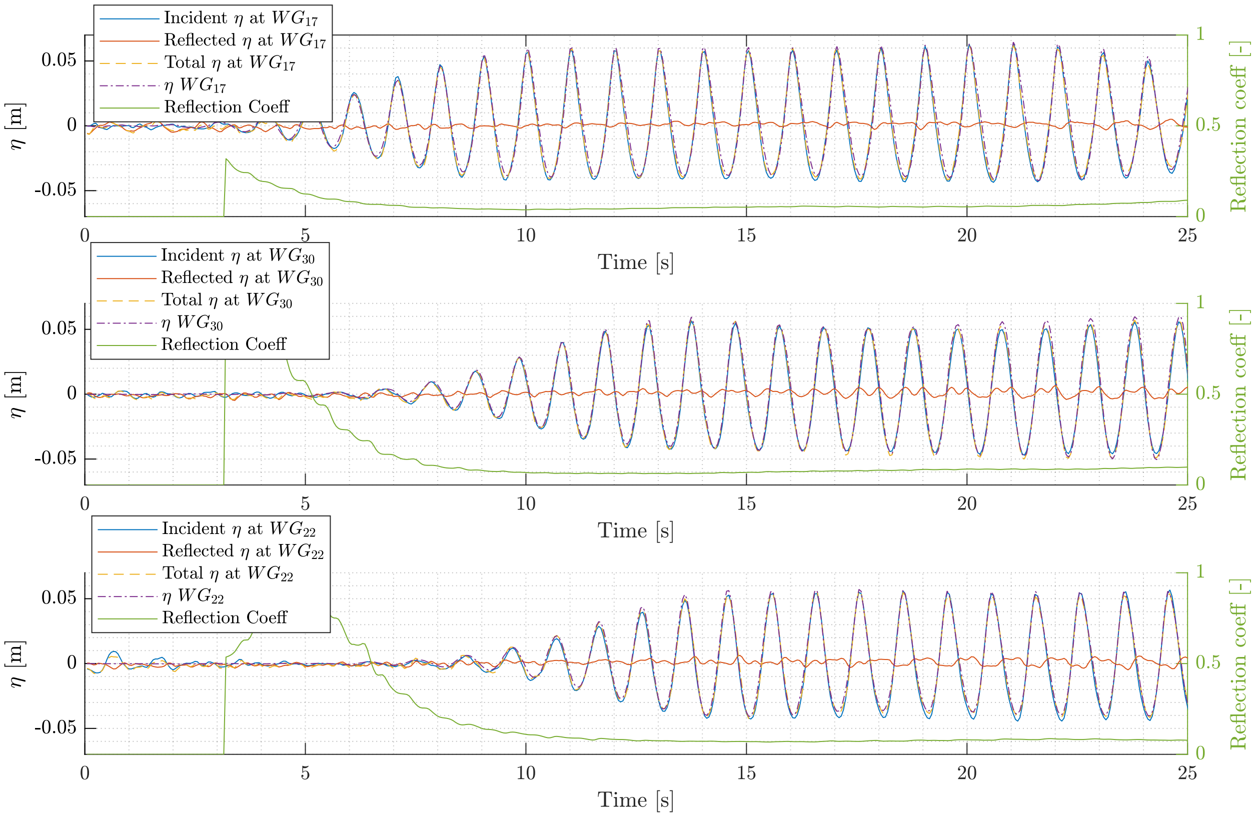

Figure D.11: Reflection analysis at WG_{17}, WG_{30} and WG_{22} for *First-order irregular waves*. *Incident η at WG_{xx}*, *Reflected η at WG_{xx}* and *Total η at WG_{xx}* are obtained from the reflection analysis of η WG_{xx}, which corresponds to the simulated surface elevation at each WG_{xx}.

D.2.2 Reflection analysis *Stokes* 5^th *order*

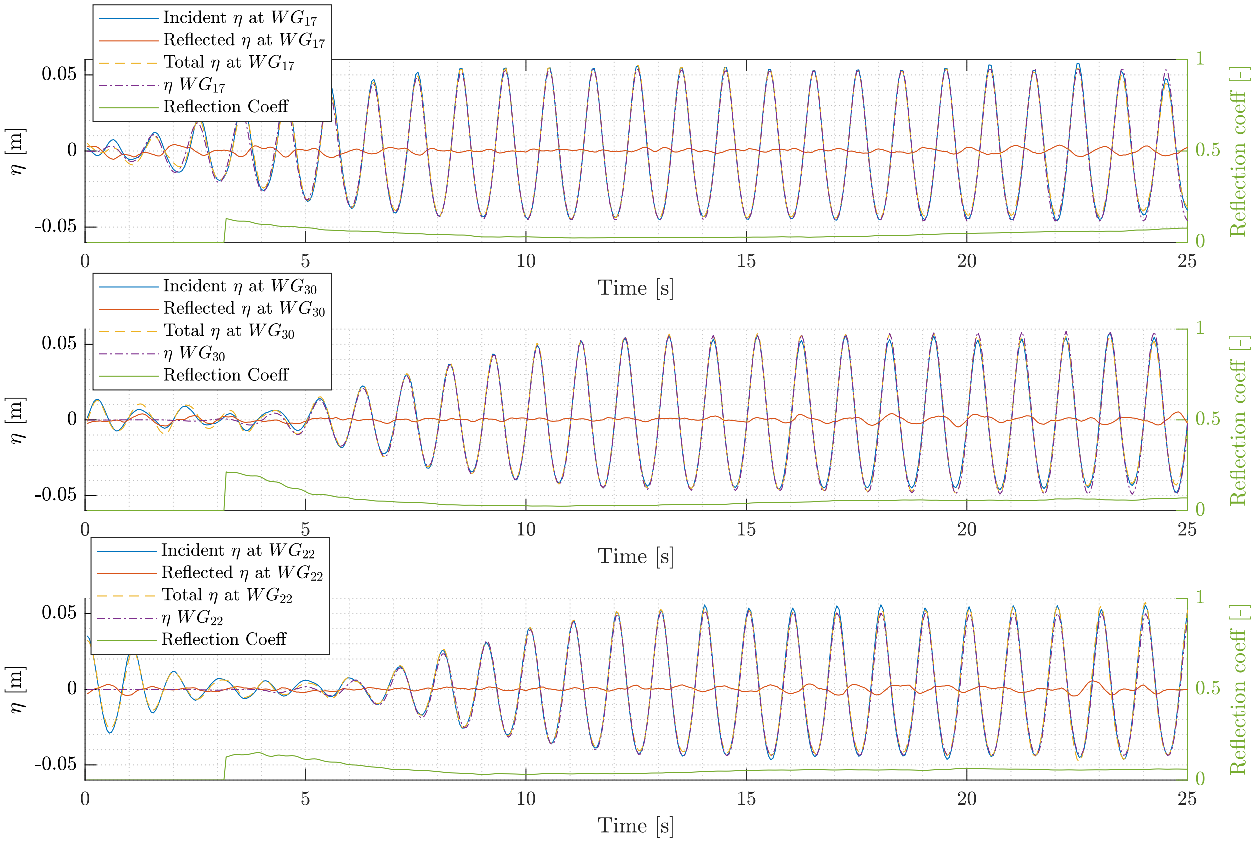

Figure D.12: Reflection analysis at WG_{17}, WG_{30} and WG_{22} from Stokes 5^{th} order wave generation. *Incident* η *at* WG_{xx}, *Reflected* η *at* WG_{xx} and *Total* η *at* WG_{xx} are obtained from the reflection analysis of η WG_{xx}, which corresponds to the simulated surface elevation at each WG_{xx}.

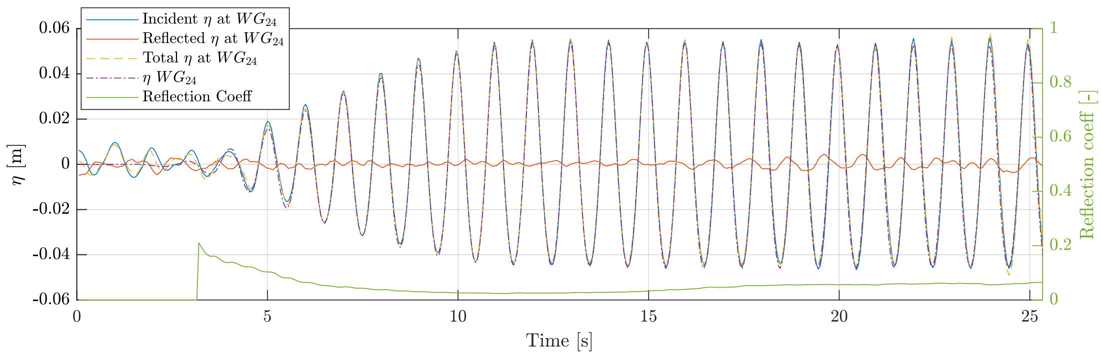

Figure D.13: Reflection analysis at WG_{24} from Stokes 5^{th} order wave generation. *Incident* η *at* WG_{24}, *Reflected* η *at* WG_{24} and *Total* η *at* WG_{24} are obtained from the reflection analysis of η WG_{24}, which corresponds to the simulated surface elevation at each WG_{24}.

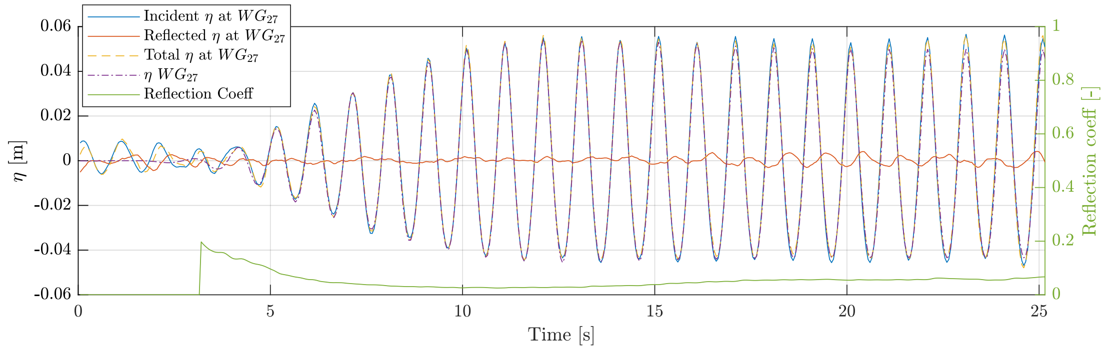

Figure D.14: Reflection analysis at WG_{27} from Stokes 5^{th} order wave generation. *Incident* η *at* WG_{27}, *Reflected* η *at* WG_{27} and *Total* η *at* WG_{27} are obtained from the reflection analysis of η WG_{27}, which corresponds to the simulated surface elevation at each WG_{27}.

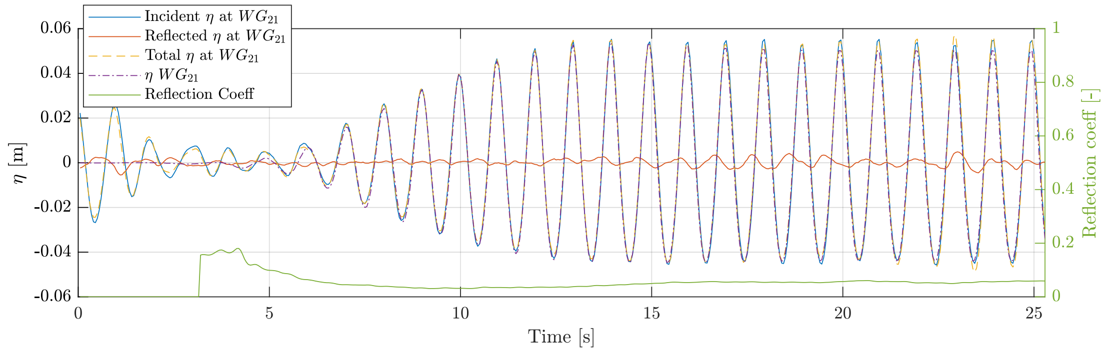

Figure D.15: Reflection analysis at WG_{20} from Stokes 5^{th} order wave generation. *Incident* η *at* WG_{20}, *Reflected* η *at* WG_{20} and *Total* η *at* WG_{20} are obtained from the reflection analysis of η WG_{20}, which corresponds to the simulated surface elevation at each WG_{20}.

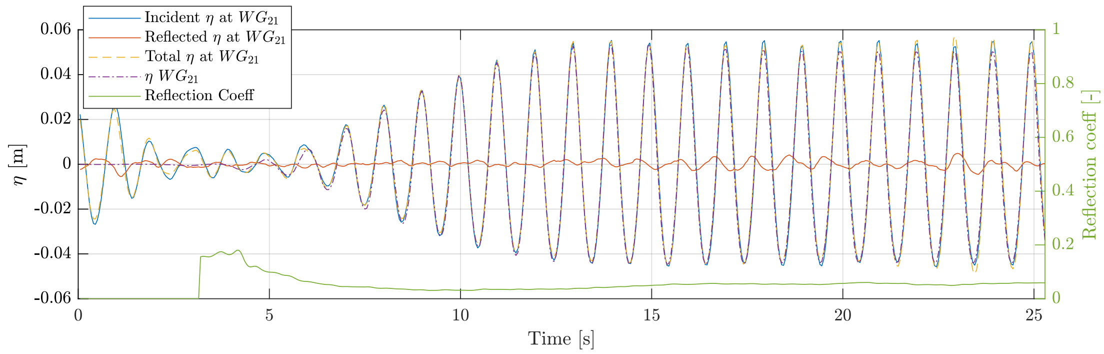

Figure D.16: Reflection analysis at WG_{21} from Stokes 5^{th} order wave generation. *Incident* η *at* WG_{21}, *Reflected* η *at* WG_{21} and *Total* η *at* WG_{21} are obtained from the reflection analysis of η WG_{21}, which corresponds to the simulated surface elevation at each WG_{21}.

D.3 Validation 3D model A4 chamber configuration

In this section extra data that is not included on the main report for the analysis of the wave-structure interaction of the A4 chamber configuration is presented.

D.3.1 Validation of A4 chamber for wave test number 18. Steepness 3.80 %

In this section some extra information is illustrated for the validation of the A4 chamber configuration of wave test number 18 with $s = 3.80\%$.

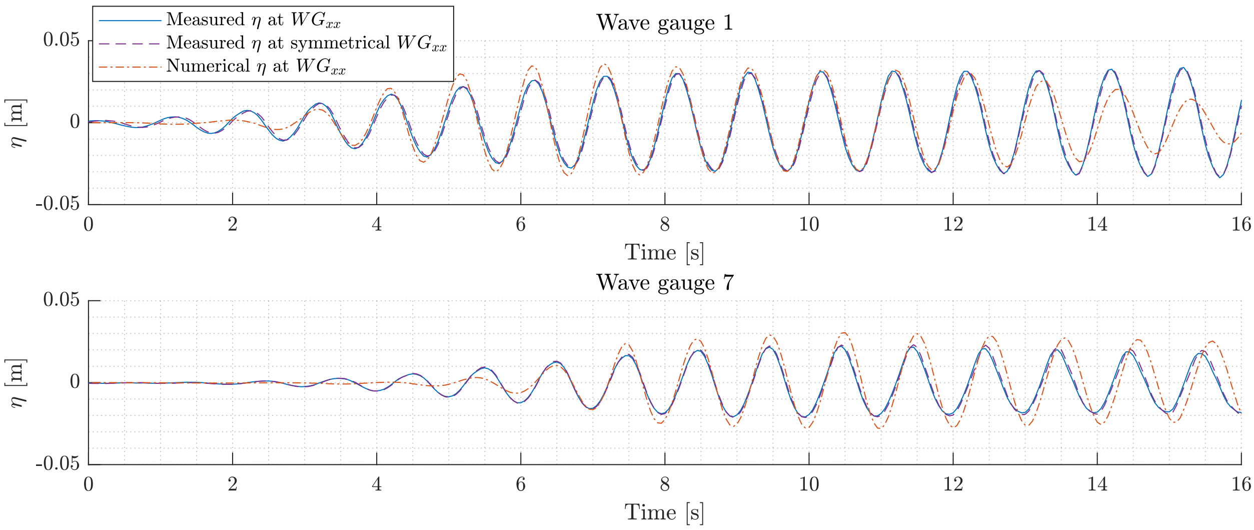

Figure D.17: Free surface elevation at different wave gauges locations, see Figure B.2, for A4 chamber configuration, see Figure B.3, and wave test number 18. 2 WG measurement from empirical data are plotted together, the actual location and the symmetrical WG measurement (i.e. $WG-1$ and $WG-8$)

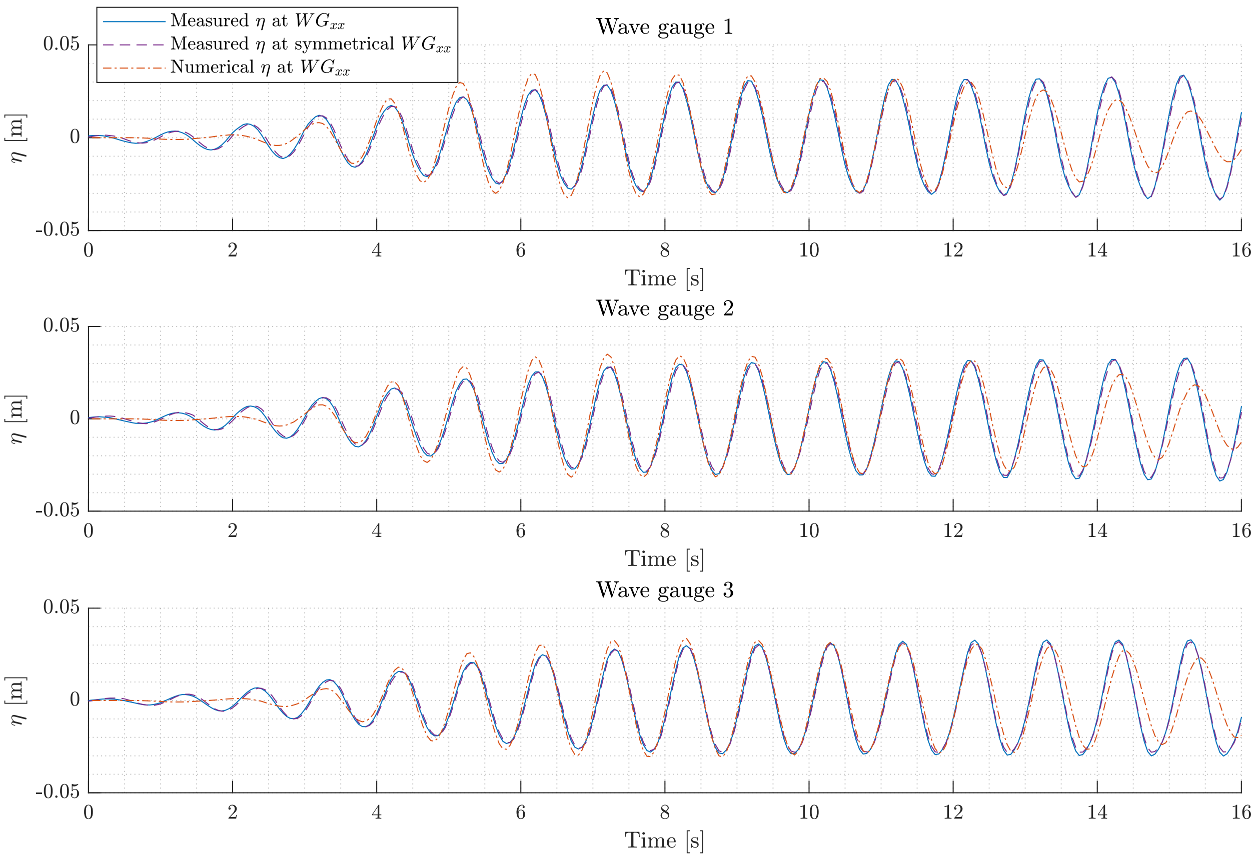

Figure D.18: Free surface elevation at different wave gauges locations, see Figure B.2, for A4 chamber configuration, see Figure B.3, and wave test number 18. 2 WG measurement from empirical data are plotted together, the actual location and the symmetrical WG measurement (i.e. $WG-1$ and $WG-8$)

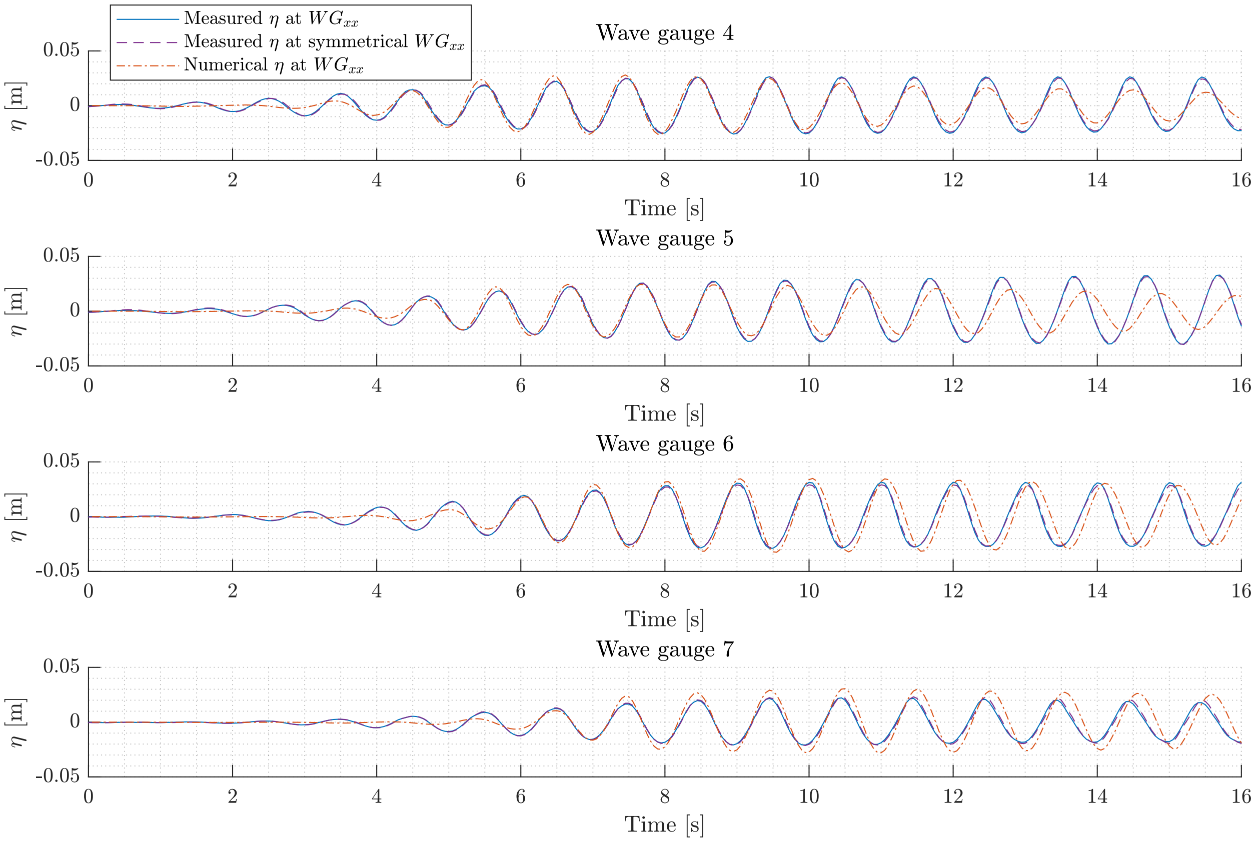

Figure D.19: Free surface elevation at different wave gauges locations, see Figure B.2, for A4 chamber configuration, see Figure B.3, and wave test number 18. 2 WG measurement from empirical data are plotted together, the actual location and the symmetrical WG measurement (i.e. $WG-4$ and $WG-11$)

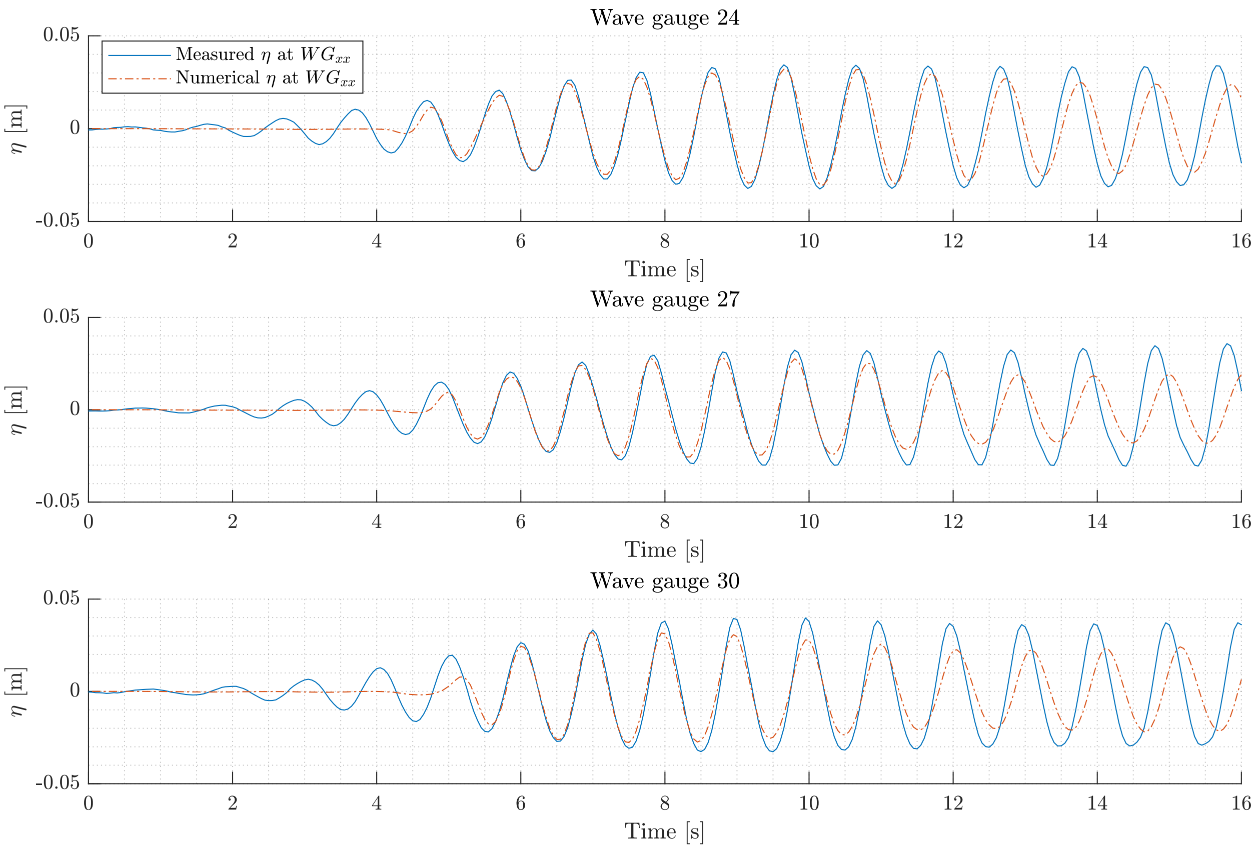

Figure D.20: Free surface elevation at different wave gauges locations, see Figure B.2, for A4 chamber configuration, see Figure B.3, and wave test number 18

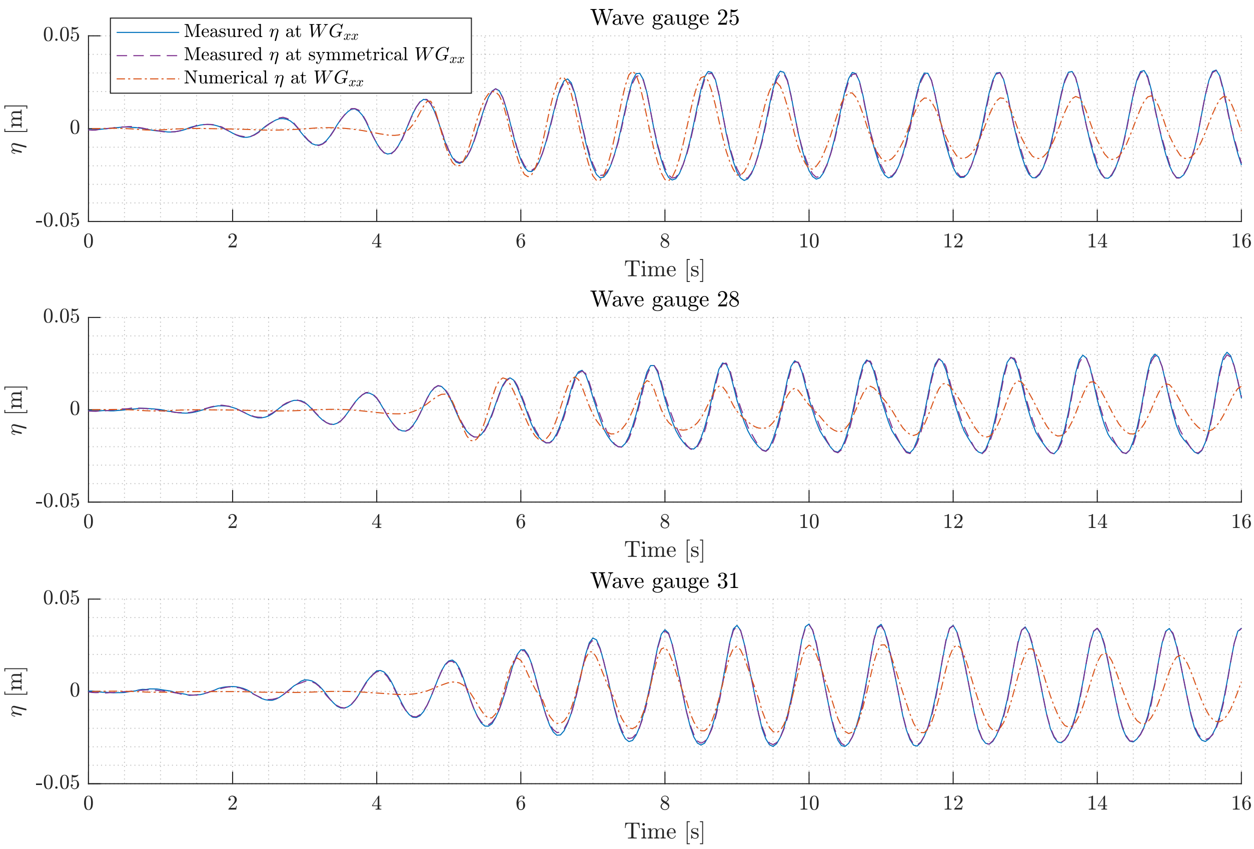

Figure D.21: Free surface elevation at different wave gauges locations, see Figure B.2, for A4 chamber configuration, see Figure B.3, and wave test number 18. 2 WG measurement from empirical data are plotted together, the actual location and the symmetrical WG measurement (i.e. $WG-25$ and $WG-23$)

Sensitivity analysis wave gauge location

In this section a sensitivity analysis is conducted for different wave gauge location to measure the influence of small deviations on the measured points location on the results of the numerical model. This is done see if specific areas with large gradients on the waves amplitudes magnitudes are the reason of having such as large differences between the experimental and numerical models.

This analysis is conducted for 6 wave gauges (24, 25, 27, 28, 30 and 31) by taking measurements at the location indicated on Figure B.2. Then, 4 more points are obtained by moving the wave gauge location along the x-axis $\pm 2cm$ every $1cm$. Also 2 more points are extracted by fixing the x-axis and moving along the y-axis $\pm 1cm$. Therefore, in total 7 different points are extracted and compared between each other to measure the influence of this parameter on the results.

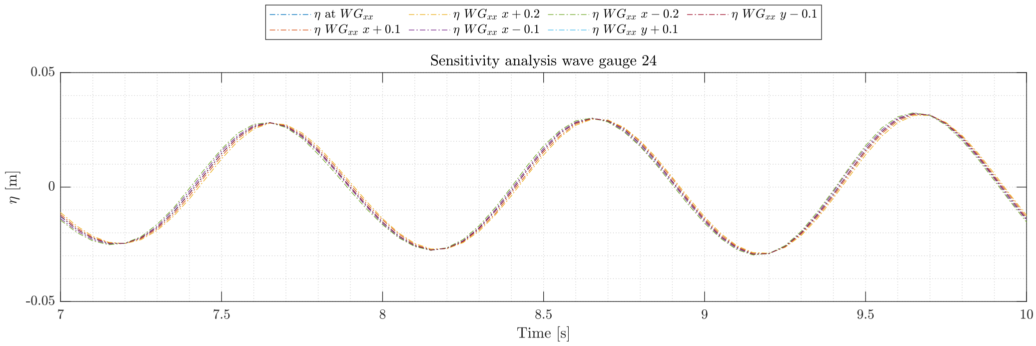

Figure D.22: Sensitivity analysis of wave gauge location on the free surface elevation inside the chamber)

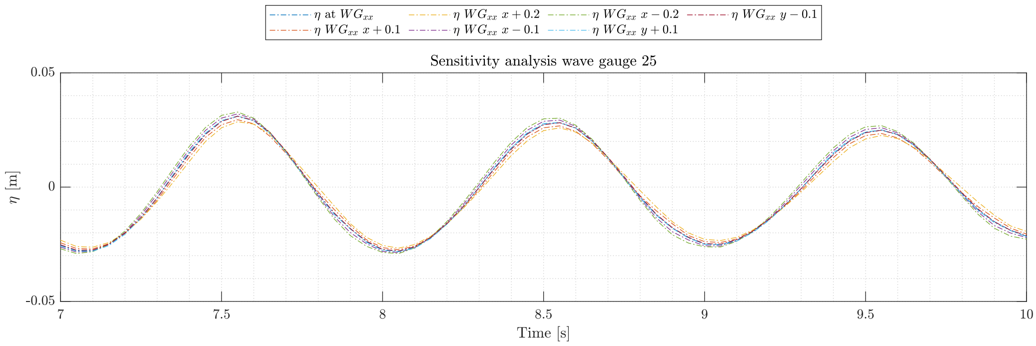

Figure D.23: Sensitivity analysis of wave gauge location on the free surface elevation inside the chamber)

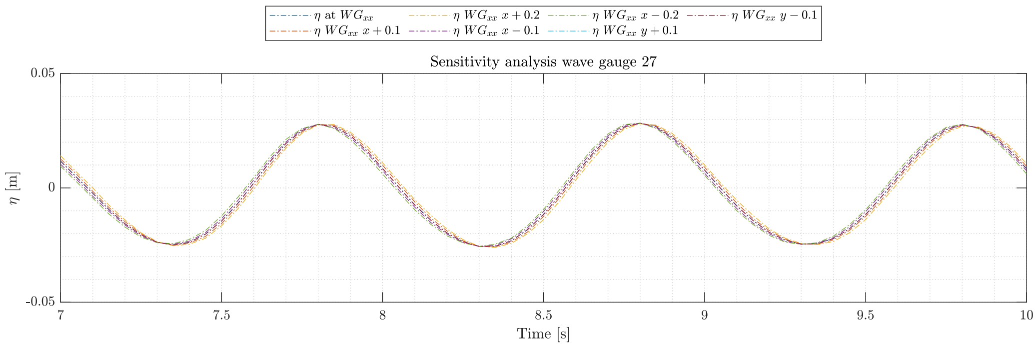

Figure D.24: Sensitivity analysis of wave gauge location on the free surface elevation inside the chamber)

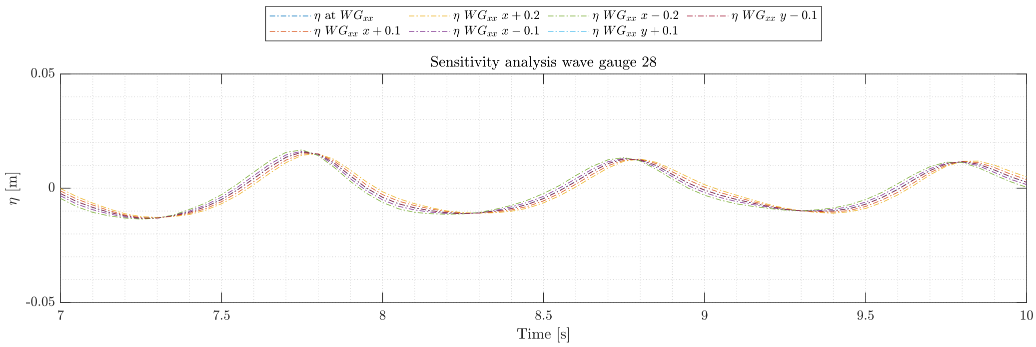

Figure D.25: Sensitivity analysis of wave gauge location on the free surface elevation inside the chamber)

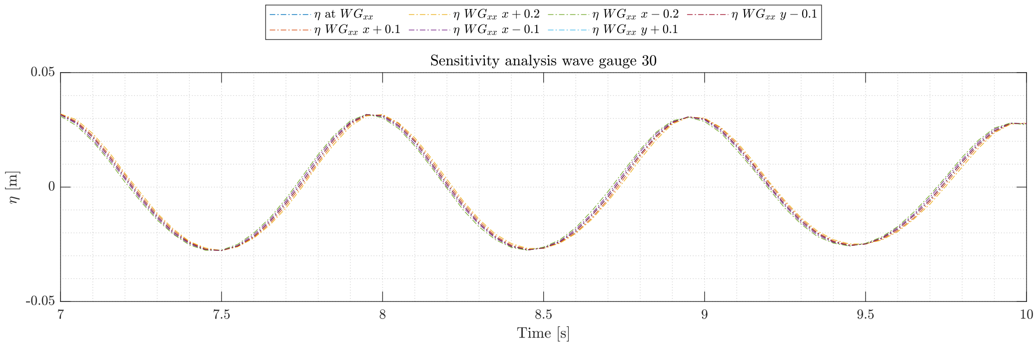

Figure D.26: Sensitivity analysis of wave gauge location on the free surface elevation inside the chamber)

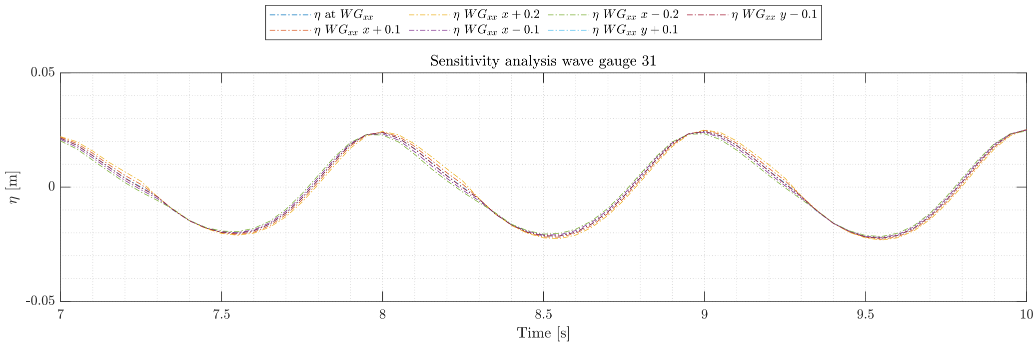

Figure D.27: Sensitivity analysis of wave gauge location on the free surface elevation inside the chamber)

It can be seen from previous Figures of the free surface elevation, measured at different locations around the original location, that there is a slightly variation on the phase and peaks and troughs. On one hand, the differences on phase shift are expected, this indicates that the wave is measured in different locations. On the other hand, the change on the surface elevation is not enough to explain the large difference found on the validation analysis of the 3D model. However, this slightly difference on peaks and troughs is caused by the strong wave-chamber hydrodynamics interaction happening inside the chamber.

Y+ value

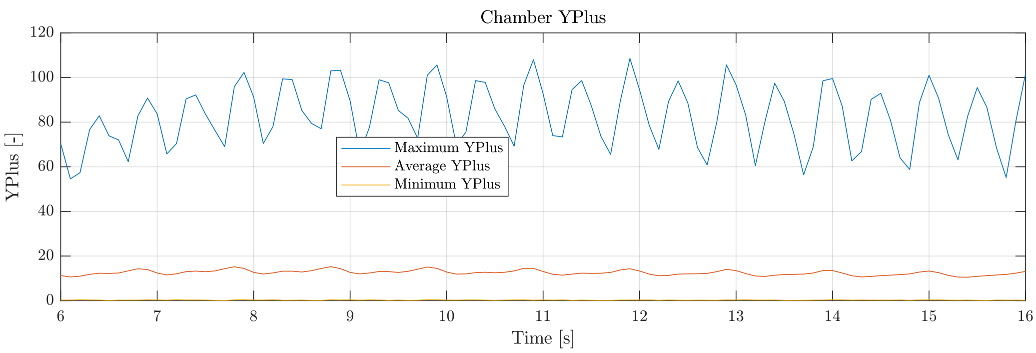

Figure D.28: Maximum, minimum and average Y+ value of the entire A4 chamber configuration over the time for $H = 0.06$ meters and $T = 1$ second

D.3.2 Validation of A4 chamber for wave test number 20. Steepness 6.23 %

In this section some extra information is illustrated for the validation of the A4 chamber configuration of wave test number 20 with $s = 6.23\%$.

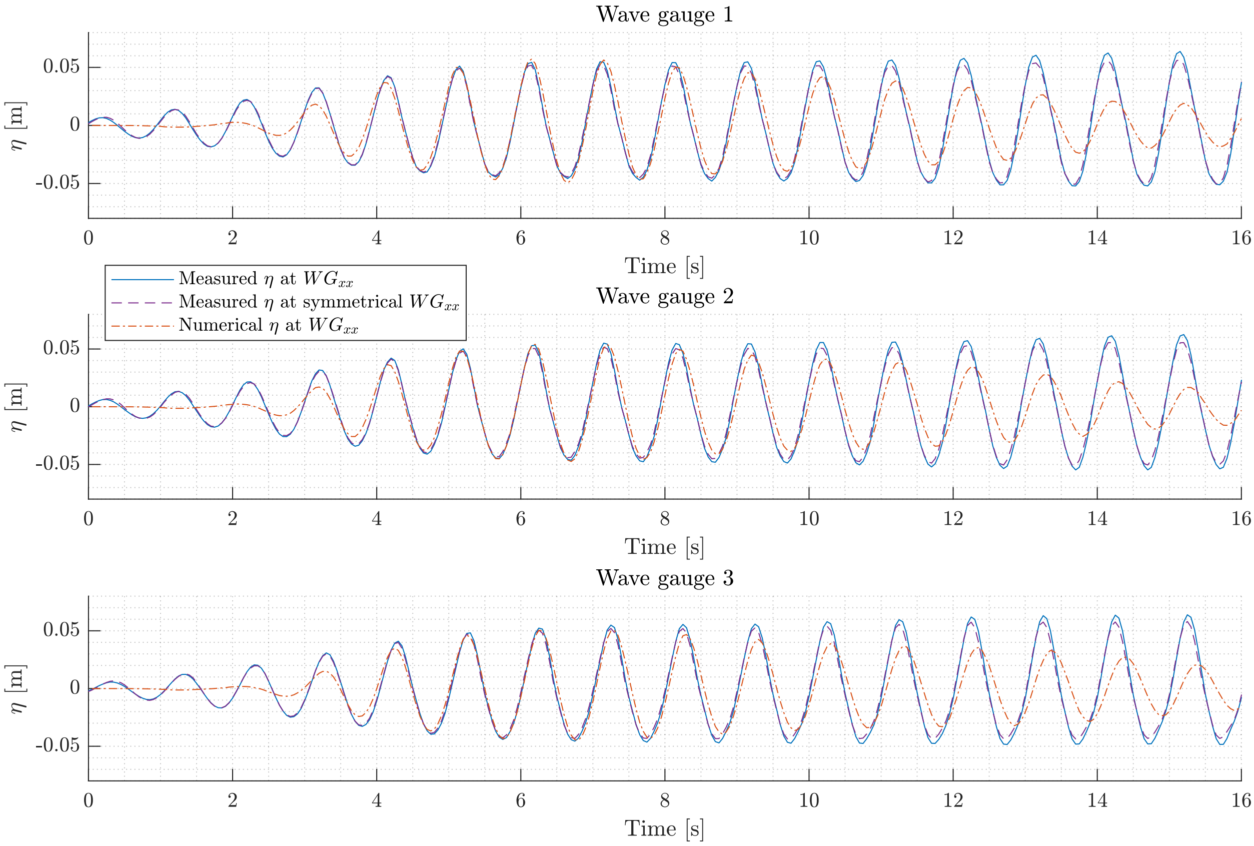

Figure D.29: Free surface elevation at different wave gauges locations, see Figure B.2, for A4 chamber configuration, see Figure B.3, and wave test number 20. 2 WG measurement from empirical data are plotted together, the actual location and the symmetrical WG measurement (i.e. $WG-1$ and $WG-8$)

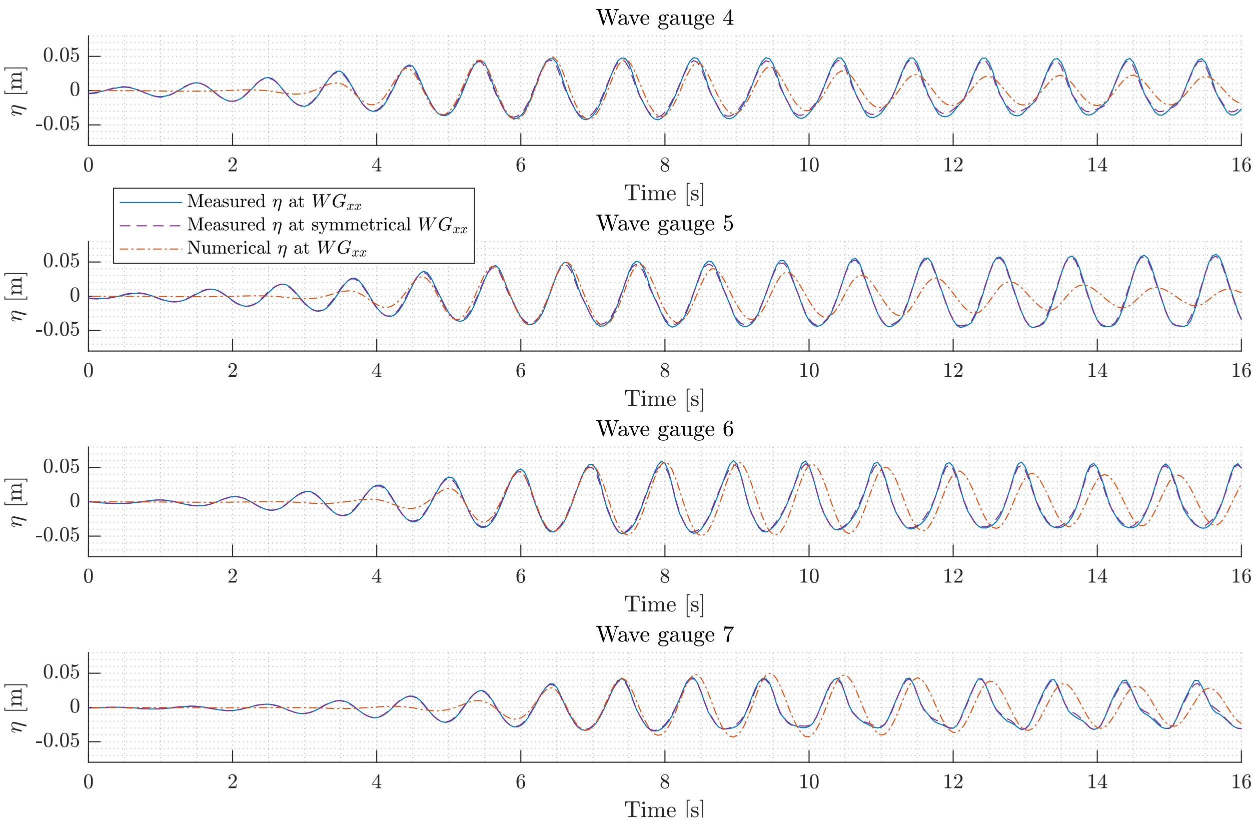

Figure D.30: Free surface elevation at different wave gauges locations, see Figure B.2, for A4 chamber configuration, see Figure B.3, and wave test number 20. 2 WG measurement from empirical data are plotted together, the actual location and the symmetrical WG measurement (i.e. $WG-4$ and $WG-11$)

Sensitivity analysis wave gauge location

This sensitivity analysis is conducted in the same way as the analysis for A4 chamber configuration and wave $s = 3.80$ on Appendix D.3.1. This analysis is performed in specific areas with large gradients of the wave amplitude magnitudes. Then, a comparison of 6 different wave gauges see Figure B.2, is conducted for 7 new locations per wave gauge, as explained on Appendix D.3.1. Those results are illustrated on the following Figures:

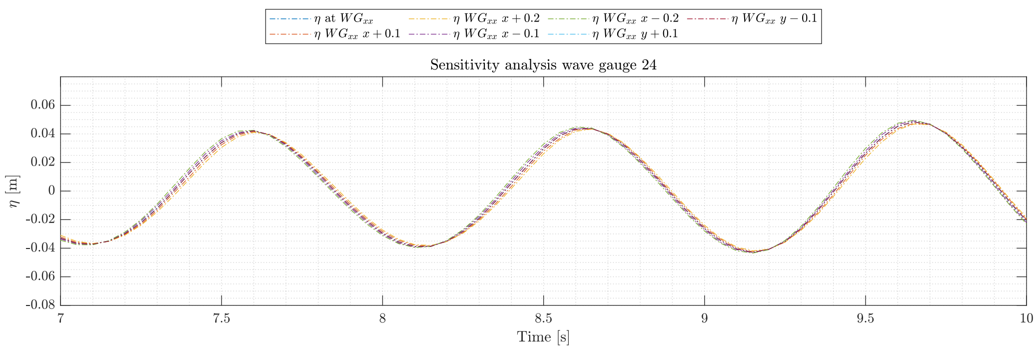

Figure D.31: Sensitivity analysis of wave gauge location on the free surface elevation inside the chamber)

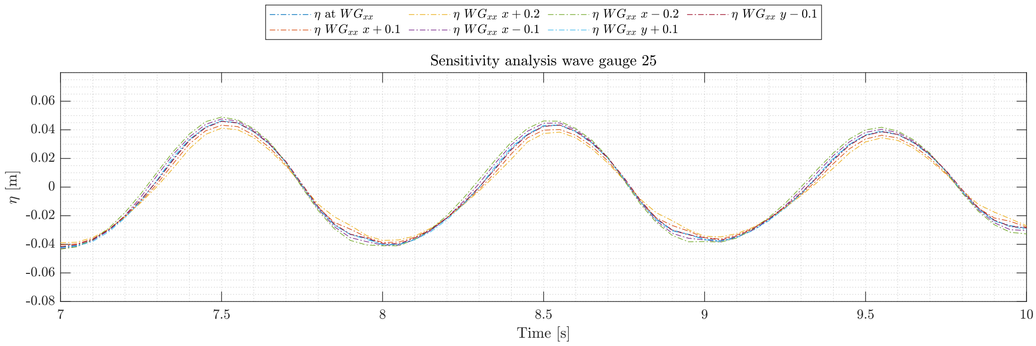

Figure D.32: Sensitivity analysis of wave gauge location on the free surface elevation inside the chamber)

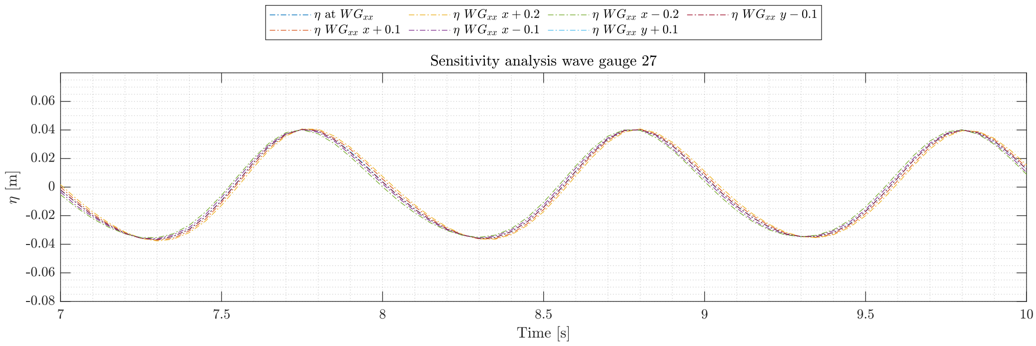

Figure D.33: Sensitivity analysis of wave gauge location on the free surface elevation inside the chamber)

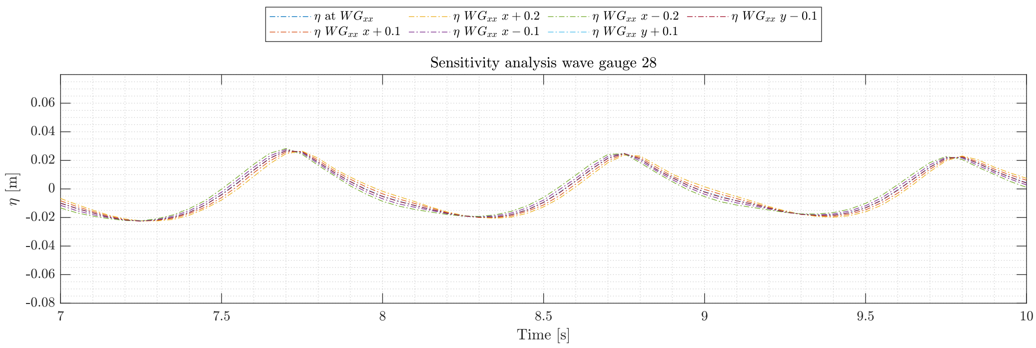

Figure D.34: Sensitivity analysis of wave gauge location on the free surface elevation inside the chamber)

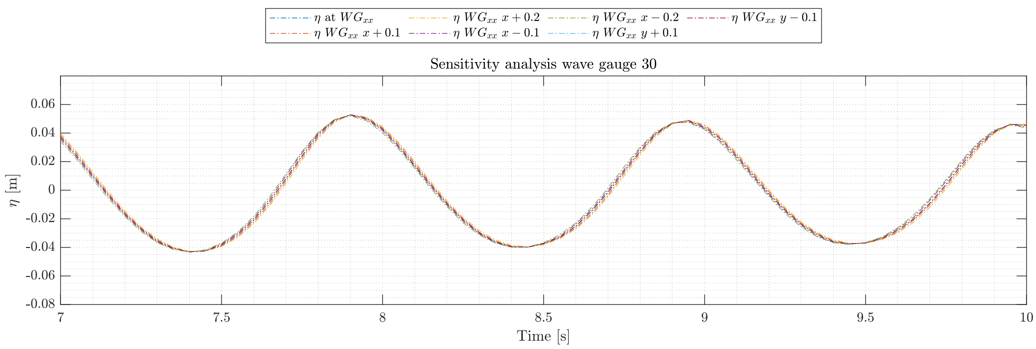

Figure D.35: Sensitivity analysis of wave gauge location on the free surface elevation inside the chamber)

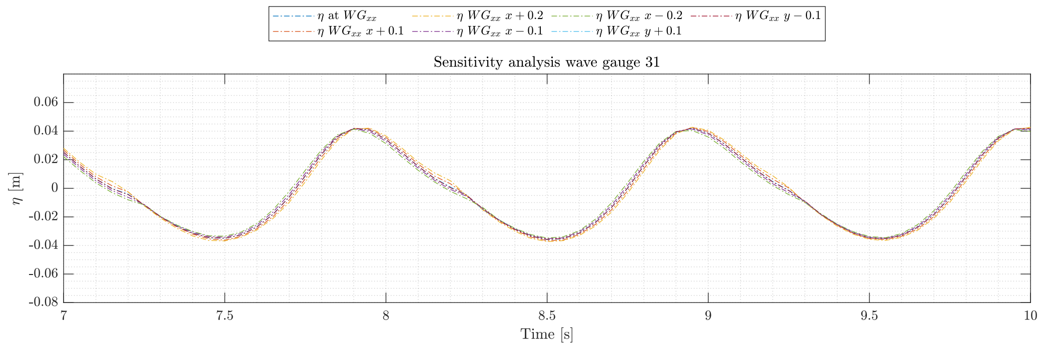

Figure D.36: Sensitivity analysis of wave gauge location on the free surface elevation inside the chamber)

Similar conclusions as the sensitivity analysis on wave 18 are obtained. The phase difference between the measured free surface elevation is caused by the difference location points. Also, there is a variation on the wave amplitudes, which it is caused by the strong wave-chamber interaction that generates a complex state inside the chamber. However, following the same trend as wave $s = 3.80$ this does not explain the large difference found on the validation analysis of the 3D model.

Y+ value

In this section the Y+ value is presented in two different ways, the first one (Figure D.37) illustrates the maximum, average and minimum values over the entire simulation. The second Figure D.38, illustrates this parameter at the surface of the body. This last one helps to understand the distribution of this parameter at the surface of the body.

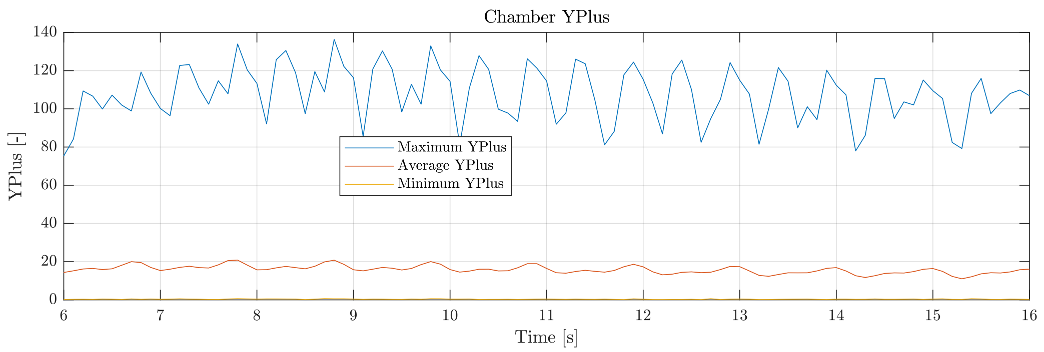

Figure D.37: Maximum, minimum and average Y+ value of the entire A4 chamber configuration over the time for $H = 0.1$ meters and $T = 1$ second

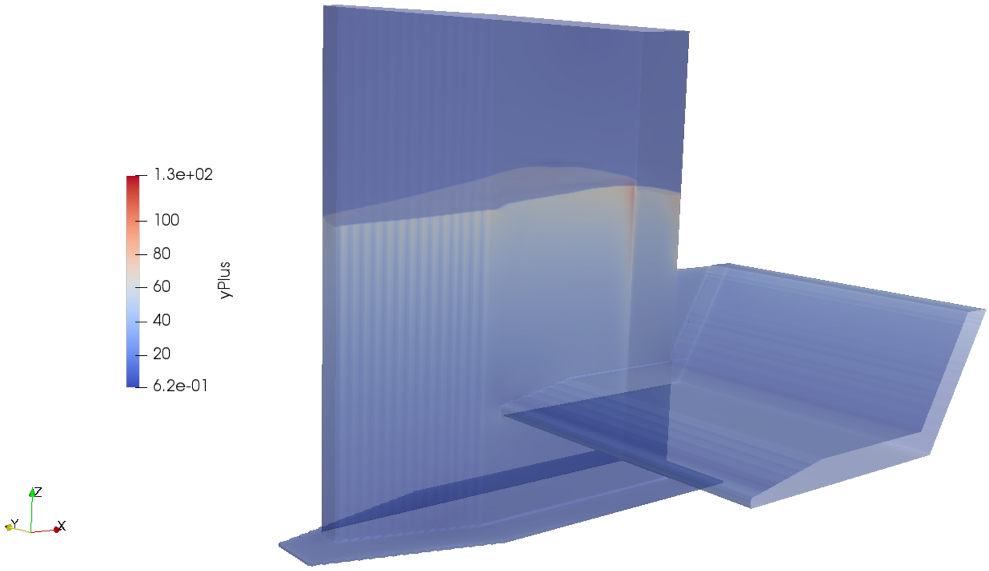

Figure D.38: Y+ value over the entire chamber surface for $time = 8.9$, see Appendix D.3.2 Figure D.37

D.4 Validation 3D model A5 chamber configuration

In this section extra data that is not included on the main report for the analysis of the wave-structure interaction of the A5 chamber configuration is presented.

D.4.1 Validation of A5 chamber for wave test number 18. Steepness 3.80 %

In this section some extra information is illustrated for the validation of the A5 chamber configuration of wave test number 18 with $s = 3.80\%$.

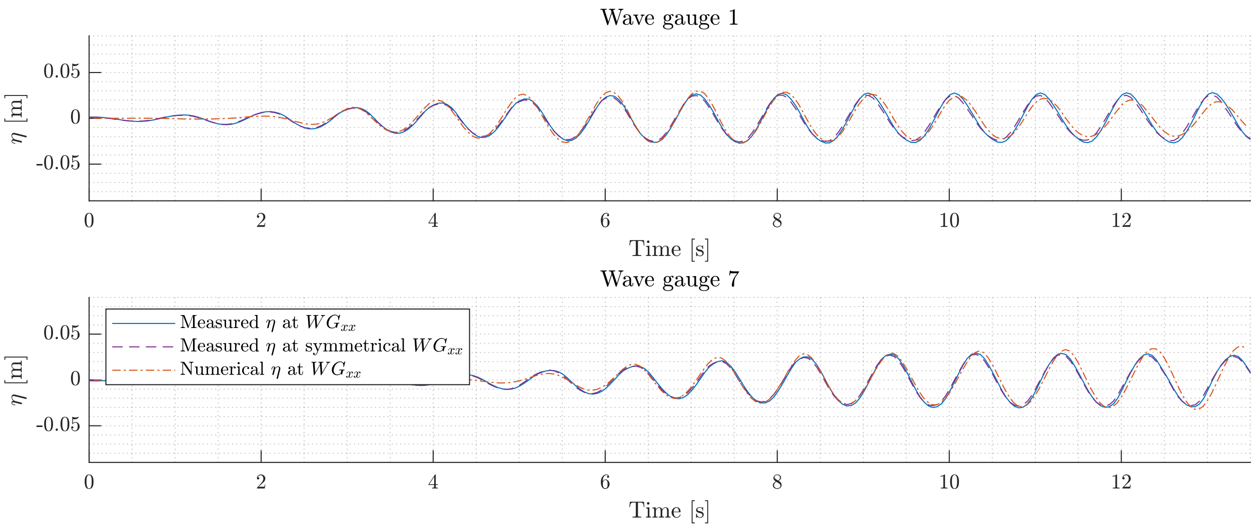

Figure D.39: Free surface elevation at different wave gauges locations, see Figure B.2, for A5 chamber configuration, see Figure B.4, and wave test number 18. 2 WG measurement from empirical data are plotted together, the actual location and the symmetrical WG measurement (i.e. $WG-1$ and $WG-8$)

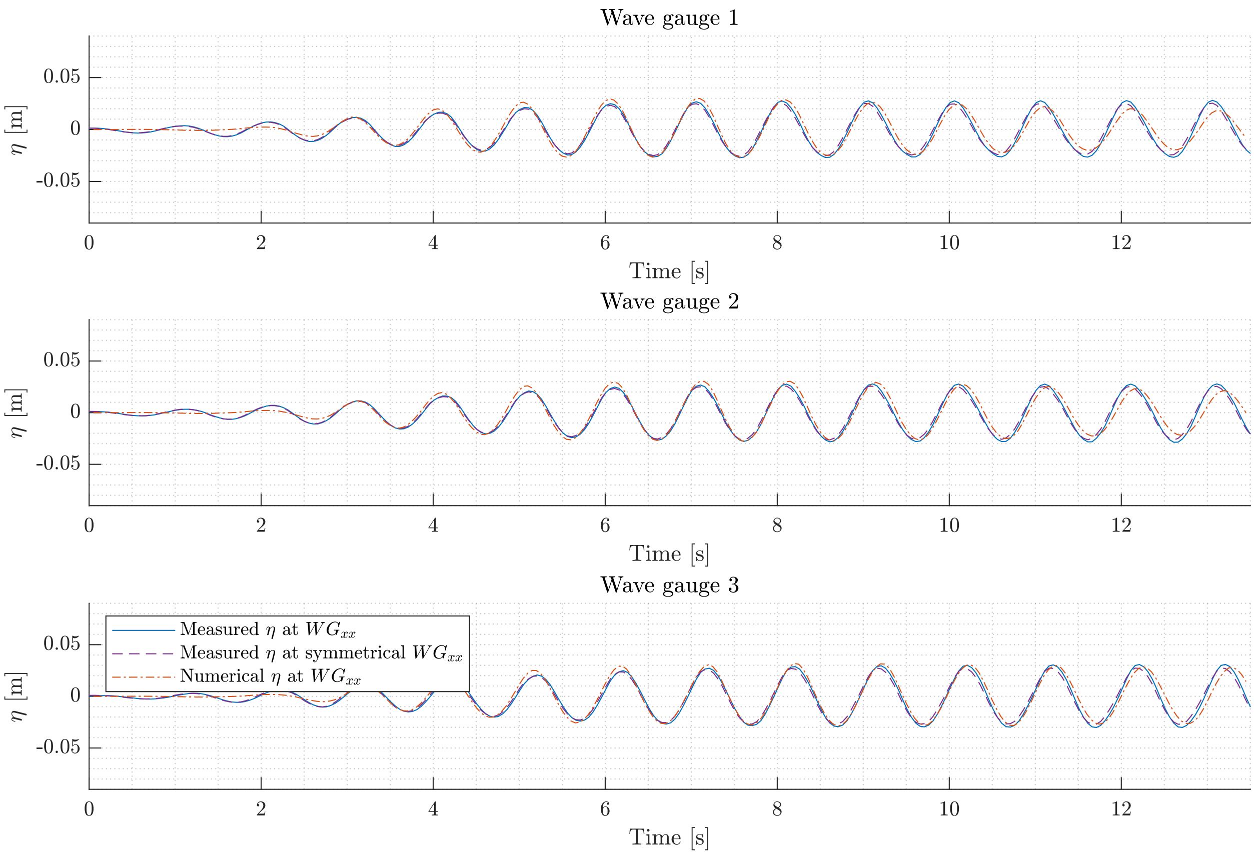

Figure D.40: Free surface elevation at different wave gauges locations, see Figure B.2, for A4 chamber configuration, see Figure B.4, and wave test number 18. 2 WG measurement from empirical data are plotted together, the actual location and the symmetrical WG measurement (i.e. $WG-1$ and $WG-8$)

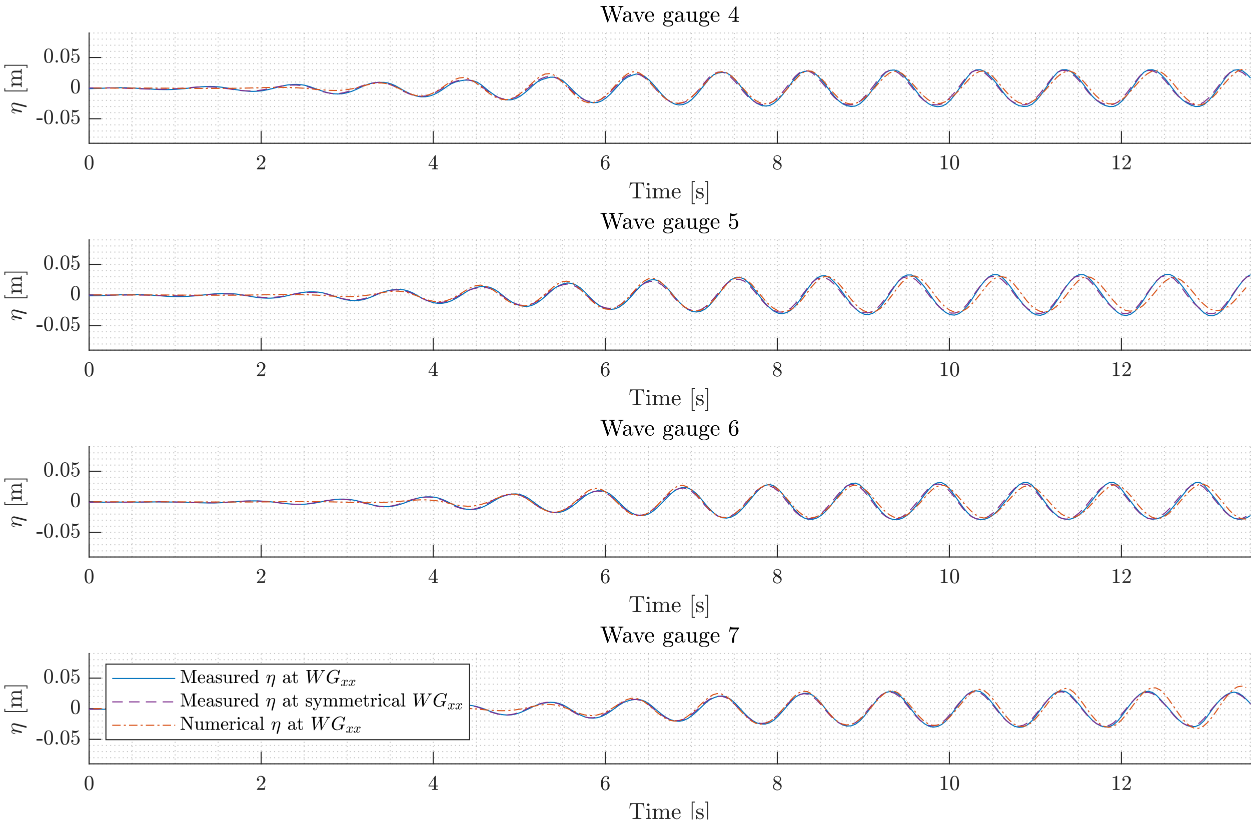

Figure D.41: Free surface elevation at different wave gauges locations, see Figure B.2, for A5 chamber configuration, see Figure B.4, and wave test number 18. 2 WG measurement from empirical data are plotted together, the actual location and the symmetrical WG measurement (i.e. $WG-4$ and $WG-11$)

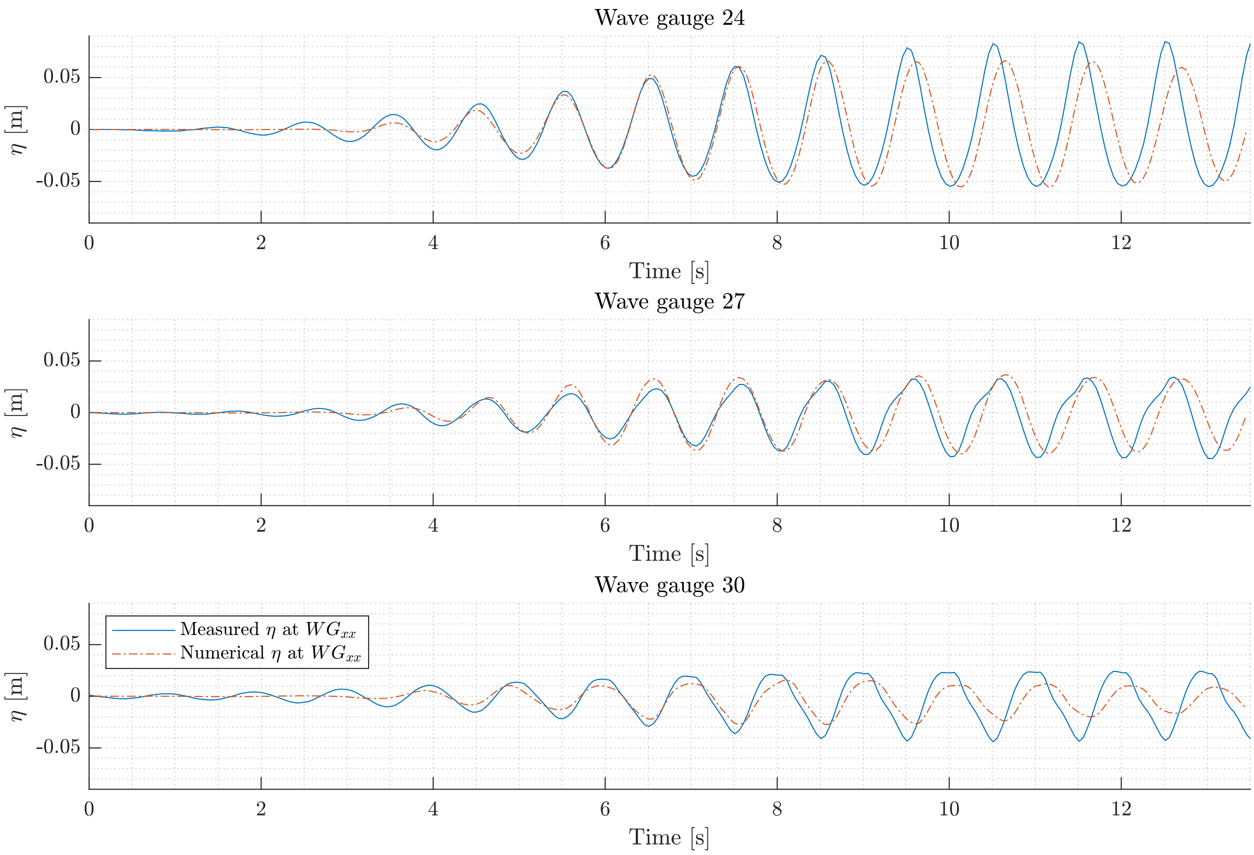

Figure D.42: Free surface elevation at different wave gauges locations, see Figure B.2, for A5 chamber configuration, see Figure B.4, and wave test number 18

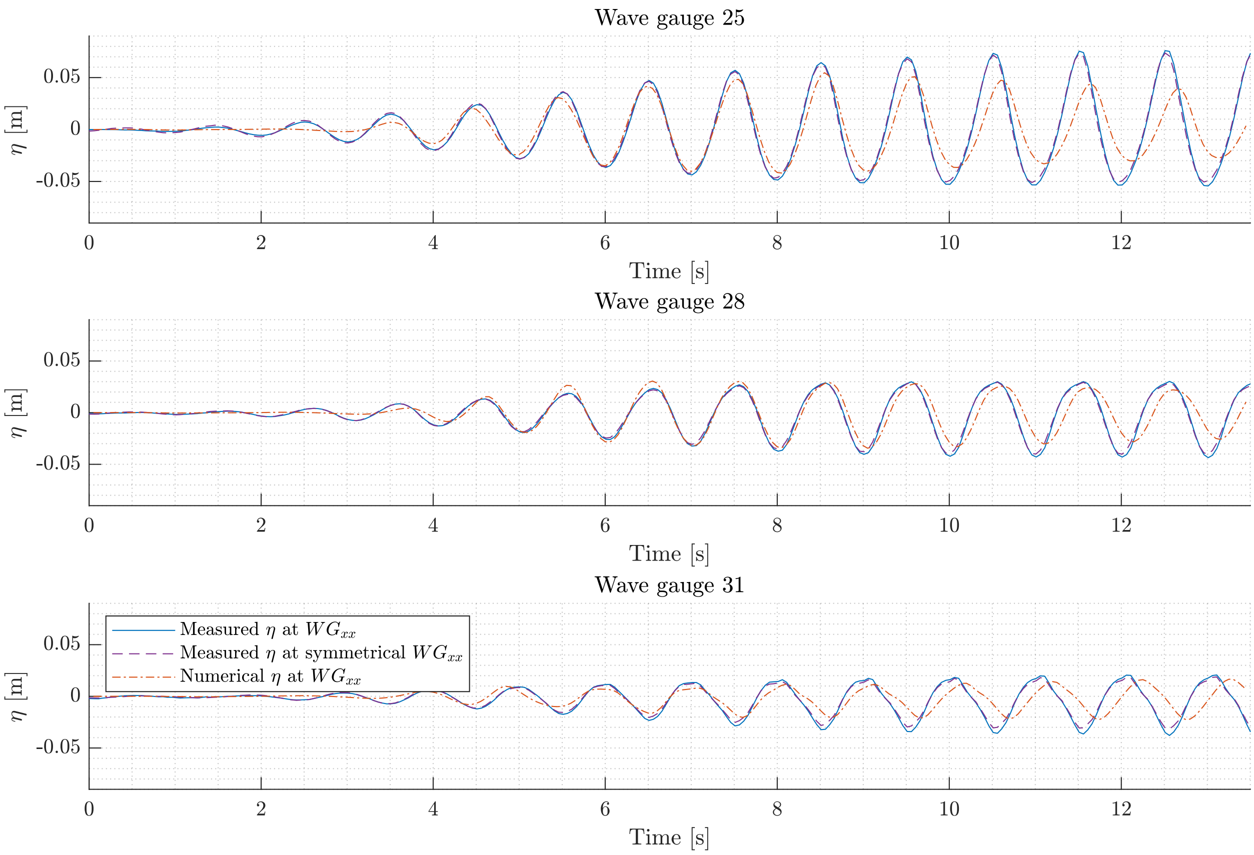

Figure D.43: Free surface elevation at different wave gauges locations, see Figure B.2, for A5 chamber configuration, see Figure B.4, and wave test number 18. 2 WG measurement from empirical data are plotted together, the actual location and the symmetrical WG measurement (i.e. $WG-25$ and $WG-23$)

Sensitivity analysis wave gauge location

This sensitivity analysis is conducted in the same way as the analysis for A4 chamber configuration and wave $s = 3.80$ on Appendix D.4.2. This analysis is performed in specific areas with large gradients of the wave amplitude magnitudes. Then, a comparison of 6 different wave gauges see Figure B.2, is conducted for 7 new locations per wave gauge, as explained on Appendix D.4.1. Those results are illustrated on the following Figures:

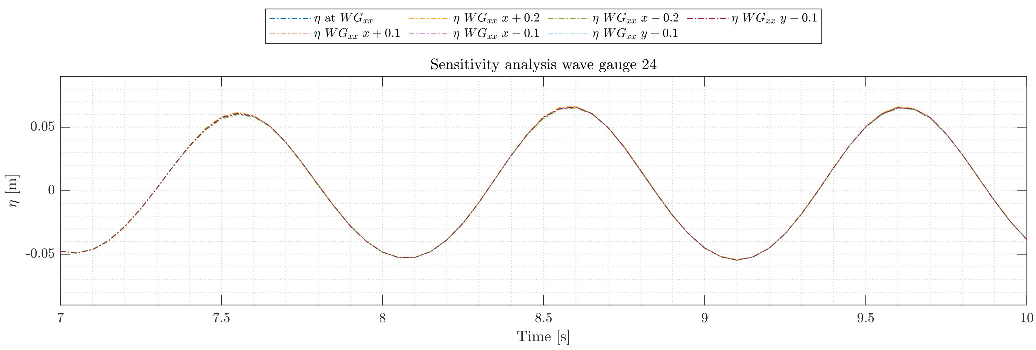

Figure D.44: Sensitivity analysis of wave gauge location on the free surface elevation inside the chamber)

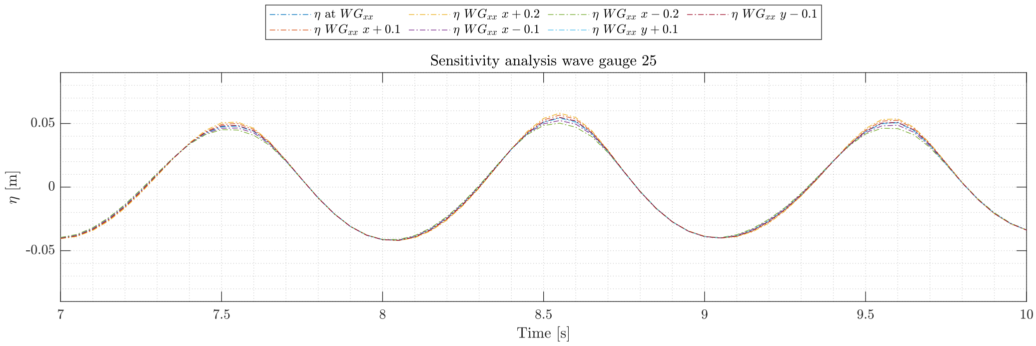

Figure D.45: Sensitivity analysis of wave gauge location on the free surface elevation inside the chamber)

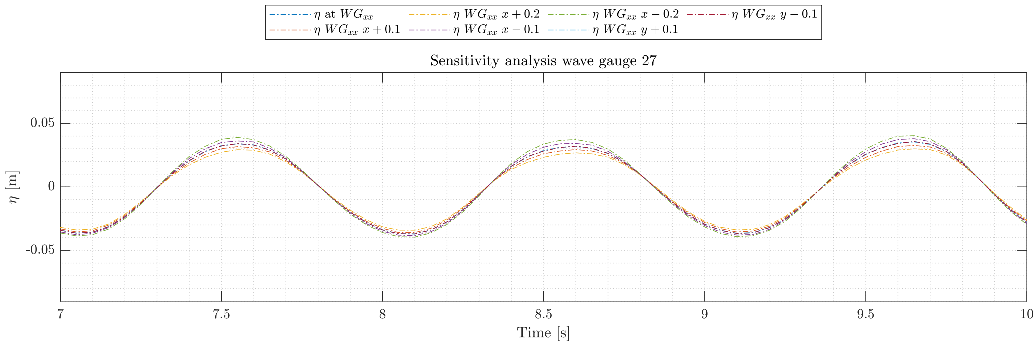

Figure D.46: Sensitivity analysis of wave gauge location on the free surface elevation inside the chamber)

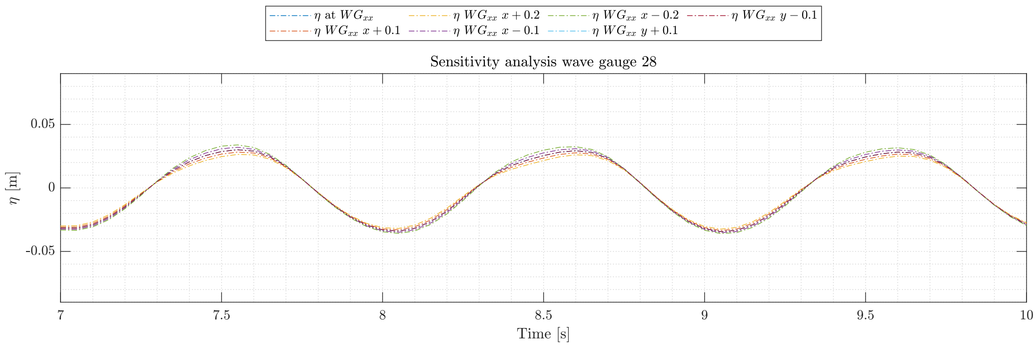

Figure D.47: Sensitivity analysis of wave gauge location on the free surface elevation inside the chamber)

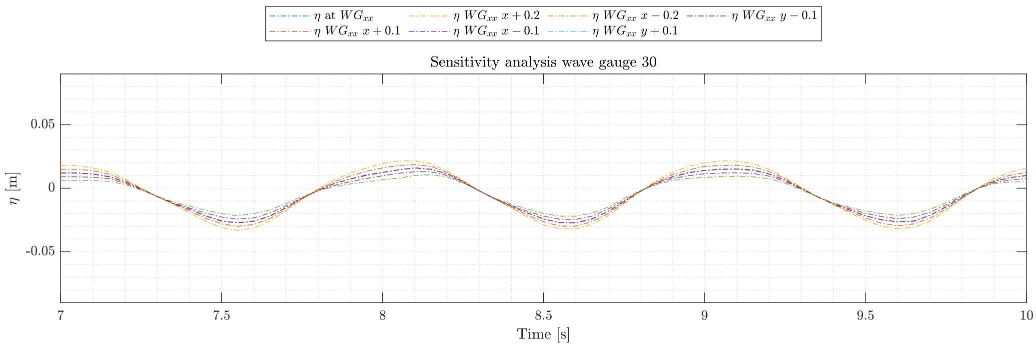

Figure D.48: Sensitivity analysis of wave gauge location on the free surface elevation inside the chamber)

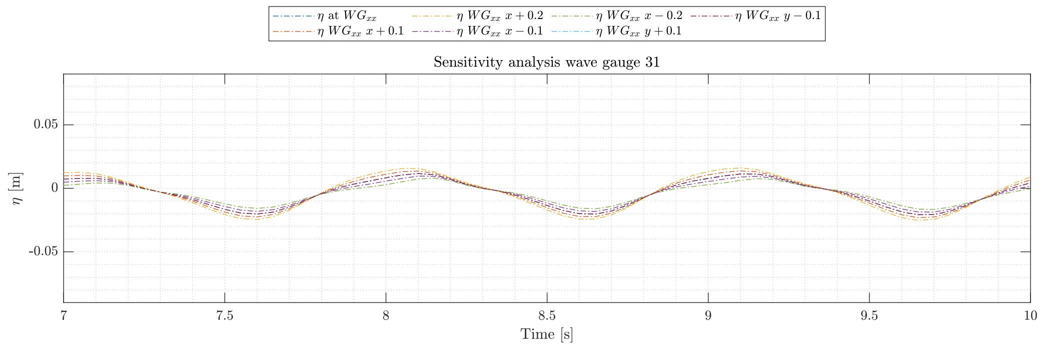

Figure D.49: Sensitivity analysis of wave gauge location on the free surface elevation inside the chamber)

Y+ value

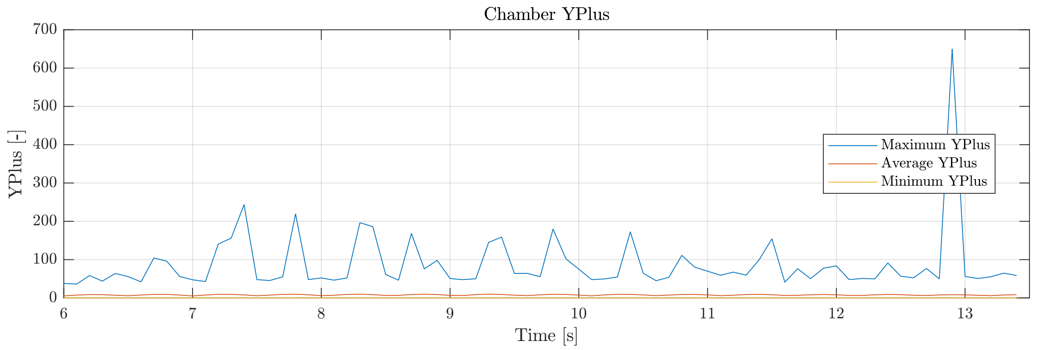

Figure D.50: Maximum, minimum and average Y+ value of the entire A5 chamber configuration over the time

D.4.2 Validation of A5 chamber for wave test number 20. Steepness 6.23 %

In this section some extra information is illustrated for the validation of the A5 chamber configuration of wave test number 20 with $s = 6.23\%$.

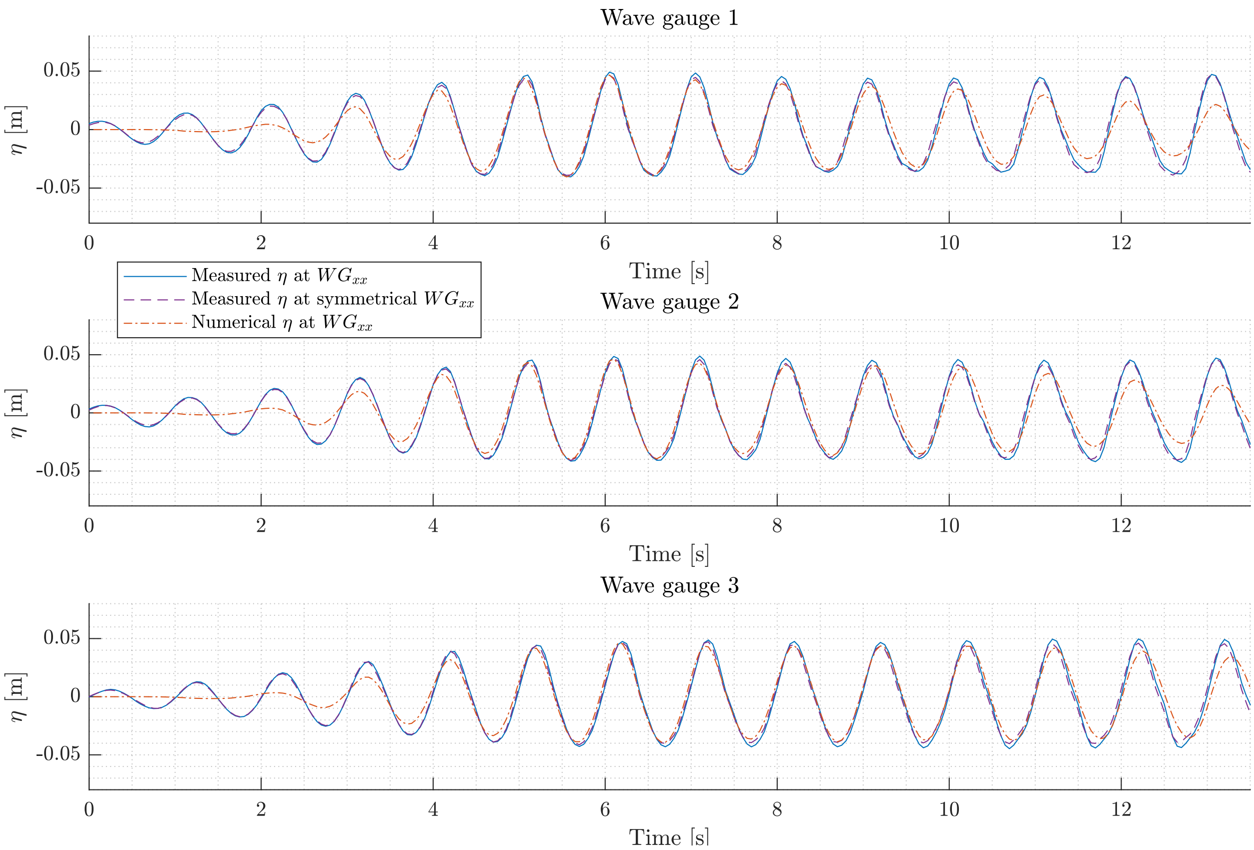

Figure D.51: Free surface elevation at different wave gauges locations, see Figure B.2, for A4 chamber configuration, see Figure B.4, and wave test number 20. 2 WG measurement from empirical data are plotted together, the actual location and the symmetrical WG measurement (i.e. $WG-1$ and $WG-8$)

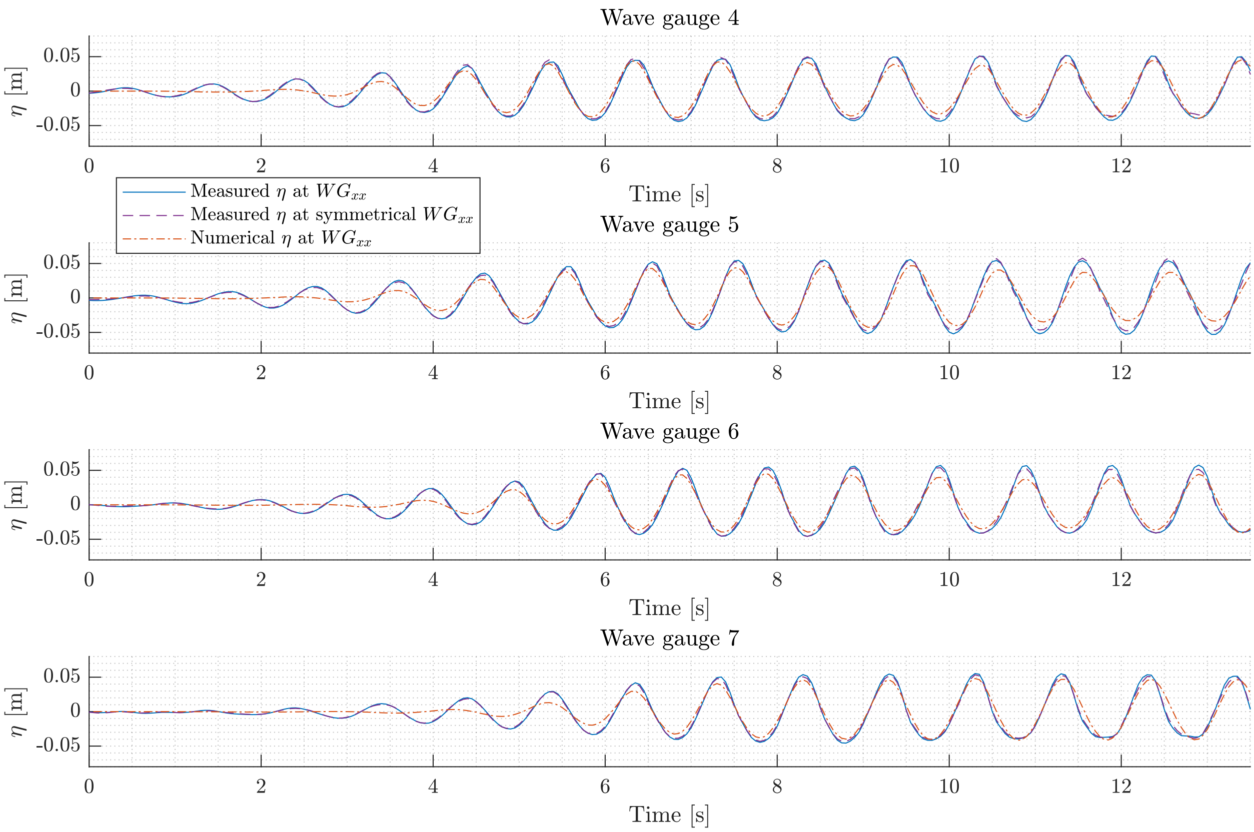

Figure D.52: Free surface elevation at different wave gauges locations, see Figure B.2, for A5 chamber configuration, see Figure B.4, and wave test number 20. 2 WG measurement from empirical data are plotted together, the actual location and the symmetrical WG measurement (i.e. $WG-4$ and $WG-11$)

Sensitivity analysis wave gauge location

This sensitivity analysis is conducted in the same way as the analysis for A4 chamber configuration and wave $s = 6.23$ on Appendix D.4.2. This analysis is performed in specific areas with large gradients of the wave amplitude magnitudes. Then, a comparison of 6 different wave gauges see Figure B.2, is conducted for 7 new locations per wave gauge, as explained on Appendix D.4.2. Those results are illustrated on the following Figures:

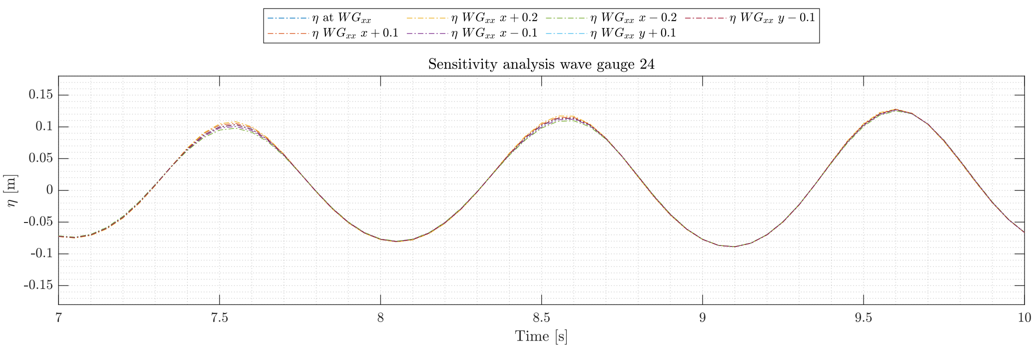

Figure D.53: Sensitivity analysis of wave gauge location on the free surface elevation inside the chamber)

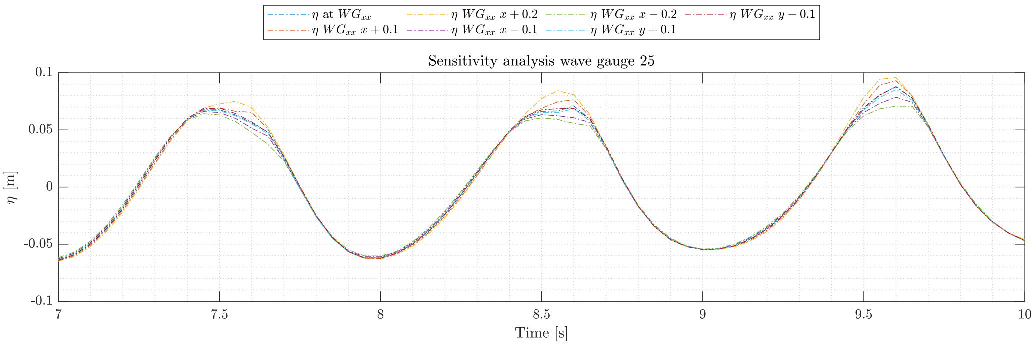

Figure D.54: Sensitivity analysis of wave gauge location on the free surface elevation inside the chamber)

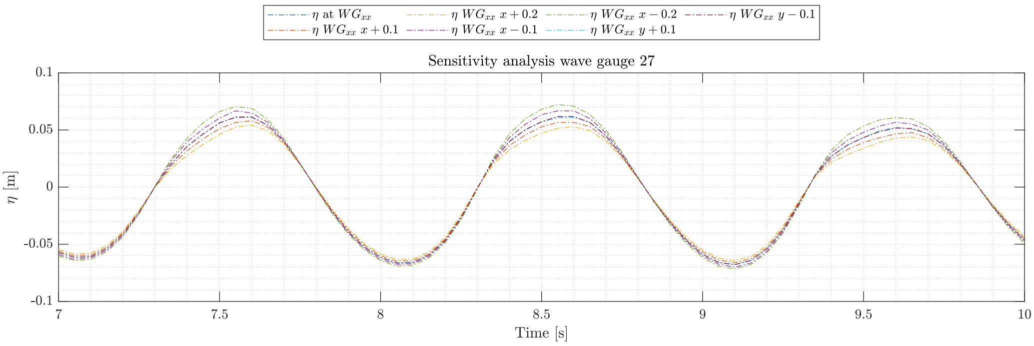

Figure D.55: Sensitivity analysis of wave gauge location on the free surface elevation inside the chamber)

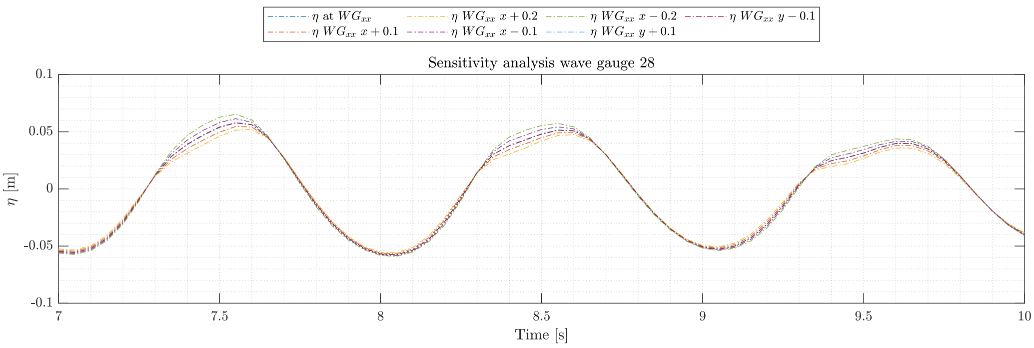

Figure D.56: Sensitivity analysis of wave gauge location on the free surface elevation inside the chamber)

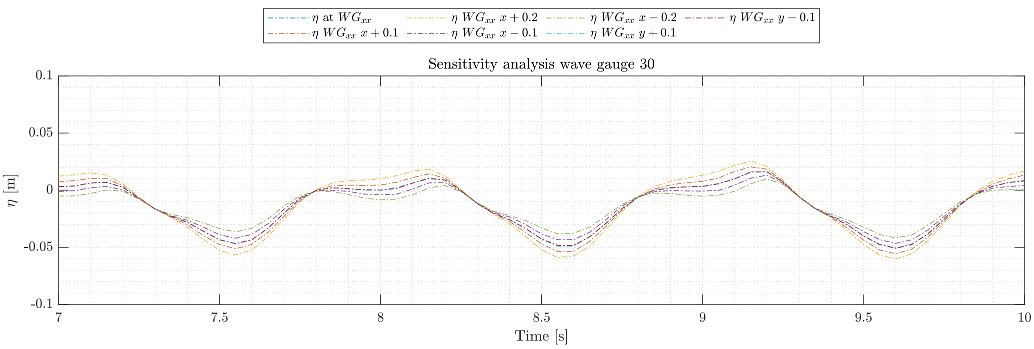

Figure D.57: Sensitivity analysis of wave gauge location on the free surface elevation inside the chamber)

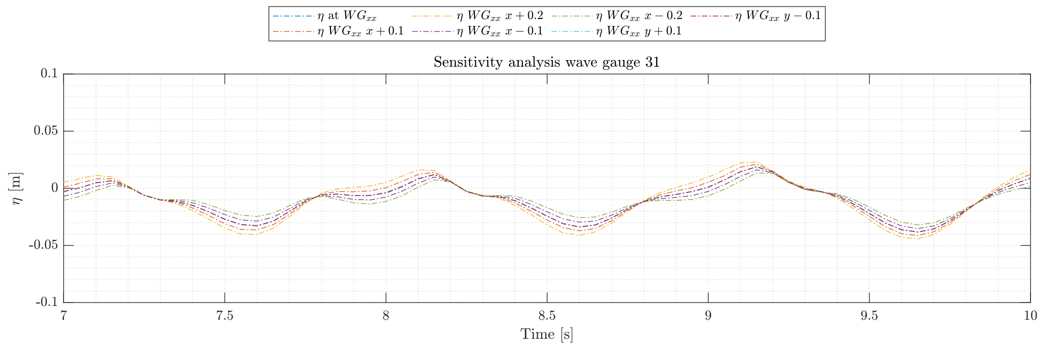

Figure D.58: Sensitivity analysis of wave gauge location on the free surface elevation inside the chamber)

Y+ value

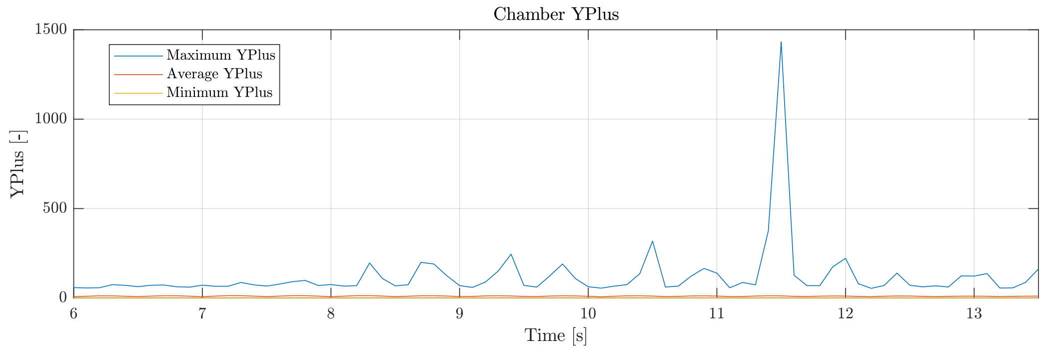

Figure D.59: Maximum, minimum and average Y+ value of the entire A5 chamber configuration over the time

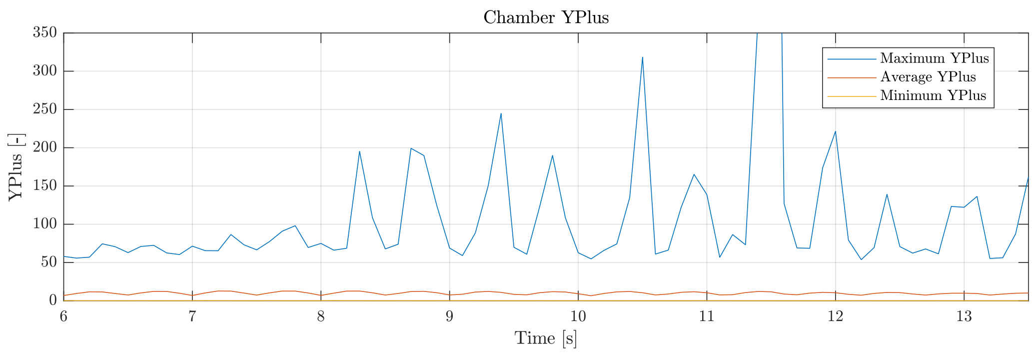

Figure D.60: Maximum, minimum and average Y+ value of the entire A5 chamber configuration over the time

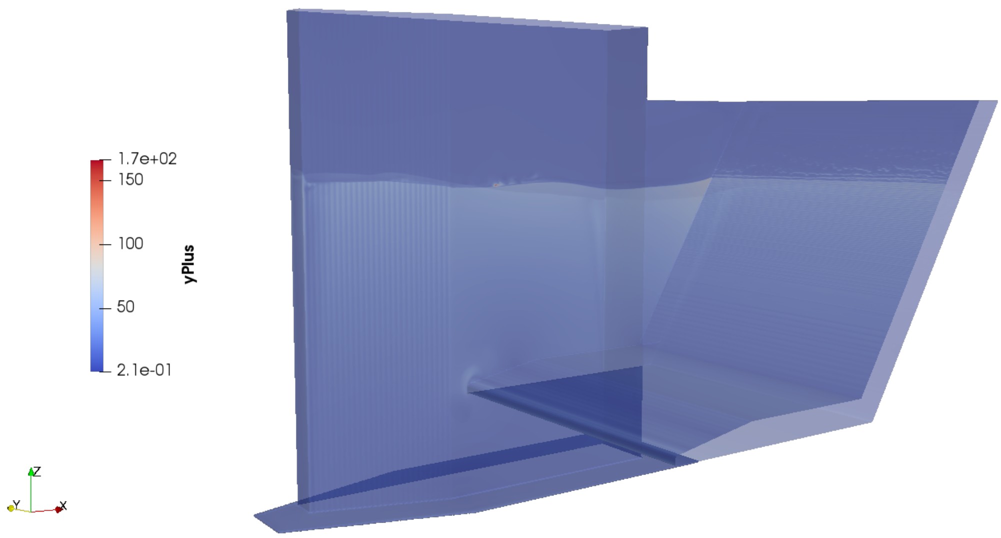

Figure D.61: Y+ value over the entire chamber surface for $time = 8.8$, see Appendix D.4.2 Figures D.59 and D.60

Analysis numerical model E

In this appendix all relevant information related to Section 6 is illustrated, which is related to the analysis of the CFD simulations. Mainly plots from numerical models taken with paraView visualizer are shown. Those figures illustrates the free surface elevation, the Y+ value, and the vortex generated around the chamber by terms of the so-called Q factor.

E.1 Introduction and main data

The following table summarize the main parameter of the waves implemented on the 3D analysis. Those values are implemented on Section 6 for the CFD and some of the WAMIT simulations

Wave test nº	Wave height [m]	Period [s]	λ [m]	Wave Number [-]	Steepness [%]
1	0.06	1.00	1.58	3.98	3.80
2	0.06	1.50	3.36	1.87	1.79
3	0.06	1.70	4.12	1.53	1.46
4	0.06	2.00	5.22	1.20	1.15
5	0.06	2.50	6.99	0.90	0.86
6	0.10	1.00	1.62	3.91	6.23
7	0.10	1.50	3.37	1.87	2.96
8	0.10	1.70	4.12	1.53	2.43
9	0.10	2.00	5.23	1.20	1.91
10	0.10	2.50	7.00	0.90	1.43
11	0.20	1.50	3.41	1.84	6.15
12	0.32	2.00	5.31	1.18	6.03
13	0.44	2.50	7.22	0.87	6.10
14	1.80	13.70	209.70	0.03	0.86

Table E.1: Wave characteristics implemented on the 3D analysis

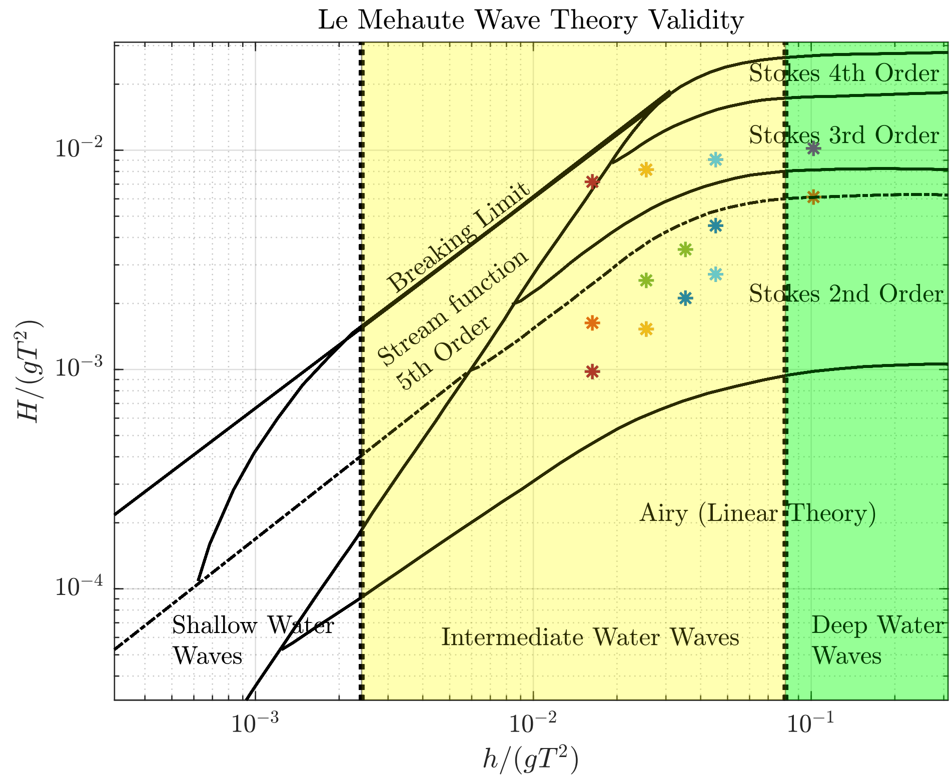

Figure E.1: Le Mehaute diagram for waves from Table E.1 used on the 3D analysis of wave-chamber interaction

E.2 Wave amplification factor

This section aims to give a better understanding of Section 6.3 by giving extra information that supports the ideas explained on the analysis of the wave amplification factor.

In order to get a different perspective of the wave amplification factor, this is illustrated as a function of the steepness to check if there is any relation between both parameters. This is illustrated o Figure E.2, which is taken from the data illustrated on Figure 6.9.

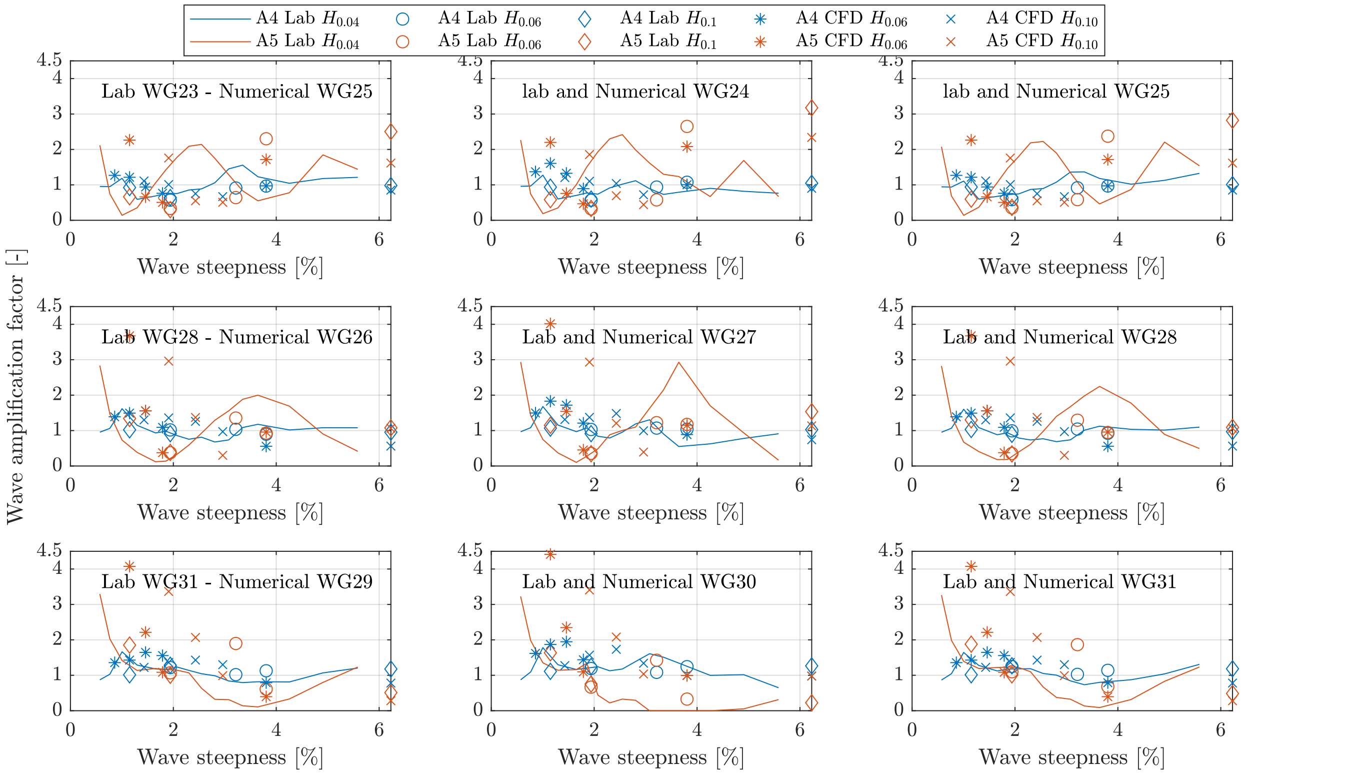

Figure E.2: Comparison between experimental and numerical wave amplification factors over the steepness - WG 23, 26 and 29 from experimental results are compared to WG 25, 28 and 31 respectively due to the symmetry applied on CFD model

As it can be seen on Table 6.1, some cases with high amplitudes are also simulated, those sea states have a steepness around 6%. Then, the wave amplification factor with all cases shown on Table 6.1 are illustrated on Figure E.3. In this case it can clearly be seen that all cases with a high steepness are barely amplified. This is caused by two reasons. The first reason is caused by the relation between wave height and length and chamber size. Then *A4 absorber* $s \approx 6\%$ and *A5 absorber* $s \approx 6\%$ are too extreme waves to have a proper interaction between the chamber and the wave, which might lead into a wrong understanding of the wave-chamber interaction.

The second reason it caused by the fact that waves are hitting the structure violently, causing a very unstable conditions inside the chamber. This totally change the beneficial influence of the chamber on them. It has been seen that in some cases waves are breaking as the chamber is acting as a wall, this is totally the opposite purpose of this chamber as dissipation of energy is occurring on breaking waves.

Therefore, cases *A4 absorber* $s \approx 6\%$ and *A5 absorber* $s \approx 6\%$ might lead into a wrong understanding of the influence of the chamber in the amplification of waves as breaking is expected to occur, which it is not the scope of this project. However, it is decided to include it on the appendix as this can be useful on future work.

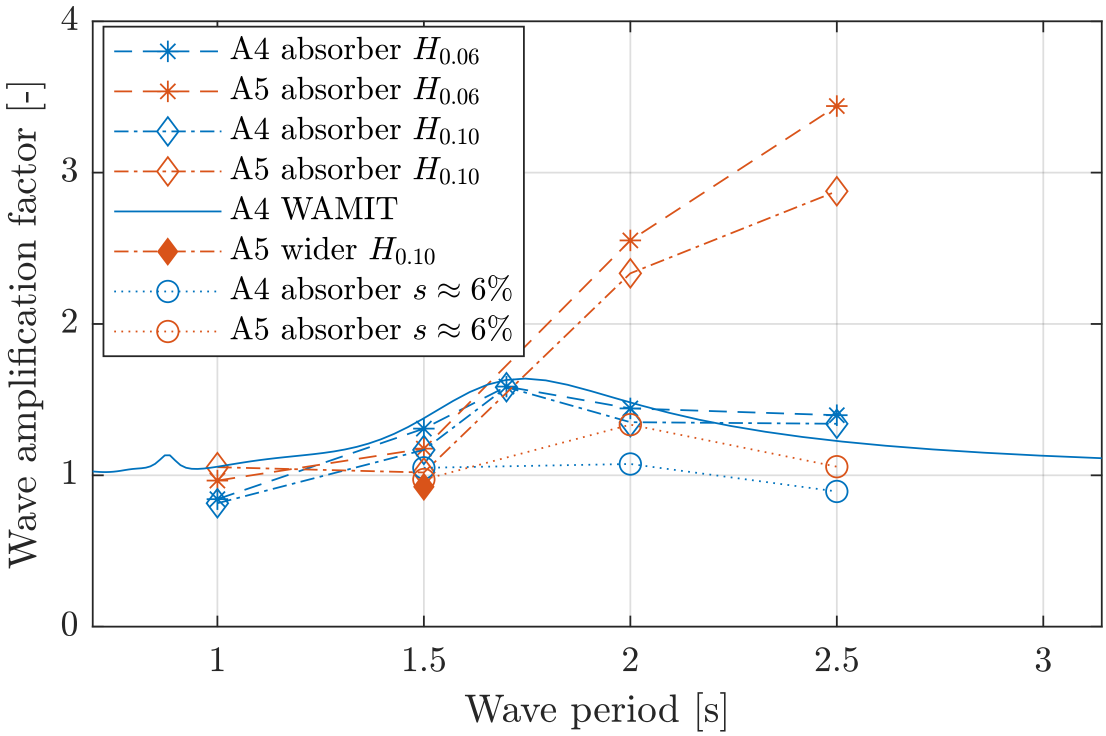

Figure E.3: Comparison of the mean wave amplification factor over periods at the area where the absorber would be located - CFD and WAMIT results

E.2.1 Wave amplification factor from experimental data

The following figure illustrates the wave amplification factor at different wave gauges locations, See Figure 3.2, for different chamber configurations, this analysis is conducted for wave height of 0.04 meters and varying the wave periods, This is only used to understand the influence of each individual part of the structure, as a different normalization is applied than the wave amplification factors applied on the main report.

It can be seen that reflected waves from the side wall have a high influence on the wave amplification factor at different locations. This can be understood by looking at A2 configuration, where only side walls are included. From wave gauge number 30 it can be seen, especially for low periods, that the side walls are being more amplified in this location than in any other position. This indicates that reflected waves from the wall, as explained on Section 6.4 are of importance to understand this behaviour. Also, another element that amplifies this effect it is the bottom part of the spoiler, which is illustrated by A3 configuration. This element amplifies the behaviour of reflected waves inside the chamber for higher periods. Then, A4 chamber configuration increases more the peak of resonance and amplifies its influence. This increase on the wave amplification factor is caused by a phenomenon called shoaling, which it is clear to see that there are some resonance peaks, and varies at different locations. Then, the last three configurations (A5-A6-A7) shows a similar behaviour, where the resonance frequency of the wave amplification factor is totally changed, those configurations are affected, not only by the previous phenomenons mentioned before, but also by the run up on the sloped wall. However, the main reason that causes to change the amplification factors are reflected waves from the sloped wall.

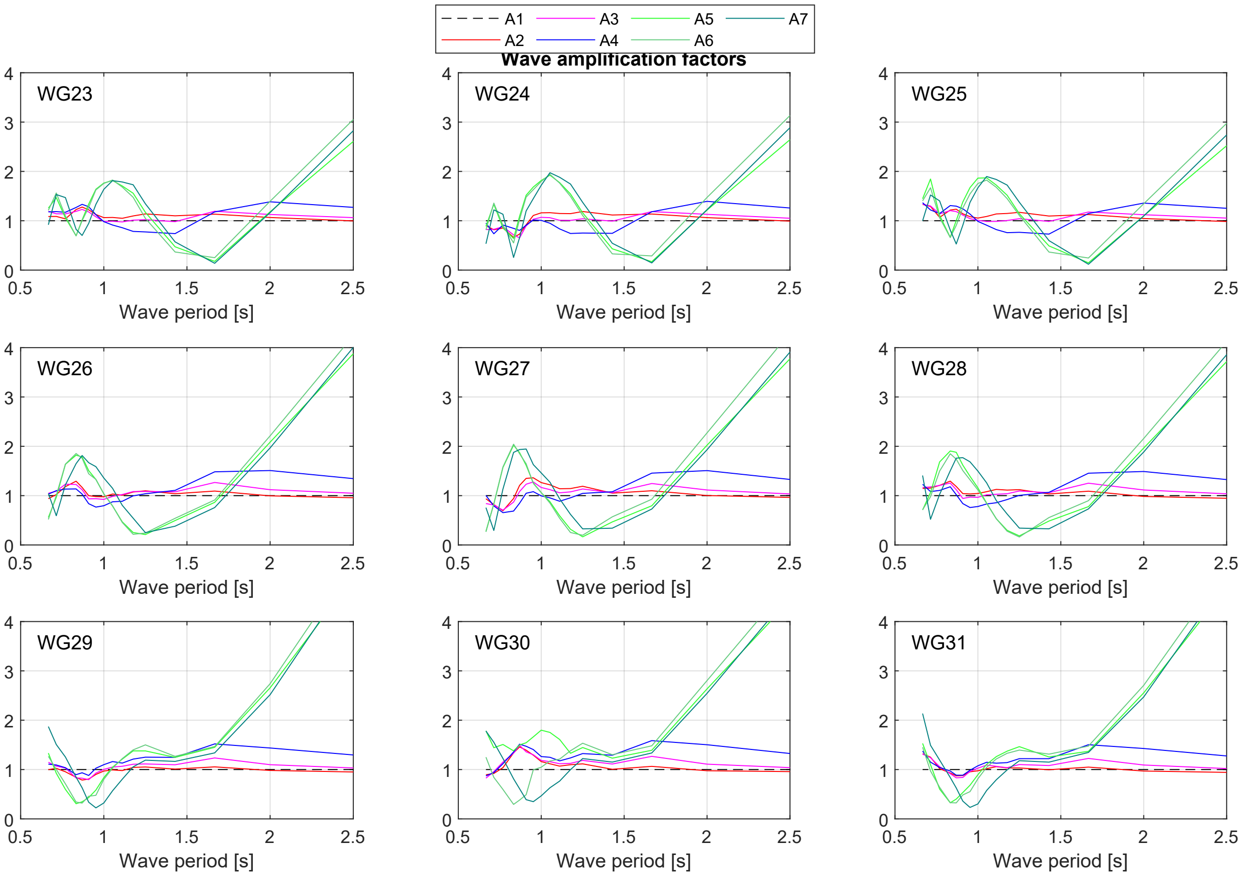

Figure E.4: Wave amplification factor for different sea states and different chamber configurations. A1 configuration are only propagated waves, A2 only side walls, A3 side walls and bottom spoiler, A4 original configuration, A5 extended spoiler, A6 lowered extended spoiler and moved and A7 lowered spoiler. M. Kramer (2020)

Then, it can be concluded that each part of the chamber interacts differently for different sea states for A4 chamber configuration. This theory is supported by experimental data as shown on Figure 3.6, where lower periods are more influenced by side walls, see Figure 6.10, while waves with periods around 1.7, see Figure 6.12, where the resonance peak is found, are more influenced by both the bottom part of the spoiler and the sloped wall, being the second one the one that influences the most. Also, is found that the sloped wall has a major influence on a wide range of periods, specially for those between 1.4 to 2.5 seconds.

E.3 Free surface elevation

In this section an area of 3 meters in the x-axis and 1.5 meters in the y-axis around the chamber is used to represent the free surface elevation from non-linear models based on CFD. Those illustrations presented in the following sections are taken from a visualizer called paraView. This tool is very useful for this task and also is able to illustrates some other parameters such us the velocity field, the Y+ value, the vortexes generated around the structure, the pressure field, etc.

E.3.1 A4 chamber configuration

In this section the free surface elevation for A4 chamber configuration is illustrated for 4 different waves over one period

Wave H=0.06 [m] T=1 [s]

In this section the free surface elevation for A4 configuration and wave H=0.06 [m] T=1 [s] is illustrated over one period, which is referred to run time $8-9$ seconds on the simulation.

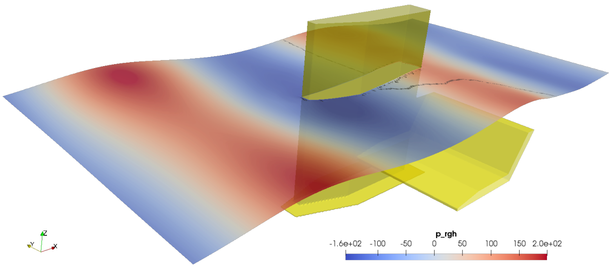

(a)

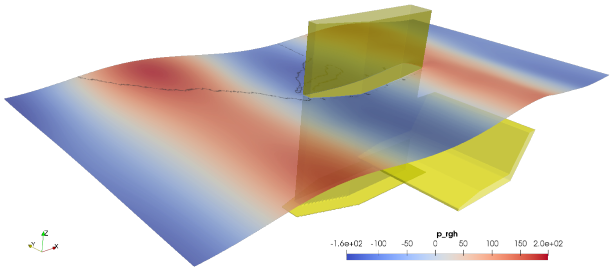

(b)

Figure E.5: Free surface elevation for $\alpha = 0.5$ and different t/T - a) t/T = 0.1, b) t/T = 0.2

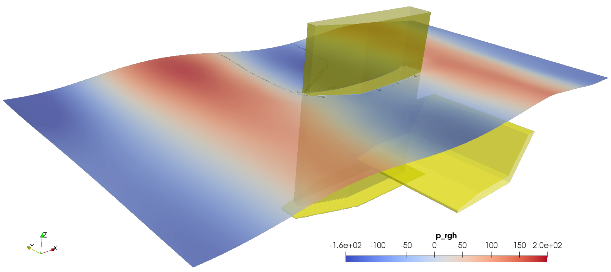

(a)

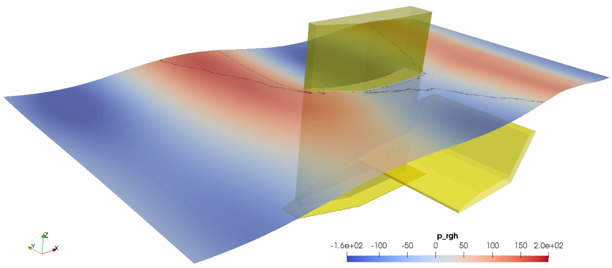

(b)

Figure E.6: Free surface elevation for $\alpha = 0.5$ and different t/T - a) t/T = 0.3, b) t/T = 0.4

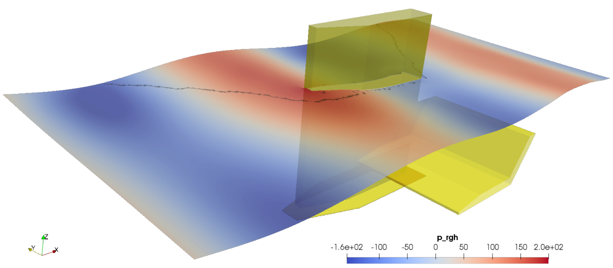

(a)

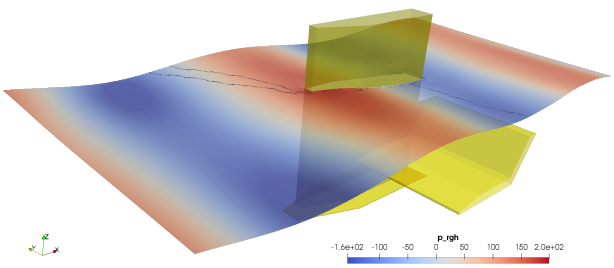

(b)

Figure E.7: Free surface elevation for $\alpha = 0.5$ and different t/T - a) t/T = 0.5, b) t/T = 0.6

In the following time step only t/T = 0.7 is presented as t/T = 0.8 data is corrupted and it is not possible to obtain any data from that specific time.

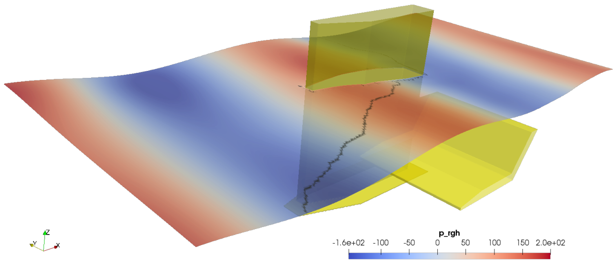

(a)

Figure E.8: Free surface elevation for $\alpha = 0.5$ and different t/T - a) t/T = 0.7, b) t/T = 0.8 (corrupted)

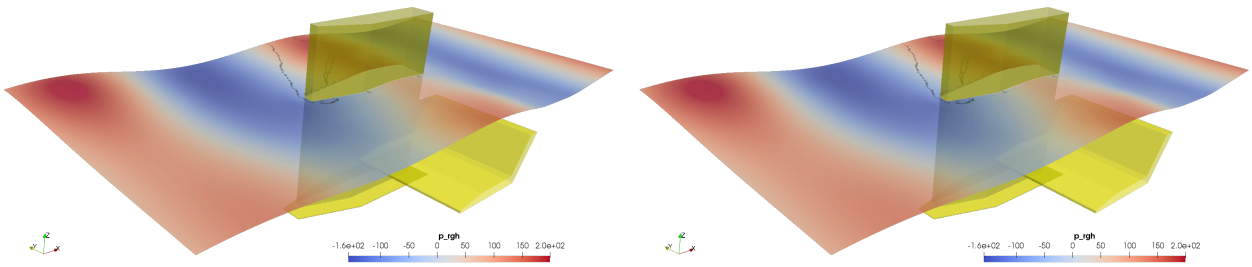

(a) (b)

Figure E.9: Free surface elevation for $\alpha = 0.5$ and different t/T - a) t/T = 0.9, b) t/T = 1

Wave H=0.06 [m] T=2 [s]

In this section the free surface elevation for A4 configuration and wave H=0.06 [m] T=2 [s] is illustrated over one period, which is referred to run time $14 - 16$ seconds on the simulation.

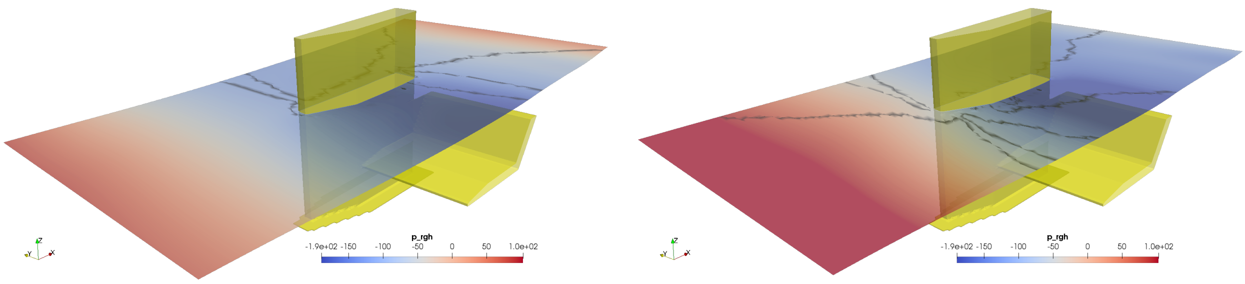

(a) (b)

Figure E.10: Free surface elevation for $\alpha = 0.5$ and different t/T - a) t/T = 0.1, b) t/T = 0.2

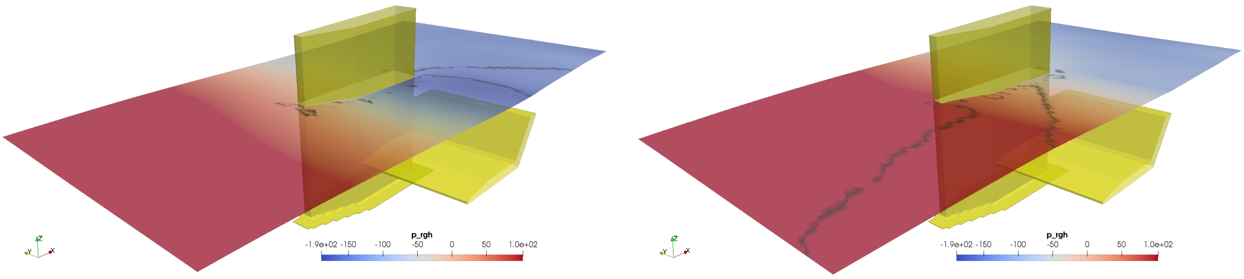

(a) (b)

Figure E.11: Free surface elevation for $\alpha = 0.5$ and different t/T - a) t/T = 0.3, b) t/T = 0.4

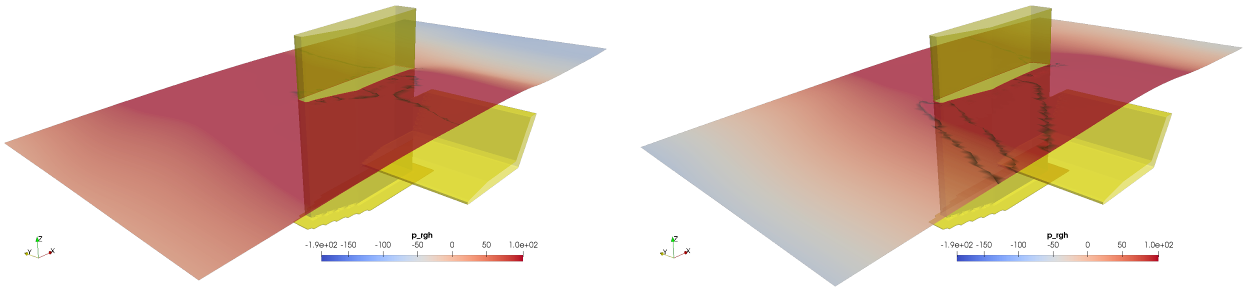

(a) (b)

Figure E.12: Free surface elevation for $\alpha = 0.5$ and different t/T - a) t/T = 0.5, b) t/T = 0.6

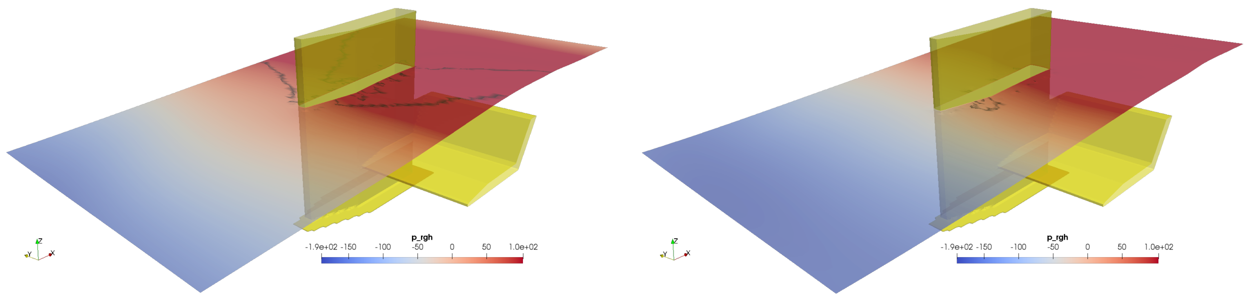

(a) (b)

Figure E.13: Free surface elevation for $\alpha = 0.5$ and different t/T - a) t/T = 0.7, b) t/T = 0.82

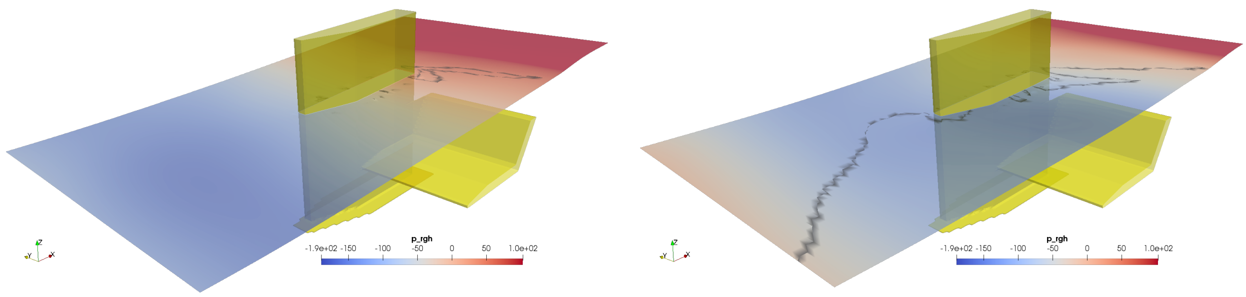

(a) (b)

Figure E.14: Free surface elevation for $\alpha = 0.5$ and different t/T - a) t/T = 0.9, b) t/T = 1

Wave H=0.1 [m] T=1 [s]

In this section the free surface elevation for A4 configuration and wave H=0.1 [m] T=1 [s] is illustrated over one period, which is referred to run time $8-9$ seconds on the simulation.

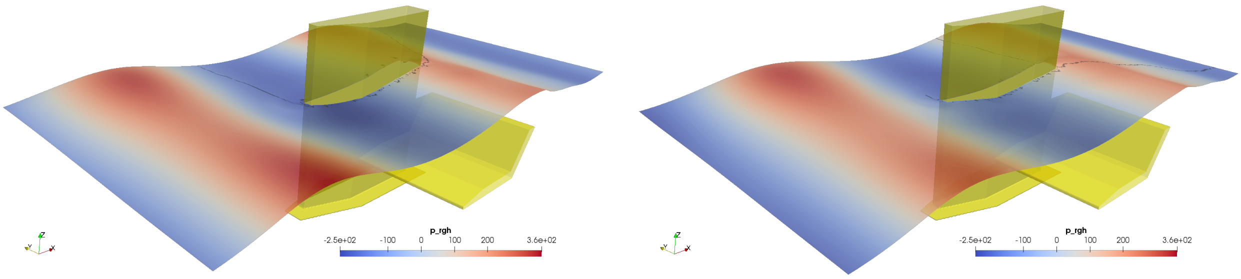

(a) (b)

Figure E.15: Free surface elevation for $\alpha = 0.5$ and different t/T - a) t/T = 0.1, b) t/T = 0.2

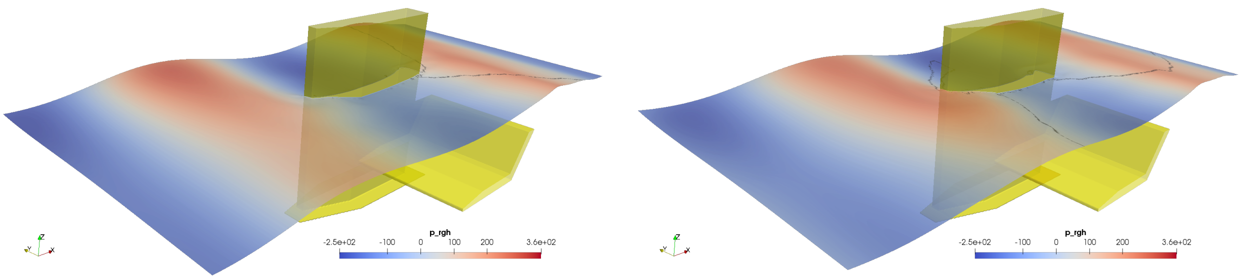

(a) (b)

Figure E.16: Free surface elevation for $\alpha = 0.5$ and different t/T - a) t/T = 0.3, b) t/T = 0.4

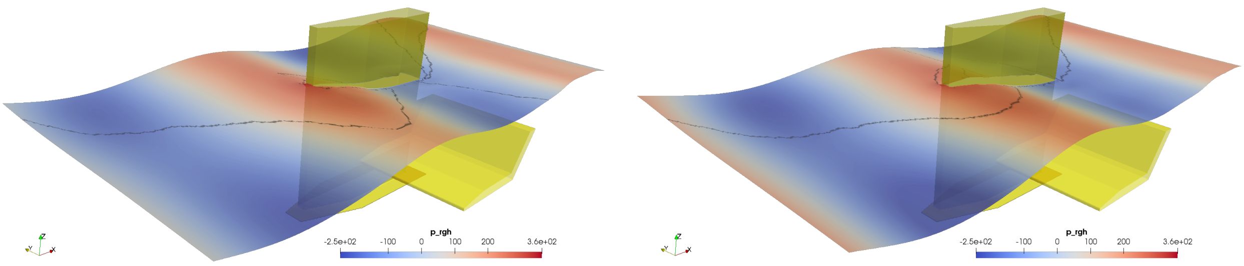

(a) (b)

Figure E.17: Free surface elevation for $\alpha = 0.5$ and different t/T - a) t/T = 0.5, b) t/T = 0.6

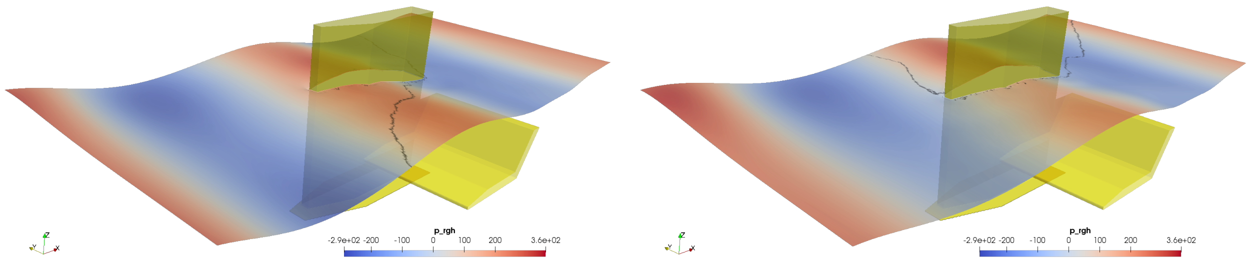

(a) (b)

Figure E.18: Free surface elevation for $\alpha = 0.5$ and different t/T - a) t/T = 0.7, b) t/T = 0.8

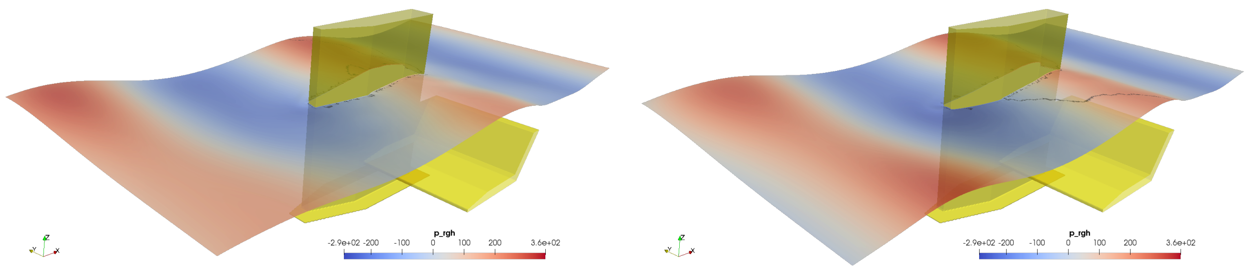

(a) (b)

Figure E.19: Free surface elevation for $\alpha = 0.5$ and different t/T - a) t/T = 0.9, b) t/T = 1

Wave H=0.1[m] T=2 [s]

In this section the free surface elevation for A4 configuration and wave H=0.1 [m] T=2 [s] is illustrated over one period, which is referred to run time $14 - 16$ seconds on the simulation.

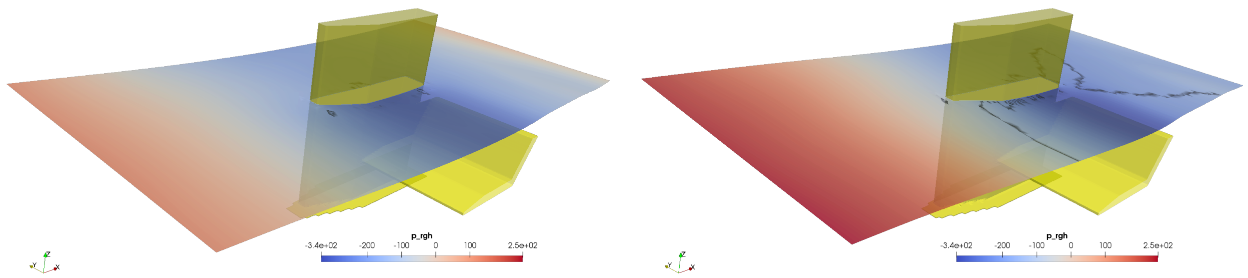

(a) (b)

Figure E.20: Free surface elevation for $\alpha = 0.5$ and different t/T - a) t/T = 0.1, b) t/T = 0.2

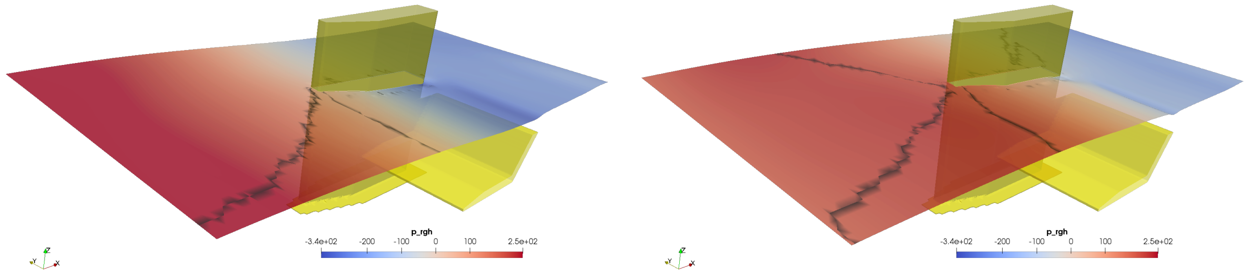

(a) (b)

Figure E.21: Free surface elevation for $\alpha = 0.5$ and different t/T - a) t/T = 0.3, b) t/T = 0.4

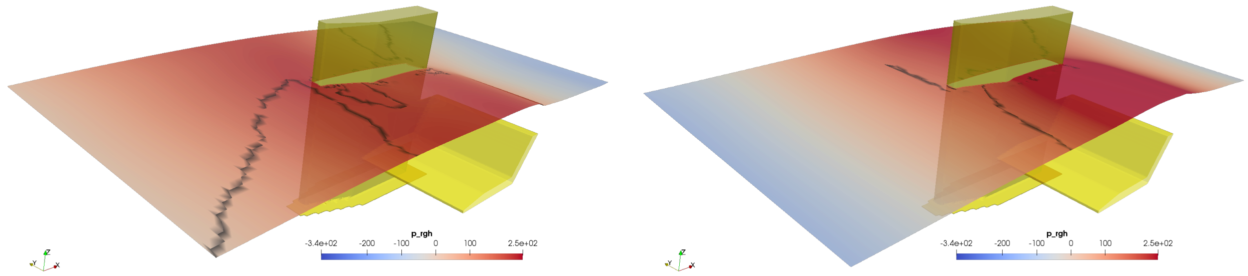

(a) (b)

Figure E.22: Free surface elevation for $\alpha = 0.5$ and different t/T - a) t/T = 0.5, b) t/T = 0.6

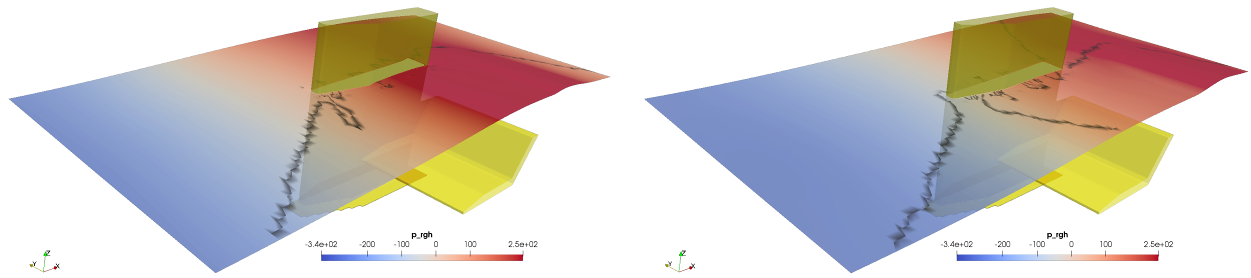

(a) (b)

Figure E.23: Free surface elevation for $\alpha = 0.5$ and different t/T - a) t/T = 0.7, b) t/T = 0.82

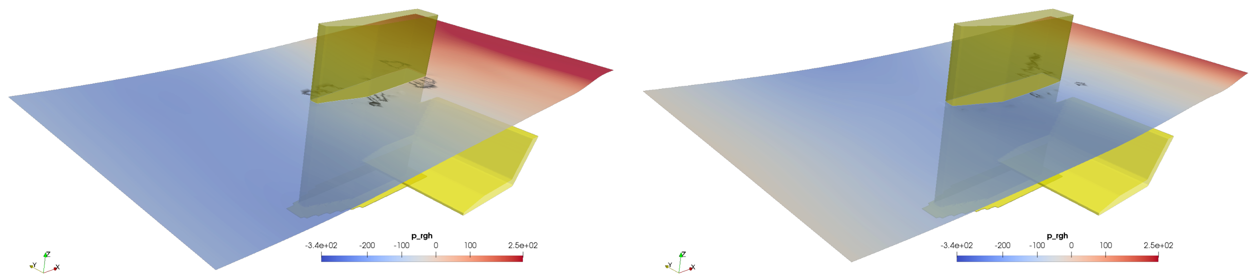

(a) (b)

Figure E.24: Free surface elevation for $\alpha = 0.5$ and different t/T - a) t/T = 0.9, b) t/T = 1

E.3.2 A5 chamber configuration

In this section the free surface elevation for A5 chamber configuration is illustrated for 4 different waves over one period.

Wave H=0.06 [m] T=2 [s]

In this section the free surface elevation for A5 configuration and wave H=0.06 [m] T=2 [s] is illustrated over one period, which is referred to run time 14 – 16 seconds on the simulation.

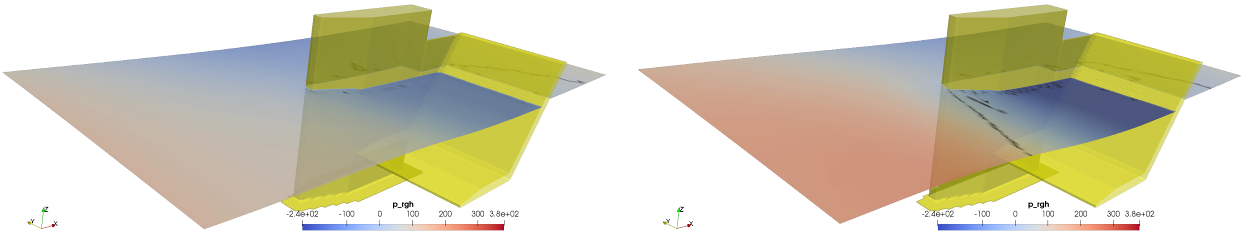

(a) (b)

Figure E.25: Free surface elevation for $\alpha = 0.5$ and different t/T - a) t/T = 0.1, b) t/T = 0.2

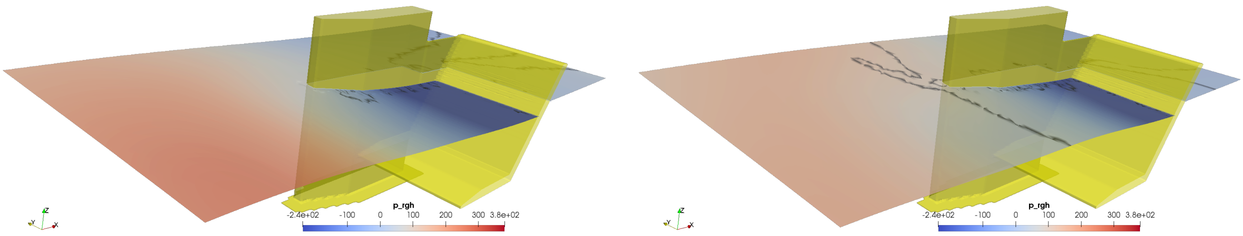

(a) (b)

Figure E.26: Free surface elevation for $\alpha = 0.5$ and different t/T - a) t/T = 0.3, b) t/T = 0.4

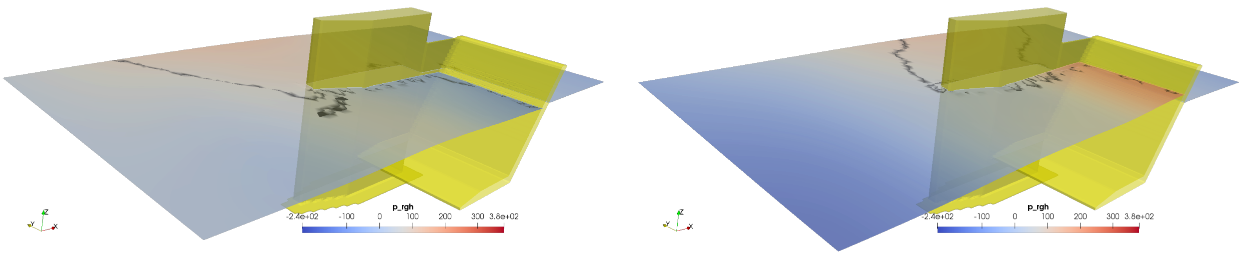

(a) (b)

Figure E.27: Free surface elevation for $\alpha = 0.5$ and different t/T - a) t/T = 0.5, b) t/T = 0.6

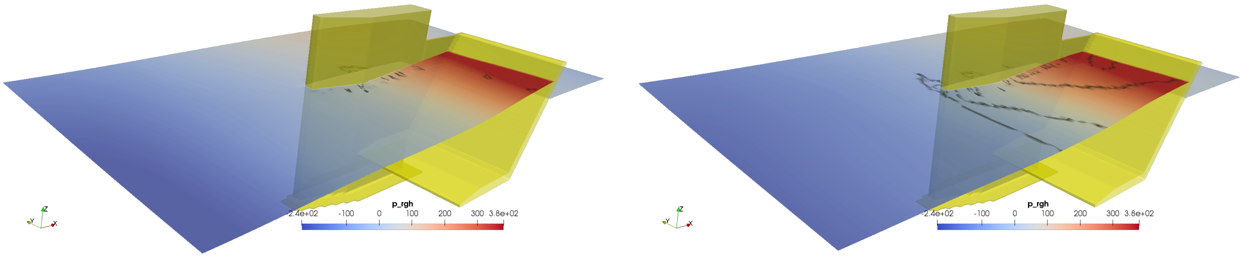

(a) (b)

Figure E.28: Free surface elevation for $\alpha = 0.5$ and different t/T - a) t/T = 0.7, b) t/T = 0.82

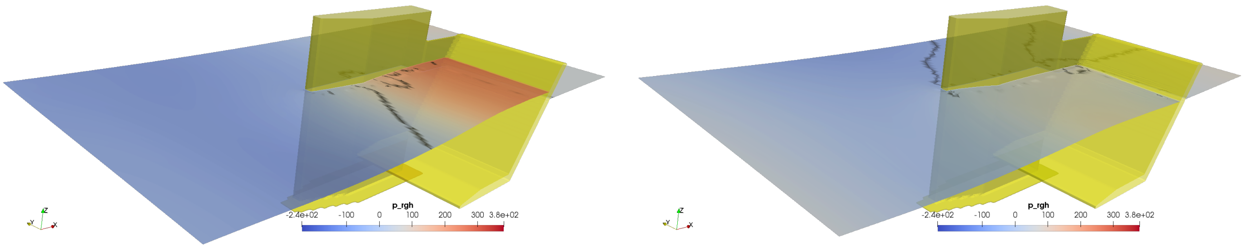

(a) (b)

Figure E.29: Free surface elevation for $\alpha = 0.5$ and different t/T - a) t/T = 0.9, b) t/T = 1

Wave H=0.1 [m] T=1 [s]

In this section the free surface elevation for A5 configuration and wave H=0.1 [m] T=1 [s] is illustrated over one period, which is referred to run time $8 - 9$ seconds on the simulation.

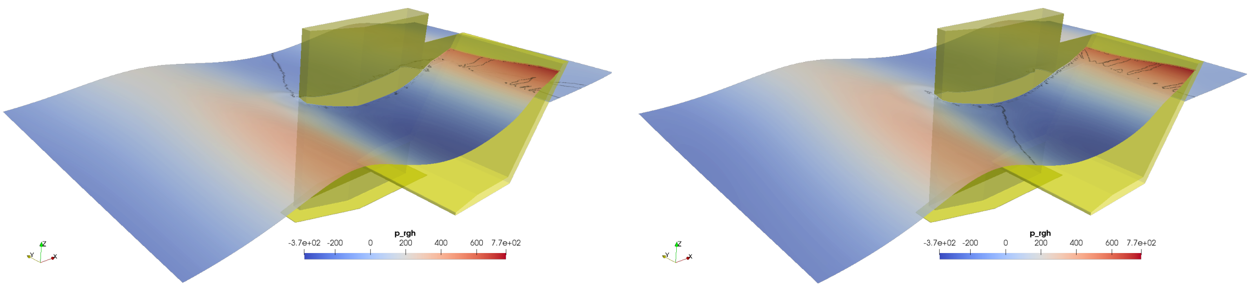

(a) (b)

Figure E.30: Free surface elevation for $\alpha = 0.5$ and different t/T - a) t/T = 0.1, b) t/T = 0.2

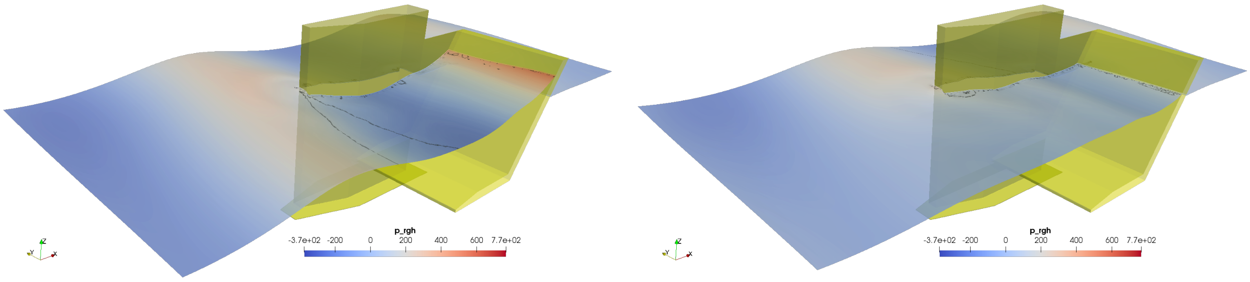

(a) (b)

Figure E.31: Free surface elevation for $\alpha = 0.5$ and different t/T - a) t/T = 0.3, b) t/T = 0.4

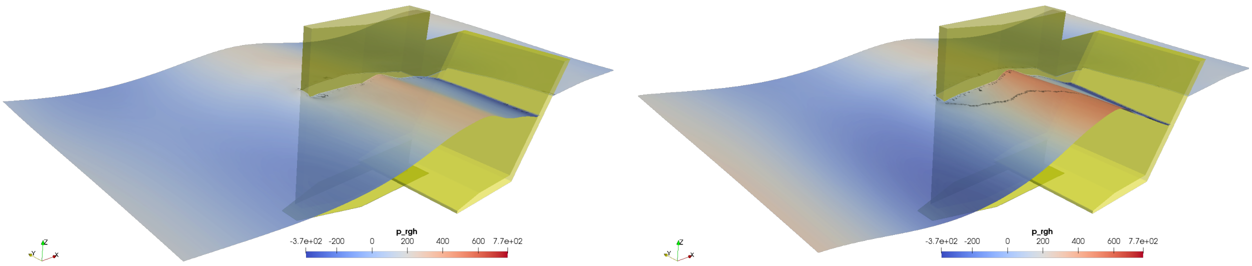

(a) (b)

Figure E.32: Free surface elevation for $\alpha = 0.5$ and different t/T - a) t/T = 0.5, b) t/T = 0.6

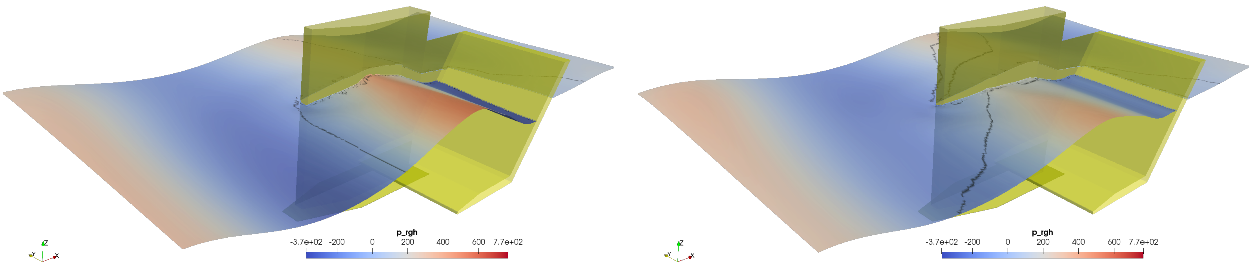

(a) (b)

Figure E.33: Free surface elevation for $\alpha = 0.5$ and different t/T - a) t/T = 0.7, b) t/T = 0.8

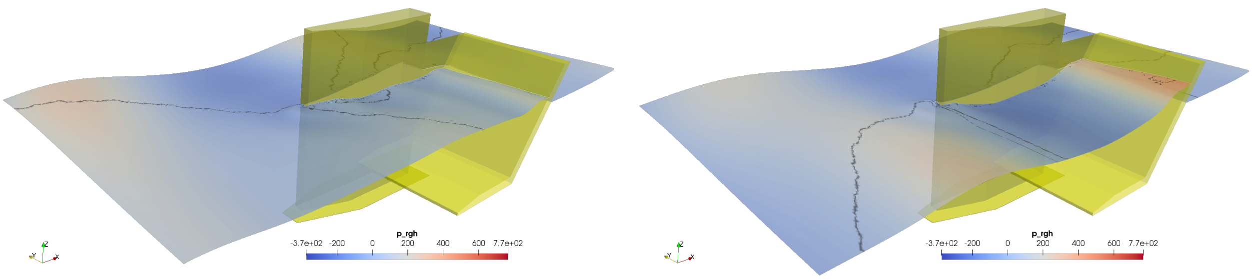

(a) (b)

Figure E.34: Free surface elevation for $\alpha = 0.5$ and different t/T - a) t/T = 0.9, b) t/T = 1

Wave H=0.1 [m] T=2 [s]

In this section the free surface elevation for A5 configuration and wave H=0.1 [m] T=2 [s] is illustrated over one period, which is referred to run time $14 - 16$ seconds on the simulation.

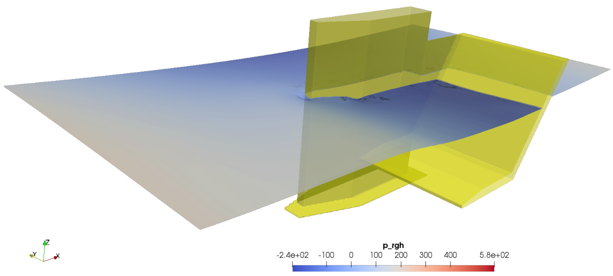

(a)

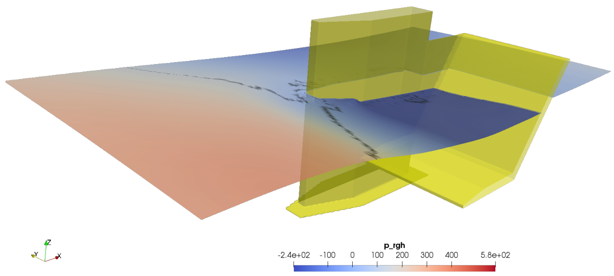

(b)

Figure E.35: Free surface elevation for $\alpha = 0.5$ and different t/T - a) t/T = 0.1, b) t/T = 0.2

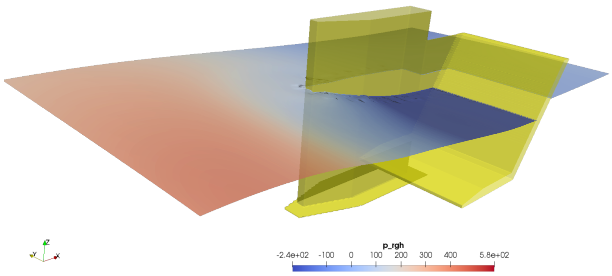

(a)

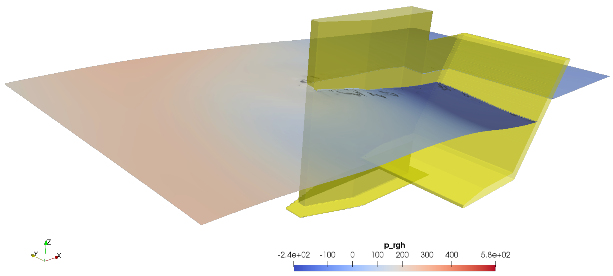

(b)

Figure E.36: Free surface elevation for $\alpha = 0.5$ and different t/T - a) t/T = 0.3, b) t/T = 0.4

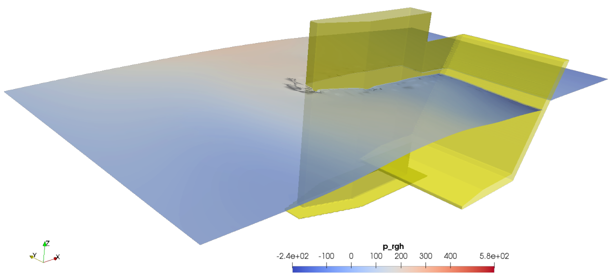

(a)

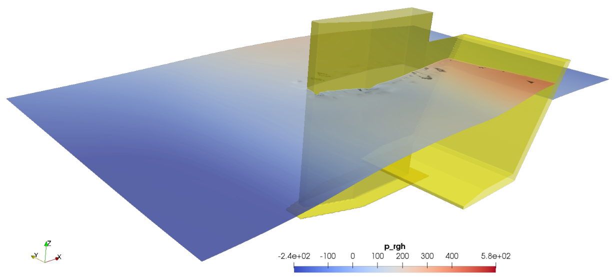

(b)

Figure E.37: Free surface elevation for $\alpha = 0.5$ and different t/T - a) t/T = 0.5, b) t/T = 0.6

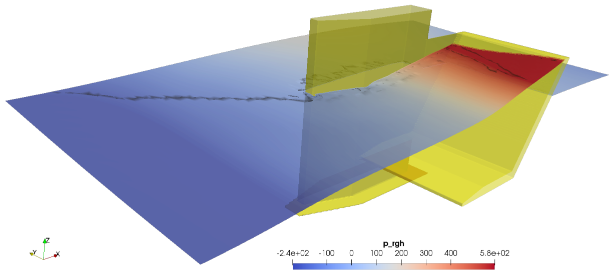

(a) (b)

Figure E.38: Free surface elevation for $\alpha = 0.5$ and different t/T - a) t/T = 0.7, b) t/T = 0.82

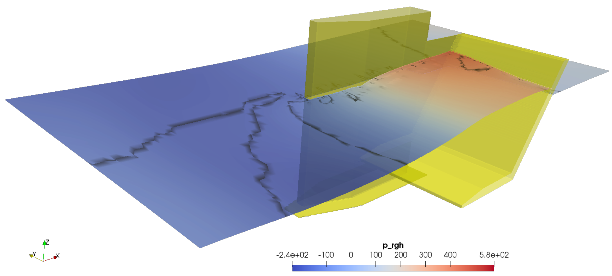

(a) (b)

Figure E.39: Free surface elevation for $\alpha = 0.5$ and different t/T - a) t/T = 0.9, b) t/T = 1

E.4 Vortexes

In this section the Q-factor is illustrated for A4 and A5 chamber configuration and 4 different sea states.

E.4.1 A4 chamber configuration

In this section the Q-factor for A4 chamber configuration is illustrated for 2 different waves over one period.

Wave H=0.06 [m] T=1 [s]

In this section the Q-factor with a value of $Q = 15$ for A4 configuration and wave H=0.06 [m] T=1 [s] is illustrated over one period, which is referred to run time $8 - 8.9$ seconds on the simulation.

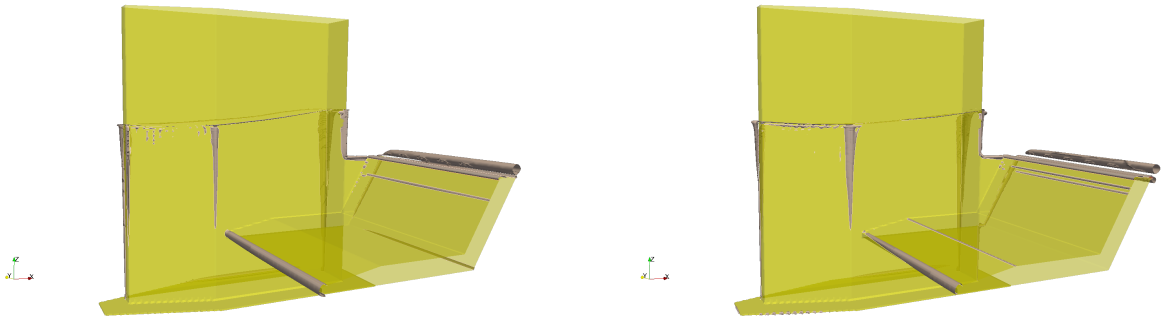

(a) (b)

Figure E.40: Q-factor with $Q = 15$ and different t/T - a) t/T = 0.1, b) t/T = 0.2

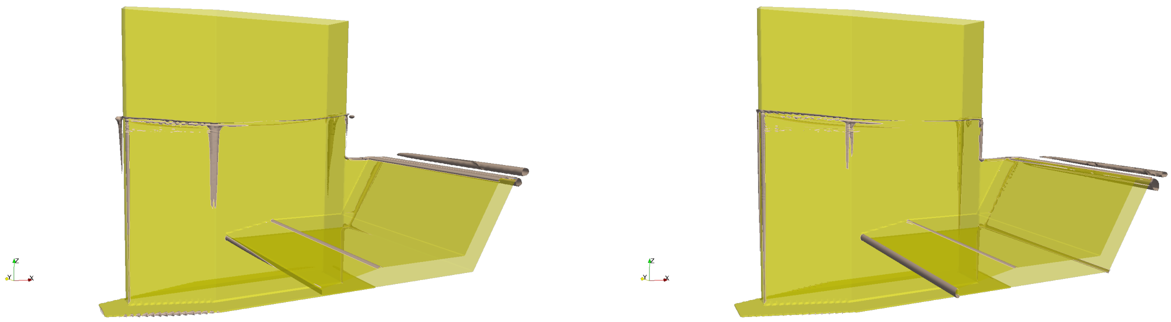

(a) (b)

Figure E.41: Q-factor with $Q = 15$ and different t/T - a) t/T = 0.3, b) t/T = 0.4

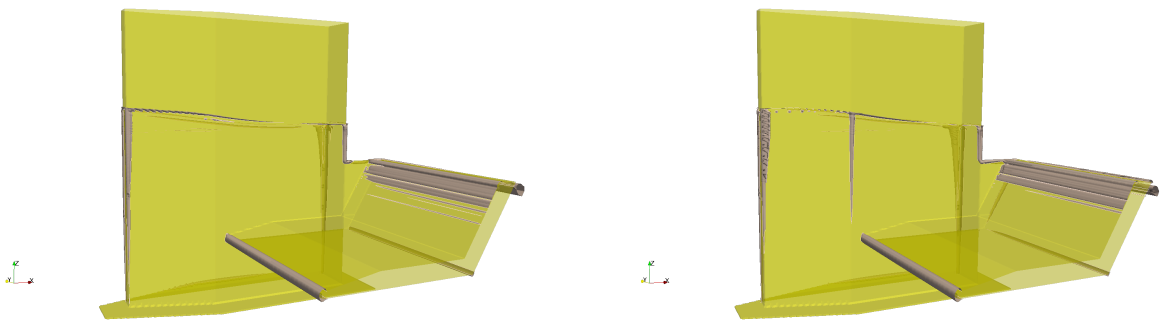

(a) (b)

Figure E.42: Q-factor with $Q = 15$ and different t/T - a) t/T = 0.5, b) t/T = 0.6

In the following time step only t/T = 0.7 is presented as t/T = 0.8 data is corrupted and it is not possible to obtain any data from that specific time.

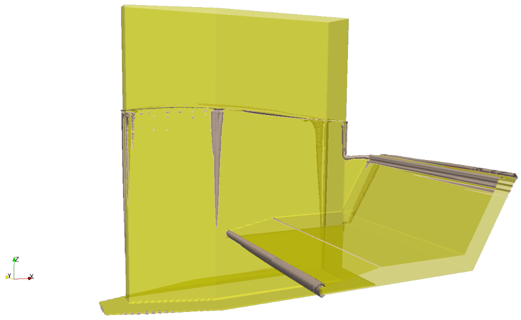

(a)

Figure E.43: Q-factor with $Q = 15$ and different t/T - a) t/T = 0.7, b) t/T = 0.8 (corrupted)

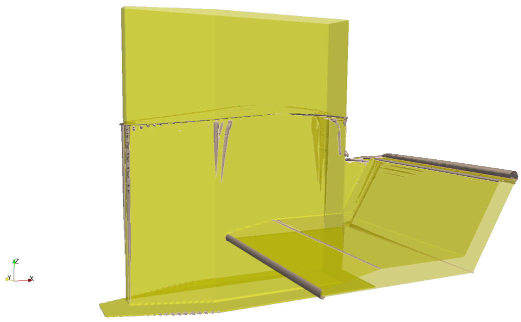

(a)

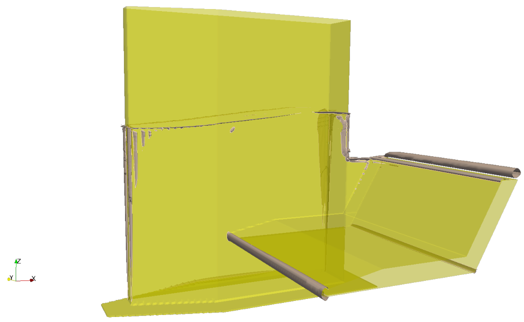

(b)

Figure E.44: Q-factor with $Q = 15$ and different t/T - a) t/T = 0.9, b) t/T = 1

Wave H=0.06 [m] T=2 [s]

In this section the Q-factor with a value of $Q = 15$ for A4 configuration and wave H=0.06 [m] T=2 [s] is illustrated over one period, which is referred to run time $14 - 16$ seconds on the simulation.

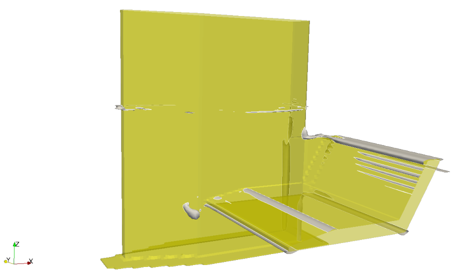

(a)

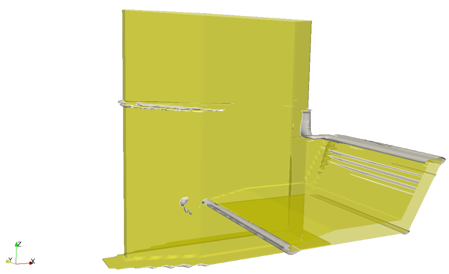

(b)

Figure E.45: Q-factor with $Q = 15$ and different t/T - a) t/T = 0.1, b) t/T = 0.2

(a) (b)

Figure E.46: Q-factor with $Q = 15$ and different t/T - a) t/T = 0.3, b) t/T = 0.4

(a) (b)

Figure E.47: Q-factor with $Q = 15$ and different t/T - a) t/T = 0.5, b) t/T = 0.6

(a) (b)

Figure E.48: Q-factor with $Q = 15$ and different t/T - a) t/T = 0.7, b) t/T = 0.8

(a) (b)

Figure E.49: Q-factor with $Q = 15$ and different t/T - a) t/T = 0.9, b) t/T = 1

Wave H=0.1 [m] T=1 [s]

In this section the Q-factor with a value of $Q = 15$ for A4 configuration and wave H=0.1 [m] T=1 [s] is illustrated over one period, which is referred to run time $8 - 8.9$ seconds on the simulation.

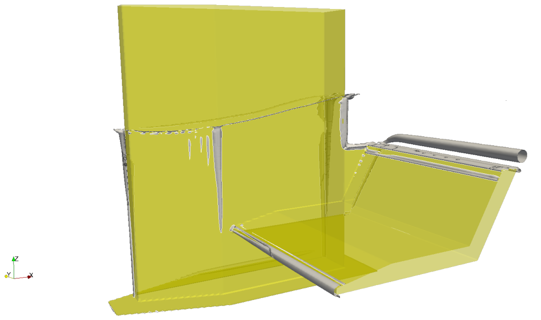

(a)

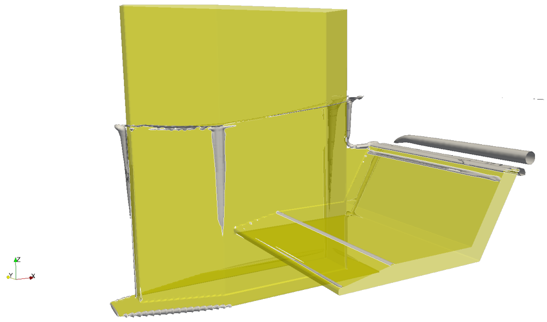

(b)

Figure E.50: Q-factor with $Q = 15$ and different t/T - a) t/T = 0.1, b) t/T = 0.2

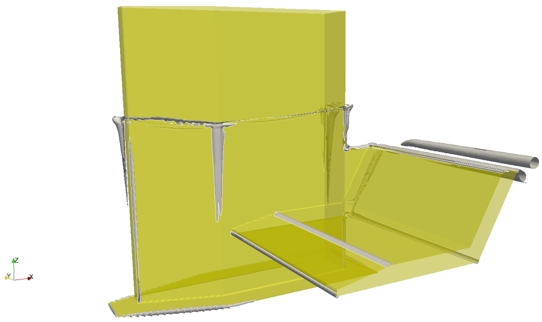

(a)

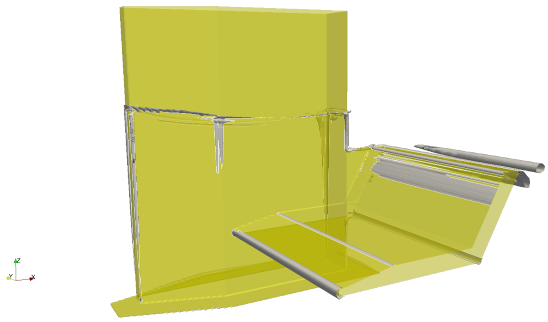

(b)

Figure E.51: Q-factor with $Q = 15$ and different t/T - a) t/T = 0.3, b) t/T = 0.4

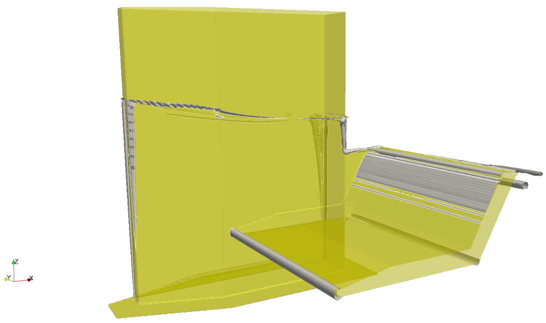

(a)

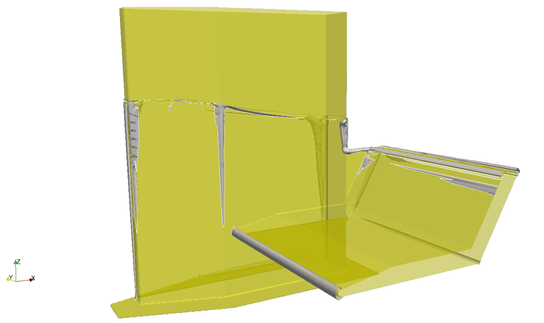

(b)

Figure E.52: Q-factor with $Q = 15$ and different t/T - a) t/T = 0.5, b) t/T = 0.6

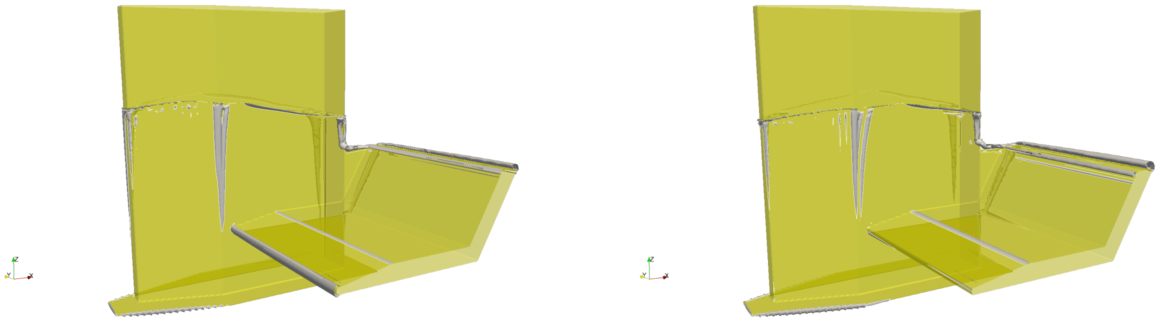

(a) (b)

Figure E.53: Q-factor with $Q = 15$ and different t/T - a) t/T = 0.7, b) t/T = 0.8

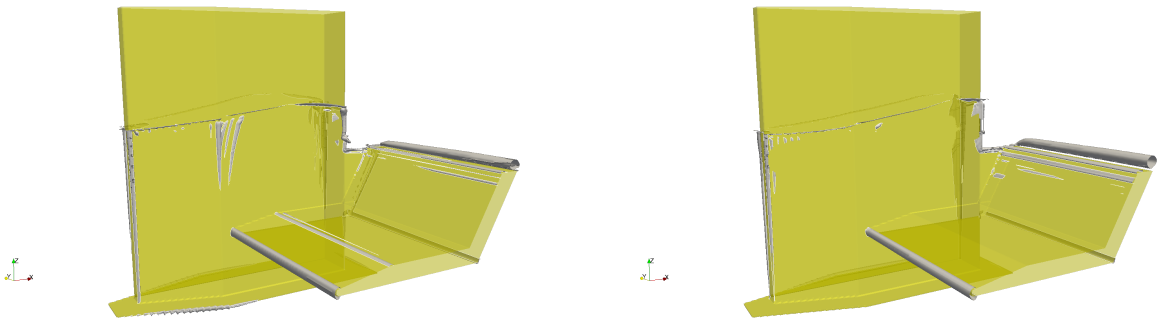

(a) (b)

Figure E.54: Q-factor with $Q = 15$ and different t/T - a) t/T = 0.9, b) t/T = 1

Wave H=0.1 [m] T=2 [s]

In this section the Q-factor with a value of $Q = 15$ for A4 configuration and wave H=0.1 [m] T=2 [s] is illustrated over one period, which is referred to run time $14 - 16$ seconds on the simulation.

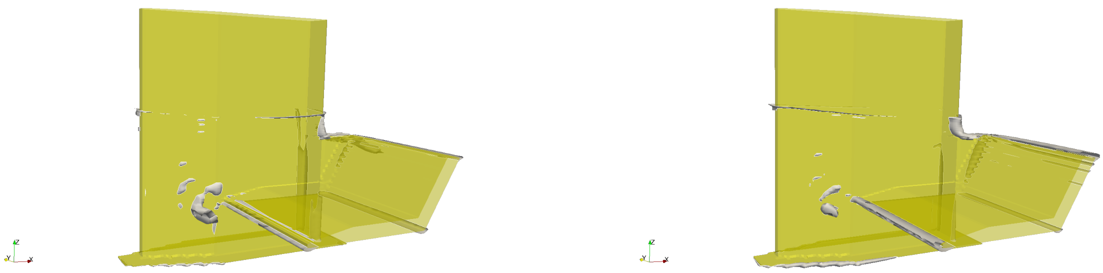

(a) (b)

Figure E.55: Q-factor with $Q = 15$ and different t/T - a) t/T = 0.1, b) t/T = 0.2

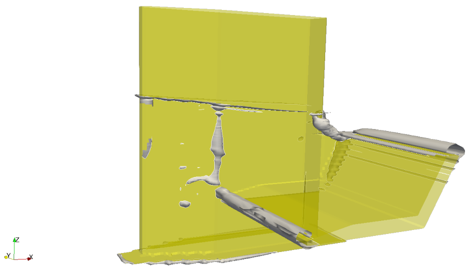

(a)

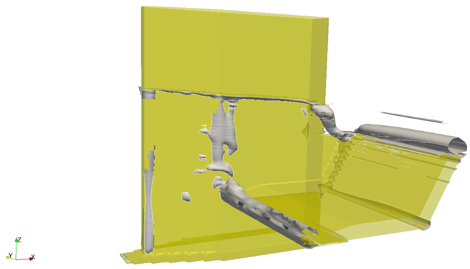

(b)

Figure E.56: Q-factor with $Q = 15$ and different t/T - a) t/T = 0.3, b) t/T = 0.4

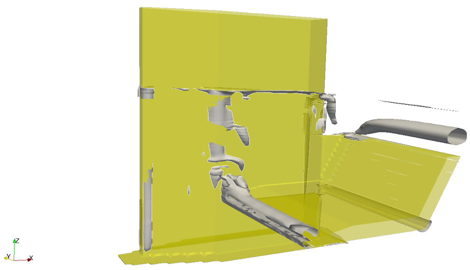

(a)

(b)

Figure E.57: Q-factor with $Q = 15$ and different t/T - a) t/T = 0.5, b) t/T = 0.6

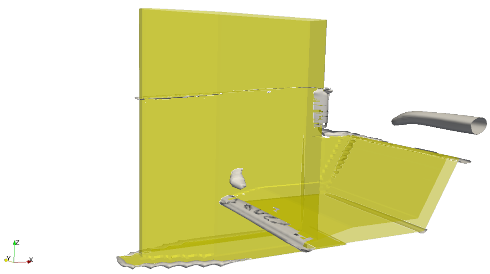

(a)

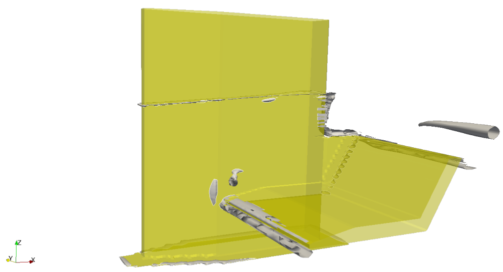

(b)

Figure E.58: Q-factor with $Q = 15$ and different t/T - a) t/T = 0.7, b) t/T = 0.8

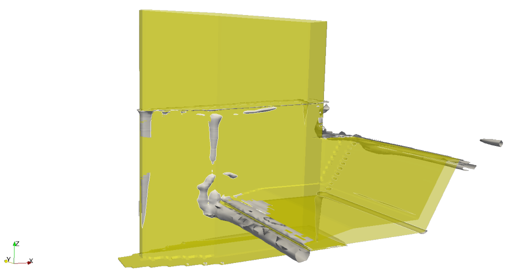

(a)

(b)

Figure E.59: Q-factor with $Q = 15$ and different t/T - a) t/T = 0.9, b) t/T = 1

E.4.2 A5 chamber configuration

In this section the Q-factor for A4 chamber configuration is illustrated for 2 different waves over one period.

Wave H=0.06 [m] T=2 [s]

In this section the Q-factor with a value of $Q = 15$ for A5 configuration and wave H=0.1 [m] T=2 [s] is illustrated over one period, which is referred to run time $14 - 16$ seconds on the simulation.

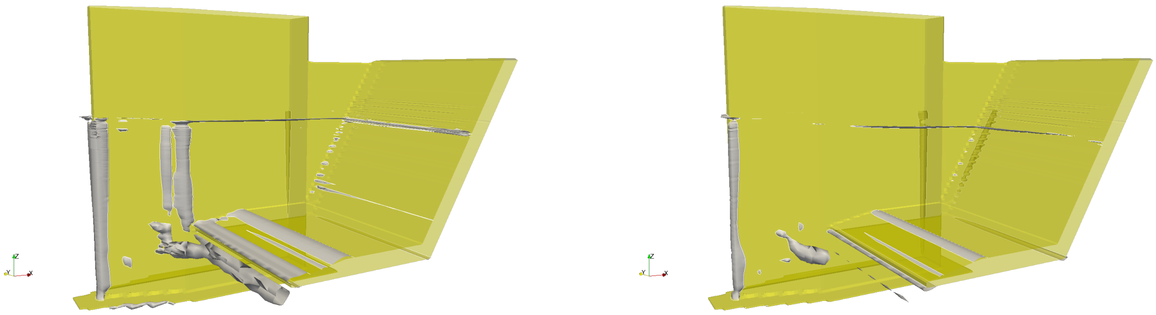

(a) (b)

Figure E.60: Q-factor with $Q = 15$ and different t/T - a) t/T = 0.1, b) t/T = 0.2

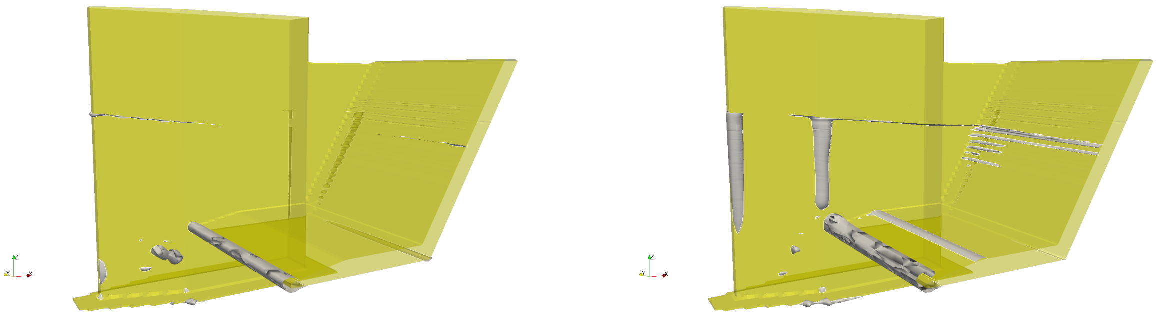

(a) (b)

Figure E.61: Q-factor with $Q = 15$ and different t/T - a) t/T = 0.3, b) t/T = 0.4

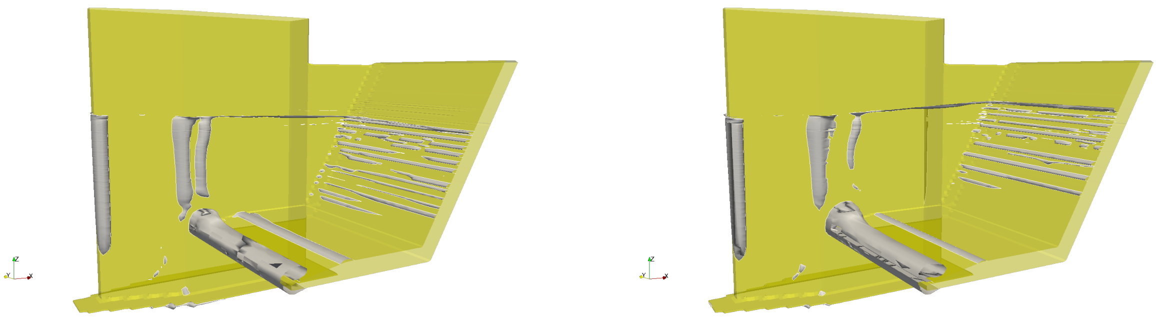

(a) (b)

Figure E.62: Q-factor with $Q = 15$ and different t/T - a) t/T = 0.5, b) t/T = 0.6

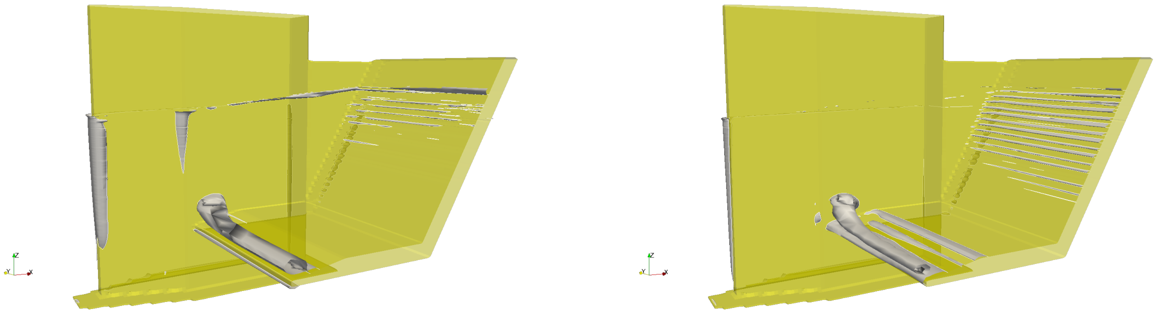

(a) (b)

Figure E.63: Q-factor with $Q = 15$ and different t/T - a) t/T = 0.7, b) t/T = 0.82

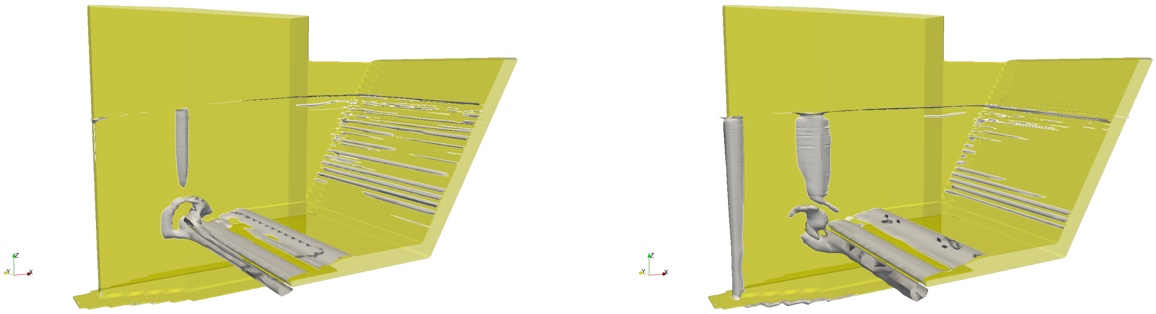

(a) (b)

Figure E.64: Q-factor with $Q = 15$ and different t/T - a) t/T = 0.9, b) t/T = 1

Wave H=0.1 [m] T=1 [s]

In this section the Q-factor with a value of $Q = 15$ for A5 configuration and wave H=0.1 [m] T=1 [s] is illustrated over one period, which is referred to run time $8 - 8.9$ seconds on the simulation.

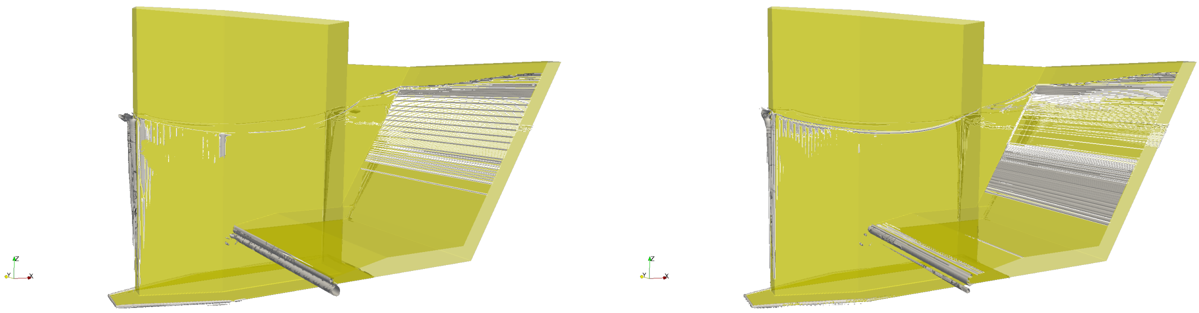

(a) (b)

Figure E.65: Q-factor with $Q = 15$ and different t/T - a) t/T = 0.1, b) t/T = 0.2

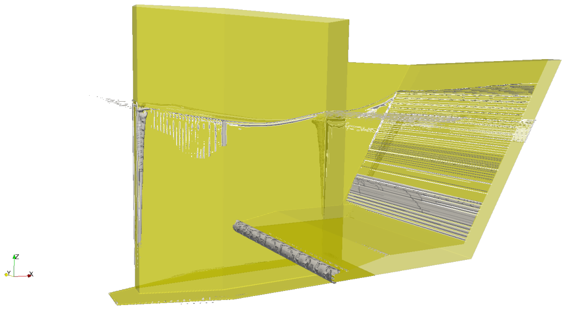

(a)

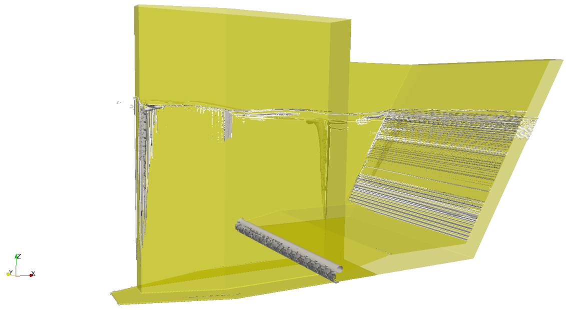

(b)

Figure E.66: Q-factor with $Q = 15$ and different t/T - a) t/T = 0.3, b) t/T = 0.4

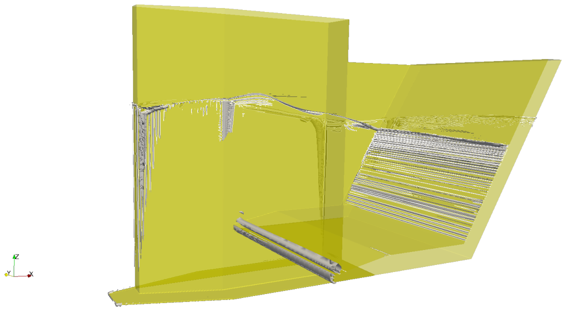

(a)

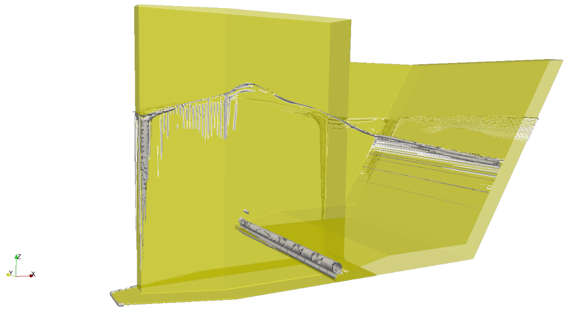

(b)

Figure E.67: Q-factor with $Q = 15$ and different t/T - a) t/T = 0.5, b) t/T = 0.6

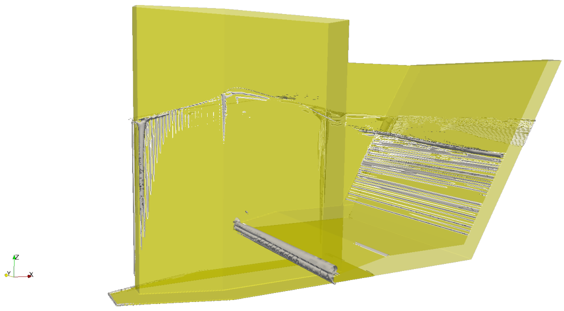

(a)

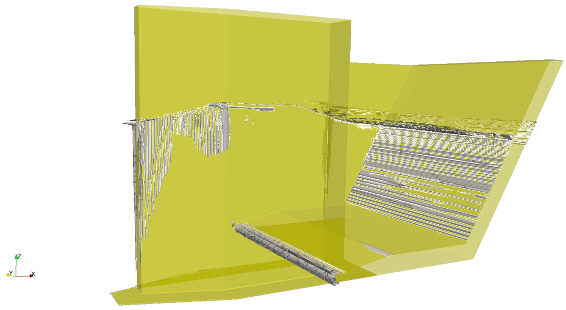

(b)

Figure E.68: Q-factor with $Q = 15$ and different t/T - a) t/T = 0.7, b) t/T = 0.8

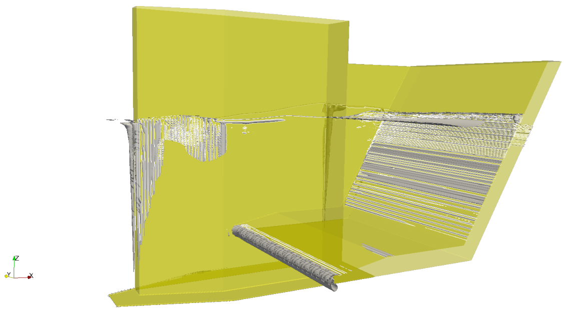

(a)

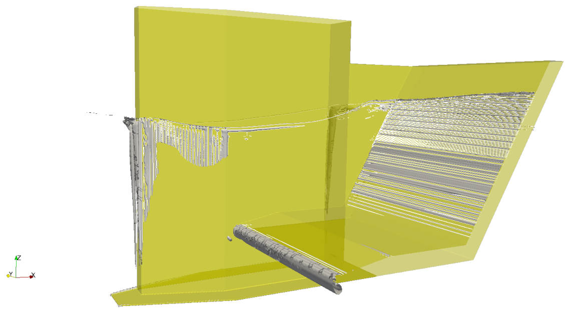

(b)

Figure E.69: Q-factor with $Q = 15$ and different t/T - a) t/T = 0.9, b) t/T = 1

Wave H=0.1 [m] T=2 [s]

In this section the Q-factor with a value of $Q = 15$ for A5 configuration and wave H=0.1 [m] T=2 [s] is illustrated over one period, which is referred to run time $14 - 16$ seconds on the simulation.

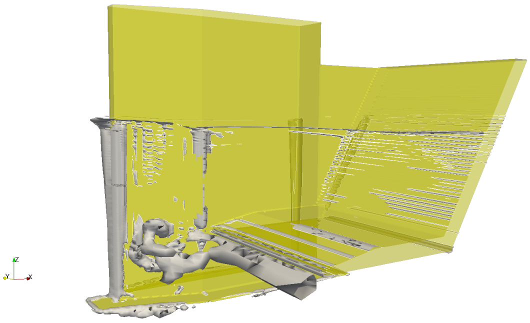

(a)

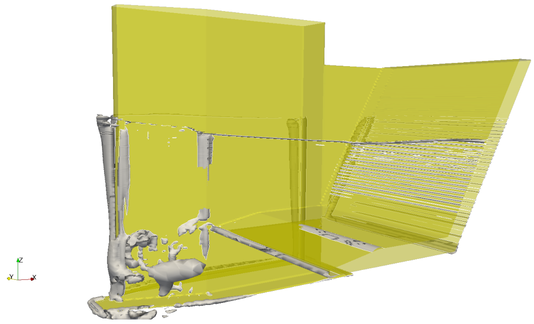

(b)

Figure E.70: Q-factor with $Q = 15$ and different t/T - a) t/T = 0.1, b) t/T = 0.2

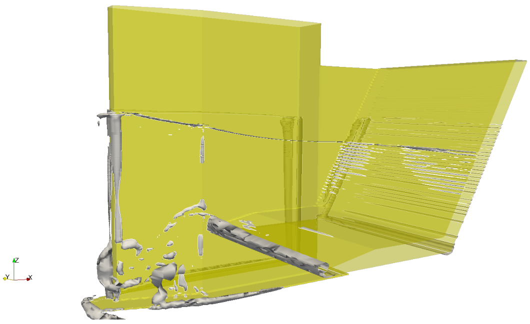

(a)

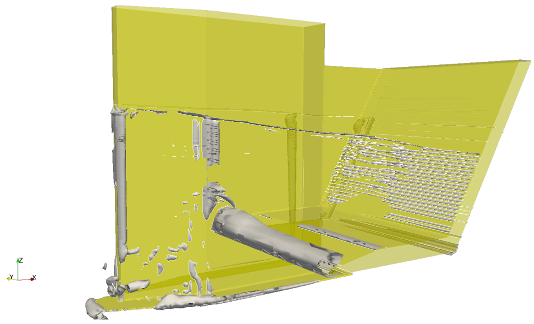

(b)

Figure E.71: Q-factor with $Q = 15$ and different t/T - a) t/T = 0.3, b) t/T = 0.4

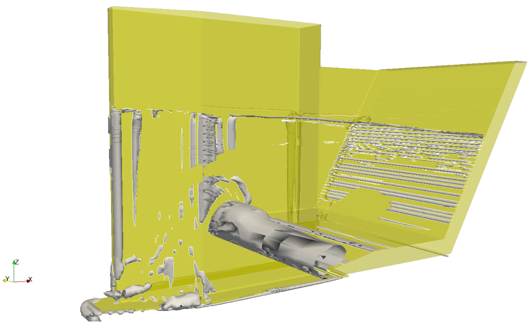

(a)

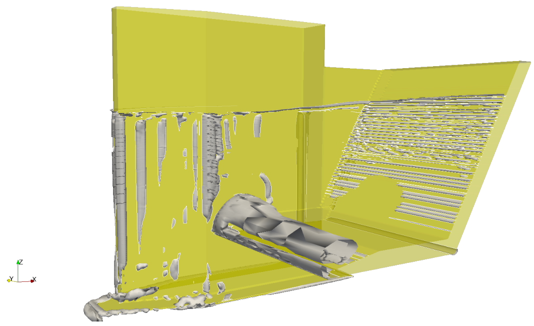

(b)

Figure E.72: Q-factor with $Q = 15$ and different t/T - a) t/T = 0.5, b) t/T = 0.6

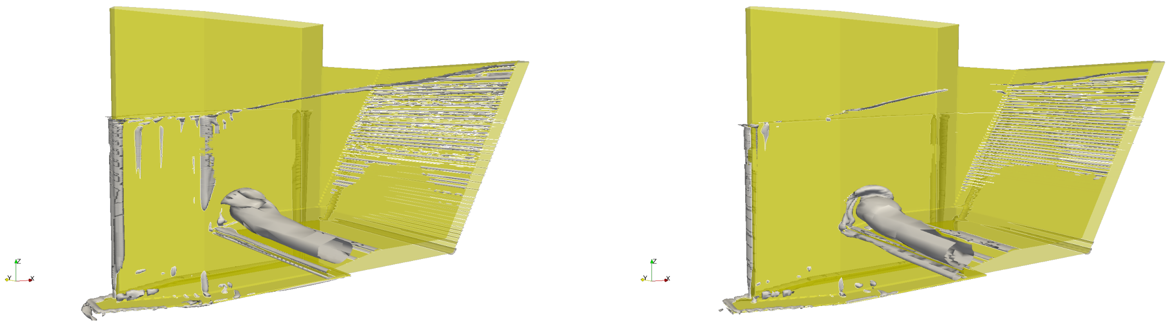

(a) (b)

Figure E.73: Q-factor with $Q = 15$ and different t/T - a) t/T = 0.7, b) t/T = 0.82

(a) (b)

Figure E.74: Q-factor with $Q = 15$ and different t/T - a) t/T = 0.9, b) t/T = 1